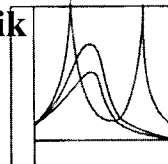
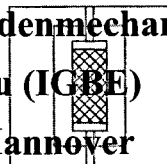
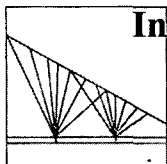
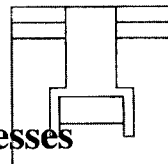
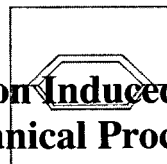
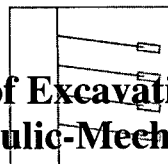
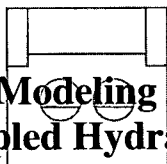
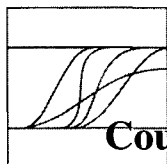
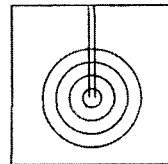
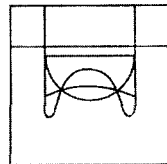
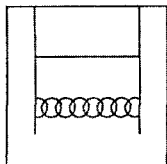
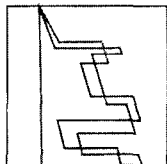


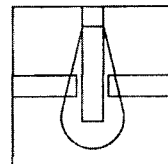
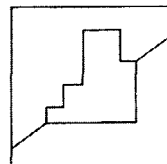
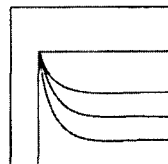
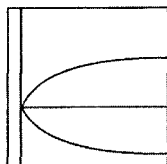
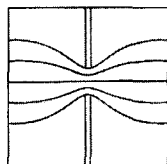
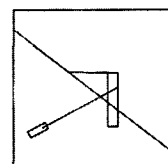
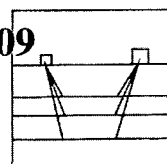
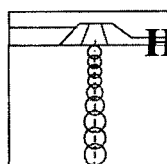
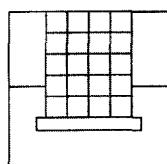
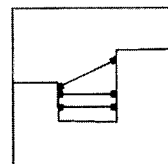
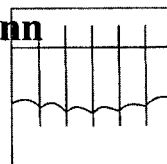
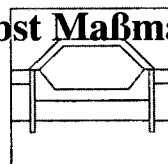
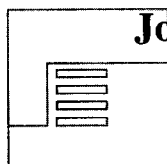
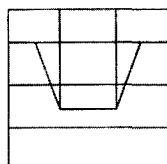
DE10F1362

MITTEILUNGEN

**Institut für Grundbau, Bodenmechanik
und Energiewasserbau (IGBE)
Leibniz Universität Hannover**



**Modeling of Excavation Induced
Coupled Hydraulic-Mechanical Processes
in Claystone**

**von****Hannover 2009**

MITTEILUNGEN

**Institut für Grundbau, Bodenmechanik
und Energiewasserbau (IGBE)
Leibniz Universität Hannover**

Heft 66

**Modeling of Excavation Induced
Coupled Hydraulic-Mechanical Processes
in Claystone**

von

Jobst Maßmann

Hannover 2009

Von der Fakultät für Bauingenieurwesen und Geodäsie der Leibniz
Universität Hannover zur Erlangung des Grades Doktor – Ingenieur
genehmigte Dissertation.

Referent: Prof. Dr.-Ing. Werner Zielke
Korreferenten: Prof. Dr.-Ing. Martin Achmus
Prof. Dr. Ove Stephansson

Tag der Promotion: 23. März 2009

Zugleich erschienen als Bericht Nr. 77/2009 des
Instituts für Strömungsmechanik und Elektronisches Rechnen im Bauwesen,
Leibniz Universität Hannover

Vorwort des Herausgebers

Die vorliegende Arbeit von Herrn Jobst Maßmann behandelt ein Thema aus dem Grenzbe- reich zwischen numerischer Strömungsmechanik und Boden- und Felsmechanik. Sie stellt insofern eine Besonderheit in der Mitteilungsreihe des Instituts dar, als sie hauptsächlich am Institut für Strömungsmechanik und Elektronisches Rechnen im Bauwesen (jetzt Institut für Strömungsmechanik und Umweltphysik im Bauwesen, ISU) entstanden ist. Ich habe allerdings nach der Emeritierung des Kollegen Prof. Zielke die Betreuung von Herrn Maßmann als Stipendiat des DFG-Graduiertenkollegs 615 "Interaktion von Modellbildung, Numerik und Software-Konzepten für technisch-wissenschaftliche Problemstellungen" übernommen. Dies und natürlich die geotechnische Ausrichtung des Themas rechtfertigt die Publikation in dieser Mitteilungsreihe.

Herr Maßmann untersucht vor dem Hintergrund der weltweiten Suche nach einem Wirtschaftsgestein für radioaktive Abfälle die komplexen Vorgänge, die in einem Tonstein durch die Herstellung eines Hohlraums ausgelöst werden. Er konzentriert sich dabei auf die numerische Modellierung hydraulisch-mechanisch gekoppelter Prozesse, und zwar konkret auf den Entwässerungsprozess des Gebirges, auf die Änderung der Gesteinsdurchlässigkeit sowie auf die Entfestigung des Gesteins im Bereich des Hohlraums. In den entwickelten Ansätzen werden unter anderem Materialanisotropie, Schrumpfen und auch Materialschädigung mit einbezogen.

Für die Validierung der Simulationen werden Ergebnisse umfangreicher Messungen herangezogen, die im Rahmen des Tournemire-Projekts in Südostfrankreich durchgeführt wurden. Hierdurch gelingt es Herrn Maßmann, die praktisch wichtigsten Prozesse und Zusammenhänge zu identifizieren und Erklärungen für beobachtete, vorher nicht vollständig verstandene Phänomene zu liefern. Damit ist die Arbeit ein wichtiger Meilenstein für das Verständnis und die Simulation der Vorgänge um einen im Tonstein aufgefahrenen Hohlraum.

Die Arbeit erscheint inhaltsgleich auch in der Mitteilungsreihe des ISU.

M. Achmus

Abstract

Concepts for the numerical modeling of excavation induced processes in claystone are investigated. The study has been motivated by the international discussion on the adequacy of claystone as a potential host rock for a final repository of radioactive waste. The processes, which could impact the safety of such a repository, are manifold and strongly interacting. Thus, a multiphysics approach is needed, regarding solid mechanics and fluid mechanics within a geological context. A coupled modeling concept is therefore indispensable.

Based on observations and measurements at an argillaceous test site (the underground laboratory Tournemire, operated by the *Institute of Radioprotection and Nuclear Safety*, France) the modeling concept is developed. Two main processes constitute the basis of the applied model: deformation (linear elasticity considering damage) and fluid flow (unsaturated one-phase flow). Several coupling phenomena are considered: *Terzaghi*'s effective stress concept, mass conservation of the liquid in a deformable porous media, drying induced shrinkage, and a permeability which depends on deformation and damage. In addition, transversely isotropic material behavior is considered.

The numerical simulations are done with the finite element code *RockFlow*, which is extended to include: an orthotropic non-linear shrinkage model, a continuum damage model, and an orthotropic permeability model. For these new methods the theory and a literature review are presented, followed by applications, which illustrate the capability to model excavation induced processes in principle.

In a comprehensive case study, the modeling concept is used to simulate the response of the Tournemire argillite to excavation. The results are compared with observations and measurements of three different excavations (century old tunnel, two galleries excavated in 1996 and 2003).

In summary, it can be concluded that the developed model concept provides a prediction of the excavation induced hydraulic and mechanical response for a time period of at least ten years. An explanation can be given for the delayed development of an excavation damaged zone. It is caused by the desaturation induced shrinkage.

Keywords: hydraulic-mechanical coupling, numerical modeling, claystone, argillite, Tournemire, excavation, desaturation, EDZ, mine-by-test, anisotropic permeability, anisotropic shrinkage, damage

Kurzfassung

Modellierung von gekoppelten hydraulisch-mechanischen Prozessen infolge von Auffahrungen im Tonstein

In der vorliegenden Dissertation werden Konzepte zur numerischen Modellierung von Prozessen im Tonstein untersucht. Motiviert ist diese Arbeit durch die internationale Diskussion um die Eignung von Tonstein als Wirtsgestein für dieendlagerung radioaktiver Abfälle. Die Sicherheit eines solchen Endlagers in tiefen geologischen Formationen ist durch unterschiedliche Prozesse beeinflusst. Es ist ein Ansatz erforderlich, der sowohl die Festkörpermechanik als auch die Strömungsmechanik in einem geologischen Kontext umfasst. Eine gekoppelte Modellierung der Prozesse ist dabei unumgänglich.

Beobachtungen und Messungen aus einem Felslabor im Tonstein (Tournemire, Südfrankreich, betrieben durch das *Institute of Radioprotection and Nuclear Safety*) bilden die Grundlage für das Modellierungskonzept. Dieses basiert im Wesentlichen auf zwei Prozessen: Mechanik (lineare Elastizität mit Schädigung) und Hydraulik (ungesättigte Ein-Phasen-Strömung). Diverse Kopplungsmechanismen werden berücksichtigt: *Terzaghis* Ansatz der effektiven Spannungen, Massenerhalt des Wassers in einem deformierbaren porösen Medium, trocknungsinduziertes Schrumpfen sowie deformations- und schädigungsinduzierte anisotrope Permeabilität. Transversal isotropes Materialverhalten wird in die Beschreibung einbezogen.

Die numerischen Simulationen werden mit dem Finite-Elemente-Code *RockFlow* durchgeführt, der im Rahmen dieser Arbeit um folgende Methoden erweitert wurde: ein orthotropes nicht-lineares Quell- und Schrumpfungsmodell, ein Kontinuumsschädigungsmodell und ein orthotropes Permeabilitätsmodell. Die Darstellung der Methoden beinhaltet die zugrunde liegende Theorie und eine Einordnung in die Literatur. Es werden Anwendungen vorgestellt, welche die Eignung der Methoden zur Modellierung von Auffahrungsproblemen darstellen.

Der entwickelte Modellansatz kommt in einer umfangreichen Fallstudie zur Anwendung. Den Untersuchungsgegenstand bilden ein Tunnel (1881 aufgefahrene) und zwei Versuchsstollen (1996 und 2003 aufgefahrene) im Felslabor Tournemire. Die Simulationsergebnisse werden mit Beobachtungen in der aufgelockerten Zone sowie Messungen von Porenwasserdrücken und Verschiebungen verglichen.

Zusammenfassend wird festgestellt, dass mit dem gewählten Modellansatz das hydraulische und mechanische Verhalten nach der Auffahrung eines Stollens über einen Zeitraum von mindestens 10 Jahren beschrieben werden kann. Der beobachtete verzögerte Schädigungsmechanismus in der aufgelockerten Zone kann durch Schrumpfen, als Folge der Austrocknung des Gesteins, erklärt werden.

Schlagworte: Hydraulisch-mechanische Kopplung, numerische Simulation, Tonstein, Argillite, Tournemire, Entstättigung, aufgelockerte Zone, anisotrope Permeabilität, anisotropes Schrumpfen, Schädigung

Preface and acknowledgements

The present thesis arose in the years 2004 to 2009 at the *Institute of Fluid Mechanics and Environmental Physics in Civil Engineering (ISU)* at the *Leibniz Universität Hannover*. During the last two years I was supported as a scholarship holder at the *Deutsche Forschungsgemeinschaft (DFG, German Research Foundation)* in the framework of the Research Training Group 615 “Interaction of Modeling, Computation Methods and Software Concepts for Scientific-Technological Problems”.

First of all, I would like to thank my supervisor and principal referee Prof. W. Zielke for the continuous support. He guided and inspired me with his broad experience and gave me the freedom to realize my own ideas. Further, I want to thank Prof. M. Achmus for carefully reading my work and his valuable suggestions as co-referee. As my 2nd co-referee I want to express special thanks to Prof. Ove Stephansson from the *Royal Institute of Technology, Stockholm*, for supporting my work in the DECOVALEX project over years.

For the review of this thesis and helpful suggestions I thank Martin Kohlmeier, Gesa Zieffle, Stefanie Haas, and Torsten Haas.

I would like to express my gratitude to all foregoing members of the groundwater modeling group. Your excellent research and programming over decades bear a well validated and tested finite element code: RockFlow. This code formed the basis for my work. When I started at the institute, the existing groundwater modeling group, at this time composed of Abderrahmane Habbar, Sylvia Moenckes, Martin Kohlmeier, and Gesa Zieffle, extended a warm welcome to me. I was fortunate enough to attend this group. Special thanks to Martin for teaching me the programming of coupled processes with RockFlow and to Gesa. You both gave me the feeling, not being alone with all the problems arising during my work. For sure I will miss the personal as well as the scientific discussions with you. Further, I want to thank the temporary colleague Meike Wulkau and ‘my Hiwi’ Zouhair Nezhi for doing modeling work for me.

I thank our secretary Mrs. Seifert for her amiable support, concerning administrative tasks. Moreover, I would like to thank all the other colleagues at the *ISU* for the always pleasant atmosphere.

Besides the institute, the interdisciplinary *DFG* Research Training Group 615 provided me preciously scientific and social environment. Thanks to all scholarship holders and associated members for many lively discussions and the always constructive but also cheerful atmosphere, especially at the seminars.

My work is highly influenced by the cooperation between the *ISU* and the *Federal Institute of Geosciences and Natural Resources (BGR)*. By this connection, I got well acquainted with Hua Shao, Thomas Nowak, Herbert Kunz, and Stefanie Krug. I appreciated the nice time we had together at all the meetings, workshops, and conferences. The collaborative projects with specific applications gave the motivation I needed to finish my thesis. Furthermore, the *BGR* enabled me to take part in the international DECOVALEX-THMC project. As a result, I learned so much about rock mechanics and coupled modeling in a unique scientific community. I contribute thanks to the whole pleasant fellowship represented by the chairman Chin-Fu Tsang. I also want to mention my task leader Amel Rejeb and my co-workers Alain Millard and Shin-Ichi Uehara for the fruitful collabora-

tion. In this context I gratefully acknowledge the *Institut de Radioprotection et de Sûreté Nucléaire (IRSN)*, personally Amel Rejeb and Karim Ben Slimane, for kindly providing the in situ and laboratory measurements, concerning the Tournemire site.

Finally, I want to pay highest tribute to my parents Gisela and Hinrich and my sister Silke for never failing to believe in me.

Dearest thanks to my fiancée Stefanie. Thank you for your loving support and your patience with me bearing scientific discussions during breakfast on Sunday.

I'm happy and grateful for having all of you around me.

Hannover, April 2009

Jobst Maßmann

Contents

Abstract	iii
Kurzfassung	iv
Preface and acknowledgements	v
Notations	xi
1 Introduction and problem description	1
1.1 Motivation	2
1.1.1 The worldwide problem of radioactive waste	2
1.1.2 The role of coupled simulations	3
1.1.3 The aim of this work	3
1.2 The object of investigation: the Tournemire site	5
1.2.1 Introduction	5
1.2.2 Geology of the site	5
1.2.3 Site exploration	6
1.2.4 Hydraulic properties	7
1.2.5 Mechanical properties	8
1.2.6 Excavation disturbed zone	9
1.2.7 Summary of parameters	10
1.3 Modeling approach	12
1.3.1 Introduction	12
1.3.2 Excavation induced processes	12
1.3.3 Modeling concept	13
1.3.4 Numerical solution	16
1.3.5 Case study	17
1.3.6 Outline	17

2 Methods	19
2.1 The basics	20
2.1.1 Introduction	20
2.1.2 The concept of volume fractions	20
2.1.3 Kinematics	22
2.1.4 Assumptions and simplifications	23
2.1.5 Mechanical quantities	23
2.1.6 Balance equations	24
2.1.7 Constitutive equations	27
2.1.8 Numerical treatment	33
2.2 Hydraulic and mechanical anisotropy	37
2.2.1 Introduction	37
2.2.2 Coordinate system	37
2.2.3 Orthotropic permeability	38
2.2.4 Transversely isotropic elasticity	39
2.2.5 Applications	40
2.2.6 Conclusions	45
2.3 Anisotropic swelling and shrinkage	46
2.3.1 Introduction	46
2.3.2 Modeling of swelling and shrinkage	46
2.3.3 Determination of swelling/shrinkage parameters	48
2.3.4 Alternative approach	50
2.3.5 Conclusions	51
2.4 Continuum damage mechanics	52
2.4.1 Introduction	52
2.4.2 Basic concepts	52
2.4.3 Isotropic damage model	58
2.4.4 Interactions of damage with material models	65
2.4.5 Applications	67
2.4.6 Conclusions	71
2.5 Permeability of deformable porous media	72
2.5.1 Introduction	72
2.5.2 Basic flow models	72
2.5.3 Permeability models	74

2.5.4	Development of an orthotropic strain based permeability model	76
2.5.5	Damage induced permeability	83
2.5.6	Applications	87
2.5.7	Conclusions	91
2.6	Element oriented deactivation of processes	92
2.6.1	Approach	92
2.6.2	Application	93
3	Case study	95
3.1	Introduction	96
3.2	Modeling the desaturation process	98
3.2.1	General remarks	98
3.2.2	Model setup	98
3.2.3	Simulation	100
3.2.4	Sensitivity study	101
3.2.5	Comparison with measurements	107
3.2.6	Conclusions	111
3.3	Modeling the mine-by-test experiment	113
3.3.1	The mine-by-test experiment	113
3.3.2	Interpretation of the measured data	114
3.3.3	Model setup	116
3.3.4	Simulation and comparison with measurements	119
3.3.5	Conclusions	131
3.4	Modeling the excavation disturbed zone	133
3.4.1	General remarks	133
3.4.2	<i>Mohr-Coulomb</i> criterion	133
3.4.3	Continuum damage model	134
3.4.4	Evaluation of stresses	136
3.4.5	Evaluation of permeability	142
3.4.6	Comparison with observations and potential failure mechanisms . .	142
3.4.7	Conclusions	146
4	Summary and conclusions	147
4.1	Summary	148
4.2	Conclusions	150

Bibliography	151
A Appendix: Additional simulation results	169
A.1 Desaturation process	170
A.1.1 Comparison of simulation results with measurements of the 2nd campaign	170
A.2 Mine-by-test experiment	173
A.2.1 Simulation and comparison with measurements	173

Notations

Abbreviations

CDM	continuum damage mechanics, page 52
EDZ	excavation disturbed zone, page 9
IRSN	<i>Institute of Radioprotection and Nuclear Safety</i> , France, page 5
REV	representative elementary volume, page 20
H-M	hydraulic-mechanical, page 3

Indices

comp	compressive, page 8
D	damaged, page 54
dev	deviatoric, page 78
eff	effective, page 28
el	elastic, page 28
f	fluid, page 21
frac	fractured, page 84
g	gaseous, page 21
init	initial, page 30
intact	intact (not fractured), page 84
l	liquid, page 21
n	normal, perpendicular, page 133
rel	relative, page 27
res	residual, page 28
s	solid, page 21
sw	swelling/shrinkage, page 30
t	indicates the value of the old time, page 35
$t + \Delta t$	indicates the (unknown) value of the new time, page 35
th	thermal, page 26
tot	total, page 31
ten	tensile, page 8
vol	volumetric, page 30
π	phase, page 20

Operators

d	differential operator, page 20
\det	determinant operator, page 22
div	divergence operator, page 25
δ_{ij}	<i>Kronecker</i> delta (1 if $i = j$; 0 if $i \neq j$), page 40
∂	partial differential operator, page 22
$\operatorname{grad}(\bullet)$	gradient operator ($= \nabla \bullet$), page 23
$\hat{H}(\bullet)$	<i>Heaviside</i> step function, page 63
$\operatorname{tr}(\bullet)$	trace operator, page 30
$(\bullet)^T$	transverse of (\bullet) , page 24
$\ \bullet\ $	vector norm of \bullet (<i>Euclidian</i> norm), page 121
$(\bullet)^{-1}$	inverse of (\bullet) , page 23
$:$	doubly contracted product, page 26
(\bullet)	temporal derivative of (\bullet) , page 22
\otimes	dyadic product, page 40
$\langle \bullet \rangle$	<i>McAuley</i> brackets, page 61
\propto	proportional to, page 74

Symbols

\mathbb{O}	Fourth rank zero tensor, page 63
\mathbb{I}	fourth rank identity tensor, page 40
$\mathbf{1}$	second rank identity tensor, page 29
\mathring{A}	material parameter for <i>Marigo</i> 's damage evolution model, page 60
a	surface element, page 24
\mathbf{a}	vector of acceleration, page 22
\mathring{B}	material parameter for <i>Marigo</i> 's damage evolution model, page 60
\mathbf{b}	vector of body forces, page 24
\mathcal{B}	body, page 20
c	cohesion, page 133
\mathbb{C}	fourth rank material tensor, page 29
\mathbf{C}	material matrix, <i>Voigt</i> notation, page 30
D	scalar damage variable, page 54
\mathbf{D}	second rank damage tensor, page 55
\mathbb{D}	fourth rank damage tensor, page 55
\mathfrak{D}	damage variable, page 56
e	fracture aperture, page 73
E	<i>Young</i> 's modulus of elasticity, page 28
\mathbf{f}	totally force vector, page 24
\mathbf{F}	deformation gradient, page 23
f_y	yield function, page 134

g	damage criterion, page 59
G	shear modulus, page 29
\mathbf{g}	acceleration due to gravity vector, page 27
H	damage evolution function, page 60
h_{rel}	relative humidity of air, page 9
k	intrinsic permeability (scalar), page 38
k_{rel}	relative permeability, page 27
\mathbf{k}	tensor of the intrinsic permeability, page 27
m	mass, page 21
M_G	2nd <i>van Genuchten</i> parameter, page 28
m_G	1st <i>van Genuchten</i> parameter, page 28
n	porosity, page 21
n^π	volume fraction of phase π , page 20
\mathbf{n}	normal vector, page 24
p	pressure, page 27
p_c	capillary pressure, page 28
p_l	pressure of the liquid phase (pore water pressure), page 27
\mathbb{P}^+	fourth rank positive projection tensor, page 62
\mathbb{P}	fourth rank projection tensor, page 63
Q	source, page 26
\mathbf{q}	vector of flux, page 25
r	damage threshold, page 59
R	strength, page 8
s	fracture spacing, page 74
\bar{s}	spacing of the damage induced fractures (material parameter for damage induced permeability), page 86
S	(liquid) saturation, page 21
T	absolute temperature, page 27
t	time, page 22
u	specific energy, page 26
\mathbf{u}	vector of solid displacements, page 22
V	volume, page 20
v	volume element, page 20
\mathbf{v}	vector of velocity, page 22
x, y, z	global coordinate axes, page 37
\mathbf{x}	spatial point, current configuration, page 22
\mathbf{X}	spatial point, reference configuration, page 22
Y	thermodynamic force conjugated to the damage variable, page 59

Greek symbols

α	<i>Biot</i> coefficient, page 25
β^{sw}	swelling coefficient, page 46
γ^{sw}	swelling exponent, page 47
γ	shear strain, page 29
Δt	time step length, page 35
$\hat{\varepsilon}_i$	<i>i</i> th principal strain, page 62
ε	strain, page 28
$\boldsymbol{\varepsilon}$	vector of strains, <i>Voigt</i> notation, page 30
$\bar{\boldsymbol{\varepsilon}}$	damage effective strain tensor, page 57
$\boldsymbol{\varepsilon}$	linearized strain tensor, page 24
η	specific entropy, page 27
κ	material parameter, page 32
Λ	cross modulus, page 29
$\dot{\lambda}$	damage consistency parameter, page 60
μ_l	dynamic viscosity of the liquid, page 27
$\bar{\mu}$	damage viscosity coefficient, page 61
ν	<i>Poisson</i> 's ratio, page 29
ρ	density, page 21
$\bar{\sigma}$	damage effective stress, page 55
$\hat{\sigma}_i$	<i>i</i> th principal stress, page 133
σ	stress (positive value belongs to tensile stress), page 28
$\boldsymbol{\sigma}$	vector of effective stresses, <i>Voigt</i> notation, page 30
$\bar{\boldsymbol{\sigma}}$	damage effective stress tensor, page 56
$\boldsymbol{\sigma}$	<i>Cauchy</i> effective stress tensor, page 24
$\bar{\tau}$	equivalent strain, page 59
τ	shear stress, page 29
Φ	internal energy dissipation, page 27
ϕ	angle of internal friction, page 133
ψ	free <i>Helmholtz</i> energy, page 27
$\bar{\phi}$	viscous damage flow function, page 61
χ	<i>Bishop</i> parameter, page 31
ξ, η, ζ	local coordinate axes, page 37
ψ^{el}	stored elastic energy, page 29
Ω	second rank void fabric tensor, page 78

Chapter 1

Introduction and problem description

1.1 Motivation

“Radioactive waste presents a potential hazard to human health and the environment and it must be managed so as to reduce any associated risks to acceptable levels.”

International Atomic Energy Agency (IAEA 2006, p. 1)

1.1.1 The worldwide problem of radioactive waste

In the year 2000 the global radioactive waste amounts to about $8.1 \times 10^6 \text{ m}^3$ (not including $1.8 \times 10^9 \text{ m}^3$ waste generated by uranium mining and milling) and $1.8 \times 10^5 \text{ t}$ heavy metal from spent fuel cells (IAEA 2008). The waste mainly originates from the 432 civil nuclear power plants, institutional activities, and defense and weapons. Only a small fraction of the waste is categorized as *high level waste (HLW)* and has to be securely isolated from the biosphere for a long time period. In Germany, a volume of $24,000 \text{ m}^3$ HLW is predicted until the year 2030 (BfS 2007). This waste contains more than 99.9 % of the radioactive activity of all German waste. Even after one million years of storage, the radioactive activity amounts to about 10^6 Bq and still represents a hazard for the biosphere, including humans (BfS 2007). Until today, no final repository for the storage of high level radioactive waste exists worldwide (IAEA 2008). The International Atomic Energy Agency recommends the storage in deep geological formations with a multi-barrier-system, consisting of a host rock as a natural geological barrier and an engineered barrier system (IAEA 2006). The most important criteria for a potential host rock are very low permeability, high thermal conductivity, no tectonic or volcanic activity, no natural resources in the neighborhood, possibility for sealing, high strength, plastic/viscous behavior, lithostatic isotropic in-situ stresses, high sorption potential, high temperature reliability, low content of water and low resolution behavior (BGR 2007a; IAEA 2006; NAGRA et al. 2002). Several rock types are being investigated in order to determine their adequacy. Major test sites for crystalline rocks are located in Sweden (Stripa, Äspö), Canada (Pinawa), Switzerland (Grimsel), U.S.A. (Yucca Mountain), and Japan (Kamaishi) (Bennett and Gens 2008; Tsang et al. 2005). Plastic clay is investigated in Belgium (Mol), rock salt in Germany (Asse, Gorleben) and the U.S.A. (New Mexico, WIPP¹) (BfS 2005; Tsang et al. 2005; Kühn 1986). Indurated clays are explored in underground laboratories in Switzerland (Mont Terri) and France (Bure, Tournemire) (Bennett and Gens 2008; BfS 2007; Tsang et al. 2005). In Germany, the Federal Government is responsible for the safe disposal of radioactive waste, but until today, no decision about the preferred host rock has been made. Thus, the *Federal Institute of Geosciences and Natural Resources (BGR)*, as the government's central advisory agency on geoscientific matters (BGR 2008), is studying all above mentioned rock types (BGR 2007a; Hoth et al. 2007; Kockel and Krull 1995; Bräuer et al. 1994) and is involved in several international research projects. One of these is the

¹ WIPP is an abbreviation for *Waste Isolation Pilot Plant*

DECOVALEX project² (Jing et al. 2008; Stephansson et al. 2006), which deals with the development of numerical models for the simulation of processes in a repository.

1.1.2 The role of coupled simulations

High-level radioactive waste has to be isolated from the biosphere for extremely long periods in deep geological formations. Especially in the near field of the waste container, the host rock is affected by the excavation and the heat production of the waste. Thermal, hydraulic, mechanical, and chemical (*T-H-M-C*) processes have to be expected. These processes could change the properties of the host rock significantly. Furthermore, the complex interaction makes it nearly impossible to treat the processes separately. Hudson et al. (2001) emphasize the importance of coupled T-H-M issues relating a radioactive waste repository. In order to evaluate the impact, coupled numerical modeling of the processes can be a great support for safety assessment. Thus, numerical codes have to be developed, verified and validated.

A general overview of numerical modeling for rock mechanics can be found in Jing (2003). Several codes for the modeling of coupled T-H-M codes have been developed as presented in Rutqvist et al. (2001). In this context, the *DECOVALEX* project plays an important international role (Tsang et al. 2008; Stephansson et al. 2006). The *Institute of Fluid Mechanics and Computer Applications in Civil Engineering (ISEB)*³ of the *Gottfried Wilhelm Leibniz Universität Hannover (LUH)* has participated in this project, funded by the *BGR* and as a result, the finite element code *RockFlow* (see chapter 1.3.4) has been extended in order to simulate hydraulic-mechanically coupled processes (Kohlmeier 2006; Ziefler 2008; BGR 2007b).

Generally, the numerical modeling of coupled processes is not restricted to waste repository. Other important fields of application are: geology, oil/gas reservoir engineering, geothermal energy, geotechnical and environmental engineering, and mining (Stephansson et al. 2003; Xu 2006; Shao and Burlion 2008).

1.1.3 The aim of this work

The work at hand focuses on the development, advancement, implementation, verification, and application of new tools and models for the numerical modeling of claystone. The objects of investigation are a century old tunnel and two new galleries built in indurated clay in the south of France. The aim is an improvement in understanding the processes,

²The *DECOVALEX* project is an international cooperative project initiated by *SKI*, the Swedish Nuclear Power Inspectorate, with participation of about 10 international organizations. The name *DECOVALEX* stands for DEvelopment of COupled models and their VALIDation against EXperiments. The general goal of this project is to encourage multidisciplinary interactive and cooperative research on modeling coupled processes in geologic formations in support of the performance assessment for underground storage of radioactive waste. Four multi-year project stages of *DECOVALEX* have been completed in the past, mainly focusing on coupled thermal-hydraulic-mechanical-chemical processes. Currently, a fifth three-year project stage of *DECOVALEX* is under way, referred to as *DECOVALEX-2011* (Birkholzer et al. 2005).

³Since Aug. 2008: *Institute of Fluid Mechanics and Environmental Physics in Civil Engineering (ISU)* (in the following termed as: *Institute of Fluid Mechanics*)

leading to the observed deferred failure mechanism around the openings. This knowledge could assist in the construction and management of a repository in claystone. For the assessment of the performance and longterm safety, the development of an *excavation disturbed/damaged zone* around excavated openings is an important issue. Alteration of physical properties in this zone could effect the hydraulic conductivity and thus create short-cut pathways (Blümling et al. 2007).

In order to identify the most important processes, the investigated site will be presented in the following section 1.2. Thereafter, a modeling approach will be developed considering in-situ observations (section 1.3). The second chapter deals with the development and description of new tools and models, which are needed to follow up the approach. Emphasis are put on anisotropy, shrinkage, damage and deformation induced permeability change. The developed modeling approach will be applied within the case study, presented in chapter 3.

1.2 The object of investigation: the Tournemire site

1.2.1 Introduction

For the French safety authority, the *Institute of Radioprotection and Nuclear Safety (IRSN)*, France, has selected the Tournemire site in order to be able to expertise the safety report and the conception options for a repository in an argillaceous media. These reports have to be presented by the *French Radioactive Waste Management Agency (ANDRA)*, and concern the Bure site in Meuse/Haute-Marne.

Since 1990, a multidisciplinary research program has been conducted at the Tournemire site, including geological, hydrogeological, geochemical and geomechanical in-situ and laboratory investigations. A summary with emphasis on the geology, the site explorations and material properties is presented in this chapter, based on the following publications: Rejeb et al. (2008b); Deniau et al. (2008); Matray et al. (2007); Cosenza et al. (2007); Rejeb and Cabrera (2006); Rejeb (2005); Constantin et al. (2004); Valés et al. (2004); Rejeb and Cabrera (2004); Patriarche et al. (2004); Charpentier et al. (2003); Rejeb (2003); Cabrera (2002); Zinszner et al. (2002); Boisson et al. (2001); Bonin (1998); Barescut and Michelot (1997); Daupley (1997); Niandou et al. (1997).

1.2.2 Geology of the site

The Tournemire site is located in a Mesozoic marine basin at the southern edge of the French *Massif Central*. The sedimentary formations are characterized by three main Jurassic layers. The argillaceous medium of the Tournemire region consists of a sub horizontal layer (250 m thick) located between two layers of limestone and dolomite (300 and 500 m thick), which constitute two aquifer layers (figure 1.1).

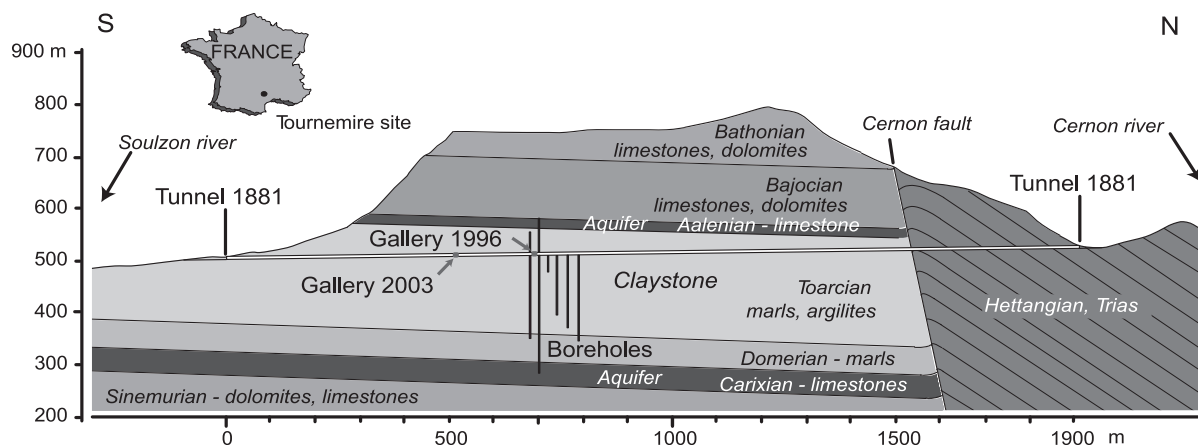


Figure 1.1: Geological cross-section of the site (based on Cabrera 2002).

This argillaceous medium is composed of argillites and marls of Toarcian and Domerian formations. The Tournemire massif is bounded by two valleys of 350 and 400 m depth that correspond to a sub horizontal monocline structure with an E-W regional fault cutting

through the northern part (Cernon fault). These discontinuities are related to different tectonic events (Cabrera 2002). Faults and fractures affect this massif. The investigated area is characterized by unfractured blocks and fractured zones as depicted in figure 1.2. The fractures scale ranges from microcracks up to fault zones. These tectonic induced fractures are mostly filled by calcite.

The argillaceous media is well compacted due to lithostatic pressure and diagenesis. It can be characterized as indurated clay (claystone), composed of thinly bedded minerals, corresponding to an anisotropic texture. The predominant clay fraction (40 – 50 %) consists of illite, kaolinite, chlorite and smectite. Calcite is the predominant carbonate (10 – 30 %). Quartz occurs as grains (10 – 20 %). Further constituents are: muscovite, biotite, albite, k-feldspars, as well as pyrite and organic matter, widespread in the matrix.

The porosity is between 3 and 14 % with an extremely small pore size of about 2.5 nm. The grain density amounts to between 2.7 and 2.8×10^3 kg/m³.

1.2.3 Site exploration

An overview of the Tournemire site with the location of the main bore holes and geological faults is shown in figure 1.2. Photos of the main openings are presented in figure 1.3.

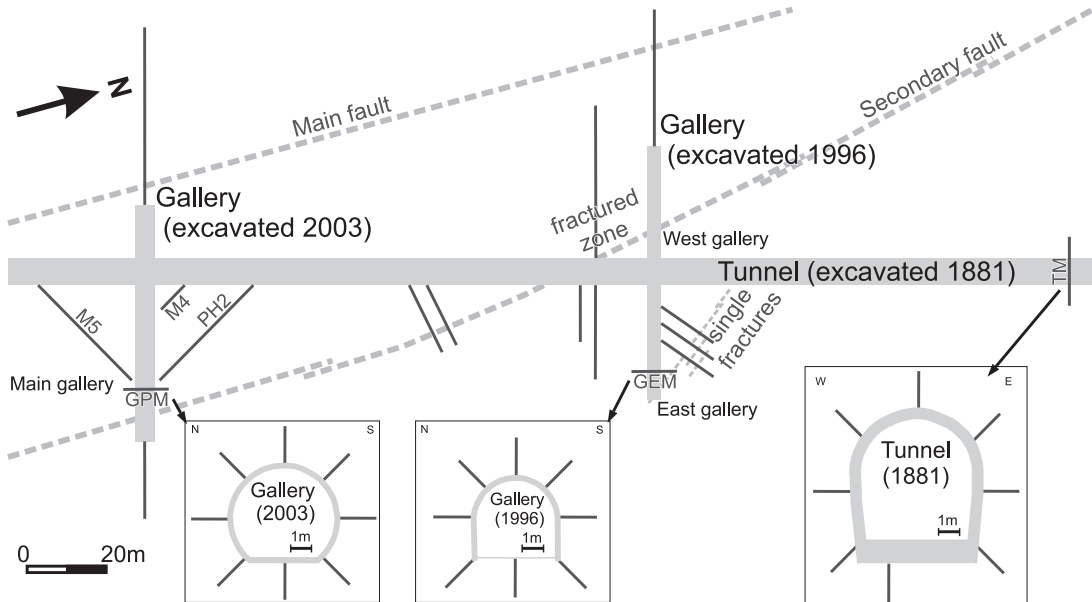


Figure 1.2: The Tournemire underground laboratory of the IRSN. Location of the galleries, main boreholes, and fault zones (based on Rejeb and Cabrera 2004).

The oldest component is a 2 km long tunnel giving direct access to the Toarcian argillite formation of interest. It was excavated manually in 1881 and is covered with limestone masonry. In 1996, two 30 m long galleries perpendicular to the tunnel have been excavated using a road header machine. The west gallery intersects a tectonic fault zone whose presence has been previously identified by radial boreholes drilled in the old tunnel in 1994. The east gallery has been excavated in an unfractured zone. These two galleries



Figure 1.3: Photos of the IRSN exploration site at Tournemire; south portal (a); old tunnel, crossed by the 2003 excavated gallery (b); 1996 excavated gallery, view from the west gallery (c); 2003 excavated gallery, view from the east (d).

are devoted to the study of argillite fracturing, desaturation and resaturation phenomena. In 2003, a new 40 m long gallery has been excavated in order to study the hydraulic and mechanical response of the argillite with respect to the excavation process (Rejeb 2005). For this purpose displacement sensors have been installed in the boreholes M4 and M5, pressure sensors along the borehole PH2 (refer to figure 1.2 and figure 3.23, p. 113). This experiment is called “mine-by-test” (see chapter 3.3). The gallery was excavated using a road header machine with a dust removal system.

Along 8 radial bore holes saturation measurements have been performed with a length between 6 and 15 m around each of the three engineered structures (see figure 1.7). The petrophysical method has been used to determine the saturation of the extracted cores.

1.2.4 Hydraulic properties

The present water circulation takes place along the lower and upper limestone aquifer layers and along the Cernon fault. The water content is very low (1 – 5 %) but the saturation seems to be around 100 %. The argillaceous medium exhibits very low permeabilities. Laboratory measurements yield permeabilities between 10^{-22} and 10^{-18} m², in-situ realized pulse tests between 10^{-21} and 10^{-17} m². The measurements do not reflect any anisotropy, probably due to their inaccuracy (Rejeb and Cabrera 2006). The pore water pressure around the tunnel has been measured with multi mini piezometers. The values vary between 0.14 and 0.6 MPa. Daupley (1997) has studied the relation between

capillary pressure and liquid saturation. The results can be well approximated with the following *van Genuchten* function (cf. chapter 2.1.7.1), as presented in figure 1.4,

$$S = \left(\left(\frac{p_c}{48 \text{ MPa}} \right)^{\frac{1}{1-0.41}} + 1 \right)^{-1}. \quad (1.1)$$

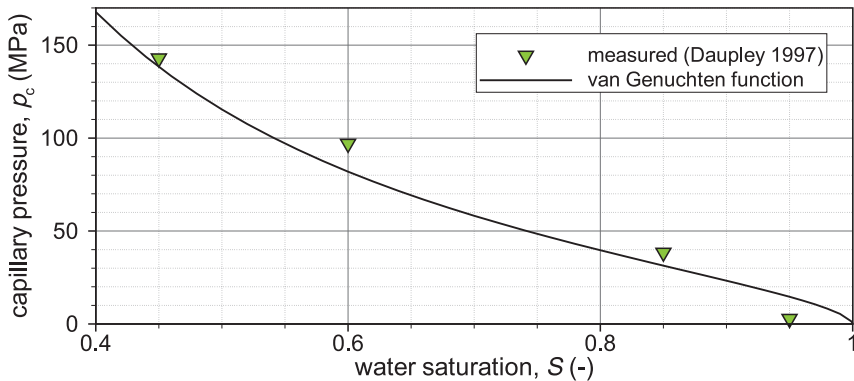


Figure 1.4: Measurements (Daupley 1997) and approximated saturation-capillary pressure relation, using the *van Genuchten* function (see chapter 2.1.7.1).

1.2.5 Mechanical properties

The argillaceous formations of the Tournemire site are well indurated, its mechanical properties are between those of elastic-plastic clay and crystalline rock. Thus, the galleries, which have been excavated in 1996 and 2003, are mechanically stable. Laboratory uniaxial and triaxial tests have brought out the strong transversely isotropic elastic properties. The *Young's* modulus in the bedding plane has been identified as 24.19 ± 4.04 GPa, perpendicular to it as 9.27 ± 4.09 GPa. The compressive strength depends on loading direction and varies between $R_{\text{comp}} = 20$ and 57 MPa. The tensile strength parallel to the bedding plane amounts to $R_{\text{ten}} = 3.6$ MPa.

The failure mechanism has been analyzed with the *Mohr-Coulomb* model (cf. chapter 3.4.2). A friction angle of $\phi = 20^\circ$ and a cohesion c between 6.6 and 10.8 MPa, depending on the loading direction, have been determined. The anisotropy of the failure strength is not very important (Niandou et al. 1997).

Creep tests have shown only low time-dependent strain (Rejeb and Cabrera 2004).

Valés et al. (2004) have investigated the influence of the state of water saturation on the material properties. A distinctive anisotropic swelling/shrinkage behavior has been observed (see chapter 2.3.3.1). Furthermore, the mechanical properties are affected. With lower saturation, the *Young's* modulus, the compressive strength, and the cohesion are increased.

Two sets of measurements of the in-situ stress field have been done by the *hydraulic tests on preexisting fractures (HTPF)* method (Cornet and Valette 1984; Cornet 1993). Although the test series were carried out in the same area, the results differ. One shows an anisotropic stress field ($\sigma_h = 2.1 \pm 1.0$ MPa, $\sigma_v = 3.8 \pm 0.4$ MPa, and $\sigma_H = 4.0 \pm 2.0$ MPa) and the other an isotropic one ($\sigma_h = \sigma_v = \sigma_H = 4.32 \pm 1.13$ MPa).

1.2.6 Excavation disturbed zone

During an excavation new surfaces are being created, which leads to a significant change in the surrounding stress field. The radial stresses (normal to the wall) vanish as long as no support is built. The other stress components increase, which can lead to a failure mechanism. This process can be influenced by hydraulic-mechanically coupling phenomena (Blümling et al. 2007). A compaction could lead to an increase of the pore water pressure, which influences the mechanical reaction by the *effective stresses* (see chapter 2.1.7.4 and 2.2.5.3). Further effects can arise due to the contact of the rock with atmospheric or ventilated air. The region around an excavation, which is affected by this kind of processes, is called *EDZ* (excavation disturbed zone), which may include a damaged zone. In the framework of performance assessment a precise distinction is made between an *excavation disturbed zone* (without negative effects on the long-term safety) and an *excavation damaged zone*, where significant changes in flow and transport properties due to hydraulic-mechanical and geochemical alteration occur (Blümling et al. 2007).

The Tournemire site provides the opportunity to study the EDZs around three openings at different time scales. The EDZ around all openings have been studied by geological mapping, measurements of ultrasonic velocity, permeability, and water saturation. Around the 1881 excavated old tunnel a distinctive fractured zone can be observed, as shown in figure 1.5. The zone of tangentially oriented fractures around the opening (“onion shape”) extends 0.7 m on average, but extensions up to 3 m have been observed. In this zone the permeability is increased up to five orders of magnitude (Matray et al. 2007). Around the



Figure 1.5: Fractured zone around the 1881 excavated tunnel. View of the floor of the 1996 excavated gallery.



Figure 1.6: Horizontal desaturation fractures at the wall of the 1996 excavated gallery. On the right: measuring device for crack aperture.

new galleries no damaged zone like this has been found. Shortly after the excavation of the 1996 and 2003 excavated galleries, small fissures occur at the sides and working faces of the gallery, as shown in figure 1.6. A strong correlation between the aperture of these fissures with the humidity ($h_{\text{rel}} = 40 \dots 100 \%$) and temperature ($\vartheta = 6 \dots 16 \text{ }^{\circ}\text{C}$) of the ambient air has been observed (Rejeb and Cabrera 2006). In the wet summer time, the fractures are nearly closed, in the dry winter time, they are open (see chapter 2.3.3.2). The cores extracted around the galleries possess microcracks, which are mainly oriented parallel to the bedding plane. The fractured zone measures about 40 cm. As a result, in figure 1.7 the profiles of the three openings are plotted together with the fractured zones at this cross section and the boreholes. The main results of the extensive investigation program, carried out by the *IRSN*, are summarized in table 1.1.

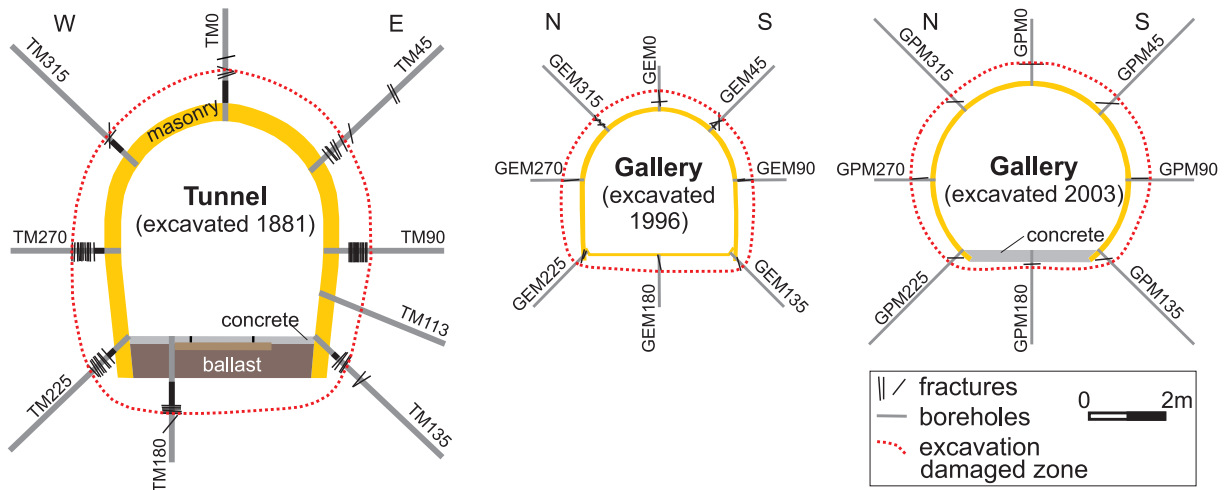


Figure 1.7: Profiles of the three openings and the surrounding fractured zones at one cross section (after Rejeb and Cabrera 2006).

Table 1.1: Characterization of the excavation disturbed zones around the three openings at the Tournemire site after Rejeb and Cabrera (2006) (*1), Rejeb et al. (2008b) (*2), and Matray et al. (2007) (*3), respectively.

	1881 excavated tunnel	1996 excavated gallery	2003 excavated gallery
(*1)	fracture shape	tangential “onion skin”	parallel to stratification
(*1), (*3)	extent of damaged zone	$0.22 \dots 0.33 \times r$ (up to $1.0 \times r$)	$0.20 \dots 0.22 \times r$
(*1)	extent of desaturated zone	$0.3 \dots 0.6 \times r$	$0.2 \dots 0.4 \times r$
(*2)	mechanically disturbed zone		$4.0 \times r$
(*2)	hydraulically disturbed zone		$6.0 \times r$
(*2)	by desaturation disturbed zone		$0.5 \times r$

r denotes the averaged radius of the corresponding opening:

$r_{\text{tunnel}} = 3.0 \text{ m}$, $r_{1996 \text{ gallery}} = 2.0 \text{ m}$, $r_{2003 \text{ gallery}} = 2.5 \text{ m}$.

1.2.7 Summary of parameters

In table 1.2 the input parameters which are needed for the simulation of the processes at the Tournemire site are listed. Since the measurements vary mostly in a range, a reference value is given. In order to reach a better agreement with measurements of the mine-by-test experiment, some reference parameters have been changed slightly for the corresponding simulations.

The parameters will be discussed in detail in the following chapters.

Table 1.2: Summary of material and simulation parameters.

Parameter	Measured	Reference	“Mine-by-test”	Unit
<i>Hydraulics</i>				
density of water, ρ_1		1000		kg/m^3
viscosity of water, μ_1		5.0×10^{-6}	1.0×10^{-6}	m^2/s
initial permeability, k	$10^{-22} \dots 10^{-17}$	10^{-20}	0.2×10^{-20}	m^2
damage-permeability parameter, \bar{s}		10^{-6}		m
<i>van Genuchten</i> parameter				
m_G	(cf. figure 1.4)	0.41		-
M_G		48.0		MPa
initial porosity, n_{init}	$0.03 \dots 0.14$	0.09		-
initial pore water pressure, p_{init}	$0.14 \dots 0.6$	0.5	0.2	MPa
<i>Mechanics</i>				
<i>Young’s modulus</i>				
in bedding plane, $E_x = E_y$	$20.15 \dots 28.23$	24.19		GPa
vertical to bedding plane, E_z	$5.18 \dots 13.36$	9.27		GPa
isotropic assumption, E		16.73	12.50	GPa
<i>Poisson’s ratio</i>				
ν_{xz}	$0.14 \dots 0.20$	0.17		-
ν_{zy}	$0.17 \dots 0.23$	0.20		-
isotropic assumption, ν		0.185		-
shear modulus, G_{xz}	$3.46 \dots 4.42$	3.94		GPa
<i>Mohr-Coulomb</i> criterion				
cohesion, c	$6.6 \dots 10.8$	6.6		MPa
angle of internal friction, ϕ	20.0	20.0		°
<i>damage model (Marigo)</i>				
initial damage threshold, r_{init}		20.0		kPa
evolution parameters, \dot{A} , \dot{B}		$10^6, 0.2$		-
damage viscosity coefficient, $\bar{\mu}$		0.001		-
initial stress, σ_{init}	$-1.1 \dots -6.0$	-4.32	-5.0	MPa
<i>Swelling/shrinkage</i>				
power-law model: (*1)				
initial swelling strain, $\varepsilon_{\text{init}}^{\text{sw}}$		0.0		-
reference saturation, $S_{\text{init}}^{\gamma_{\text{sw}}}$		1.0		-
swelling coefficient, $\beta_x^{\text{sw}} = \beta_y^{\text{sw}}$		0.0022		-
swelling coefficient, β_z^{sw}		0.0068		-
isotropic assumption, β^{sw}		0.0022		-
swelling exponent, $\gamma_x^{\text{sw}} = \gamma_y^{\text{sw}}$		4.55		-
swelling exponent, γ_z^{sw}		6.51		-
isotropic assumption, γ^{sw}		4.55		-

*1) power-law swelling/shrinkage model (chapter 2.3): $\varepsilon^{\text{sw}} = \varepsilon_{\text{init}}^{\text{sw}} + \beta^{\text{sw}}(S^{\gamma^{\text{sw}}} - S_{\text{init}}^{\gamma^{\text{sw}}})$

1.3 Modeling approach

1.3.1 Introduction

For the performance assessment of a repository a high level of understanding is required, including the understanding of observed phenomena (Tsang et al. 2005). In addition to laboratory and in-situ investigations, the use of numerical simulations can assist. Modeling of natural rocks is a complex issue. The behavior is influenced by a large number of different processes. It would be impossible to model all processes and their interactions. In the sense of classical engineering, a restriction to the most important issues is needed. This decision has to be made with consideration of the specific questions. Thus, the resulting model is limited generally to a specific case study. A comparison of simulation results with measurements or observations is indispensable. In this way, the model approach could be evaluated and improved.

The observations at the Tournemire site introduce the question:

How does the failure mechanism around the excavations happen?

This question is the starting point for the following considerations:

Which processes are involved, which are the most important ones and how can they be modeled?

1.3.2 Excavation induced processes

From the mechanical point of view, three influencing sources during the excavation stage can be distinguished. The first one is due to the excavation method itself, the second due to stress redistribution and the third is caused by back pressure of the drift support. At the Tournemire site a tunnel boring machine has been used and hence, only minor influence can be expected. The drift support does not produce a considerable back pressure, because the excavated openings have been self supporting. In consequence, the most important influence is given by the stress redistribution. The magnitude is mainly given by the in-situ stresses and leads in general to a spontaneous and delayed deformation process. The deformation can be associated with irreversible strains, fracturing, damage and a change of mechanical, hydraulic and chemical properties. Especially under undrained conditions, a deformation induced pore size change leads to a pore pressure response, which in turn should influence the mechanical response. This effect is enhanced by the low permeability of the host rock.

After the construction of the drift, rock creep and change of pore pressure could still lead to a transient deformation process, but additional processes might happen in the open drift stage. The contact of the rock with atmospheric air, maybe enforced by ventilation, could lead to a dehydration near the drift surfaces. This dehydration is of special interest in argillaceous rock, which is sensitive to water saturation. Usually, dehydration strengthens the rock, but it also causes contraction and this could induce tensile failure. Furthermore, the hydraulic flow field is influenced. The dehydration initiates a two-phase flow in the near field, air can enter into the rock. This oxidizing condition may cause chemical and biological activities, especially if the rock has not been previously exposed to aerobic conditions. Additional effects can be caused due to temperature change.

Also the permeability of the host rock is influenced by several processes. If the stress around the excavation does not exceed the rock strength, only a small decrease in radial direction and increase in tangential direction could be expected. The initiation of two-phase flow leads to a decrease due to the reduction of relative water permeability value. Indeed, the largest potential on permeability increase is given by rock failure coming along with fracturing.

1.3.3 Modeling concept

Before a numerical simulation can be applied, a physical model conception is needed. Therefore, several simplifications are adopted. In the classical engineering manner, a model has to be as simple as possible, but as complex as needed. In the following, contemplable modeling concepts will be briefly presented and discussed with respect to their capacity to model the main observed phenomena. A meaningful modeling of the excavation induced processes can be done only by the coupling between different models.

Linear elasticity is a simple approach for modeling a linear reversible stress-strain behavior of a material. Nevertheless, laboratory experiments have indicated the applicability, as long as the strength of the material is not exceeded. Linear elasticity is chosen as the basis of the mechanical model.

Plasticity is a classical approach to describe rate independent non-linear stress-strain behavior and can be used to investigate shear induced failure of geomaterials. It is understood as material slip along zones of decohesion, associated with irreversible strains. The plastic area is defined by a stress criterion: a yield surface, defined in the principal stress space. Laboratory experiments have shown, that the material behavior of the Tournemire argillite under compression can be modeled well by an elastic-plastic model. A *Mohr-Coulomb* model is recommended, but even so, its yield criterion is not exceeded by the stress redistribution, caused by the excavation process. Under tension, geomaterials show in general brittle behavior; thus, only a small amount of plastic strain could be expected before material failure. The emphasis of the work at hand will be put on tensional behavior and the pre-plastic behavior under compression. As a consequence, the *Mohr-Coulomb* yield criterion will be used as a post-processing criterion only.

Creep is understood as a rate dependent stress-strain relation. Laboratory experiments have shown only minor viscous behavior. As a first approach, viscous behavior will not be considered.

Discrete fracture mechanics simulates the fractures itself, including fracture propagation and material behavior in the near field of a single fracture. Since its large numerical effort, it is mainly used for small problems and to determine material properties on the macroscale by an upscaling procedure. There are two main reasons why no discrete fracture model is used: firstly, the heavy numerical effort for the Tournemire case study and secondly the near field of every single crack is not of special interest.

Damage is defined as irreversible degradation of mechanical properties. The observed tensile fissures at the wall of the new galleries could be modeled by a damage model. Even if the observed fissures are not on the microscale, the continuum approach seems to be feasible due to evenly distribution of fissures and no localization effect. The applied model has to be as simple as possible since there exist no specific experiments on the damage behavior in tension. The measured tensile strength of the material could assist calibrating the damage model. The effect of microcrack closing, as observed in-situ, can be modeled by a damage model with reactivation of material stiffness under compression.

Darcy flow adopts a linear relation between the liquid pressure gradient and flux velocity. It is the basis for simulating groundwater flow, as long as low fluid velocities can be assumed. The Tournemire argillite exhibit very low permeabilities. Hence, the assumption of low velocities can be made and the *Darcy* flow can be accepted for the hydraulic model. In general, the hydraulic process has to be taken into account in order to investigate the coupling effects.

Richards' approximation allows to model unsaturated one-phase flow. The desaturation process seems to be a key issue for understanding the failure mechanism around the drifts. With this approach, the desaturation process can be modeled with minimum effort. Nevertheless, the consideration of water saturation leads to non-linear flow equations, due to the non-linear pressure-saturation relation and saturation-permeability relation, respectively.

Effective stress concept describes a model approach for the coupling between pore pressure and mechanically effective stress, acting on the rigid body. Due to the fact that neither mechanical nor hydraulic processes on its own are able to predict the observed failure, attention to the coupling between these both has to be paid. Therefore, the effective stress concept presents a good basis. Further couplings are associated with the mass conservation. Additionally models, concerning hydraulic-mechanical coupling, are being presented in the following.

Shrinkage model simulates the contraction and expansion of material due to a change of water content. In general, argillaceous media show distinctive swelling/shrinkage strain. The observation of seasonally influenced desaturation cracks at the Tournemire site reveals the intensity of shrinkage and its impact on the mechanical as well as the hydraulic process. Thus, the usage of a shrinkage model is advised. Laboratory experiments on the shrinkage/swelling behavior are available (Valés et al. 2004).

Deformation dependent permeability provides another H-M coupling feature. The deformation of rock, e. g. induced by an excavation process, can change the hydraulic effective pore space. Thus, the permeability of the rock changes. Damage could cause an additional impact. These process is of special interest because the permeability is a key issue for the safety assessment of a repository. In general, the relation between deformation and permeability is non-linear and anisotropic. A strain-permeability relation considering damage will be used.

Transverse isotropy describes layered materials, which exhibit different material properties concerning two directions. Tsang et al. (2005) pointed out the importance and outstanding issue of anisotropic modeling, especially if the failure behavior in the EDZ is of interest. Triaxial tests on the Tournemire argillite has brought out distinctive transversely isotropic mechanical properties. Even if transversely isotropic hydraulic conductivity is not proven for the Tournemire clay, it can be expected due to the layered structure. Furthermore, laboratory experiments exhibits a transverse shrinkage behavior. As a consequence, transverse isotropy will be considered in stress-strain relation, shrinkage, and permeability.

Thermal model describes the heat flow. Nearly all processes observed in nature are influenced by the temperature. The impact rises with increasing temperature and temperature gradients, respectively. Hence, thermal modeling is an important issue, if heat producing waste is considered. In the investigated period at the Tournemire site, only minor temperature variations are observed ($\Delta T = 10$ K). Accordingly, isothermal conditions are assumed.

Chemical model describes the reactions taking place in the rock. Crucial reactions can happen if the excavation process disturbs the chemical equilibrium between air, pore water and rock. Of particular interest are dissolution-solution processes evoking a change of permeability or mechanical properties. Rejeb and Cabrera (2006) pointed out the negligibility of chemical processes in comparison with the hydraulic and mechanical disturbances. Thus, the chemical process is not considered in the present investigation.

Biological model simulates the biological activity. In the framework of performance assessment the grow of moss, algae, funguses and the like could change the rock properties. Furthermore, microorganisms could produce gases, which also could be a relevant issue. Indeed, no significant biological activity is observed at the Tournemire site and consequently no biological model is applied.

To sum up, two main processes constitute the applied model: deformation (**M**, mechanics) and fluid flow (**H**, hydraulics). The deformation model is stated by an elastic-damage model, the fluid flow model by a *Darcy* type flow, considering unsaturated conditions by the *Richards'* approximation. Several coupling phenomena are considered: effective stress, mass conservation of the liquid in a deformable porous media, shrinkage/swelling, and a deformation dependent permeability. Additionally, transversely isotropic material behavior is considered. An outline of the coupled model is depicted in figure 1.8.

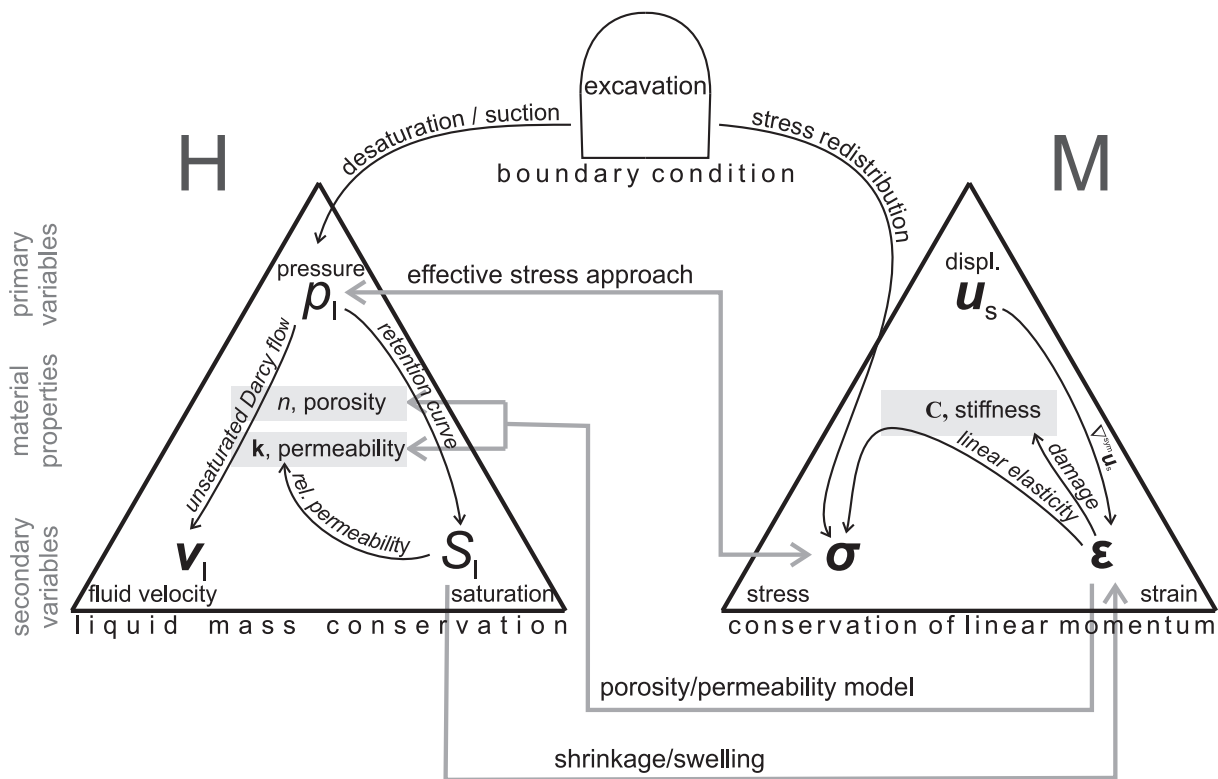


Figure 1.8: Sketch of the model approach.

1.3.4 Numerical solution

The above described model concept has to be formulated in a numerical model in order to allow a solution of the coupled problem. For this purpose, a mathematical formulation is needed at first. Furthermore, numerical methods have to be applied to solve the problem in time and space. In chapter 2 the way from conceptual considerations to numerical algorithms is recorded. Since the finite element code *RockFlow* is used, it is possible to resort to previous research. Discretization in time and space, non-linear solvers and other numerical methods in the framework of fluid and solid mechanics have been already implemented and verified. An outline of the history and capacity of *RockFlow* is given in the following. In particular the implementation of the H-M coupled model by Kohlmeier (2006) and investigations on clay material as presented by Ziefler (2008) form the foundation of the present work.

The finite element code *RockFlow* has the capacity to model flow, transport and deformation in subsurface systems. The roots can be found in the middle eighties and until today the code has been continually developed and enhanced at the *Institute of Fluid Mechanics* of the *Leibniz Universität Hannover*. In the early days, investigations with the emphasis on flow and transport in fractured porous media have been made by: Wollrath (1990); Kröhn (1991); Helmig (1993); Shao (1994); Lege (1995); Ratke et al. (1996); Kolditz (1996). Later on, *RockFlow* has been extended by spatially adaptive methods

(Barlag 1997; Thorenz 2001; Kaiser 2001), and reactive processes (Habbar 2001). Simultaneous the geometrically modeling have been done by Rother (2001) and Moenckes (2004). Recently, the code has been extended on thermal-hydraulic-mechanically coupled problems by Kohlmeier (2006) and further mechanically material models for claystone have been developed by Zieffle (2008). Furthermore, an interactive input concept has been developed and implemented (Wulkau 2005). Recent applications have been done in the context of T-H-M coupled simulations of repositories (Maßmann et al. 2008b; Shao et al. 2006a) and underground coal fires (Weßling 2007).

The investigations have been done in collaboration with the *Federal Institute of Geosciences and Natural Resources (BGR)*, the *Leibniz Institute for Applied Geosciences (LIAG)*, and the *Center for Applied Geoscience (ZAG)*, *University of Tübingen*. More information can be found at the web site (ISU 2009), where also a manual (Kohlmeier et al. 2009) and a tutorial (Maßmann and Ahmari 2006) is available.

1.3.5 Case study

The above presented model will be used to investigate three topics in the framework of the numerical modeling of the Tournemire site:

- ▷ desaturation process (chapter 3.2),
- ▷ mine-by-test experiment (chapter 3.3), and
- ▷ evolution of the EDZ (chapter 3.4).

The desaturation process is of special interest, because the properties of the argillite strongly depend on the saturation.

The measurements of displacement and pore water pressure during and after the excavation of a gallery allows an investigation of the excavation induced processes considering different modeling approaches. The experience of the first two studies will be used to investigate the excavation induced processes in the near field of the excavation.

A comparison of the simulation results with in-situ observations and measurements will be used to discuss the capacity, validity, and restrictions of the model approach.

1.3.6 Outline

The work at hand is divided into three main parts:

- ▷ introduction and problem description (chapter 1),
- ▷ methods (chapter 2), and
- ▷ case study (chapter 3).

The first chapter, the current one, gives a broad introduction into the main topics of the work, including the motivation, a site description and the modeling approach.

The second chapter accounts for the methods, which are applied to follow up the modeling approach. It starts out with the theoretical background of the problem. Based on the

finite element code *RockFlow*, special emphasis is laid on new developments. Methods have been investigated, developed, implemented and tested, namely: transversely isotropic elasticity, orthotropic shrinkage and permeability, continuum damage mechanics, and deformation dependent permeability. For all these topics, firstly the theoretical background will be briefly presented including a literature review, followed by the presentation of the developed model itself and its implementation. Applications will be used to illustrate the effectiveness and the capacity in order to simulate excavation induced processes.

In the third part, the model approach will be applied on some tasks relating the development of the EDZ around three openings at the Tournemire site. All results will be compared with in-situ observations and will be evaluated.

The work closes with a summary and conclusions in chapter 4.

Chapter 2

Methods

“It is common sense to take a method and try it. If it fails, admit it frankly and try another. But above all, try something.”

FRANKLIN D. ROOSEVELT (1882 - 1945)

2.1 The basics

2.1.1 Introduction

Geomaterials are natural products and in general their composition and structure are quite complex. For the description of ground water flow in a deformable medium, an overall description of partially saturated soils is required. In the present work the material will be treated as a composition of three phases: solid, liquid, and gaseous. The liquid phase is represented by water and the gaseous phase by air. Isothermal conditions are assumed and an exchange between the phases is not considered. In this section the theoretical basis for this description of a porous medium will be briefly presented. It will be restricted to a macroscopic point of view and is founded on the *Theory of Porous Media* (Bowen 1980; de Boer 1992; Ehlers 2002). It can be understood as the mixture theory (Truesdell and Toupin 1960) extended by the concept of volume fractions. For further details the reader could refer to: Lewis and Schrefler (1998); Zienkiewicz et al. (1999); Haupt (2002); Ehlers (2002); Ehlers and Graf (2003). These publications are the basis for the following section.

2.1.2 The concept of volume fractions

The description of a porous medium depends strongly on the size of the considered domain. In general it can be distinguished between the *microscopic level*, where the scale of inhomogeneity is of the same order of magnitude as the dimension of a pore or grain and the *macroscopic level*, where each phase presented in the system is assumed to fill up the entire domain (Lewis and Schrefler 1987). The latter is within the framework of continuum mechanics, and it is of major practical interest because commonly only the averaged picture of the subsurface system is needed or even possible. On the macroscopic level all quantities are averaged over a *representative elementary volume (REV)* (Bear 1972). This representative elementary volume contains by definition an even distribution of each constituent wherever it is placed in the considered domain (homogenized model). All geometrical and physical quantities are understood as statistical averages of the real quantities (Bowen 1980; Ehlers 2002). The volume V of a body \mathcal{B} representing the REV is composed by the sum of the volumes v^π of k single phases π

$$V = \int_{\mathcal{B}} dv = \sum_{\pi=1}^k v^\pi, \quad \text{where} \quad v^\pi = \int_{\mathcal{B}} dv^\pi =: \int_{\mathcal{B}} n^\pi dv \quad (2.1)$$

with the volume element v and the volume fraction

$$n^\pi = \frac{dv^\pi}{dv}. \quad (2.2)$$

Assuming a three-phase medium as shown in figure 2.1, totally filled by a solid (s), a liquid (l) and a gaseous phase (g), equation 2.2 directly leads to the saturation condition

$$\sum_{\pi=1}^k n^\pi = 1, \quad \text{with } \pi = (s, l, g). \quad (2.3)$$

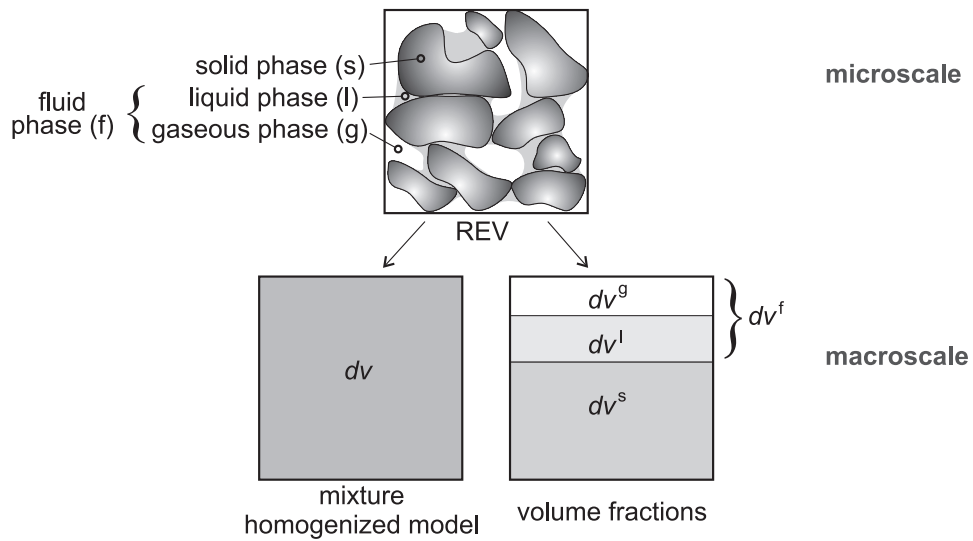


Figure 2.1: Micro- and macroscopic model of a three-phase porous medium.

With the introduction of the fluid phase (f) with the volume $v^f = v^l + v^g$ the saturation S of a fluid phase can be defined as follows

$$S^l = \frac{dv^l}{dv^f}, \quad \text{and} \quad S^g = \frac{dv^g}{dv^f}, \quad \text{with} \quad S^l + S^g = 1. \quad (2.4)$$

The volume of the fluid v^f can be seen as pores in a solid material. In this sense the porosity n of a porous medium is defined as the proportion of fluid volume to the total volume

$$n = \frac{dv^f}{dv}, \quad \text{with the relations} \quad n = n^l + n^g = 1 - n^s. \quad (2.5)$$

The material (realistic or effective) density $\rho^{\pi R}$ relates the local mass dm^{π} to the volume element dv^{π} in contrast to the partial (global or bulk) density ρ^{π} , which relates the local mass to the total volume element v

$$\rho^{\pi R} = \frac{dm^{\pi}}{dv^{\pi}}, \quad \rho^{\pi} = \frac{dm^{\pi}}{dv}. \quad (2.6)$$

The density of the overall medium ρ is given by the sum of all partial densities. For a three-phase medium it can be evaluated by the material densities of the constituents, the saturation and the porosity as follows

$$\rho = (1 - n)\rho^s + n\rho^f = (1 - n)\rho^s + n(S^l\rho^l + S^g\rho^g). \quad (2.7)$$

2.1.3 Kinematics

As a consequence of the description of the porous medium as a mixture, each spatial point \mathbf{x} of the current configuration is at any time t simultaneously occupied by material particles P^π of all phases. Starting from different reference positions \mathbf{X}_π , the motion for each constituent depends on its own motion function χ_π . The assumption of unique motion functions permits the inverse formulation with the *Jacobian* determinants J_π (figure 2.2)

$$\mathbf{x} = \chi_\pi(\mathbf{X}_\pi, t), \quad \mathbf{X}_\pi = \chi_\pi^{-1}(\mathbf{x}, t), \quad J_\pi = \det \frac{\partial \chi_\pi}{\partial \mathbf{X}_\pi} \neq 0. \quad (2.8)$$

Each constituent has its own velocity \mathbf{v}_π and acceleration \mathbf{a}_π field, which can be given

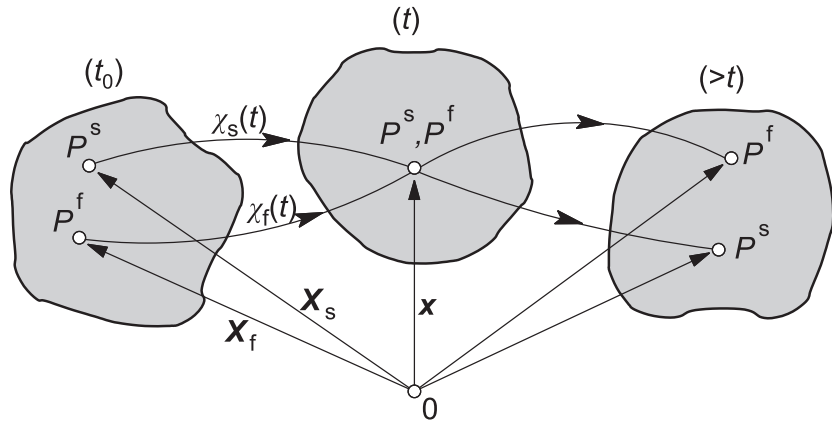


Figure 2.2: Motion of a multiphasic mixture (Ehlers 2002).

with respect to the current configuration (*Eulerian* description)

$$\mathbf{v}_\pi = \dot{\mathbf{x}}_\pi = \frac{\partial \chi_\pi(\mathbf{X}_\pi, t)}{\partial t}, \quad \mathbf{a}_\pi = \dot{\mathbf{v}}_\pi = \ddot{\mathbf{x}}_\pi = \frac{\partial^2 \chi_\pi(\mathbf{X}_\pi, t)}{\partial t^2} \quad (2.9)$$

or the reference configuration (*Lagrangian* description)

$$\mathbf{v}_\pi = \dot{\mathbf{x}}_\pi = \dot{\mathbf{x}}_\pi(\mathbf{x}, t), \quad \mathbf{a}_\pi = \dot{\mathbf{v}}_\pi = \ddot{\mathbf{x}}_\pi = \ddot{\mathbf{x}}_\pi(\mathbf{x}, t). \quad (2.10)$$

Where the operator “ $(\dot{\bullet})$ ” defines the temporal derivative of (\bullet) . In the framework of coupled solid-fluid problems it is convenient to use the *Lagrangian* description of the solid, defining the solid displacement vector $\mathbf{u}_s = \mathbf{u}$ as primary variable, whereas the fluid phase is described in an *Eulerian* manner, defining the seepage velocity vector \mathbf{w}_f as motion of the fluid with respect to the deformable solid skeleton

$$\mathbf{u} = \mathbf{x} - \mathbf{X}_s, \quad \mathbf{w}_f = \dot{\mathbf{x}}_f - \dot{\mathbf{x}}_s. \quad (2.11)$$

2.1.4 Assumptions and simplifications

In the work at hand a hydraulic-mechanically coupled problem of the geotechnical field is investigated. Before the related equations and definitions will be presented, the basic simplifications and assumptions will be listed. The most important ones will be discussed in the following sections in detail.

- ▷ isothermal conditions, $T = \text{const.}$
- ▷ incompressible solid and liquid phase, $\rho_s = \text{const.}, \rho_l = \text{const.}$
- ▷ Newtonian fluids: the shear stress τ between two fluid particles is proportional to the difference of their velocities Δv and inversely proportional to their distance Δx , $\tau \propto \Delta v / \Delta x$.
- ▷ no exchange between the phases
- ▷ small deformations \Rightarrow linear geometry (deformations can be related to the reference configuration), velocity of the solid phase can be neglected in relation to the fluid velocity
- ▷ low velocities, low *Reynolds* number \Rightarrow neglect forces due to inertia, laminar flow \Rightarrow liquid velocity is a function of the pore pressure field, static equilibrium for the mechanical problem
- ▷ pressure gradients in the gaseous phase are neglected \Rightarrow direct dependency between liquid pressure and liquid saturation (*Richards'* approximation)

Considering these simplifications, the numerical model can be stated with only two primary variables: the liquid pressure (pore water pressure) p_l and the vector of displacements \mathbf{u} . The seepage velocity and the saturation are calculated by post-processing as a function of the pressure field. Consequently, only the motion function of the solid phase χ_s is of further interest.

2.1.5 Mechanical quantities

2.1.5.1 Definition of strain

The solid material deformation gradient \mathbf{F} and its inverse \mathbf{F}^{-1} (also called spatial deformation gradient) can be determined by the equation 2.8

$$\mathbf{F} = \text{Grad}_s \mathbf{x} = \frac{\partial \chi_s}{\partial \mathbf{X}_s}, \quad \mathbf{F}^{-1} = \text{grad} \mathbf{X} = \frac{\partial \chi_s^{-1}}{\partial \mathbf{x}}. \quad (2.12)$$

Where the gradient operator “ $\text{Grad}_s (\bullet)$ ” defines the partial derivative of (\bullet) with respect to the reference configuration of the solid phase. The deformation process can also be described by the displacement gradient

$$\mathbf{H} = \text{Grad}_s \mathbf{u}, \quad \text{where} \quad \mathbf{F} = \mathbf{1} + \mathbf{H}. \quad (2.13)$$

In the following, the *Green-Lagrangeian* strain tensor \mathbf{E} will be used. In contrast to the deformation gradient this description offers the advantages of symmetry and negligence of rigid motion, as translation and rotation. Its derivation can be found in Haupt (2002) amongst others. The relation to \mathbf{H} is given by

$$\mathbf{E} = \frac{1}{2}(\mathbf{H}^T + \mathbf{H} + \mathbf{H}^T \mathbf{H}). \quad (2.14)$$

If the strains are small, the geometrically linear theory can be adapted and the *Green-Lagrangeian* strain tensor simplifies to the linearized strain tensor

$$\boldsymbol{\varepsilon} = \frac{1}{2}(\mathbf{H}^T + \mathbf{H}), \quad \text{if } \mathbf{H} \ll 1. \quad (2.15)$$

2.1.5.2 Definition of stress

Two types of forces act on a body \mathcal{B} : body forces \mathbf{b} (e. g. due to the gravity), which are defined per volume unit, and surface forces \mathbf{t} , defined per area unit. Thus, the total force vector \mathbf{f} is defined as:

$$\mathbf{f}(\mathbf{x}, t) = \int_{\mathcal{B}} \rho \mathbf{b} \, dv + \int_{\partial \mathcal{B}} \mathbf{t} \, da \quad (2.16)$$

with the volume v and the surface element a . The resulting internal forces can be described on the surface of an imaginary cut through the body. In a point P on this surface \mathbf{t} defines the stress vector as the force vector per area. The *Cauchy* theorem postulates a linear dependency between the stress vector and the outer normal vector \mathbf{n} of the surface

$$\mathbf{t}(\mathbf{x}, t, \mathbf{n}) = \boldsymbol{\sigma} \mathbf{n} \quad (2.17)$$

with the symmetric *Cauchy* stress tensor $\boldsymbol{\sigma}$.

2.1.6 Balance equations

Balance equations are the fundamental axioms in the continuum mechanics. They are valid, independent of the considered material. Generally used are the balance of mass, the linear and angular momentum as well as the balance equation of energy. Following Bear and Bachmat (1990) the balance of an extensive quantity \mathbf{e} within a domain \mathcal{B} can be verbally expressed by

$$\left\{ \begin{array}{l} \text{rate of accumulation} \\ \text{of } \mathbf{e} \text{ within } \mathcal{B} \end{array} \right\} = \left\{ \begin{array}{l} \text{net influx} \\ \text{of } \mathbf{e} \text{ into } \mathcal{B} \end{array} \right\} + \left\{ \begin{array}{l} \text{net rate of production} \\ \text{of } \mathbf{e} \text{ within } \mathcal{B} \end{array} \right\}. \quad (2.18)$$

In the following, these relations will be presented as far as they are needed for the formulation of the three-phase problem, considering the simplifications in section 2.1.4. For further details please refer to: Haupt (2002); Bear and Bachmat (1990); Lewis and Schrefler (1998); Ehlers and Bluhm (2002).

2.1.6.1 Balance of mass

This equation implies the mass m of a body \mathcal{B}

$$m(t) = \int_{\mathcal{B}_t} \rho \, dv \quad (2.19)$$

remains constant with time. For the applied model, the conservation of the liquid phase is used. In terms of equation 2.18 the quantity ϵ equals the density of the liquid ρ_l . Applying the divergence theorem, equation 2.18 can be written as a partial difference equation for the local form of the mass balance of the liquid phase. The production rate is neglected. The volume of the liquid phase equals nS_l , related to a reference volume element

$$\frac{\partial(\rho_l n S_l)}{\partial t} + \operatorname{div}(\rho_l n S_l \mathbf{v}_l) = 0. \quad (2.20)$$

With the liquid flux $\mathbf{q}_l = nS_l \mathbf{v}_l$, which will be defined in equation 2.38 as a constitutive relation, the assumption of a constant density of the liquid and the use of the product rule it yields

$$\rho_l n \frac{\partial S_l}{\partial t} + \rho_l S_l \frac{\partial n}{\partial t} + \rho_l \operatorname{div} \mathbf{q}_l = 0. \quad (2.21)$$

The time derivative of the porosity can be expressed by the displacements \mathbf{u} and the whole equation can be divided by the liquid density

$$n \frac{\partial S_l}{\partial t} + \alpha S_l \operatorname{div} \frac{\partial \mathbf{u}}{\partial t} + \operatorname{div} \mathbf{q}_l = 0. \quad (2.22)$$

The time derivative of the saturation $\frac{\partial S_l}{\partial t}$ can be replaced by $\frac{\partial S_l}{\partial p_l} \frac{\partial p_l}{\partial t}$, whereby the derivative $\frac{\partial S_l}{\partial p_l}$ can be determined by the capillary pressure-saturation relation, presented in section 2.1.7.1. The *Biot* coefficient α is defined by the bulk modulus of the porous media K and the solid grains K_s

$$\alpha = 1 - \frac{K}{K_s}. \quad (2.23)$$

Since the solid is incompressible, the *Biot* modulus equals unity and will not be mentioned in the following.

An incompressible solid phase does not imply an incompressible porous media, even if small deformations are assumed. In fact, the composition may change by the liquid flux or a change of liquid saturation. This means a change of volume in a body leads directly to an analog change in the porosity and vice versa (see section 2.1.7.3).

2.1.6.2 Balance of linear momentum

The linear momentum I of a body \mathcal{B} is defined as

$$I(t) = \int_{\mathcal{B}_t} \rho \mathbf{v} \, dv. \quad (2.24)$$

The conservation of linear momentum implies that the time rate of change of the linear momentum equals the totally force vector \mathbf{f} as defined in equation 2.16

$$\frac{d}{dt} \int_{\mathcal{B}_t} \rho \mathbf{v} \, dv = \int_{\mathcal{B}_t} \rho \mathbf{b} \, dv + \int_{\partial \mathcal{B}_t} \mathbf{t} \, da. \quad (2.25)$$

With the *Cauchy* theorem (equation 2.17), equation 2.10 and the divergence theorem the local form of the balance of momentum can be written for the solid phase with respect to the reference system as follows:

$$\rho_s \mathbf{a}_s = \rho_s \mathbf{b} + \operatorname{div} \boldsymbol{\sigma}. \quad (2.26)$$

Motivated by its low amount the acceleration term is neglected

$$0 = \rho_s \mathbf{b} + \operatorname{div} \boldsymbol{\sigma}. \quad (2.27)$$

2.1.6.3 Balance of energy

First law of thermodynamics. The *first law of thermodynamics* implies that the time rate of change of the whole energy content \mathcal{E} of a body \mathcal{B} , consisting of kinetic energy \mathcal{K} and internal energy \mathcal{U} , equals the mechanical power of the external forces \mathcal{L} and non mechanical energy, called heat \mathcal{T} :

$$\frac{d\mathcal{E}(\mathcal{B}_t)}{dt} = \frac{d}{dt}(\mathcal{K} + \mathcal{U}) = \mathcal{L} + \mathcal{T} \quad (2.28)$$

with the following specifications

$$\mathcal{K} = \frac{1}{2} \int_{\mathcal{B}_t} \rho \mathbf{v} \mathbf{v} \, dv, \quad \mathcal{U} = \int_{\mathcal{B}_t} \rho u \, dv, \quad (2.29)$$

$$\mathcal{L} = \int_{\mathcal{B}_t} \rho \mathbf{b} \mathbf{v} \, dv + \int_{\partial \mathcal{B}_t} \mathbf{n} \boldsymbol{\sigma} \mathbf{v} \, da, \quad \mathcal{T} = \int_{\mathcal{B}_t} \rho Q_{\text{th}} \, dv + \int_{\partial \mathcal{B}_t} \mathbf{n} \mathbf{q}_{\text{th}} \, da \quad (2.30)$$

with the specific internal energy per unit mass u , the specific heat source Q_{th} , and the heat flux \mathbf{q}_{th} into the body. The use of the mass balance, the divergence theorem, the product rule and the additional relations:

$$\boldsymbol{\sigma} = \boldsymbol{\sigma}^T, \quad (2.31)$$

$$\operatorname{div}(\boldsymbol{\sigma}^T \mathbf{v}) = \operatorname{div}(\boldsymbol{\sigma}) : \mathbf{v} + \boldsymbol{\sigma} : \operatorname{grad} \mathbf{v} = \operatorname{div}(\boldsymbol{\sigma}) : \mathbf{v} + \boldsymbol{\sigma} : \dot{\boldsymbol{\epsilon}} \quad (2.32)$$

yield the local form (Haupt 2002)

$$\dot{u} = \frac{1}{\rho} \operatorname{div} \mathbf{q}_{\text{th}} + Q_{\text{th}} + \frac{1}{\rho} \boldsymbol{\sigma} : \dot{\boldsymbol{\epsilon}}. \quad (2.33)$$

Where $\boldsymbol{\sigma} : \dot{\boldsymbol{\epsilon}}$ characterize the stress power with the strain rate $\dot{\boldsymbol{\epsilon}}$.

Second law of thermodynamics - principle of irreversibility. The *second law of thermodynamics* implies that the time rate of change of the entropy \mathcal{S} of a body \mathcal{B}

$$\frac{d\mathcal{S}(\mathcal{B}_t)}{dt} = \frac{d}{dt} \int_{\mathcal{B}_t} \rho \eta \, dv \quad (2.34)$$

is always equal or greater than the sum of the time rate of change of heat production and heat flux. Consequently, the entropy production is never negative. The local form can be described by the specific entropy η per unit mass and the absolute temperature T

$$\rho \dot{\eta} + \operatorname{div} \frac{\mathbf{q}_{\text{th}}}{T} - \frac{\rho Q_{\text{th}}}{T} \geq 0. \quad (2.35)$$

With the definition of the free *Helmholtz* energy $\psi = u - T\eta$ and equation 2.33 the *Clausius-Duhem* inequality can be derived (Haupt 2002), here presented for isothermal conditions ($\dot{T} = 0$) with the internal dissipation Φ

$$\Phi = \boldsymbol{\sigma} : \dot{\boldsymbol{\epsilon}} - \rho \dot{\psi} \geq 0. \quad (2.36)$$

This inequality has to be fulfilled by all thermo-mechanical processes and act as a restriction for the formulation of constitutive equations. The dissipation Φ equals zero for reversible processes and is greater than zero for irreversible processes.

2.1.7 Constitutive equations

Remark. For the sake of simplicity, the liquid saturation S_l will be replaced in the following by S , which means the water saturation, which is in fact the only liquid of interest in the work at hand.

2.1.7.1 Unsaturated one-phase flow

Darcy's law. Considering a fully water saturated porous media, the widely used *Darcy's* law gives a good approximation for the liquid flux

$$\mathbf{q}_l = -\frac{\mathbf{k}}{\mu_l} (\operatorname{grad} p_l - \rho_l \mathbf{g}) \quad (2.37)$$

with the second rank tensor of the intrinsic permeability \mathbf{k} , the viscosity of the liquid μ_l , the pressure of the liquid phase p_l , and the acceleration due to gravity vector \mathbf{g} . This equation is valid in case of small velocities and laminar flow. It can also be derived from the balance of fluid momentum, if the acceleration of the fluid is neglected (Bear and Bachmat 1990). In order to describe the flow in an unsaturated medium, a modification of *Darcy's* law is used, introducing the relative permeability k_{rel} as a function of the water saturation S (Bear 1972)

$$\mathbf{q}_l = n S \mathbf{v}_f = -\frac{k_{\text{rel}} \mathbf{k}}{\mu_l} (\operatorname{grad} p_l - \rho_l \mathbf{g}). \quad (2.38)$$

In general, the relative permeability is a non-linear function of the saturation, which has to be determined experimentally.

Richards' approximation. Considering a soil system, which is connected to the atmosphere, the pressure differences in the gaseous phase can be assumed to equal zero (Richards 1931). The amount of gaseous pressure in the pore space can be completely neglected in relation to the atmospheric pressure. Thus, the definition of the pore pressure p and the capillary pressure p_c can be simplified as follows:

$$p = Sp_l + S_g p_g \approx Sp_l \quad \text{and} \quad p_c = p_g - p_l \approx -p_l. \quad (2.39)$$

This leads to a direct dependency between the liquid pressure and the liquid saturation and only one variable is needed to formulate the hydraulic problem. If the liquid pressure is chosen, positive liquid pressure means fully saturated, negative pressure means partially saturated pore space. The amount of the negative liquid pressure equals the suction or capillary pressure. The relation between saturation and capillary pressure, also called retention curve, has to be defined experimentally.

Gawin et al. (2006) figure out that the capillary pressure can also be formally defined at low moisture content, even if water is not present in pores, as the product of the water potential and the density of water.

Van Genuchten function. For many geomaterials, including argillite (Semete et al. 2008), the *van Genuchten* function (van Genuchten 1980) gives a good approximation for the relative permeability of the liquid phase

$$k_{\text{rel}} = S_{\text{eff}}^{0.5} \left(1 - \left(1 - S_{\text{eff}}^{1/m_G} \right)^{m_G} \right)^2, \quad \text{where} \quad S_{\text{eff}} = \frac{S - S_{\text{res}}}{S_{\text{full}} - S_{\text{res}}}, \quad 0 \leq S_{\text{eff}} \leq 1. \quad (2.40)$$

Here, S_{eff} denotes the effective saturation, S_{res} the residual saturation, and S_{full} the saturation, for which the maximal relative permeability is reached. m_G is an additional material parameter.

Also for the relation between capillary pressure and liquid saturation a *van Genuchten* function provides a common used approximation (cf. equation 1.1):

$$S_{\text{eff}} = \left(\left(\frac{p_c}{M_G} \right)^{\frac{1}{1-m_G}} + 1 \right)^{-1}. \quad (2.41)$$

2.1.7.2 Linear elasticity (isotropic)

Linear elasticity is the most prevalent material model in solid mechanics. It is based on the assumption of a linear relation between the stress σ and the elastic strain ε^{el} with the definition of *Young's* modulus of elasticity E

$$\sigma = E \varepsilon^{\text{el}}. \quad (2.42)$$

Equation 2.42 is called *Hooke's law*, although it is not a law in the sense of general validity. Generalization of the scalar format is based on the concept that the triaxial state of stress is proportional to the triaxial state of strain through the linear transformation

$$\boldsymbol{\sigma} = \mathbb{C} : \boldsymbol{\varepsilon}^{\text{el}} \quad (2.43)$$

with the second rank tensor of the stresses $\boldsymbol{\sigma}$ and the elastic strains $\boldsymbol{\varepsilon}^{\text{el}}$ and the fourth rank material tensor \mathbb{C} . The stored elastic energy ψ^{el} of a body is given by

$$\psi^{\text{el}} = \frac{1}{2} \int_{\mathcal{B}} \boldsymbol{\varepsilon}^{\text{el}} : \mathbb{C} : \boldsymbol{\varepsilon}^{\text{el}} \, dv. \quad (2.44)$$

Elasticity also implies reversibility. Thus, the dissipation as defined by the *Clausius-Duhem* inequality (equation 2.36) becomes zero. Assuming linear elasticity only, it follows for isothermal conditions $\psi^{\text{el}} = \rho u$ and the definition of the elastic stress in the local form can be given as

$$\boldsymbol{\sigma} = \frac{\partial \psi^{\text{el}}}{\partial \boldsymbol{\varepsilon}^{\text{el}}}. \quad (2.45)$$

The second derivative of the elastic energy yields the material tensor

$$\mathbb{C} = \frac{\partial^2 \psi^{\text{el}}}{\partial \boldsymbol{\varepsilon}^{\text{el}}^2} = \frac{\partial \boldsymbol{\sigma}}{\partial \boldsymbol{\varepsilon}^{\text{el}}}. \quad (2.46)$$

With the introduction of major symmetry ($\mathbb{C} = \mathbb{C}^T$), 21 elastic moduli are needed to define the material tensor. Further simplification are possible, if specific classes of symmetry are involved, whereby orthotropic elasticity leads to nine, and transversely isotropic elasticity to five elastic moduli. In the case of isotropy, two material parameters are sufficient and the linear-elastic relation reduces to

$$\boldsymbol{\sigma} = \Lambda \operatorname{tr} \boldsymbol{\varepsilon}^{\text{el}} \mathbf{1} + 2G \boldsymbol{\varepsilon}^{\text{el}}, \text{ where } \Lambda = \frac{E\nu}{(1+\nu)(1-2\nu)}, \text{ and } G = \frac{E}{2(1+\nu)} \quad (2.47)$$

with the two *Lamé* constants G (shear modulus) and Λ (cross modulus), and the *Poisson's* ratio ν . More details can be found in Haupt (2002) or Stein and Barthold (1996), amongst others.

Voigt notation. In engineering praxis, the symmetry of the stress, strain and material tensor is used to obtain a compact notation and represent the tensors in a vector and matrix scheme, respectively (Haupt 2002):

$$\boldsymbol{\sigma} = [\sigma_{11} \ \sigma_{22} \ \sigma_{33} \ \tau_{12} \ \tau_{23} \ \tau_{31}]^T \text{ and } \boldsymbol{\varepsilon} = [\varepsilon_{11} \ \varepsilon_{22} \ \varepsilon_{33} \ \gamma_{12} \ \gamma_{23} \ \gamma_{31}]^T \quad (2.48)$$

with the definition of the shear stresses τ and shear strains γ

$$\tau_{ij} = \sigma_{ij}, \text{ and } \gamma_{ij} = 2\varepsilon_{ij}, \quad \forall i \neq j. \quad (2.49)$$

The definition of the matrix notation of the material tensor is done accordingly. Thus, the equation 2.43 can be written as a simple matrix vector multiplication as follows

$$\boldsymbol{\sigma} = \mathbf{C} \boldsymbol{\varepsilon}^{\text{el}}, \quad (2.50)$$

$$\begin{bmatrix} \sigma_{11} \\ \sigma_{22} \\ \sigma_{33} \\ \tau_{12} \\ \tau_{23} \\ \tau_{13} \end{bmatrix} = \begin{bmatrix} C_{1111} & C_{1122} & C_{1133} & C_{1112} & C_{1123} & C_{1131} \\ & C_{2222} & C_{2233} & C_{2212} & C_{2223} & C_{2231} \\ & & C_{3333} & C_{3312} & C_{3323} & C_{3331} \\ & & & C_{1212} & C_{1223} & C_{1231} \\ & & & & C_{2323} & C_{2331} \\ & & & & & C_{3131} \end{bmatrix} \begin{bmatrix} \varepsilon_{11} \\ \varepsilon_{22} \\ \varepsilon_{33} \\ \gamma_{12} \\ \gamma_{23} \\ \gamma_{13} \end{bmatrix}. \quad (2.51)$$

sym.

2.1.7.3 Determination of the porosity

The porosity n can be determined depending on the initial value, the elastically volumetric strain, and swelling/shrinkage strain of the material, as introduced in section 2.5. Since incompressible grains are assumed, the elastic volumetric strain affects the pore space, not the size of particles. Consequently, an expansion will lead to an increase, a compression or contraction to a decrease of pore space (figure 2.3, left). Swelling or shrinkage leads to a change of the particle size of the soil. The pore space will decrease with swelling and increase if shrinkage occurs (figure 2.3, right). Consideration of both effects leads to the following porosity equation

$$n = n_{\text{init}} + \varepsilon_{\text{vol}} - \varepsilon_{\text{vol}}^{\text{sw}}. \quad (2.52)$$

Where n_{init} is the initial porosity, ε_{vol} ($= \text{tr } \boldsymbol{\varepsilon}$) the volumetric strain and $\varepsilon_{\text{vol}}^{\text{sw}}$ the volumetric swelling strain.

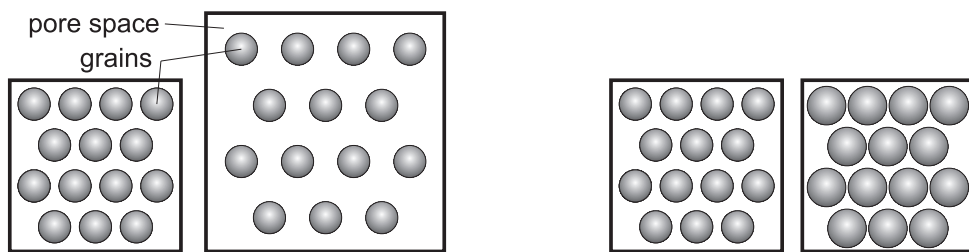


Figure 2.3: Porosity change due to volumetric strain (left) and swelling (right).

2.1.7.4 The effective stress concept

The concept of effective stress describes the stress state in a porous media by separating the total stress $\boldsymbol{\sigma}_{\text{tot}}$ into two parts: the pore pressure p , acting in the fluid phase, and the effective stress $\boldsymbol{\sigma}$, acting in the solid phase (figure 2.4). All mechanical aspects of a saturated soil are governed by the effective stress. A detailed discussion can be found in: Fredlund and Rahardjo (1998); Zienkiewicz et al. (1999); Voyiadjis and Song (2006);

Lu and Likos (2004); Lewis and Schrefler (1998). The following definition of the effective stress for water saturated soils dates from *Terzaghi*¹,

$$\boldsymbol{\sigma}_{\text{eff}} = \boldsymbol{\sigma} = \boldsymbol{\sigma}_{\text{tot}} - \mathbf{1}p \quad (2.53)$$

and was developed in the context of consolidation problems of soils (von Terzaghi and Fröhlich 1936; von Terzaghi 1936, 1954), whereby important contributions have been given by *Fillunger* (Fillunger 1913).

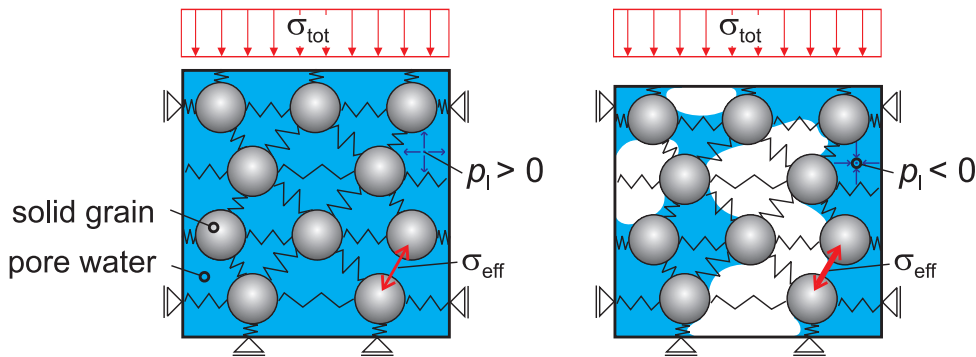


Figure 2.4: Interaction of stresses and liquid pressures in a saturated (left) and unsaturated (right) porous medium. Here, the desaturation process leads to an increase of the effective stresses.

Biot (Biot 1941, 1956) and *Skempton* (Skempton 1960, 1961; Niechcial 2002) have also done important work on this topic, especially to apply the concept to an unsaturated medium. The behavior of unsaturated soil is much more complex. Effects, induced by the interaction with the gaseous phase, like surface tension, has to be taken into account. A broad, ongoing scientific discussion can be observed in the questions, how to describe unsaturated soil/rock behavior and how it can be modeled. It cannot be expected that one effective stress expression is valid for all materials and phenomena. More information can be found in: Bear (1972); Fredlund and Rahardjo (1998); Gens (1995); Lu and Likos (2004); Schanz (2007) amongst others. In the work at hand, a relation based on *Bishop* (Bishop and Blight 1963) will be used for unsaturated conditions, with the assumption as presented in equation 2.39

$$\boldsymbol{\sigma} = \boldsymbol{\sigma}_{\text{tot}} - \chi(S_l) \mathbf{1} p_l \quad (2.54)$$

with the *Bishop* parameter χ that has to be defined experimentally as a function of saturation. Figure 2.5 shows relations based on measurements. Widely used is the relation

$$\dot{\chi} = S. \quad (2.55)$$

¹An overview of *Terzaghi*'s life and writings is given in Bjerrum et al. (1960). The historical development of the effective stress concept with emphasis on *Terzaghi* and *Fillunger* can be found in de Boer and Ehlers (1990) and de Boer (1992).

According to Lu and Likos (2004), the following function shows a good fit to experimental results for capillary pressures up to 1500 kPa (see figure 2.6)

$$\chi = \begin{cases} 0 & S \leq S_{\text{res}}, S \neq 1 \\ \left(\frac{S - S_{\text{res}}}{1 - S_{\text{res}}} \right)^\kappa & S_{\text{res}} < S < 1 \\ 1 & S = 1 \end{cases} \quad (2.56)$$

with the material parameter κ .

The choice of the *Bishop* parameter has a significant influence on the behavior of the hydraulic-mechanically coupled system. Especially in materials with small pores, as claystone, very high capillary pressures can be obtained, which could lead to an overestimation of the effective stresses. Figure 2.7 shows the liquid pressure and the mechanically effective pressure $p_{1\chi}$ at different levels of saturation of a claystone. The reference parameter set is used (table 1.2, p. 11). Obviously, this approach has the capacity to restrict the influence of capillary pressure on the stresses.

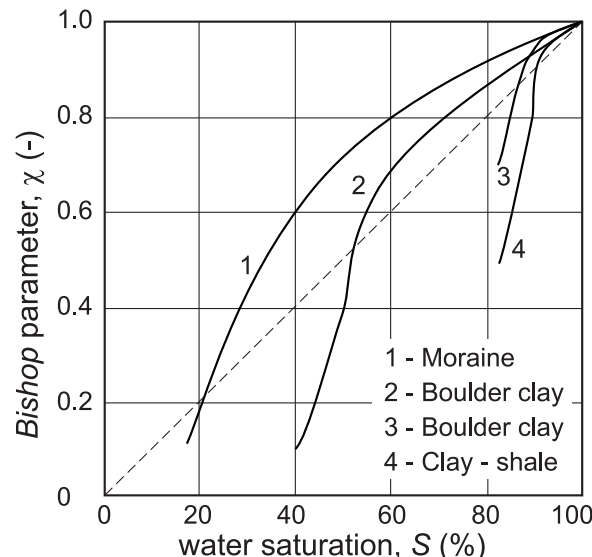


Figure 2.5: Measured relations between the water saturation S and the *Bishop* parameter χ (Bishop and Blight 1963).

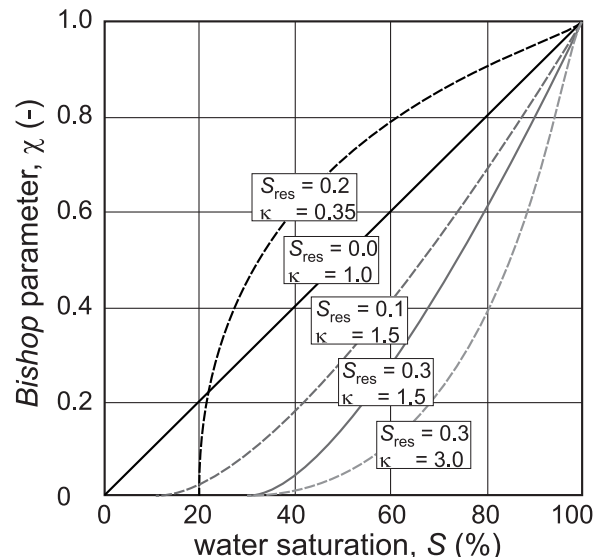


Figure 2.6: Approximation of relations between water saturation S and the *Bishop* parameter χ , using equation 2.56.

The *Bishop* parameter has also a meaning for numerical stability, because it defines the shape of the relations, as plotted in figure 2.7; if κ is chosen less than 1, instabilities might occur in the zone of the residual saturation, and if the residual saturation S_{res} is close to 1, a kink will worsen the numerical behavior at the transition point between saturated and unsaturated condition.

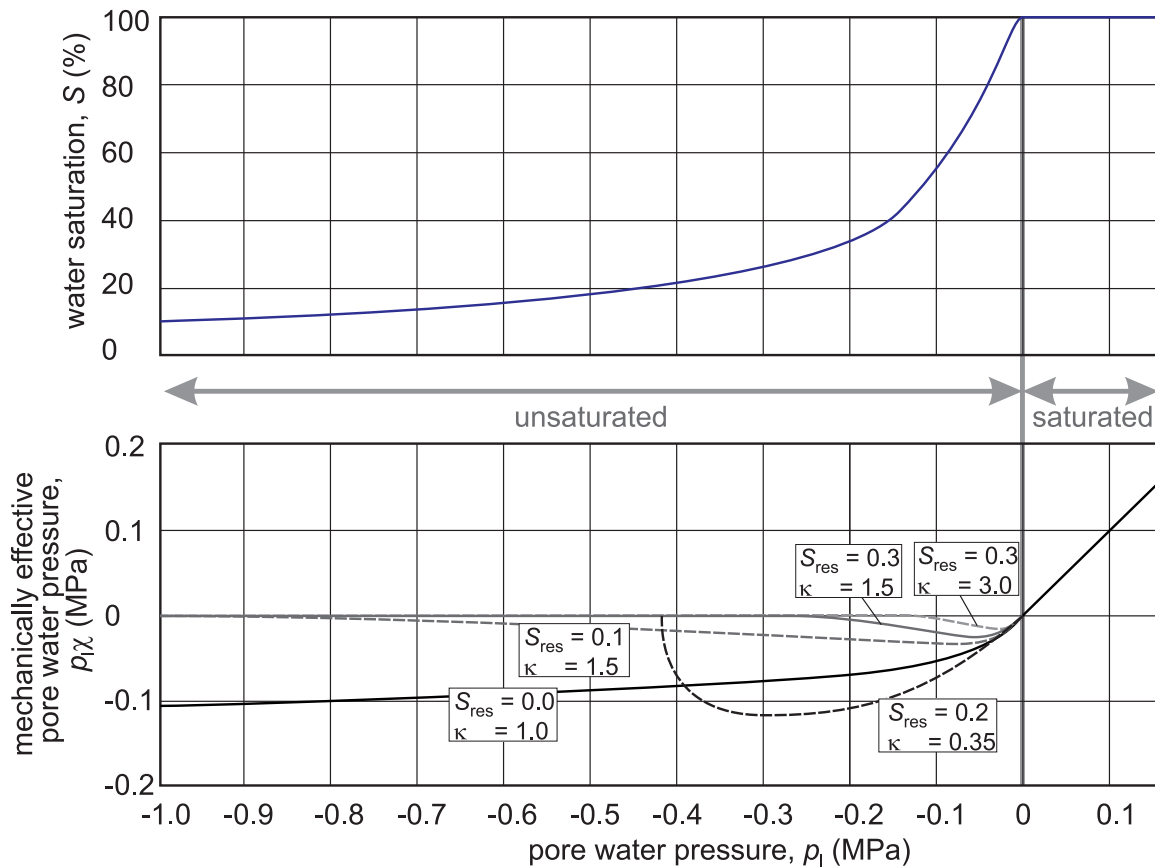


Figure 2.7: Pore water pressure versus mechanically effective pore water pressure and saturation.

2.1.8 Numerical treatment

2.1.8.1 General remarks

The numerical treatment of the problem is based on the weak formulation of the governing field equations, namely the balance of linear momentum and the balance of liquid mass, combined with the finite difference discretization in time and finite element discretization in space. The used approach originates from Lewis and Schrefler (1998, 1987). The finite element code *RockFlow* (section 1.3.4) has been used.

Detailed information about the implementation of the hydraulic-mechanically coupled model can be found in Kohlmeier (2006). A general review of numerical models in rock mechanics can be found in Jing (2003).

2.1.8.2 The finite element formulation

The *finite element method (FEM)* is used for the approximation of partial differential equations. It is widely applied and proved in several fields of engineering, e. g. for the

solution of complex problems in structural and fluid mechanics. The basic idea is given by the representation of a domain \mathcal{B} by n_{ele} finite elements Ω_{ele} :

$$\mathcal{B} \approx \bigcup_{\text{ele}=1}^{n_{\text{ele}}} \Omega_{\text{ele}} \quad (2.57)$$

This decomposition refers to the geometry and the field variables. Within a finite element *ansatz functions* form the spatial distribution of the unknown variable defined by its nodal values. In the used method, the geometry and the field variable are approximated by the same shape functions (*isoparametric* approach). Applying the *Bubnov-Galerkin* method, these functions equal the *weighting* functions, which are needed for the variational formulation. For the considered problem, different ansatz functions are used for the hydraulic and the mechanical sub-problem. This is motivated by the coupling between the liquid pressure and the stress (section 2.1.7.4). The liquid pressure is a primary variable but the stress is calculated by the derivative of the displacements. In order to obtain an accurate solution, the ansatz functions of the displacements have to be defined one order higher. Here, linear functions N_p are used for the hydraulic sub-problem and quadratic functions N_u for the approximation of the displacement field. The variational form of the problem can be derived from the balance equations (section 2.1.6) by multiplying a weighting function, integration by parts and application of the divergence theorem. In the following, the formulation for the mechanical and the hydraulic sub-problem will be presented. More information about the FEM can be found in Zienkiewicz and Taylor (2000), about the application on coupled problems in Lewis and Schrefler (1998) and the implementation in the *RockFlow* code in Kohlmeier (2006) and Zieffle (2008). With the consideration of the constitutive equations (section 2.1.7) and applying the standard *Galerkin* method, the coupled problem can be formulated in the weak form:

$$\mathbf{C}\tilde{\mathbf{p}}_l + \mathbf{S}\frac{d\tilde{\mathbf{p}}_l}{dt} + \mathbf{Q}^T\frac{d\tilde{\mathbf{u}}}{dt} = \mathbf{f}_p^{\text{ext}} \quad (2.58a)$$

$$\mathbf{K}\frac{d\tilde{\mathbf{u}}}{dt} + \mathbf{Q}\frac{d\tilde{\mathbf{p}}_l}{dt} = \frac{d(\mathbf{f}_u^{\text{ext}} - \mathbf{f}_u^{\text{int}})}{dt} \quad (2.58b)$$

with the vector of the unknown pressures $\tilde{\mathbf{p}}_l$ and displacements $\tilde{\mathbf{u}}$.

The matrices and vectors \mathbf{C} , \mathbf{K} , \mathbf{S} , \mathbf{Q} , $\mathbf{f}_p^{\text{ext}}$, $\mathbf{f}_u^{\text{ext}}$, and $\mathbf{f}_u^{\text{int}}$ can be determined by assembling the corresponding element matrices, which are defined as follows:

$$\mathbf{C}^{(\text{ele})} = \int_{\Omega_{\text{ele}}} (\nabla N_p)^T \frac{\mathbf{k}k_{\text{rel}}}{\mu_l} \nabla N_p \, d\Omega_{\text{ele}} \quad \text{conductance matrix} \quad (2.59a)$$

$$\mathbf{S}^{(\text{ele})} = \int_{\Omega_{\text{ele}}} N_p \frac{\partial S}{\partial p_l} n N_p \, d\Omega_{\text{ele}} \quad \text{storativity matrix} \quad (2.59b)$$

$$\mathbf{f}_p^{\text{ext}} = \int_{\Omega_{\text{ele}}} (\nabla N_p)^T \frac{\mathbf{k}k_{\text{rel}}}{\mu_l} \nabla N_p \rho_l \mathbf{g} \, d\Omega_{\text{ele}} + \int_{\Gamma_{\text{ele}}} N_p \mathbf{q} \mathbf{n} \, d\Gamma_{\text{ele}} \quad \text{external source vector} \quad (2.59c)$$

$$\mathbf{Q}^{(\text{ele})} = \int_{\Omega_{\text{ele}}} \mathbf{B}^T S \mathbf{m}^T N_p \, d\Omega_{\text{ele}} \quad \text{coupling matrix} \quad (2.59\text{d})$$

$$\mathbf{K}^{(\text{ele})} = \int_{\Omega_{\text{ele}}} \mathbf{B}^T \mathbf{C} \mathbf{B} \, d\Omega_{\text{ele}} \quad \text{stiffness matrix} \quad (2.59\text{e})$$

$$\mathbf{f}_u^{(\text{ext})} = \int_{\Omega_{\text{ele}}} \mathbf{N}_u \rho \mathbf{g} \, d\Omega_{\text{ele}} + \int_{\Gamma_{\text{ele}}} \mathbf{N}_u \boldsymbol{\sigma} \mathbf{n} \, d\Gamma_{\text{ele}} \quad \text{external force vector} \quad (2.59\text{f})$$

$$\mathbf{f}_u^{(\text{int})} = \int_{\Omega_{\text{ele}}} \mathbf{B}^T (\boldsymbol{\sigma} - \chi p_l \mathbf{m}^T) \, d\Omega_{\text{ele}} \quad \text{internal force vector} \quad (2.59\text{g})$$

With the source vector \mathbf{q} , the outward normal vector \mathbf{n} , the vector representation of the first rank unit tensor \mathbf{m} , and the matrix \mathbf{B} , which consists of the spatial derivatives of the ansatz function \mathbf{N}_u in the *Euclidean* space. The integration on the elements is done numerically by the *Gaussian* quadrature rule.

2.1.8.3 Boundary conditions

Two kinds of boundary conditions can be distinguished:

Dirichlet. This type of boundary condition defines the value of the unknown field variable directly; here, the displacement for the mechanical and the liquid pressure for the hydraulic sub-problem. For the concerned nodes these values can be regarded as known and can be eliminated from the system of equations.

Neumann. With this kind of boundary condition the gradient of the extensive variable is given. This means here external forces or liquid sources, which are considered in the external force vector and external source vector, respectively (equation 2.59).

Mixed boundary conditions are also possible, but will not be considered in the work at hand.

2.1.8.4 Time discretization

For the discretization in time, finite differences are used. Time derivations are approximated by a single step scheme:

$$\frac{d\mathbf{b}}{dt} = \frac{\mathbf{b}_{(t+\Delta t)} - \mathbf{b}_{(t)}}{\Delta t}, \quad (2.60)$$

whereby $\frac{d\mathbf{b}}{dt}$ symbolizes the time derivations, which occur in equation 2.58, $\mathbf{b}_{(t)}$ indicates the value of the old time and $\mathbf{b}_{(t+\Delta t)}$ the value of the new time and Δt the time step length.

Each transient quantity \mathbf{c} , which occurs in equation 2.58, can be approximated in the general form

$$\mathbf{c} = (1 - \vartheta)\mathbf{c}_{(t)} + \vartheta\mathbf{c}_{(t+\Delta t)}, \quad (2.61)$$

with the time collocation factor ϑ . Not only the main variables $(\tilde{\mathbf{p}}_l, \tilde{\mathbf{u}})$, but also element matrices can be time-dependent due to non-linear material behavior and have to be evaluated in time. In the work at hand, the fully implicit (*Backward-Euler*) scheme is used, where $\vartheta = 1$. This has the advantage of numerical stability, even if long time steps are used.

Applying this temporal discretization on equation 2.58 and transformation in order to isolate the unknowns yields

$$\mathbf{C}\tilde{\mathbf{p}}_{l(t+\Delta t)} + \frac{\mathbf{S}}{\Delta t}\tilde{\mathbf{p}}_{l(t+\Delta t)} + \frac{\mathbf{Q}^T}{\Delta t}\Delta\tilde{\mathbf{u}} = \mathbf{f}_{p}^{ext}(t+\Delta t) - \frac{\mathbf{S}}{\Delta t}\tilde{\mathbf{p}}_{l(t)} \quad (2.62a)$$

$$\mathbf{K}\Delta\tilde{\mathbf{u}} + \mathbf{Q}\tilde{\mathbf{p}}_{l(t+\Delta t)} = \mathbf{f}_{u}^{ext}(t+\Delta t) - \mathbf{f}_{u}^{int}(t) - \mathbf{Q}\tilde{\mathbf{p}}_{l(t)} \quad (2.62b)$$

with the temporal incremental of the displacements $\Delta\tilde{\mathbf{u}} = \tilde{\mathbf{u}}_{(t+\Delta t)} - \tilde{\mathbf{u}}_{(t)}$ and the absolute values of the liquid pressure $\tilde{\mathbf{p}}_{l(t+\Delta t)}$.

2.1.8.5 Solving the equation system

With

$$\mathbf{K}_{uu} = \mathbf{K}, \quad \mathbf{C}_{up} = \mathbf{Q}, \quad (2.63)$$

$$\mathbf{C}_{pu} = \frac{\mathbf{Q}^T}{\Delta t}, \quad \mathbf{K}_{pp} = \mathbf{C} + \frac{\mathbf{S}}{\Delta t}, \quad (2.64)$$

$$\mathbf{R}_u = \mathbf{f}_{u}^{ext}(t+\Delta t) - \mathbf{f}_{u}^{int}(t) - \mathbf{Q}\tilde{\mathbf{p}}_{l(t)}, \quad \text{and} \quad \mathbf{R}_p = \mathbf{f}_{p}^{ext}(t+\Delta t) - \frac{\mathbf{S}}{\Delta t}\tilde{\mathbf{p}}_{l(t)} \quad (2.65)$$

equation 2.62 can be formulated in the compact format:

$$\begin{bmatrix} \mathbf{K}_{uu} & \mathbf{C}_{up} \\ \mathbf{C}_{pu} & \mathbf{K}_{pp} \end{bmatrix} \begin{bmatrix} \Delta\tilde{\mathbf{u}} \\ \tilde{\mathbf{p}}_{l(t+\Delta t)} \end{bmatrix} = \begin{bmatrix} \mathbf{R}_u \\ \mathbf{R}_p \end{bmatrix} \quad (2.66)$$

$$\text{which equals the classical form } [\mathbf{A}] [\mathbf{x}] = [\mathbf{b}]. \quad (2.67)$$

Consequently, the equation system $[\mathbf{A}][\mathbf{x}] = [\mathbf{b}]$ has to be solved. The coupled system is solved in a monolithic setup. Since nonlinearities are involved due to the unsaturated flow, the coupling, and non-linear mechanical behavior, a non-linear solver is needed. Thus, the *Newton-Raphson* iteration scheme is used, as described in Kohlmeier (2006) and Zieffle (2008) and in more detail in Wriggers (2001) or Zienkiewicz and Taylor (2005). For the solution of the embedded linear problem the *bi-conjugate gradient stabilized method (Bi-CGStab)* (Meister 2008; van der Vorst 1992) is applied.

2.2 Hydraulic and mechanical anisotropy

2.2.1 Introduction

The grain structure of natural rocks is often characterized by anisotropy, related to its genesis. Sedimentary rock, as claystone, has been formed by deposition and consolidation. Consequently, the micro structure is characterized by the appearance of multiple layers. This composition has a significant influence on the macroscopic behavior of the material. In practical engineering it is a common approach to replace the structured medium by an equivalent continuum, in the sense of the representative elementary volume (see section 2.1.2). Within this phenomenological concept, the rock is still described as a homogeneous medium and its anisotropic material properties are described by additional tensorial measures. The type of anisotropy can be specified by symmetry groups (Flügge 1965). In the case of a layered structure, the material properties in one plane are isotropic. A rotation of the material around the normal of this plane does not change its properties. This type of symmetry is called *transverse* isotropy and can be seen as a special case of *orthotropic* material (see figure 2.8).

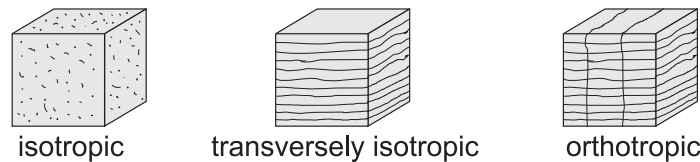


Figure 2.8: Commonly used models for grain structure. In a macroscopic view the grain structure is assumed to be homogeneous.

Investigations on the Tournemire argillite have proved its transversely isotropic structure (see chapter 1.2). In the hydraulic-mechanical model the most important material parameters are the second rank tensor of permeability \mathbf{k} and the fourth rank material tensor \mathbb{C} . In the following sections the transversely isotropic description and practical handling of these tensors will be presented. Further, the meaning of transversely isotropic material will be discussed by examples, concerning the hydraulic, mechanical and hydraulic-mechanically coupled behavior.

2.2.2 Coordinate system

The orientation of transverse isotropy in a global coordinate system can be defined by one vector \mathbf{a} ($\|\mathbf{a}\| = 1$) being normal to the plane of isotropy, as shown in figure 2.9. In general, this vector does not coincide with one axis of the global coordinate system. The transversely isotropic material behavior will be described in a second coordinate system, which is linked to the orientation of anisotropy. This local coordinate system has the axes ξ , η , and ζ and is rotated by the angles α and β in reference to the global coordinate system.

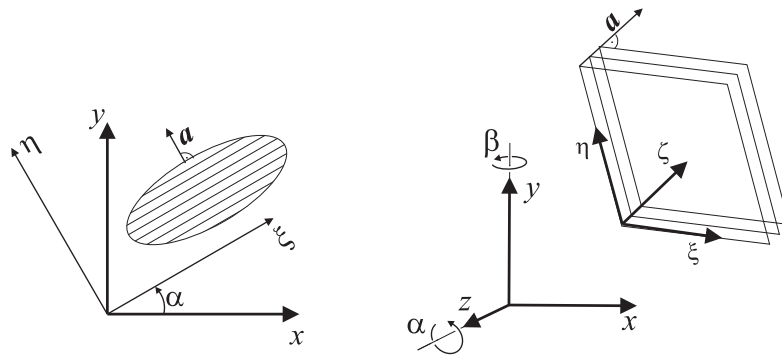


Figure 2.9: Definition of angles and coordinate systems. The axes x , y , and z define the global coordinate system, ξ , η , and ζ the local one. Left: the plane of isotropy coincides with the $\xi\zeta$ -plane; right: the plane of isotropy coincides with the $\xi\eta$ -plane.

2.2.3 Orthotropic permeability

Transversely isotropic geomaterials exhibit mostly a higher permeability in the bedding plane, which equals the plane of isotropy (Domenico and Schwartz 1990). This is founded in the arrangement of the flat minerals. The liquid flux is governed by the modified *Darcy*'s law, as presented in equation 2.37. Considering a three-dimensional orthotropic material representation, the intrinsic permeability tensor consists in general of nine components but can be reduced due to its symmetry as follows

$$\mathbf{k} = \begin{bmatrix} k_{xx} & k_{xy} & k_{xz} \\ & k_{yy} & k_{yz} \\ sym. & & k_{zz} \end{bmatrix}. \quad (2.68)$$

In the coordinate system of anisotropy (figure 2.9), the principal directions of permeability coincide with the coordinate axes; consequently, the non diagonal components of the permeability tensor $\hat{\mathbf{k}}$ equal zero

$$\hat{\mathbf{k}} = \begin{bmatrix} k_{\xi\xi} & 0 & 0 \\ & k_{\eta\eta} & 0 \\ sym. & & k_{\zeta\zeta} \end{bmatrix}. \quad (2.69)$$

Three permeabilities and a local coordinate system are sufficient to define the permeability tensor of an orthotropic material. In the case of transverse isotropy, two of these permeabilities are equal. In order to achieve the permeability in the global system, a transformation is necessary:

$$\mathbf{k} = \mathbf{T}_k \hat{\mathbf{k}} \mathbf{T}_k^T \quad (2.70)$$

with the transformation matrix

$$\mathbf{T}_k = \begin{bmatrix} \cos \alpha \cdot \cos \beta & -\sin \alpha & \cos \alpha \cdot \sin \beta \\ \sin \alpha \cdot \cos \beta & \cos \alpha & \sin \alpha \cdot \sin \beta \\ -\sin \beta & 0 & \cos \beta \end{bmatrix}. \quad (2.71)$$

An application on transversely isotropic fluid flow is presented in section 2.2.5.1.

2.2.4 Transversely isotropic elasticity

In general, sedimentary rocks show a higher stiffness in the bedding plane than perpendicular to it (Wittke 1984), as presented in figure 2.10.

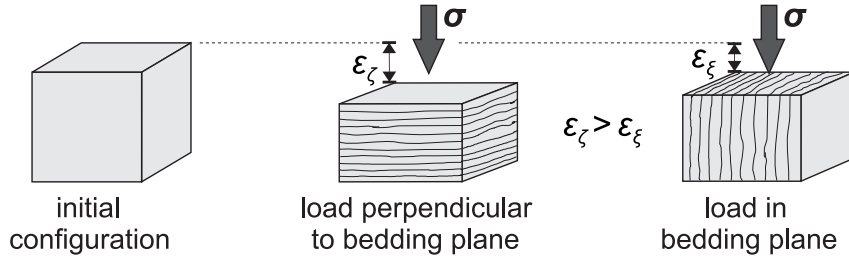


Figure 2.10: Transversely isotropic deformation behavior.

In order to describe anisotropic behavior, the material matrix, as introduced in equation 2.43, cannot longer be represented with only two variables. With the introduction of transverse isotropy, five independent material parameters and the orientation of anisotropy are needed (Ding et al. 2006; Schröder 1996).

Supposed that the plane of isotropy coincides with the $\xi\eta$ -plane in an *Euclidean* coordinate system as depicted in figure 2.9, it is common to use the *Young's* modulus $E_\xi = E_\eta$ in bedding plane and E_ζ perpendicular to it, the shear modulus acting in the bedding plane $G_{\xi\zeta}$, and the two independent *Poisson's* ratios $\nu_{\xi\eta}$, and $\nu_{\eta\zeta}$ in order to define the material matrix $\hat{\mathbf{C}}$ in the coordinate system of anisotropy (Wittke 1984):

$$\hat{\mathbf{C}} = \begin{bmatrix} E_\xi \frac{1-n\nu_{\eta\zeta}^2}{(1+\nu_{\xi\eta})m} & E_\xi \frac{\nu_{\xi\eta}+n\nu_{\eta\zeta}^2}{(1+\nu_{\xi\eta})m} & E_\xi \frac{\nu_{\eta\zeta}}{m} & 0 & 0 & 0 \\ E_\xi \frac{1-n\nu_{\eta\zeta}^2}{(1+\nu_{\xi\eta})m} & E_\xi \frac{\nu_{\eta\zeta}}{m} & 0 & 0 & 0 & 0 \\ E_\xi \frac{\nu_{\eta\zeta}}{m} & 0 & E_\xi \frac{1-\nu_{\xi\eta}}{m} & 0 & 0 & 0 \\ 0 & E_\xi \frac{1-\nu_{\xi\eta}}{m} & 0 & \frac{E_\xi}{2(1+\nu_{\xi\eta})} & 0 & 0 \\ 0 & 0 & 0 & 0 & G_{\xi\zeta} & 0 \\ 0 & 0 & 0 & 0 & 0 & G_{\xi\zeta} \end{bmatrix} \quad (2.72)$$

with the relations: $n = E_\xi/E_\zeta$ and $m = 1 - \nu_{\xi\eta} - 2n\nu_{\eta\zeta}^2$.

In the general case, the direction of anisotropy does not coincide with the global coordinate system. With the definition of a 6×6 transformation matrix \mathbf{T}_u , the linear elasticity for the transversely isotropic case can be written as (see equation 2.43)

$$\boldsymbol{\sigma} = \mathbf{T}_u^T \hat{\mathbf{C}} \mathbf{T}_u \boldsymbol{\varepsilon}^{el}. \quad (2.73)$$

The transformation matrix \mathbf{T}_u can be defined as a function of the angles α and β as shown in Wittke (1984) and Goodman (1996).

Schröder (1996) gives the definition of the material tensor in the tensor form directly:

$$\mathbb{C} = \Lambda \mathbf{1} \otimes \mathbf{1} + 2G_{\xi\eta} \mathbb{I} + \alpha [\mathbf{a} \otimes \mathbf{a} \otimes \mathbf{1} + \mathbf{1} \otimes \mathbf{a} \otimes \mathbf{a}] \quad (2.74)$$

$$+ 2(G_{\xi\eta} - G_{\eta\zeta}) \mathbf{a} \mathbb{I} \mathbf{a} + \beta \mathbf{a} \otimes \mathbf{a} \otimes \mathbf{a} \otimes \mathbf{a} \quad (2.75)$$

with the angles α , β and the vector \mathbf{a} , as defined in figure 2.9, the fourth order identity tensor \mathbb{I} , and $\{\mathbf{a}\mathbb{I}\mathbf{a}\}_{ijkl} = [a_i(\delta_{jk} a_l + \delta_{jl} a_k) + a_j(a_k \delta_{il} + a_l \delta_{ik})]$.

An extensive description, with consideration of different directions of isotropy can be found in Kohlmeier (2006). There is also shown a *RockFlow* application with comparison against literature for the two-dimensional case, which will be expanded to the three-dimensional case, as presented in section 2.2.5.2.

2.2.5 Applications

2.2.5.1 Transversely isotropic flow

A simple two-dimensional application has been carried out in order to illustrate the influence of anisotropic material properties on the fluid flow and the plausibility of the model. The initial and boundary conditions are defined in figure 2.11. Different permeability tensors have been used. The results are given in table 2.1.

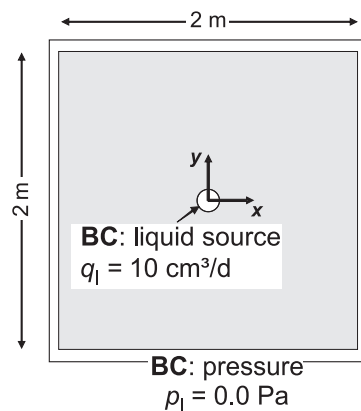
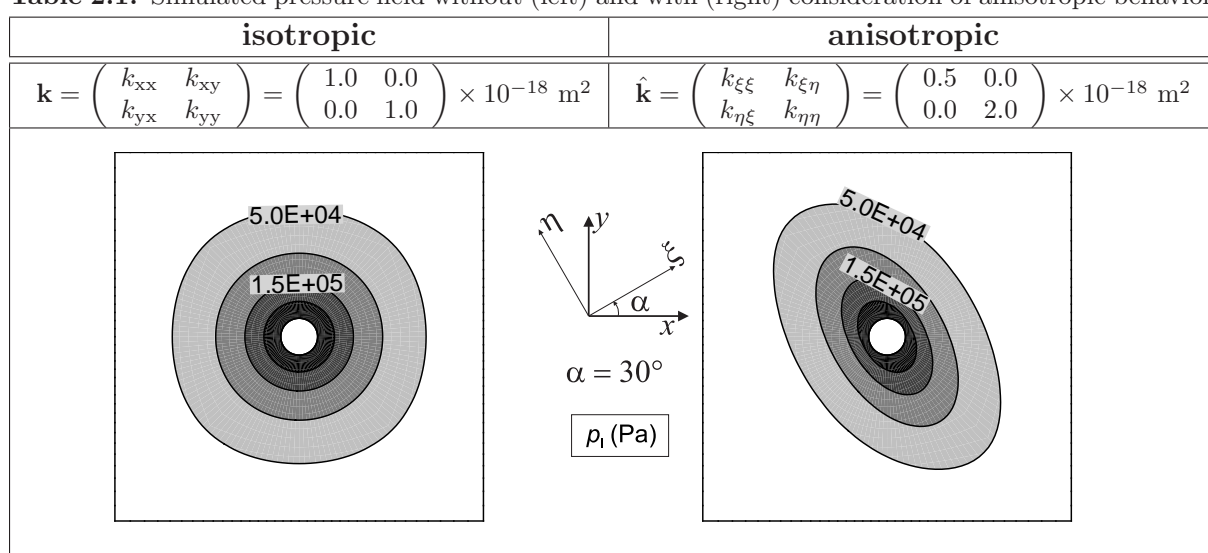


Figure 2.11: Boundary conditions (BC) for the anisotropic flow example.

Table 2.1: Simulated pressure field without (left) and with (right) consideration of anisotropic behavior.



2.2.5.2 Tensile test considering transversely isotropic elasticity

This application is motivated by a tensile test performed in plane strain conditions. The model setup is shown in figure 2.12, the material properties in table 2.2. This two-

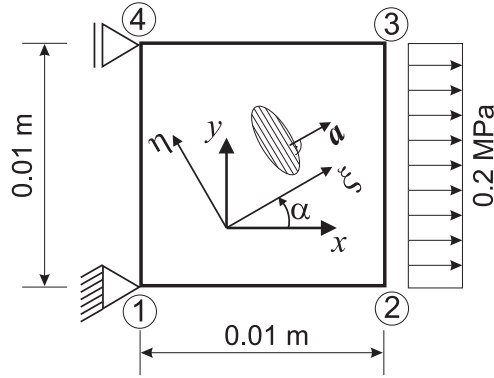


Figure 2.12: Setup of the tensile test.

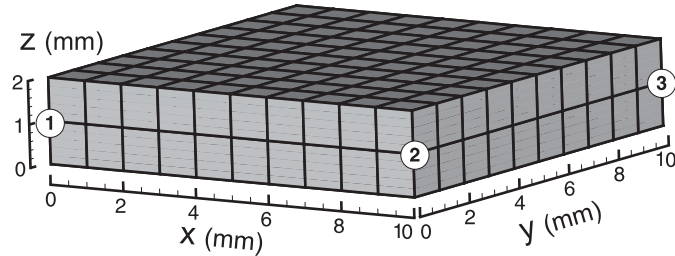


Figure 2.13: Three-dimensional discretization of the tensile test.

Table 2.2: Material properties for the tensile test.

Parameter	Value	Unit
<i>Young's modulus</i>		
perpendicular to bedding plane, E_ξ	1.312	GPa
in bedding plane, $E_\eta = E_\zeta$	0.561	GPa
<i>Poisson's ratio</i>		
$\nu_{\xi\eta}$	0.184	—
$\nu_{\eta\zeta}$	0.603	—
shear modulus, $G_{\xi\eta}$	0.375	GPa

dimensional problem has been simulated by a three-dimensional model. The boundary conditions have been adapted accordingly. The used mesh is presented in figure 2.13, the corresponding results in comparison with the reference solution from Schröder (1996) and the two-dimensional simulation (Kohlmeier 2006) are depicted in figure 2.14.

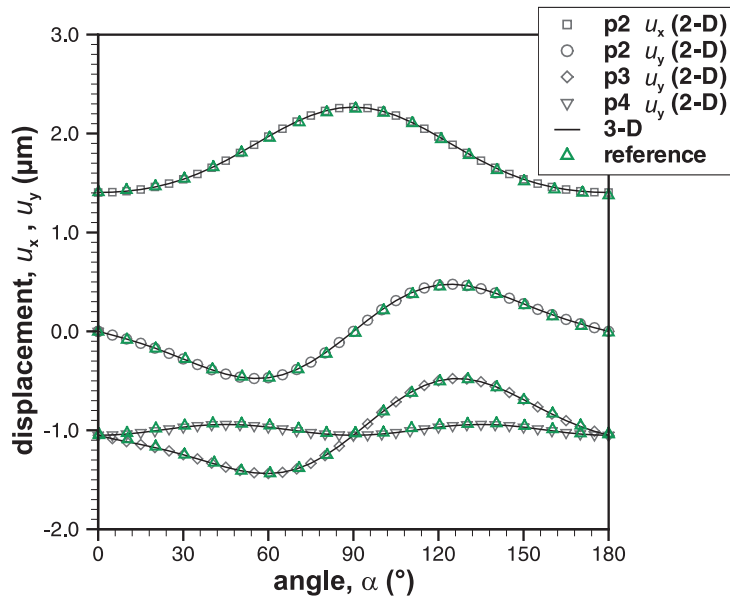


Figure 2.14: Tensile test. Results of the two-dimensional (Kohlmeier 2006) and three-dimensional model, as well as the reference solution by Schröder (1996).

2.2.5.3 Hydraulic-mechanically coupled simulation of an excavation considering transverse isotropy

In order to study the influence of anisotropy on the hydraulic-mechanically coupled behavior, an idealized excavation process is carried out. The model setup of the double symmetric domain is given in figure 2.15. The problem is stated in a 200 m times 200 m quadratic area, with an initial stress state and no-displacement boundary conditions. The initial liquid pressure equals the pressure at the boundary with 0.0 Pa. Before the circular hole in the center has been excavated, the system was in an equilibrium. The material parameters which differ from the reference parameter set (table 1.2, p. 11) are summarized in table 2.3. Comparative simulations with consideration of anisotropy in the initial stress field, in the permeability and in the material matrix have been done. As a response to the excavation process, a rearrangement of the stresses around the hole and a displacement towards the center occur. Due to the coupling, the liquid pressure is also influenced. In general, the pore space near the hole decreases and the liquid pressure increases. This leads to a flux towards the opening, where a pressure boundary condition of 0.0 Pa allows a free outflow. As long as no anisotropy is considered, the zone of increased pressure is equidistant to the hole and the value is moderate, as it is shown in figure 2.11a.

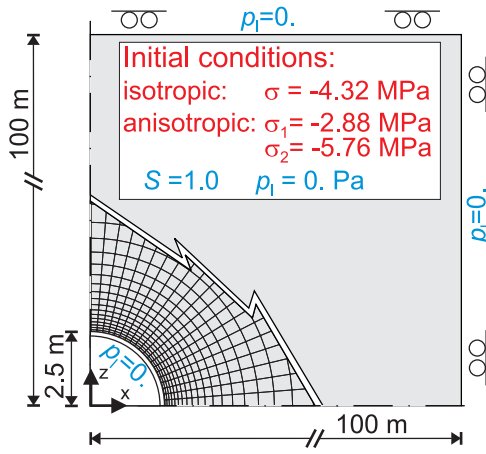
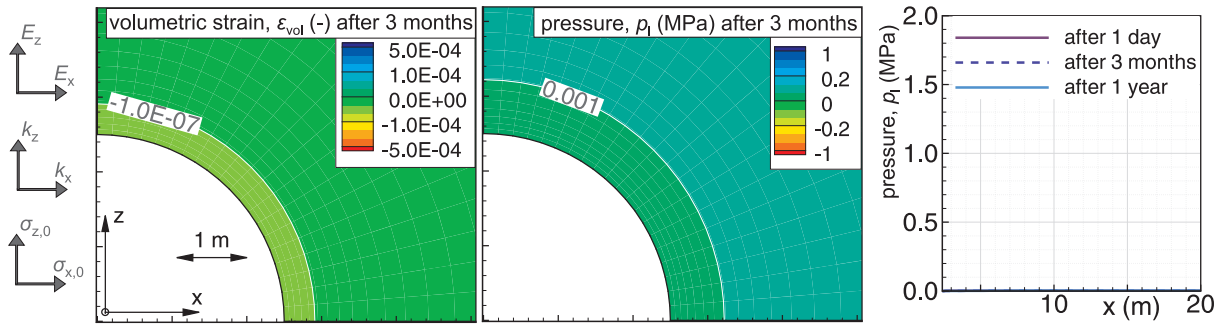


Figure 2.15: H-M coupled study on anisotropic behavior, model setup.

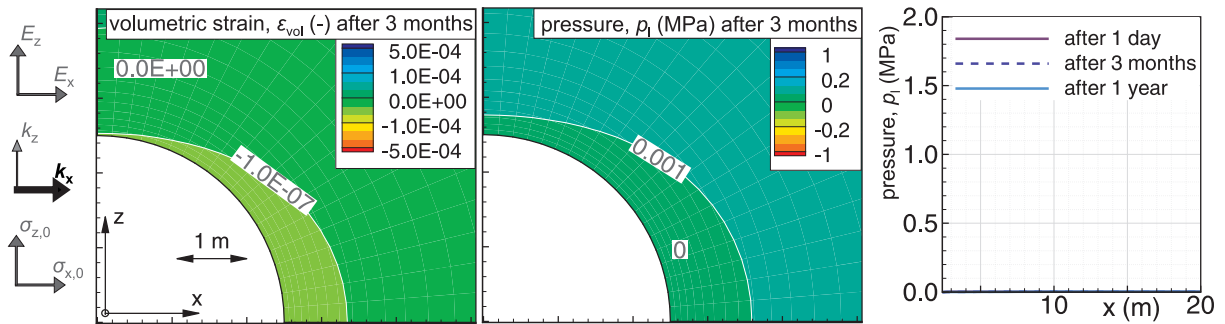
Table 2.3: Model parameters for the H-M coupled study on anisotropic behavior.

Parameter	Value	Unit
intrinsic permeability, k	0.18, 1.0 , 1.8 (*)	10^{-20} m^2
Young's modulus, E	9.29, 16.73 , 24.19 (*)	GPa
Poisson's ratio, ν	0.17, 0.185 , 0.2 (*)	—

(*) The bold printed values are used for the isotropic case.



(a) Isotropic case.



(b) Anisotropic permeability tensor: Permeability in the x -direction is higher than in the z -direction.

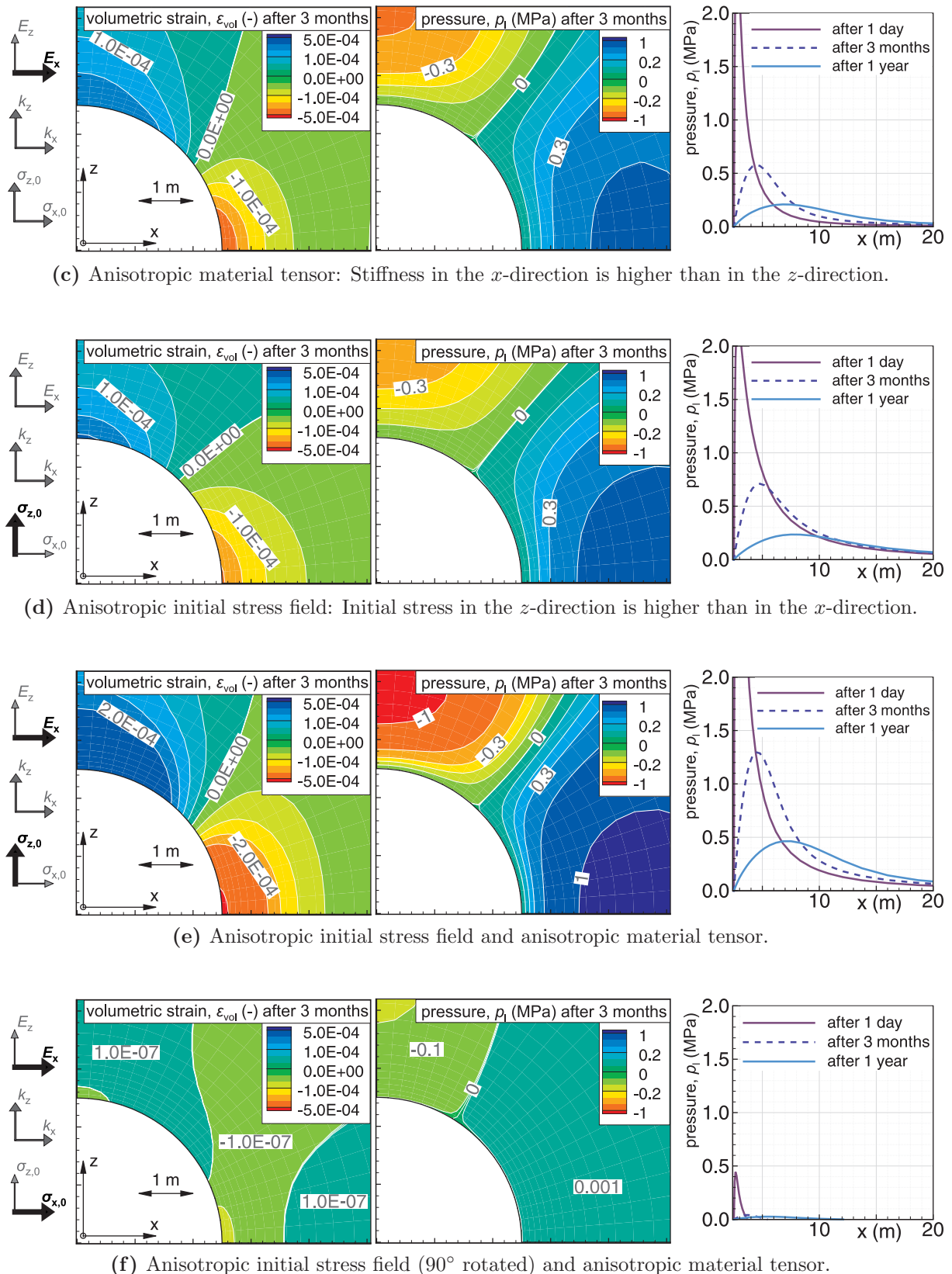


Figure 2.11: Investigation of the H-M response to an idealized excavation process. Contour plots of the simulated volumetric strains ε_{vol} , the liquid pressure (pore water pressure) p_l , and line plots of p_l versus the x -axis at different times. Different combinations of anisotropy are considered.

Even if an anisotropic permeability tensor is considered, only minor changes can be observed (figure 2.11b) in contrast to the influence of mechanically induced anisotropy. There exist at least two ways, how an anisotropic deformation behavior can be caused: anisotropic material behavior and an anisotropic initial stress field. Both types on its own have an enormous and similar impact, as presented in figure 2.11c and 2.11d, respectively. In both cases, higher strains in the z -direction than in the x -direction appear, which leads to a higher amount of volumetric strains as in the isotropic configuration. As a consequence, next to the hole negative volumetric strains occur and the liquid pressure increases; above and beneath the hole positive volumetric strains occur and the liquid pressure decreases. Considering an excavation process in an anisotropic material, loaded by an anisotropic initial stress field, an amplification (figure 2.11e) or an attenuation (figure 2.11f) can happen - depending on the orientation.

Altogether, it seems obvious that anisotropy, especially in the material tensor and the stress field, has to be considered if the hydraulic-mechanical response to an excavation is the object of investigation.

2.2.6 Conclusions

Hydraulic and mechanical anisotropy has been investigated. The presented approach offers the possibility to simulate transversely isotropic elasticity and orthotropic permeability in porous media. The axes of isotropy do not have to coincide with the global coordinate-system. Numerical examples verify the implementation in the finite element code *RockFlow* for the two- and three-dimensional case, respectively. An application on a hydraulic-mechanically coupled excavation problem demonstrates the strong impact of anisotropy on the results.

2.3 Anisotropic swelling and shrinkage

2.3.1 Introduction

The swelling and shrinkage behavior is of special interest in the framework of the safety of a repository, because on the one hand it can lead to a loss of integrity, on the other hand it contributes to self-healing of the EDZ and natural fractures (Mazurek et al. 2003). For the understanding of the behavior of the argillaceous rock at the Tournemire site, the shrinkage and swelling behavior plays an important role. This is demonstrated by observations of shrinkage cracks at the site (Rejeb and Cabrera 2004) and laboratory experiments on the swelling/shrinkage behavior (Valés et al. 2004).

In the work at hand, swelling/shrinkage is understood as a change of volume of a material due to adsorption/resorption of water on clay materials. This adsorption at the surface of clay particles leads to the forming of electrostatic double-layers, which expand the clay or, under constraint conditions, induce swelling pressure (Pusch and Yong 2006; Meunier 2005; Zhang et al. 2004). If platy clay minerals are considered (as at the Tournemire site), a stronger effect perpendicular to the bedding plane than in bedding plane could be expected, caused by the orientation of the clay minerals.

2.3.2 Modeling of swelling and shrinkage

A phenomenological model will be used to model the shrinkage/swelling behavior. The model is directly related to experimental data. It is based on the decomposition of the strain tensor $\boldsymbol{\epsilon}$ into an elastic $\boldsymbol{\epsilon}^{\text{el}}$ part and the swelling strain $\boldsymbol{\epsilon}^{\text{sw}}$ ($\boldsymbol{\epsilon} = \boldsymbol{\epsilon}^{\text{el}} + \boldsymbol{\epsilon}^{\text{sw}}$). This means for the stress strain relation with equation 2.43

$$\boldsymbol{\sigma} = \mathbb{C} : \boldsymbol{\epsilon}^{\text{el}} = \mathbb{C} : (\boldsymbol{\epsilon} - \boldsymbol{\epsilon}^{\text{sw}}). \quad (2.76)$$

In this approach, shrinkage strain is handled similarly to thermal strain, as a stress independent part of the strain tensors (Zienkiewicz and Taylor 2000). Under constraint conditions, no expansion is possible but swelling pressure $\boldsymbol{\sigma}^{\text{sw}}$ occurs. Applying a linear-elastic material model, the swelling pressure becomes

$$\boldsymbol{\sigma}^{\text{sw}} = -(\mathbb{C} : \boldsymbol{\epsilon}^{\text{sw}}). \quad (2.77)$$

Carlson (1937) has shown that for concrete it is a good approximation to take the moisture loss proportional to the shrinkage strain. Following an approach from Bazant (1989), the swelling strain is calculated as a function of saturation. Zieffle (2008) has used an isotropic, linear relationship

$$d\boldsymbol{\epsilon}^{\text{sw}} = \mathbf{1} \beta^{\text{sw}} dS, \quad (2.78)$$

which is widely applied in the modeling of concrete shrinkage (Benboudjema et al. 2005) and will be used as basis for the work at hand. Only one material parameter, the scalar swelling coefficient β^{sw} has to be defined. Experiments on the shrinkage behavior of the Tournemire clay (Valés et al. 2004) have indicated a distinctive anisotropy in the swelling strain. Furthermore, the linear relationship cannot be held. Consequently, the model has

to be extended in order to consider anisotropy and non-linearities. In the most general case, the swelling strain tensor consists of nine coefficients. Equivalent to the section 2.2, the swelling strain tensor can be reduced to the diagonal values in its principal coordinate system by a transformation matrix \mathbf{T}_{sw} :

$$\boldsymbol{\varepsilon}^{sw} = \begin{bmatrix} \varepsilon_{xx}^{sw} & \varepsilon_{xy}^{sw} & \varepsilon_{xz}^{sw} \\ & \varepsilon_{yy}^{sw} & \varepsilon_{yz}^{sw} \\ sym. & & \varepsilon_{zz}^{sw} \end{bmatrix} = \mathbf{T}_{sw}^T \hat{\boldsymbol{\varepsilon}}^{sw} \mathbf{T}_{sw} = \mathbf{T}_{sw}^T \begin{bmatrix} \varepsilon_{\xi\xi}^{sw} & 0 & 0 \\ 0 & \varepsilon_{\eta\eta}^{sw} & 0 \\ 0 & 0 & \varepsilon_{\zeta\zeta}^{sw} \end{bmatrix} \mathbf{T}_{sw}. \quad (2.79)$$

For the definition of the transformation matrix \mathbf{T}_{sw} refer to section 2.2. A power-law is supposed for the calculation of the diagonal values

$$\varepsilon_{\xi\xi}^{sw} = \varepsilon_{init}^{sw} + \beta_{\xi}^{sw} (S^{\gamma_{\xi}^{sw}} - S_{init}^{\gamma_{\xi}^{sw}}), \quad (2.80a)$$

$$\varepsilon_{\eta\eta}^{sw} = \varepsilon_{init}^{sw} + \beta_{\eta}^{sw} (S^{\gamma_{\eta}^{sw}} - S_{init}^{\gamma_{\eta}^{sw}}), \quad (2.80b)$$

$$\varepsilon_{\zeta\zeta}^{sw} = \varepsilon_{init}^{sw} + \beta_{\zeta}^{sw} (S^{\gamma_{\zeta}^{sw}} - S_{init}^{\gamma_{\zeta}^{sw}}). \quad (2.80c)$$

Whereby six material parameters have to be determined ($\beta_{\xi}^{sw}, \beta_{\eta}^{sw}, \beta_{\zeta}^{sw}, \gamma_{\xi}^{sw}, \gamma_{\eta}^{sw}, \gamma_{\zeta}^{sw}$), two parameters to define the initial state ($\varepsilon_{init}^{sw}, S_{init}$) and the corresponding coordinate system. In the case of transverse isotropy, the swelling behavior equals in two directions and the number of independent material parameters is reduced to four. In figure 2.12 a schematic sketch of an orthotropically swelling material is shown.

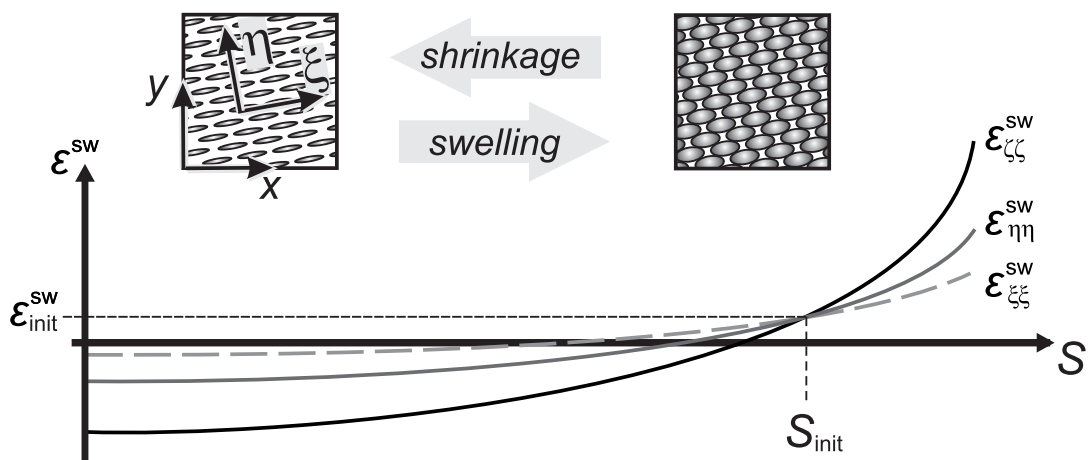


Figure 2.12: Schematic behavior of an orthotropically swelling material.

2.3.3 Determination of swelling/shrinkage parameters

2.3.3.1 Laboratory investigations

Valés et al. (2004) have done a laboratory study on the swelling/shrinkage properties of the Tournemire argillite. Within this experiment, tube samples with a diameter of 36 mm and a length of 80 mm are put into a tight box whose humidity is controlled. The evolution of strain in bedding plane and perpendicular to it has been recorded by strain gauges (figure 2.13), while the humidity has been changed stepwise by the help of different saline solutions. A change of humidity has not been done before the strain and weight evolution have been stabilized, so an equilibrium of the species with the controlled atmosphere can be assumed. In order to simulate this experiment, a three-dimensional, double symmetrical model, representing the tube sample, has been built up. The geometry is shown in figure 2.14 together with the saturation field and the flux vectors. The reference

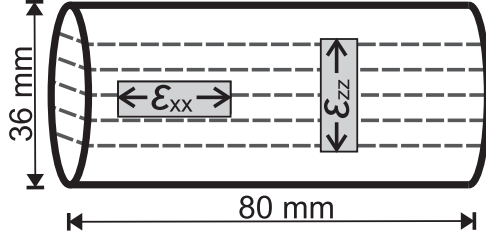


Figure 2.13: Tube sample of the Tournemire argillite with strain gauges (after Valés et al. 2004). The drilling direction was oriented parallel to the bedding plane.

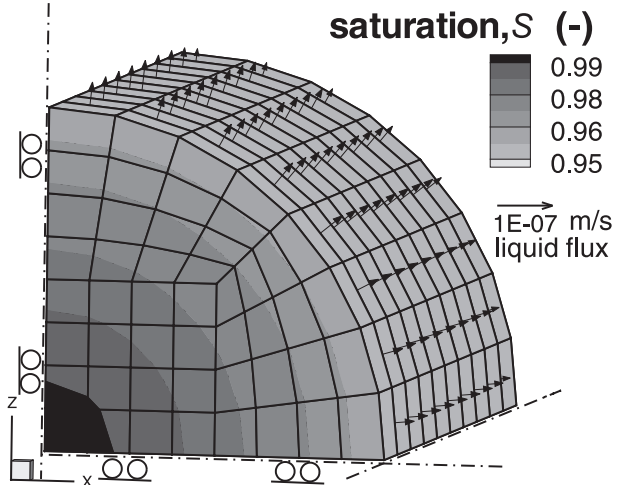


Figure 2.14: Model geometry and saturation field during the desaturation process.

material parameters for the Tournemire argillite, as presented in chapter 1.2.7 (table 1.2, p. 11), have been used. The change of humidity has been modeled by a pressure boundary condition. The value for the capillary pressure at the boundary p_c can be determined with the *Kelvin* equation (Fisher and Israelachvili 1979) as a function of relative humidity h_{rel} :

$$p_c = \frac{\rho_l R T}{M_v} \ln h_{\text{rel}} \quad (2.81)$$

with the density of the liquid ρ_l , here water ($\approx 1000.0 \text{ kg/m}^3$), the perfect gas constant R ($\approx 8.314 \text{ J/(mol K)}$), and the molecular weight of vapor M_v ($\approx 0.018 \text{ kg/mol}$). The temperature is constant ($T = 301 \text{ K}$). In order to determine the swelling parameters, a simplex method after Nelder and Mead (1965) has been used. A power-law has shown good results.

The comparison between measured strains and simulated strains is shown in figure 2.15. The following parameters have been ascertained:

$$\beta_{\xi}^{\text{sw}} = \beta_x^{\text{sw}} = \beta_{\eta}^{\text{sw}} = \beta_y^{\text{sw}} = 0.0022, \quad \beta_{\zeta}^{\text{sw}} = \beta_z^{\text{sw}} = 0.0068, \quad (2.82\text{a})$$

$$\gamma_{\xi}^{\text{sw}} = \gamma_x^{\text{sw}} = \gamma_{\eta}^{\text{sw}} = \gamma_y^{\text{sw}} = 4.55, \quad \gamma_{\zeta}^{\text{sw}} = \gamma_z^{\text{sw}} = 6.51, \quad (2.82\text{b})$$

$$\varepsilon_{\text{init}}^{\text{sw}} = 0.0, \quad \text{and} \quad S_{\text{init}} = 0.893. \quad (2.82\text{c})$$

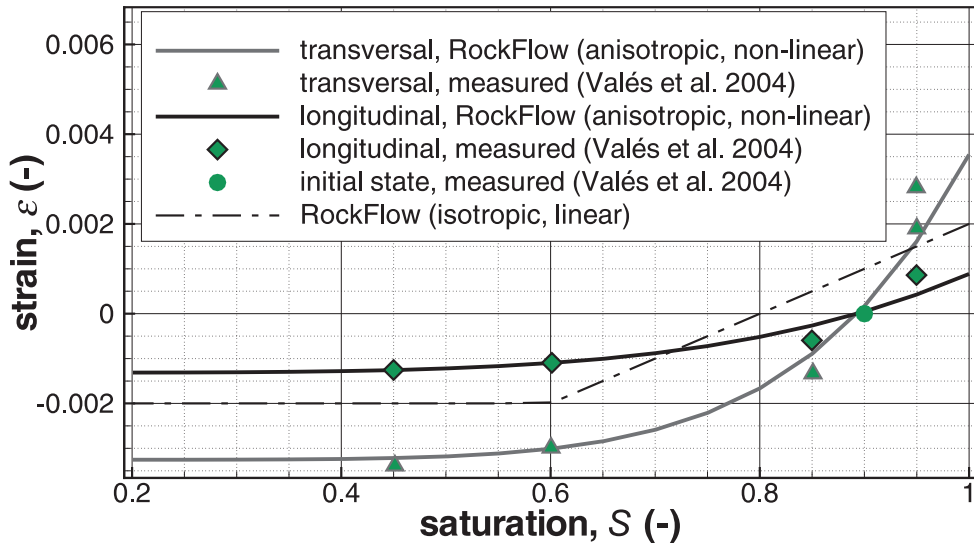


Figure 2.15: Comparison between measured and calculated strains, using strain based swelling models. Longitudinal denotes strain in bedding plane (xy -plane) and transversely perpendicular to the bedding plane (z -direction).

A good agreement has been obtained. This approach has the capacity to consider the orthotropic swelling behavior. For the purpose of comparison, as well the results from a linear isotropically swelling model are shown.

Unfortunately, not all rock samples show the same shrinkage behavior. For another sample, where the bedding plane is perpendicular to the drilling direction, isotropic shrinkage with a much lower amount of shrinkage strain about 0.001 was observed. This difference could be explained by heterogeneity (Valés et al. 2004).

2.3.3.2 In-situ observations

As already mentioned in chapter 1.2.6, a seasonal opening-closing mechanism of fractures has been observed at the Tournemire site (figures 2.16, 2.17). Rejeb and Cabrera (2004) reported a seasonal change of fracture aperture of $\Delta e = 1 \dots 3$ mm. The humidity varies on average between $h_{\text{rel}}^{\text{min}} = 59\%$ in the winter time and $h_{\text{rel}}^{\text{max}} = 91\%$ in the summer time. This causes a seasonal fluctuation of saturation between $S^{\text{min}} = 66\%$ and $S^{\text{max}} = 96\%$ (cf. figure 3.2, p. 99). Additionally, a rather regular spacing between the fractures of

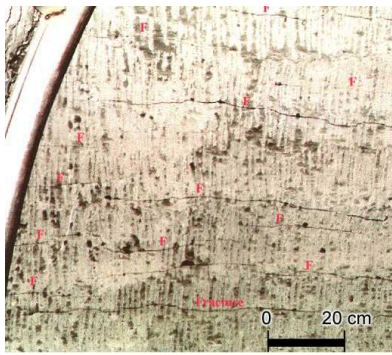


Figure 2.16: Desaturation fractures at the Tournemire site (Rejeb and Cabrera 2004).

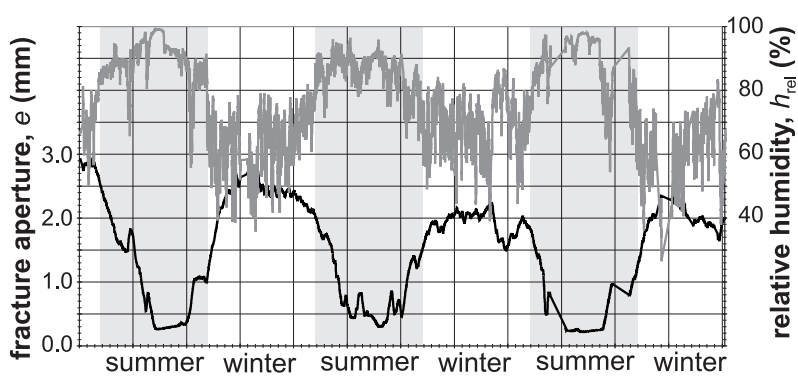


Figure 2.17: Measured fracture opening and relative humidity at the Tournemire site (after Rejeb and Cabrera 2004).

about 0.2 m is recognized, as depicted in figure 2.16. Herewith, it is possible to make a rough estimation of the swelling strain as

$$\Delta\varepsilon_{zz, \text{insitu}}^{\text{sw}} \approx \frac{0.001 \dots 0.003 \text{ m}}{0.2 \text{ m}} = 0.005 \dots 0.015. \quad (2.83)$$

With the proposed non-linear shrinkage model and the parameters as presented in equation 2.82, a swelling strain of $\Delta\varepsilon_{zz}^{\text{sw}} = 0.005$ is predicted, which is within the estimated range.

2.3.4 Alternative approach

An alternative approach for the simulation of shrinkage can be given by a pressure or stress based formulation, as done by Zhang et al. (2004), Kolditz et al. (2002), and Komine and Ogata (2003). Furthermore, the microscale can be taken into account to develop constitutive relations, involving geochemical and electrochemical effects, respectively, as done by: Gens and Alonso (1992); Thomas and Cleall (1999); Ehlers et al. (2003); Xie et al. (2007), amongst others.

The shrinkage behavior in unsaturated conditions is influenced by two mechanisms: first by swelling strain, as a function of the saturation and second, by the suction, due to capillary pressure and the effective stress concept (see section 2.1.7.4). In the simulation as shown before, the *Bishop* parameter χ has been set to zero in unsaturated conditions, in order to eliminate the influence of suction. One could say, the shrinkage model is redundant and the behavior could be modeled by suction only. To investigate this topic, several simulations with different coupling parameters have been done. As a result it can be stated that even without adding a special swelling model, the hydraulic-mechanically coupled model can be used to simulate the effect of shrinkage. However, the developed model can provide better results, especially at high and low levels of saturation, as can be seen in figure 2.18. Additionally, it is more simple to handle, because the results do not depend on the used capillary pressure-saturation relation or any coupling parameters.

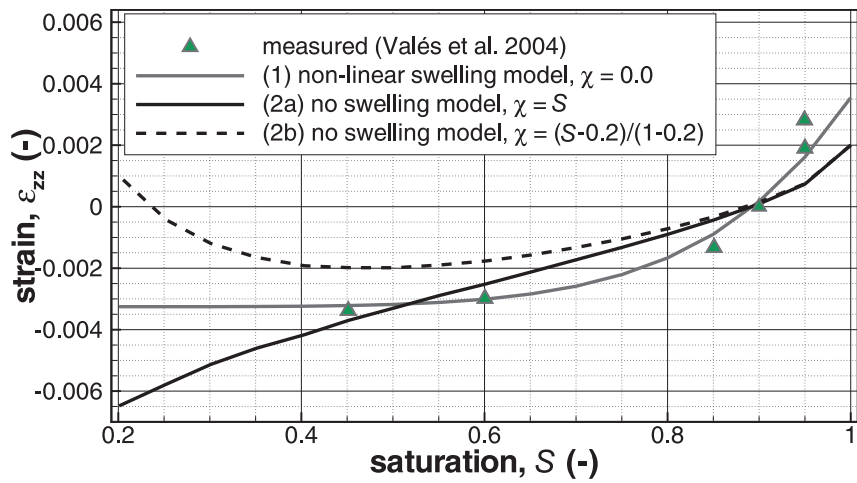


Figure 2.18: Comparison between measured and calculated strains during a desaturation process. The shrinkage is modeled (1) by a non-linear swelling model and (2) by the effective stress concept.

2.3.5 Conclusions

A model has been developed to simulate anisotropic swelling/shrinkage behavior. Even if the strain based phenomenological model is relatively simple in comparison with some other approaches, it has the capacity to simulate the shrinkage of the Tournemire argillite, as described by laboratory tests and in-situ observations. It seems to be meaningful to use the model parameters as described in equation 2.82, being affirmed by in-situ observations at the Tournemire site.

2.4 Continuum damage mechanics

2.4.1 Introduction

The excavation of galleries at the Tournemire site leads to contact of the initially saturated claystone with the ambient air. The induced desaturation process yields tensile strains and as a consequence desaturation cracks (see chapter 1.2.6). In a purely linear-elastic mechanical approach, the arising tensile stresses are not restricted and will exceed the tensile strength of the rock. Furthermore, the degradation of the material due to the occurring cracks is not considered. In order to simulate this tensile failure mechanism of the rock, a damage model will be applied.

In this chapter an introduction in the field of continuum damage mechanics will be given. Special emphasis is put on brittle damage behavior with the consideration of microcrack opening-closing mechanism. Furthermore, a damage model for brittle material, considering damage induced anisotropy will be presented in detail. The capabilities of this model will be proven by verifying examples.

The starting point of *continuum damage mechanics (CDM)* has been set by Kachanov (1958) with the introduction of a continuous field variable describing the damage state in material. Further developments on this concept have been done including thermodynamic and micro-mechanical considerations. The field of applications has also been broadened from ductile metals to brittle concrete (Ortiz 1987, 1985) and to geomaterials (Shao et al. 2006b; Swoboda and Yang 1999a,b; Salari et al. 2004) including claystone (Chiarelli et al. 2003; Conil et al. 2004). Ongoing research is done on the fields of anisotropic damage mechanics and the coupling between damage mechanics and visco-plasticity. Recently, damage mechanics have been applied in the framework of hydraulic-mechanically simulations (Shao et al. 2006c).

An overview of the most important issues of damage mechanics including computational aspects and applications can be found in the textbooks of Lemaitre and Desmorat (2005), Lemaitre (1992), Skrzypek and Ganczarski (1999), Voyiadjis and Kattan (2005), Kattan and Voyiadjis (2002), and Kachanov (1986).

2.4.2 Basic concepts

2.4.2.1 Definition of continuum damage

In the work at hand, *damage* is understood as permanent degradation of mechanical properties of a material, caused by initiation or extension of micro defects, resulting from applied loadings. While elasticity is directly related to the relative movement of atoms (or other micro structures) without changing the bonding in between them, plasticity leads to a displacement of bonds. In geomaterials, plasticity is governed by slips along surfaces of decohesion. When debonding occurs, the damage process begins (Lemaitre 1992). Different types of damage can be mentioned, depending on the applied mechanism. A distinction is made between fatigue, creep, ductile, brittle, chemical, thermal and environmental damage. Whereby the latter is understood as a change of material properties under the influence of the environment, e. g. due to humidity (Kachanov 1986). The

mechanism of brittle damage is the formation and growth of microcracks as take place in ceramics, geomaterials, or concrete (Gross and Seelig 2006). Ductile and creep damage is mainly induced due to the nucleation, growth, and coalescence of micro voids. Fatigue damage is governed by retarded growth of microcrack, caused by cyclic loading. Since natural rock, as a kind of geomaterial, stands in the focus of the current work, brittle damage is of special interest. In general, brittle behavior is characterized by a small amount of plastic strain. As a consequence, an elastic-damage model can be sufficient, without considering plastic deformation.

In the framework of CDM, the damaged material is still treated as a continuum. Although the origin for damage can be found on the microscale, the CDM describes the damage on the macroscale. On the size of the REV (chapter 2.1.2), the damage is defined by a change of the elastic behavior of the material solely. Thus, special damage phenomena cannot be considered, as single cracks, stress peaks in the near field of cracks, interaction and merging of cracks, development of macrocracks, rupture, and localization of failure zones.

In figure 2.19 the stress-strain behaviors of a linear-elastic, perfect elasto-plastic, and elastic-damage material model are depicted. The damage model is characterized by a decreased stiffness, after a damage threshold is exceeded. In contrast to the perfect elasto-plastic model, no irreversible strain occurs. Energy dissipation takes place in both non-linear models. While in plasticity the dissipation is modeled by irreversible plastic strains, the damage leads to an irreversible degradation of stiffness.

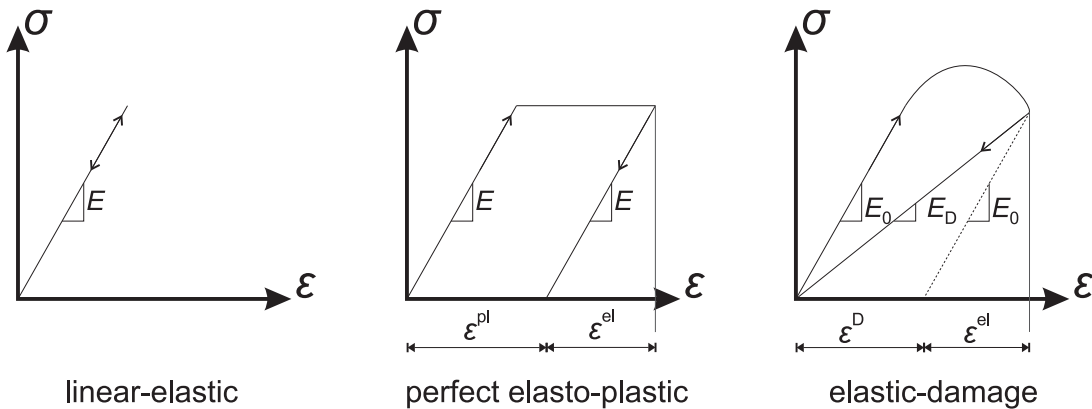


Figure 2.19: Stress-strain relations of different material models.

2.4.2.2 Description of damage

Isotropic

Kachanov (1958) has founded the principle of CDM with the introduction of a scalar damage variable D , defined as the averaged density of intersections. The following definitions are related to a REV of a damaged body depicted in figure 2.20. At the point P , dA defines the area of a plane within the REV and dA_D the area of intersections of

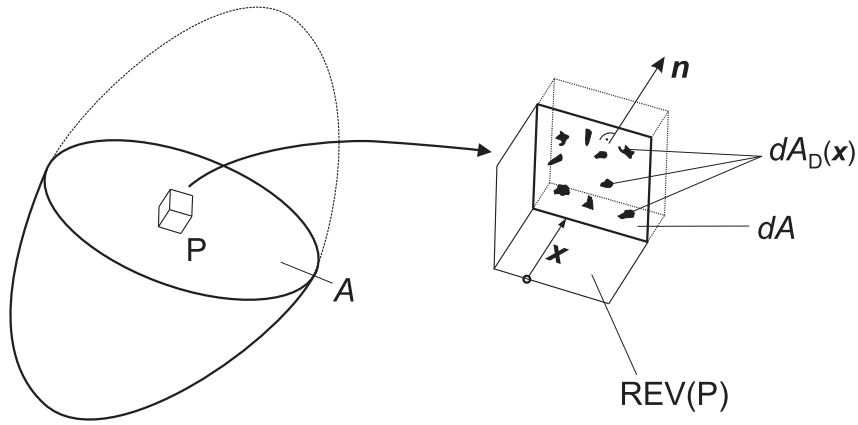


Figure 2.20: Definition of damage (after Lemaitre 1992; Kachanov 1958).

all microcracks or cavities in dA . The latter depends on the location within the REV, defined by \mathbf{x} and its orientation. The value of damage in point P , with respect to the direction \mathbf{n} and the abscissa \mathbf{x} is defined as

$$D(P, \mathbf{x}, \mathbf{n}) = \frac{dA_D(\mathbf{x})}{dA}. \quad (2.84)$$

For the description of the failure mechanism in the direction of \mathbf{n} , the maximally damaged plane, of all planes varying with \mathbf{x} , is significant

$$D(P, \mathbf{n}) = \frac{\max (dA_D(\mathbf{x}))}{dA}. \quad (2.85)$$

As a consequence, the damage variable does not depend on \mathbf{x} . From this definition the range and meaning of the scalar damage variable D follows

$$0 \leq D \leq 1 \quad (2.86)$$

$D = 0 \Rightarrow$ undamaged, virgin REV

$D = 1 \Rightarrow$ fully damaged, ruptured material.

In the case of isotropic damage, or in case of a one-dimensional approach (figure 2.21), also the dependency on the orientation vanishes and the damaged area is understood as an averaged value and can be described as presented in equation 2.88.

Anisotropic

In general, damage is an anisotropic phenomenon, especially if cracks are involved. The cracks follow preferential directions, defined by material properties, as for example in anisotropic fabric, and are guided by the stress distribution. Therefore, the damage variable has to be tensor valued. First (vector), second, fourth and higher rank tensors are used to represent damage. A detailed literature review is given in Skrzypek and Ganczarski (1999). Ju (1990) pointed out the advantages of tensor valued damage description, even

in the isotropic case. In contrast to higher rank tensors, for second rank tensors, a geometrical definition can be given analogously to the isotropic case (Lemaitre 1992): The principal values D_i of \mathbf{D} can be described as the relation between intersections and undamaged areas at three orthogonal planes, defined by \mathbf{n}_i (Murakami 1988)

$$\mathbf{D} = \sum_{i=1}^3 D_i \mathbf{n}_i \otimes \mathbf{n}_i. \quad (2.87)$$

Herewith, an orthotropically damaged continuum can be described, which covers a wide range of applications (Lemaitre 1992). Consequently, this approach is widely used (e. g. Kolari 2007; Shao et al. 2006b; Voyiadjis and Kattan 2005; Conil et al. 2004; Chiarelli et al. 2003; Kattan and Voyiadjis 2002; Murakami and Kamiya 1997; Murakami 1988). Indeed, Lubarda and Krajcinovic (1993) have stated the shortcoming of second rank damage tensors for modeling experimentally determined distribution of cracks. A fourth rank tensor provides superior estimation. Theories based on a fourth rank representation of damage can be found in: Swoboda and Yang (1999a), Chaboche (1993, 1981a,b), Ju (1989), Simo and Ju (1987a), and Ortiz (1985), amongst others. Since the damaged material tensor \mathbb{C}_D has a one-to-one correspondence with the fourth rank damage tensor \mathbb{D} , \mathbb{C}_D itself can be defined as damage variable, in order to limit the data base requirements (Simo and Ju 1987a; Ju 1989; Ortiz 1985).

Even if a geometrical depiction can be given for some damage variables, the direct experimental verification becomes difficult. On the microscale it leads to destructive material testing combined with crack analysis and on the macroscale the determination is done indirectly, by the measuring the change of material properties, as the *Young's* modulus, acoustic wave speed, thermal conductivity, electrical resistance, x-ray diffraction and the like (Lemaitre 1992; Skrzypek and Ganczarski 1999).

2.4.2.3 Damage effective stress concept

Isotropic description

Considering a one-dimensional element, loaded by a force $\mathbf{f} = \mathbf{n}f$ as depicted in figure 2.21, the isotropic scalar damage variable becomes

$$D = \frac{A_D}{A}, \quad (2.88)$$

and the uniaxial stress is

$$\sigma = \frac{f}{A}. \quad (2.89)$$

It is convenient to define a *damage effective stress* $\bar{\sigma}$ acting on the area that effectively resists the load ($A - A_D$)

$$\bar{\sigma} = \frac{f}{A - A_D} = \frac{f}{A(1 - \frac{A_D}{A})} = \frac{\sigma}{1 - D}. \quad (2.90)$$

Obviously, the effective stresses are higher than the nominal ones. This concept has been developed by Rabotnov in 1968 (Lemaitre 1992).

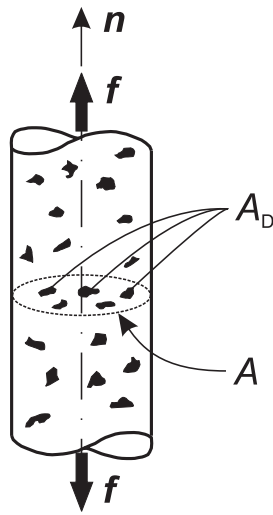


Figure 2.21: One-dimensional damaged element (after Lemaitre 1992).

Anisotropic description

In order to expand the principle of damage effective stress on a more general state of deformation and damage, the fourth rank damage effect tensor \mathbb{M} is introduced as a linear transformation operator (Chow and Lu 1992)

$$\bar{\sigma} = \mathbb{M}(\mathfrak{D}) \sigma. \quad (2.91)$$

The damage effect tensor can be defined as a function of the damage variable \mathfrak{D} , regardless of how the damage is specified as a scalar, vector, second or fourth rank tensor. In order to observe symmetry in the description of stresses, the effective stress tensor has to be symmetrized. Several options have been presented in Voyiadjis and Kattan (2005). Analogously to section 2.1.7.2, a matrix representation of \mathbb{M} can be given (Skrzypek and Ganczarski 1999). Voyiadjis and Kattan (2005) express it in terms of the principal values of a second rank damage tensor in its eigensystem

$$\hat{\mathbb{M}} = \begin{bmatrix} \frac{1}{1-D_{\xi\xi}} & 0 & 0 & 0 & 0 & 0 \\ 0 & \frac{1}{1-D_{\eta\eta}} & 0 & 0 & 0 & 0 \\ 0 & 0 & \frac{1}{1-D_{\zeta\zeta}} & 0 & 0 & 0 \\ 0 & 0 & 0 & \frac{(1-D_{\eta\eta})+(1-D_{\xi\xi})}{2(1-D_{\eta\eta})(1-D_{\xi\xi})} & 0 & 0 \\ 0 & 0 & 0 & 0 & \frac{(1-D_{\zeta\zeta})+(1-D_{\eta\eta})}{2(1-D_{\zeta\zeta})(1-D_{\eta\eta})} & 0 \\ 0 & 0 & 0 & 0 & 0 & \frac{(1-D_{\zeta\zeta})+(1-D_{\xi\xi})}{2(1-D_{\zeta\zeta})(1-D_{\xi\xi})} \end{bmatrix}. \quad (2.92)$$

2.4.2.4 Equivalence principles

In order to formulate constitutive equations in CDM, equivalence principles have been introduced. They are hypotheses and only experimentally firmed for some special cases (Lemaitre 1992).

Principle of strain equivalence. The principle of strain equivalence, as introduced by *Lemaitre*, implies that the strain corresponding to the damaged state under applied stress is equivalent to the strain corresponding to the undamaged state under effective stress (Ju 1989; Skrzypek and Ganczarski 1999; Lemaitre 1992). In figure 2.22 a schematic explanation is given. Lemaitre (1992, p. 13) postulated: “Any strain constitutive equation

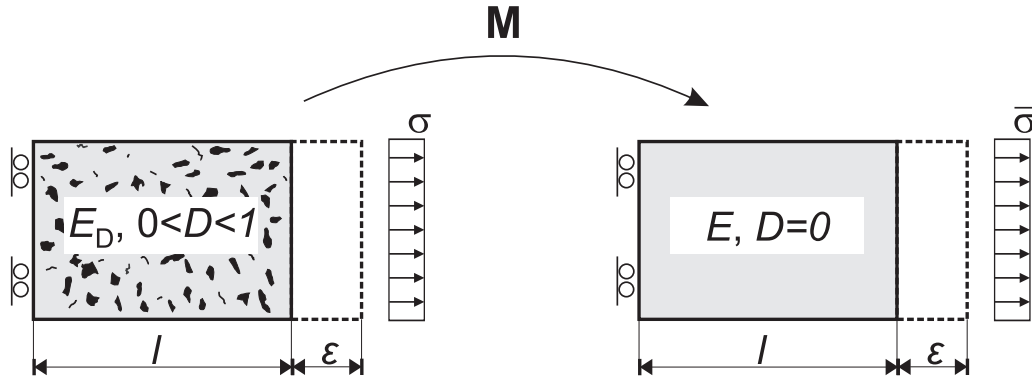


Figure 2.22: One-dimensional visualization of the strain equivalence concept (after Ju 1989).

for a damaged material may be derived in the same way as for a virgin material except that the usual stress is replaced by the effective stress”.

The damage effective stresses and strains are calculated as follows (Skrzypek and Ganczarski 1999)

$$\bar{\epsilon}(\bar{\sigma}, 0) = \epsilon(\sigma, \mathfrak{D}) = \mathbb{C}^{-1} : \bar{\sigma} = \mathbb{C}_D^{-1} : \sigma, \quad (2.93)$$

$$\bar{\sigma} = \mathbb{M}(\mathfrak{D}) \sigma = \mathbb{C} \mathbb{C}_D^{-1} : \sigma = \mathbb{C} : \epsilon, \quad (2.94)$$

$$\text{where } \mathbb{C}_D = \mathbb{M}^{-1}(\mathfrak{D}) \mathbb{C}. \quad (2.95)$$

For isotropic damage it yields

$$\mathbb{M}_{\text{iso}}^{-1}(D) = (1 - D)\mathbb{I}, \quad \bar{\sigma}_{\text{iso}} = \frac{\sigma}{1 - D}. \quad (2.96)$$

The strain equivalence principle leads to a linear decrease of the *Young's* modulus with damage. Thus, for the one-dimensional case it can be stated

$$E_D = E(1 - D), \quad D = 1 - \frac{E_D}{E}. \quad (2.97)$$

Principle of stress equivalence. The principle of stress equivalence can be deduced analogously (Skrzypek and Ganczarski 1999; Simo and Ju 1987a). The principle of strain equivalence is naturally associated to strain-based formulations while the principle of stress equivalence corresponds to stress-based formulations (Simo and Ju 1987a).

Principle of energy equivalence. Since the material tensor in the virgin state and in the damaged configuration are symmetric, the equation 2.95 is a substantial restriction for the definition of \mathbb{M} for anisotropic damage. Assuming the strain equivalence principle, the *Poisson's* ratio does not change with damage, which cannot be held in general for engineering materials (Skrzypek and Ganczarski 1999). A more general approach is given by the use of complementary elastic energy equivalence, as postulated by Cordebois and Sidoroff (1983). Within this theory, both stress and strain distribution are effected. It is based on the definition of the elastic energy of a pseudo-undamaged configuration ψ_D^{el} (cf. equation 2.44, p. 29) with the corresponding effective variables $\bar{\boldsymbol{\sigma}}$ and $\bar{\boldsymbol{\varepsilon}}$

$$\psi_D^{\text{el}}(\bar{\boldsymbol{\varepsilon}}, 0) = \psi^{\text{el}}(\boldsymbol{\varepsilon}, \mathfrak{D}) \quad (2.98)$$

$$= \frac{1}{2} \bar{\boldsymbol{\sigma}} : \bar{\boldsymbol{\varepsilon}} = \frac{1}{2} \boldsymbol{\sigma} : \boldsymbol{\varepsilon}. \quad (2.99)$$

This hypothesis leads to the relations

$$\bar{\boldsymbol{\varepsilon}} = \mathbb{M}^{-1}(\mathfrak{D}) : \boldsymbol{\varepsilon} = \mathbb{C}^{-1} : \bar{\boldsymbol{\sigma}}, \quad (2.100)$$

$$\bar{\boldsymbol{\sigma}} = \mathbb{M}(\mathfrak{D}) \boldsymbol{\sigma} = \mathbb{C}^{1/2} \mathbb{C}_D^{-1/2} : \boldsymbol{\sigma} = \mathbb{C} : \bar{\boldsymbol{\varepsilon}}. \quad (2.101)$$

In contrast to the strain equivalence principle (equation 2.97), the energy equivalence principle leads to the following relation for the one-dimensional case

$$E_D = E(1 - D)^2, \quad D = 1 - \left(\frac{E_D}{E} \right)^2. \quad (2.102)$$

2.4.3 Isotropic damage model

2.4.3.1 Introduction

In the following, an isotropic elastic damage model will be presented. It is based mainly on the phenomenological model as presented in Simo and Ju (1987a,b) and Ju (1989), whereby the critics done by Chaboche (1992, 1993) and Chaboche et al. (1995) have been considered. The strain equivalence principle is applied.

2.4.3.2 Thermodynamic basis

In order to describe the constitutive behavior of material, additional variables will be used, namely *internal variables*. Together with the deformation and entropy (see section 2.1.6.3), the local thermodynamic equilibrium can be described. The following locally averaged free energy function is considered

$$\psi^{\text{el}}(\boldsymbol{\varepsilon}^{\text{el}}, D) = (1 - D) \psi_{\text{init}}^{\text{el}}(\boldsymbol{\varepsilon}^{\text{el}}). \quad (2.103)$$

With the undamaged energy function $\psi_{\text{init}}^{\text{el}}$.

Substituting the time derivative of equation 2.103 into the *Clausius-Duhem* inequality for purely mechanical theory (equation 2.36) yields (cf. equation 2.45)

$$\boldsymbol{\sigma} = \frac{\partial \psi^{\text{el}}}{\partial \boldsymbol{\varepsilon}^{\text{el}}} = (1 - D) \frac{\partial \psi_{\text{init}}^{\text{el}}}{\partial \boldsymbol{\varepsilon}^{\text{el}}} \quad (2.104)$$

and the dissipative inequality

$$\psi_{\text{init}}^{\text{el}}(\boldsymbol{\varepsilon}^{\text{el}}) \dot{D} \geq 0. \quad (2.105)$$

From equation 2.103 it follows that the initial (undamaged) elastic strain energy function $\psi_{\text{init}}^{\text{el}}$ is the thermodynamic force $-Y$ conjugated to the damage variable in the sense that $Y \dot{D}$ is the dissipated energy during the damage process. It can be defined as

$$-Y = -\frac{\partial \psi^{\text{el}}(\boldsymbol{\varepsilon}^{\text{el}}, D)}{\partial D} = \psi_{\text{init}}^{\text{el}}(\boldsymbol{\varepsilon}^{\text{el}}). \quad (2.106)$$

2.4.3.3 Damage criterion

The progressive degradation of mechanical properties due to damage is characterized by an isotropic mechanism. The state of damage in the material is then defined by a damage criterion in the following functional form

$$g(\bar{\tau}_t, r_t) = \bar{\tau}_t - r_t \leq 0. \quad (2.107)$$

The index t refers to the value at current time, $\bar{\tau}$ is the equivalent strain, and r defines the damage threshold (energy barrier). The criterion states that damage increases, if the equivalent strain exceeds the threshold. In the initial (undamaged) state the damage threshold r_{init} defines the damage initiation; later the relation $r_t \geq r_{\text{init}}$ has to be held. The equivalent strain $\bar{\tau}$ is introduced in order to define the damage criterion in a more general way as a function of the strains (Simo and Ju 1987a). For brittle damage mechanism, the equivalent strain can be defined with respect to a positive (tensile) or negative (compressive) state of strain. Several definitions can be found in literature:

$$\bar{\tau}_a = \sqrt{2 \psi_{\text{init}}^{\text{el}}(\boldsymbol{\varepsilon}^{\text{el}})} = \sqrt{\boldsymbol{\varepsilon}^{\text{el}} : \mathbb{C}_{\text{init}} : \boldsymbol{\varepsilon}^{\text{el}}} \quad (\text{Simo and Ju 1987a}) \quad (2.108a)$$

$$\bar{\tau}_b = \sqrt{2 \psi_{\text{init}}^{\text{el}}(\boldsymbol{\varepsilon}^{\text{el}+})} = \sqrt{\boldsymbol{\varepsilon}^{\text{el}+} : \mathbb{C}_{\text{init}} : \boldsymbol{\varepsilon}^{\text{el}+}} \quad (2.108b)$$

$$\bar{\tau}_c = \psi_{\text{init}}^{\text{el}}(\boldsymbol{\varepsilon}^{\text{el}}) = \frac{1}{2} \boldsymbol{\varepsilon}^{\text{el}} : \mathbb{C}_{\text{init}} : \boldsymbol{\varepsilon}^{\text{el}} \quad (\text{Ju 1989}) \quad (2.108c)$$

$$\bar{\tau}_d = \psi_{\text{init}}^{\text{el}}(\boldsymbol{\varepsilon}^{\text{el}+}) = \frac{1}{2} \boldsymbol{\varepsilon}^{\text{el}+} : \mathbb{C}_{\text{init}} : \boldsymbol{\varepsilon}^{\text{el}+} \quad (\text{Ju 1989}) \quad (2.108d)$$

$$\bar{\tau}_e = \sqrt{\boldsymbol{\varepsilon}^{\text{el}+} : \boldsymbol{\varepsilon}^{\text{el}+}} \quad (\text{Conil et al. 2004}) \quad (2.108e)$$

$$\bar{\tau}_f = \sqrt{\sum_{i=1}^3 \langle \hat{\varepsilon}_i \rangle} \quad (\text{Mazars 1986}) \quad (2.108f)$$

with the positive (expansion) part of the strains $\boldsymbol{\varepsilon}^{\text{el}+}$, determined by the fourth rank positive projection tensor \mathbb{P}^+ (see section 2.4.3.7)

$$\boldsymbol{\varepsilon}^+ = \mathbb{P}^+ : \boldsymbol{\varepsilon}. \quad (2.109)$$

In the work at hand, a brittle material is investigated. The main damage mechanism is tension. In general it is observed that in brittle geomaterials the damage evolution is directly related to the tensile strains (Chiarelli et al. 2003). Thus, the use of the positive part of the strains seems to be meaningful. Equations 2.108e and 2.108f do not give an energy equivalent value for initially anisotropic material and so they cannot be used for the modeling of the transversely isotropic claystone.

2.4.3.4 Damage evolution

In order to describe the growth of microcracks and cavities, it is necessary to define evolution equations for D and r . Here, a phenomenological description of the kinetics is attempted. The evolution equations are defined as follows

$$\dot{D}_t = \dot{\lambda} H(\bar{\tau}_t, D_t, \dots) \quad (2.110)$$

$$\dot{r}_t = \dot{\lambda} \quad (2.111)$$

with the damage evolution function H , given in dependency of the equivalent strain, the damage variable and several material properties, e. g. spacing of inclusions, the grain size, the microcrack size, and the porosity, together symbolized by (...). $\dot{\lambda}$ is the damage consistency parameter. According the *Kuhn-Tucker* relations, $\dot{\lambda}$ defines damage loading/unloading conditions

$$\dot{\lambda} \geq 0, \quad g(\bar{\tau}_t, r_t) \leq 0, \quad \dot{\lambda} g(\bar{\tau}_t, r_t) = 0. \quad (2.112)$$

Two cases can be mentioned:

(1) if $g(\bar{\tau}_t, r_t) < 0$, the damage criterion is not satisfied and $\dot{\lambda}$ becomes zero. From equation 2.110 it follows that no further damage occurs ($\dot{D} = 0$).

(2) if $\dot{\lambda} > 0$, further damage takes place and due to equation 2.112, $g(\bar{\tau}_t, r_t)$ has to be zero. As a consequence, the damage threshold can be given by the expression

$$r_t = \max \left(r_{\text{init}}, \max_{s \in (0, t)} \bar{\tau}_s \right). \quad (2.113)$$

The damage evolution function H can be derived on the microscale or as a phenomenological relation by experimental investigations. Commonly used are exponential functions, as the following, which is introduced by Mazars (1986)

$$H = \frac{r_{\text{init}}(1 - A)}{\bar{\tau}_t^2} + AB \exp(B(r_{\text{init}} - \bar{\tau}_t)) \quad (2.114)$$

with the three material parameters A , B , and r_{init} . The damage variable can be stated as

$$D_t = 1 - \frac{r_{\text{init}}(1 - A)}{r_t} - A \exp(B(r_{\text{init}} - r_t)), \quad \text{if } r_t > r_{\text{init}}. \quad (2.115)$$

Another simple but general damage evolution law is given by *Marigo* (Lemaitre and Desmorat 2005):

$$\dot{D}_t = \left(\frac{r_t - r_{\text{init}}}{\dot{A}} \right)^{\dot{B}} \quad (2.116)$$

with the damage parameters r_{init} , \dot{A} , and \dot{B} .

2.4.3.5 Tangent modulus

Even if the mechanical problem is considered solely, the damage behavior leads to a non-linear material behavior, which has to be handled by a non-linear solver. As presented in chapter 2.1.8.5, the *Newton-Raphson* iteration scheme is used, which needs tangent moduli for the numerical solution of the problem. The elastic-damage tangent moduli can be determined by the derivation of the stress tensor with respect to the strain tensor and is given by Ju (1989) as

$$\mathbb{C}_{\tan} = (1 - D) \frac{\partial^2 \psi_{\text{init}}^{\text{el}}}{\partial \boldsymbol{\epsilon}_{\text{el}}^2} - H \bar{\boldsymbol{\sigma}} \otimes \bar{\boldsymbol{\sigma}} = (1 - D) \mathbb{C}_{\text{init}} - H \bar{\boldsymbol{\sigma}} \otimes \bar{\boldsymbol{\sigma}}. \quad (2.117)$$

2.4.3.6 Rate dependency

The motivation for considering the rate dependent damage mechanism is given by two reasons. The first one is of physical nature: Some experimental results on rocks have shown rate sensitivity to the applied rate of loading. The second one's origin is numerical: The softening of the material leads to a loss of strong ellipticity of the problem, associated with numerical difficulties in finite element computations (Häußler-Combe 2007).

The introduced viscous damage mechanism is analogous to the visco-plastic model of the *Przyna* type (Przyna 1966). It is based on replacing the damage consistence parameter λ by $\bar{\mu} \bar{\phi}(g)$, its rate dependent counterpart. Herein $\bar{\mu}$ equals the damage viscosity coefficient and $\bar{\phi}(g)$ the viscous damage flow function. With the equations 2.110 and 2.111 it can be written:

$$\dot{D}_t = \bar{\mu} \langle \bar{\phi}(g) \rangle H(\bar{\tau}_t, D_t, \dots) \quad (2.118)$$

$$\dot{r}_t = \bar{\mu} \langle \bar{\phi}(g) \rangle \quad (2.119)$$

whereby $\langle \bullet \rangle$ denotes the *McAuley* brackets, defined as

$$\langle \bullet \rangle = \begin{cases} 0, & \text{if } \bullet \leq 0, \\ \bullet, & \text{if } \bullet > 0. \end{cases} \quad (2.120)$$

In the case of linear viscous damage mechanism, $\bar{\phi}(g)$ becomes g and the equations 2.118 and 2.119 simplify to

$$\dot{D}_t = \bar{\mu} \langle g \rangle H(\bar{\tau}_t, D_t, \dots) \quad (2.121)$$

$$\dot{r}_t = \bar{\mu} \langle g \rangle. \quad (2.122)$$

Two extremal cases can be mentioned: (1) if $\bar{\mu} \mapsto \infty$, inviscid damage is recovered, and (2) if $\bar{\mu} \mapsto 0$, instantaneous elastic response is obtained. If experimental data of the time-dependent damage behavior are available, the damage viscosity coefficient $\bar{\mu}$ could be determined as a material constant. Otherwise it has to be chosen as high as possible, as long as numerical stability can be preserved. The latter has been done in the work at hand.

2.4.3.7 Microcrack opening and closing mechanism

Concerning the crack initiation and progression, three different modes can be distinguished. One of them is the tensile-mode crack (*mode I*), two of them are shear-mode cracks: *mode II* denotes sliding and *mode III* tearing. In the work at hand, the damage model will be used in order to model tensile-mode cracks. If a single crack is considered two loading conditions could be mentioned, as depicted in figure 2.23. In the tensile

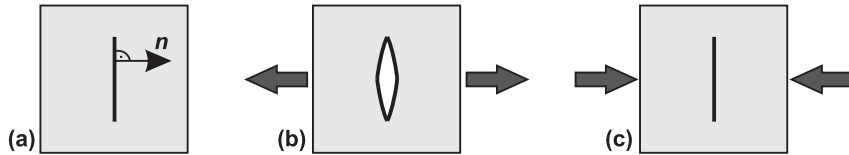


Figure 2.23: *Mode I* crack opening-closing mechanism (after Ortiz 1985). Initial crack geometry (a); crack opening under tension leads to activation of damage (b); crack closing under compression leads to deactivation of damage (c).

loading mode there exist tensile stress in the direction normal to the crack, which will lead to a crack opening mechanism. In the compressive loading mode, the compressive strain normal to the crack initiates a crack closing mechanism. Ortiz (1985) proposed the deactivation of damage in the direction of compression and reactivation of the damage in tension. In the general case of three-dimensional state of stress, the definition of tension or compression becomes more difficult. It is assumed that the microcracks coincide with the principal directions of the strain tensor. A spectral decomposition of the strain tensor is introduced:

$$\boldsymbol{\varepsilon}^+ = \sum_{i=1}^3 \langle \hat{\varepsilon}_i \rangle \mathbf{n}_i \otimes \mathbf{n}_i \quad (2.123)$$

with the i th principal strain $\hat{\varepsilon}_i$ corresponding to the unit principal direction \mathbf{n}_i . With the introduction of the fourth rank positive projection tensor \mathbb{P}^+ the relation to the strain tensor can be described

$$\boldsymbol{\varepsilon}^+ = \mathbb{P}^+ : \boldsymbol{\varepsilon}. \quad (2.124)$$

The positive projection tensor eliminates the negative parts of the strain tensor by setting the negative eigenvalues to zero. The first definition of the projection tensor originates from Ortiz (1985), further developments have been done by Ju (1989), amongst others. A detailed discussion can be found in Tikhomirov (2000); therein, the following definition is supposed, which is used in the work at hand

$$\mathbb{P}^+_{ijkl} = \frac{1}{2} \sum_{A=1}^3 \sum_{B=1}^3 \hat{H}(\hat{\varepsilon}^A) \hat{H}(\hat{\varepsilon}^B) (n_i^A n_j^B n_k^A n_l^B + n_i^B n_j^A n_k^A n_l^B). \quad (2.125)$$

with the *Heaviside step function* \hat{H} , defined as (Bronstein et al. 2008)

$$\hat{H}(\bullet) = \begin{cases} 0, & \text{if } \bullet < 0, \\ 1, & \text{if } \bullet \geq 0. \end{cases} \quad (2.126)$$

Although the damage model presented in this section is isotropic, the microcrack opening-closing mechanism can be considered. Thus, the stress formulation in equation 2.104 is reformulated to

$$\boldsymbol{\sigma} = (\mathbb{I} - \mathbb{D}^{\text{act}}) : \frac{\partial \psi_{\text{init}}^{\text{el}}}{\partial \boldsymbol{\epsilon}^{\text{el}}}, \quad (2.127)$$

$$\text{with } \mathbb{D}^{\text{act}} = D\mathbb{P}^+ \mathbb{I} \mathbb{P}^+, \quad (2.128)$$

with the fourth rank active anisotropic damage tensor \mathbb{D}^{act} (Ju 1989). Two extremal cases can be mentioned:

- (1) if all principal strains are tensile ($\hat{\varepsilon}_i > 0, \forall i = 1, 2, 3$), \mathbb{P}^+ becomes \mathbb{I} and $\mathbb{D}^{\text{act}} = D\mathbb{I}$. All microcracks are open (active) and isotropic damage is applied;
- (2) if all principal strains are compressive ($\hat{\varepsilon}_i \leq 0, \forall i = 1, 2, 3$), \mathbb{P}^+ and \mathbb{D}^{act} becomes \mathbb{O} . All microcracks are closed (passive).

The damage secant material tensor takes the form

$$\mathbb{C}_D = (\mathbb{I} - \mathbb{D}^{\text{act}})\mathbb{C}_{\text{init}}. \quad (2.129)$$

A more general form is given by Chaboche (1993), which is also valid for initially anisotropic elasticity and arbitrary fourth rank damage tensor \mathbb{D} , because it enforces symmetry

$$\mathbb{C}_D^{\text{sym}} = \frac{1}{2} ((\mathbb{I} - \mathbb{D}^{\text{act}}) : \mathbb{C}_{\text{init}} + \mathbb{C}_{\text{init}} : (\mathbb{I} - \mathbb{D}^{\text{act}})). \quad (2.130)$$

Chaboche (1992) criticized the damage opening-closing approach from Ju (1989), because it could lead to discontinuous stress-strain response. He proposed an alternative definition of the material tensor (Chaboche et al. 1995; Chaboche 1993). Applied to the isotropic damage model as presented in this section, his approach of the damaged material tensor can be given as:

$$\mathbb{C}_D^{Cha} = (\mathbb{I} - D\mathbb{I})\mathbb{C}_{\text{init}} + \sum_{i=1}^3 \hat{H}(-\text{tr}(\mathbb{P}_i : \boldsymbol{\epsilon})) \mathbb{P}_i : (\mathbb{C}_{\text{init}} - (\mathbb{I} - D\mathbb{I})\mathbb{C}_{\text{init}}) : \mathbb{P}_i, \quad (2.131)$$

where the fourth rank projection tensor is defined on the principal direction \mathbf{n}_i as

$$\mathbb{P}_i = \mathbf{n}_i \otimes \mathbf{n}_i \otimes \mathbf{n}_i \otimes \mathbf{n}_i. \quad (2.132)$$

In contrast to the approach of Ju (1989), only the diagonal term corresponding to a negative normal strain is replaced by its value corresponding to the initial undamaged state. In this way, the continuity of the stress-strain response is preserved (Chaboche 1993).

2.4.3.8 Algorithm

(1) Strain update

- ▷ At every *Gaussian* point: calculation of the strain tensor from the displacement field

$$\boldsymbol{\varepsilon}_{t+\Delta t} = \frac{1}{2} \left((\text{Grad}_s \boldsymbol{u}_{t+\Delta t})^T + \text{Grad}_s \boldsymbol{u}_{t+\Delta t} \right) \quad (2.133)$$

If tensile sensitive material is considered:

(1b) Determination of the tensile part of strain

- ▷ Calculation of the positive projection tensor \mathbb{P}^+ by equation 2.125
- ▷ Calculation of the positive strain tensor: $\boldsymbol{\varepsilon}_{t+\Delta t}^{\text{el}} = \mathbb{P}^+ : \boldsymbol{\varepsilon}_{t+\Delta t}^{\text{el}}$

(2) Damage evolution

- ▷ Calculation of the equivalent strain $\bar{\tau}_{t+\Delta t}$ with equation 2.108
- ▷ Update the scalar damage variable

$$D_{t+\Delta t} = \begin{cases} D_t, & \text{if } \bar{\tau}_{t+\Delta t} - r_t \leq 0, \\ D_t + (\bar{\tau}_{t+\Delta t} - r_t) H_{t+\Delta t}, & \text{else} \end{cases} \quad (2.134)$$

- ▷ Update the damage threshold $r_{t+\Delta t} = \max(r_{t+\Delta t}, \bar{\tau})$
- ▷ Update the secant material tensor \mathbb{C}_D by equations 2.129, 2.131, respectively
- ▷ Update the stress tensor and damage effective stress tensor:

$$\boldsymbol{\sigma}_{t+\Delta t} = \mathbb{C}_{D\,t+\Delta t} : \boldsymbol{\varepsilon}_{t+\Delta t}^{\text{el}}, \quad (2.135)$$

$$\bar{\boldsymbol{\sigma}}_{t+\Delta t} = \mathbb{C}_{\text{init}} : \boldsymbol{\varepsilon}_{t+\Delta t}^{\text{el}} \quad (2.136)$$

(3) Determination of the tangent modulus

$$\mathbb{C}_{\tan, t+\Delta t} = \mathbb{C}_{D\,t+\Delta t} - H_{t+\Delta t} \bar{\boldsymbol{\sigma}}_{t+\Delta t} \otimes \bar{\boldsymbol{\sigma}}_{t+\Delta t} \quad (2.137)$$

(4) Solving

- ▷ Assembling the global equation system
- ▷ Solving the linearized equation system
- ▷ Check the global equilibrium (residuum)
 - if residuum < admitted error → next time step
 - else → new iteration, go to (1) Strain update

2.4.4 Interactions of damage with material models

2.4.4.1 Linear elasticity

As mentioned before, the damage leads to a degradation of material, which is modeled by a decrease of material stiffness. As a consequence, the elastic strains increase with increasing damage assuming constant external loading. Otherwise, under constraint conditions the elastic stresses becomes smaller with damage.

2.4.4.2 Hydraulic-mechanical coupling

In general, the coupling due to the effective stress approach (see section 2.1.7.4) can be held under damaged conditions. In the following, the consolidation process will be discussed for damaged and undamaged conditions by means of figure 2.24. The porous media

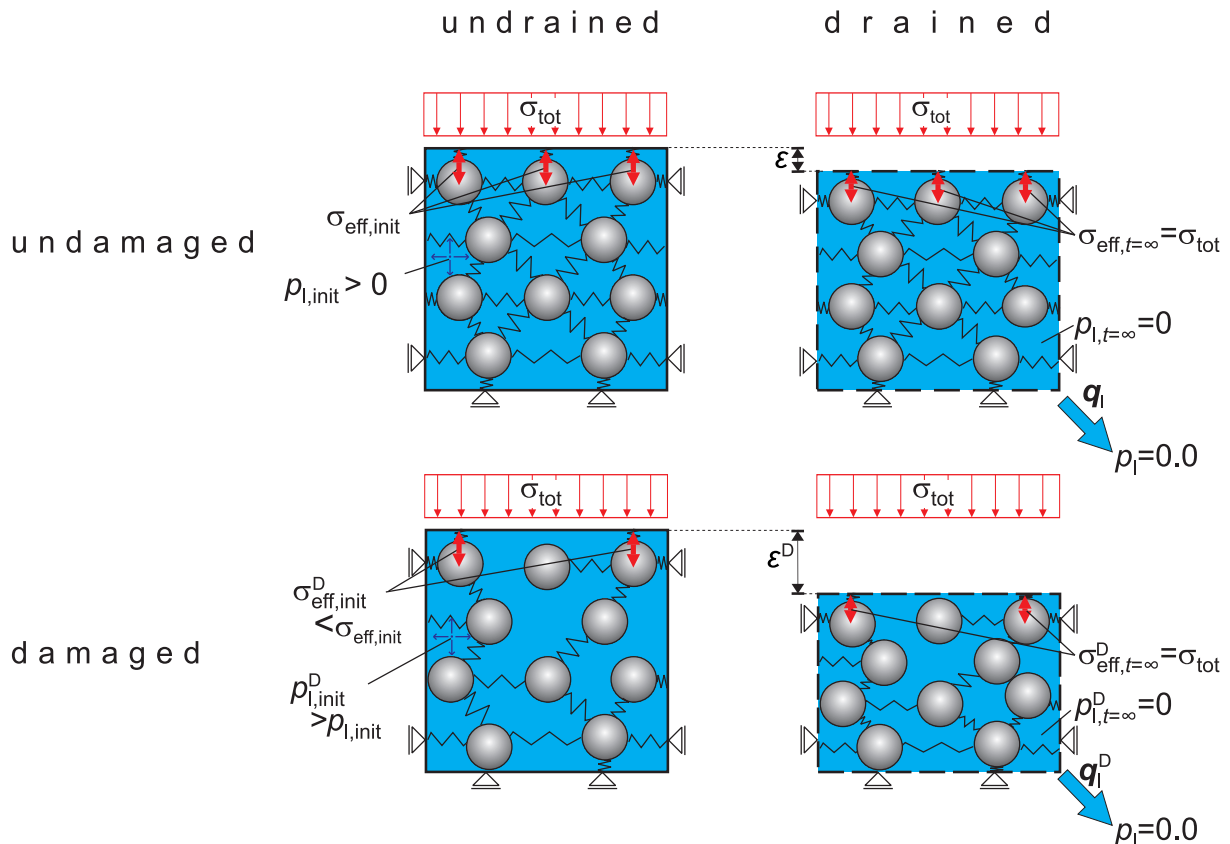


Figure 2.24: Model of the consolidation process of a undamaged (top) and damaged (beneath) porous media. The superscript D indicates the value in the damage configuration in contrast to the undamaged one.

is idealized by rigid spheres connected by springs representing the elastic matrix. In the damaged configuration, some springs are absent in order to represent some loss of integrity. Since the grains and the liquid is assumed to be incompressible, no deformation occurs under undrained conditions in the damaged and undamaged configuration, respectively. Thus, also the state of strains remains unchanged, which leads to lower effective stresses

in the damaged state, where the stiffness is reduced. In order to conserve the balance between inner and outer forces, the pore pressure increases with damage.

The effective stress σ_{eff} is understood as a mean value within a REV, acting on the rock matrix, while the damage effective stress $\bar{\sigma}$ is a microscopic measure, which quantifies the stress acting between grains in the undamaged areas. Hence, the damage effective stress remains unchanged with increasing damage under undrained conditions.

Under drained conditions, as depicted in figure 2.24 on the right hand side, an outward liquid flux is initiated by the pressure gradient. The liquid pressure within the domain decreases with time, until the pressure gradient vanishes. If low permeabilities are present, this consolidation process could take long time. With decreasing liquid pressure, the effective stress increases. Since the stiffness is reduced in the damaged state, greater deformations can be expected, compared with the undamaged state. This behavior can also be observed, if the liquid pressure and external load are fixed on an arbitrary value: the effective stresses are equal in the damaged and undamaged state, but the strains differ.

2.4.4.3 Swelling and shrinkage

It is assumed that the swelling/shrinkage strain is not influenced by the damage. The induced microcracks should not influence the chemical and physical process at the grain. Thus, the swelling stress σ^{sw} , as introduced in equation 2.77 decreases with damage

$$\sigma^{\text{sw}} = -(\mathbb{C}_{\text{init}} : \boldsymbol{\varepsilon}^{\text{sw}}) \quad (2.138)$$

$$\geq \sigma^{\text{swD}} = -(\mathbb{C}_D : \boldsymbol{\varepsilon}^{\text{sw}}). \quad (2.139)$$

2.4.4.4 Plasticity

Plastic behavior is in general indicated by a stress criterion. Consequently, the microscopic “real” stresses between the grains are of interest, namely the damage effective stresses $\bar{\sigma}$. Since increasing damage leads commonly to increasing damage effective stresses, a plastic failure mechanism will be reached earlier than in undamaged material.

2.4.4.5 Permeability

In the current work, a strain-permeability model is used, as described in section 2.5. The damage usually leads to a change of strain and thus the permeability is involved. Since the microcrack initiation changes the geometry of the pores essentially, additional influences on the permeability could be expected and the model approach has been enhanced by an additional, damage induced permeability.

2.4.5 Applications

2.4.5.1 Isotropic damage in tension

The first example deals with the damage evolution at a plate with a hole. The plate is loaded in tension, as depicted in figure 2.25 (left). This example is supposed to get a flavor of the performance of the damage model. The distribution of the scalar damage variable is shown in figure 2.25 (right).

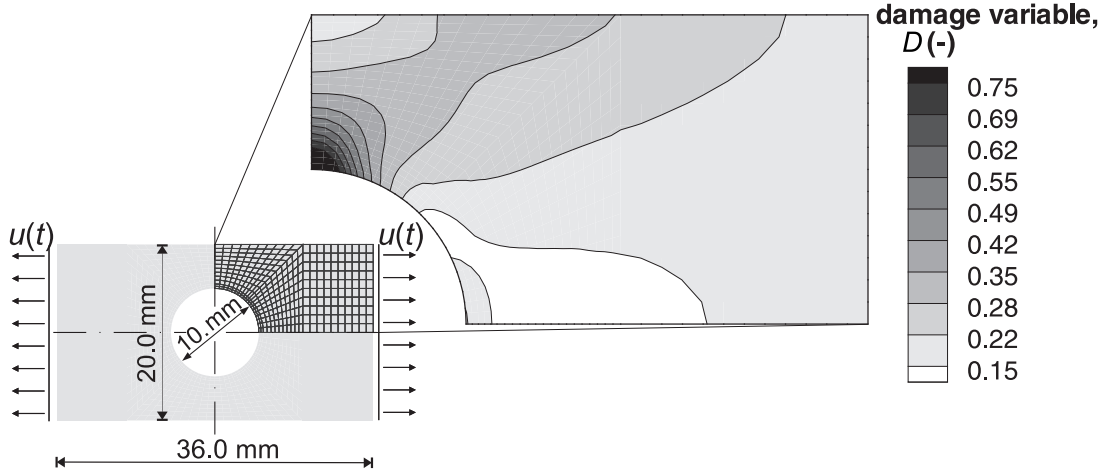


Figure 2.25: Plate with hole under tensional load conditions; left: System; right: Distribution of the damage variable as computed with *RockFlow*.

The damage criterion as presented in equation 2.108c has been used combined with the *Mazars* model for the damage evolution (equation 2.114). For qualitative comparison, the solution from Tikhomirov (2000) is presented in figure 2.26.

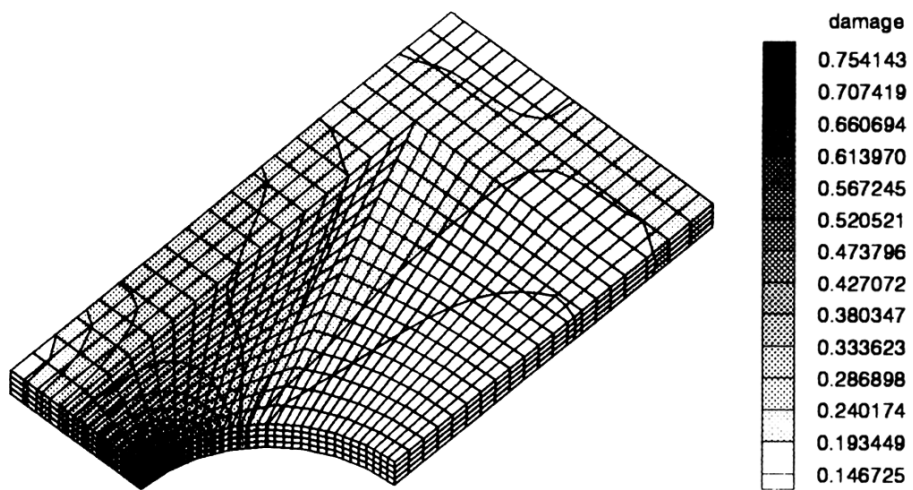


Figure 2.26: Distribution of the damage variable (Tikhomirov 2000, p. 53).

2.4.5.2 Brittle damage with consideration of microcrack opening-closing

In the second example, brittle damage behavior will be mentioned. The distinctive differences of the material behavior under compression and tension will be mentioned by using an equivalent strain measure, which is determined by the positive part of the strain tensor only (equation 2.108d). Furthermore, the microcrack opening-closing mechanism is considered. The behavior will be presented exemplary at a single finite element as depicted in figure 2.27, loaded in compression and tension. The displacement boundary

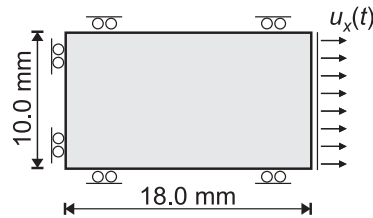


Figure 2.27: System for the investigation of damage evolution under cyclic loading.

condition and the response of the system are plotted in figure 2.28. Three phases can be distinguished:

Linear, undamaged behavior is observed before damage is initiated at point A and between C and D, where the material damage is deactivated due to microcrack closing under compression.

Damage evolution in the intervals A-B and E-F leads to non-linear material behavior. After the initial damage threshold is exceeded (A), the damage increases with increasing tensional load. Since the second loading cycle exceeds the first, a second damage propagation phase is initiated at E.

Linear, damaged behavior is observed in the intervals B-C, D-E, and F-G. During these phases, the state of damage is considered by a reduced, but constant stiffness. Since a higher load condition has been applied before, no damage evolution happens. This is the typical behavior during unloading.

This example demonstrates the principal material behavior under cyclic loading. It also presents the capacity of this approach, to limit the maximal tensional stresses in an element.

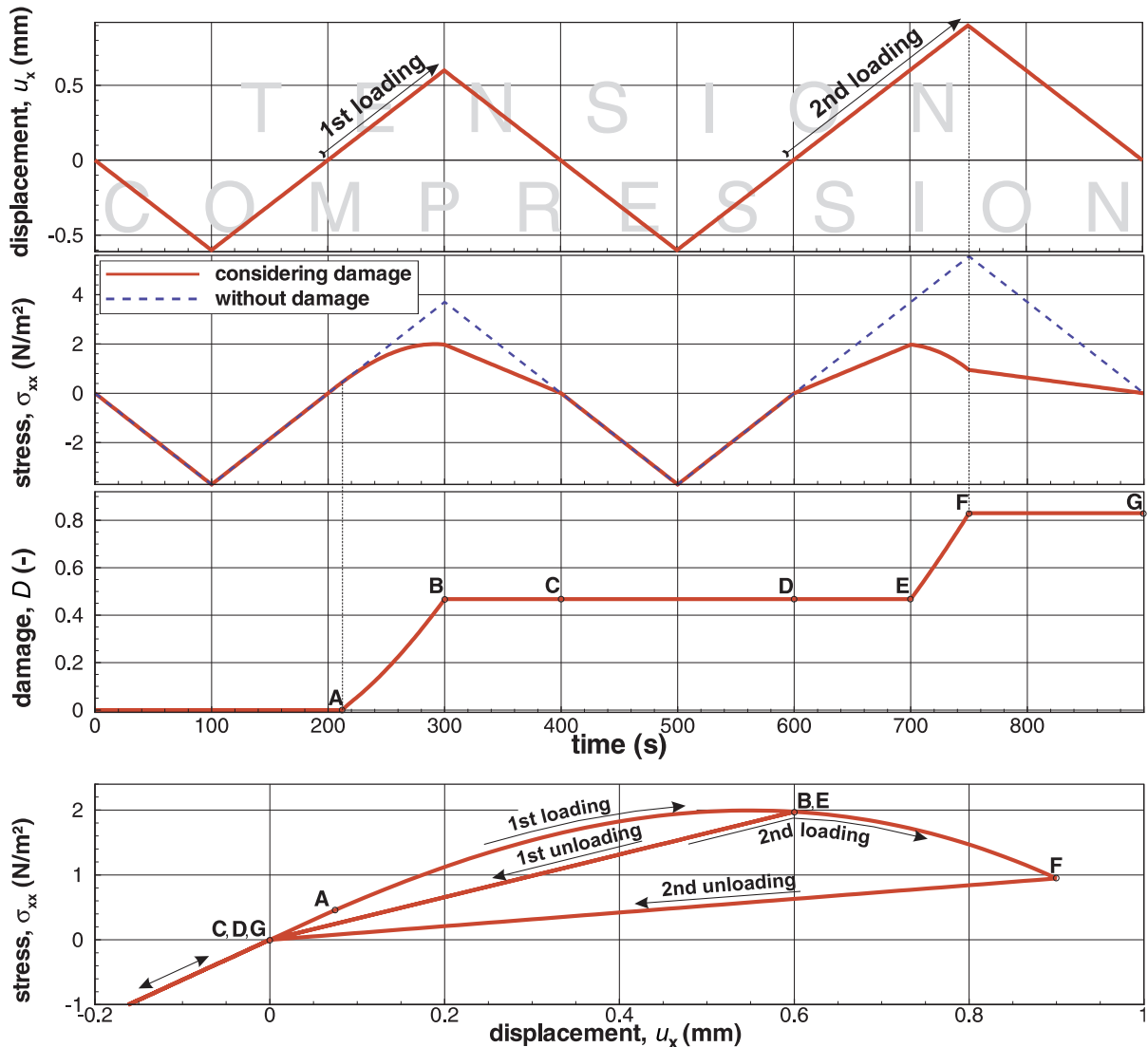


Figure 2.28: Evolution of damage and stresses under cyclic loading. A-B: damage propagation under tension; B-C: constant active damage under tension; C-D: inactive damage due to microcrack closing under compression; D-E reactivated damage due to microcrack opening under tension; E-F: 2nd damage propagation phase; F-G: constant active damage under tension.

2.4.5.3 Shrinkage induced damage

The following example deals with shrinkage induced damage in the framework of coupled hydraulic-mechanical simulations. The object of investigation is a two-dimensional quadratic domain with a centered hole, from which the desaturation process will be induced, as depicted in figure 2.29. Analogously to section 2.5.6.2, the sample is initially saturated and the reference material properties for the isotropic case have been used (table 1.2, p. 11) with a constant permeability of $k = 10^{-20} \text{ m}^2$. The *Marigo* damage evolution model has been applied (equation 2.116) and the damage criterion as defined by equation 2.108d.

The numerical result of this example proves the capacity of the proposed approach to

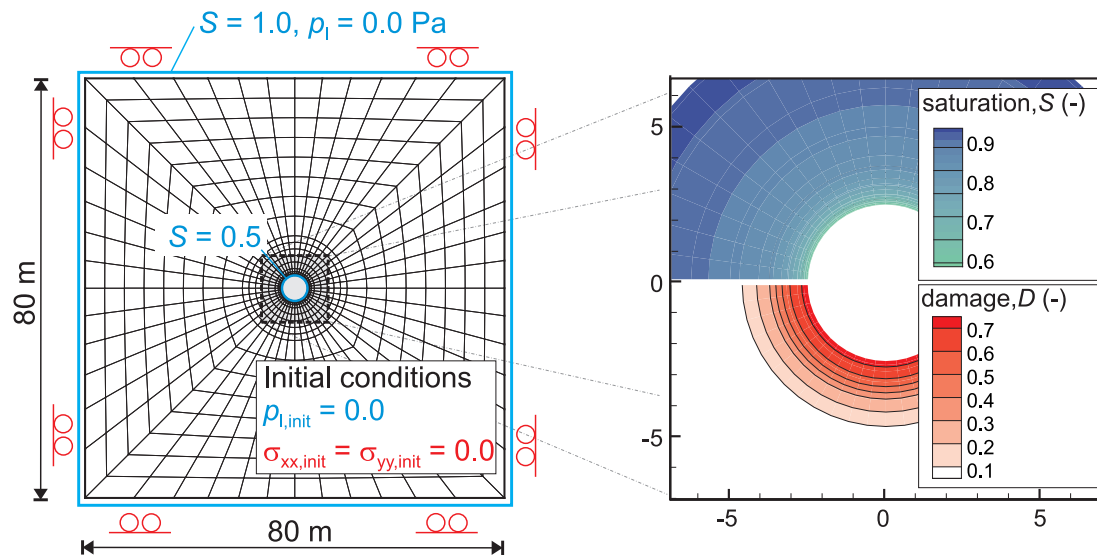


Figure 2.29: Model setup (left); simulation results (right): saturation field (top) and damage state (below).

model shrinkage induced degradation of material. With the used material properties, a damaged zone around the opening is simulated. It measures approximately 3 m and the damage state decreases with distance to the opening. The damage state influences the stress field, as can be seen in figure 2.30. The tensional stresses (positive values) have been reduced by the use of the damage model.

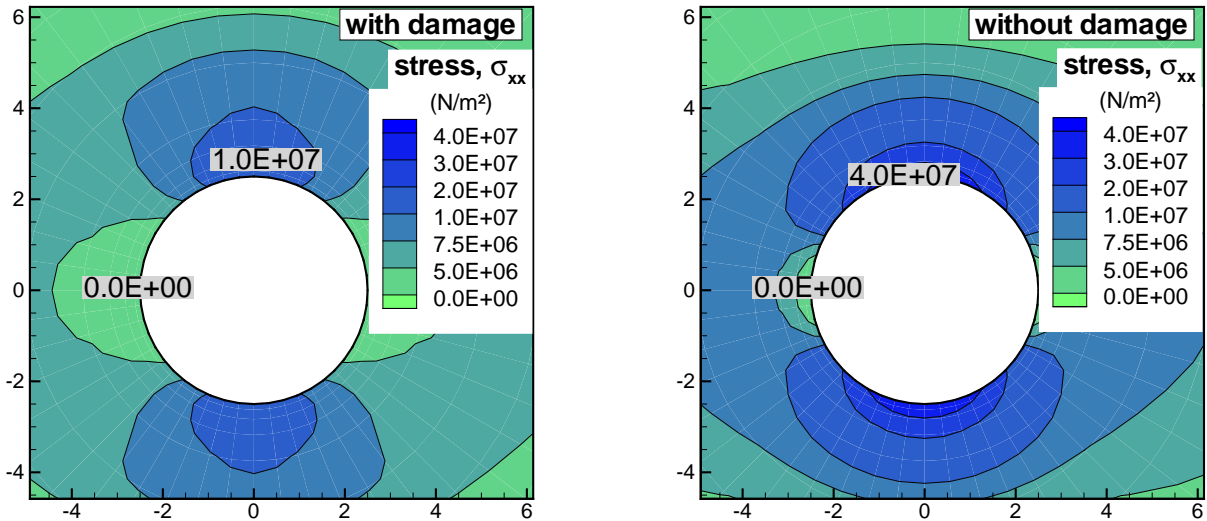


Figure 2.30: Comparison of the horizontal stress field around the opening; with (left) and without (right) consideration of damage.

2.4.6 Conclusions

A damage model for brittle material has been developed and implemented. With help of basic mechanical simulations the model has been tested on plausibility. Even if the damage description is scalar valued, anisotropic effects can be mentioned by the microcrack opening-closing mechanism. Furthermore, the damage model has been applied on a H-M coupled problem: the desaturation process at a circular opening with consideration of shrinkage. Here, shrinkage induced damage can be modeled. In comparison with linear-elastic simulations the shrinkage induced tensional stresses are restricted, which leads to a more realistic prediction of the stress field around the opening.

2.5 Permeability of deformable porous media

2.5.1 Introduction

The permeability is the most important parameter describing the fluid flow through porous media. It is of special interest for geology and engineering applications, e. g. for reservoir simulation, geothermal systems, mining, tunneling, and disposal of waste. In a natural rock system, the permeability is not a constant parameter - it can change with direction (anisotropy), location (inhomogeneity), and with time. The most important influences come from the diagenesis of the rock, by chemical, thermal, and mechanical impacts. In the framework of safety assessment of a repository, the permeability and its development is of special interest, whereby the anisotropy has to be taken into account (Tsang et al. 2005). The determination of the permeability, in particular in claystone, is very complex, because several processes are involved.

Regarding the Tournemire site, there exist several experiments and in-situ measurements of the permeability, but the values vary in a wide range and the influencing parameters can only be guessed. In this context, it seems unsuitable to develop a more complex model, which would involve additional uncertain parameters.

In the work at hand, the influence of an excavation induced deformation on the permeability will be investigated, based on simple assumptions and relations. Nevertheless, such models have the capacity to describe the impact of some effects and can help to identify the most important processes for safety assessment.

In the literature many different permeability models can be found, only a few of them will be discussed in the following. Most of them can be categorized as hybrid models, as they combine theoretical deliberations with empirical observations. Important distinguishing characteristics are the considered soil or rock type, the input parameters, isotropy/anisotropy, and the underlying flow model. Some models define a kind of relative permeability by a product and/or a power-law ($k = \widehat{k}_{\text{rel}} k_{\text{init}}^a$), others add a new term ($k = \widehat{k} + k_{\text{init}}$). The concept of the first one is based on the assumption that the structure of the material does not change in principle, e. g. no additional flow paths come up. The second concept brings in an additional term, which can be interpreted as a second mechanism, like the genesis of new fractures, discussed in detail in section 2.5.5.

Statistical models are not considered here.

2.5.2 Basic flow models

Darcy's law (equation 2.37) is the fundamental equation for determining the permeability in a porous medium. In the following, relations for the identification of the permeability tensor or its scalar representation will be derived. Many permeability models base on simple flow models. The most important ones are the flow through a tube and the flow through a fissure, which is idealized by a flow through two parallel plates. Hydraulically smooth walls are assumed in these models. Bear (1972) gives an overview and derivation of these models. The assumptions, as listed in section 2.1.4, have to be mentioned.

2.5.2.1 Capillary tube model

Poiseuille has investigated flow through a circular capillary at the beginning of the 19th century. Based on his work, the following equation was derived, named after him *Poiseuille's law* (Sutera 1993)

$$\mathbf{q}_l = \frac{\pi d^4}{128\mu_l} \text{grad } p_l \quad (2.140)$$

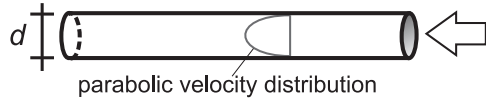


Figure 2.31: Flow through a single tube.

with the diameter d of a capillary as depicted in figure 2.31 (Bear 1972).

Comparing this with the closely analogous *Darcy's law* for a single tube result in an equivalent permeability of

$$k = \frac{d^2}{32}. \quad (2.141)$$

A unit cube (edge length $a = 1$ m) with i equal tubes, oriented parallel to the x -axis (figure 2.35), has the permeability:

$$k_{xx} = i \frac{\pi d^4}{128a^2}. \quad (2.142)$$

2.5.2.2 Fissure model (*cubic law*)

Snow (1965, 1969) has investigated flow through a single fissure as shown in figure 2.32. He derived the permeability as a function of the aperture e between two parallel plates

$$k = \frac{e^2}{12}. \quad (2.143)$$

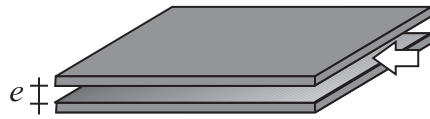


Figure 2.32: Flow through a single fissure.

An unit cube with i equal fissures, oriented parallel to the xy -plane, with the fissure spacing s_z (figure 2.36), has the permeability (Snow 1969)

$$k_{xx} = \frac{e_z^3}{12s_z}. \quad (2.144)$$

This relation is commonly known as the *cubic law*. Additionally, a second set of fissures, parallel to the xz -plane, can be considered

$$k_{xx} = \frac{e_z^3}{12s_z} + \frac{e_y^3}{12s_y}. \quad (2.145)$$

Until today, the cubic law is the basis for many researchers working on the determination of the permeability of natural fractures and fractured rocks, whereby additional effects, as the roughness of the fractures, have been taken into account (e. g. Kelsall et al. 1984; Pusch 1989; Durham 1997; Zhang et al. 2007; Walsh et al. 2008; Giacomini et al. 2008). The principal validity for deformable rock fracture has been proved by Witherspoon et al. (1980). Iwai (1976) has shown the dependency of the cubic law on the stress.

2.5.3 Permeability models

2.5.3.1 Porosity dependent permeability

There exist many approaches to define the permeability k as a function of the porosity n but none of them exhibits general validity. An overview of the classical approaches can be found in Scheidegger (1957). Widely used is the *Kozeny-Carman equation* (Bear 1972). This relation was derived by Kozeny (1927) solving the *Navier-Stokes* equation in a bundle of small tubes (capillaries). Carman (1937) modified it and published the common known *Kozeny-Carman* equation for granular media:

$$k = \frac{n^3}{(1-n)^2} \frac{1}{5M_{\text{spec}}^2} \quad (2.146)$$

with the specific surface M_{spec} , defined as the total interstitial surface area of the pores per total volume. Variations have been done by several researchers mainly on the last term ($\frac{1}{5M_{\text{spec}}^2}$). The *Kozeny-Carman* equation is still the basis for many recent publications, e. g. Xu and Yu (2008) and Takashima and Kurita (2008). Even if this relation has been developed for granular medium, it is also used for clay materials (Zhang et al. 2004) and has also been implemented in the *RockFlow* code (Zieffle 2008).

Bernabé et al. (2003) pointed out that usually a power-law relationship is used in the general form

$$k \propto n^\alpha. \quad (2.147)$$

The exponent α depends on the processes, which lead to the change of porosity and the material. For elastic compaction of sandstones, a wide range for the exponent is given with $\alpha = 1 \dots 20$ (Bernabé et al. 2003).

All porosity-permeability models share the limitation to an isotropic change in permeability due to the scalar valued description of porosity. This criticism has already been formulated by *Collis-George* with special emphasis on clays (Scheidegger 1957). In order to illustrate this restriction, in figure 2.33 a porous medium with directional oriented

voids is presented. The deviatoric deformation does not change the porosity. Consequently, a porosity-permeability model will predict no change in permeability. A more general description of the voids in a porous medium can be done with the definition of directional porosity, as described in section 2.5.4.2. If only hydraulic-mechanically coupled

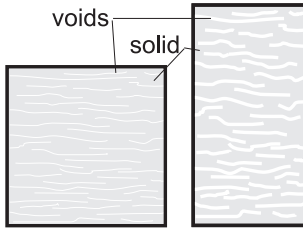


Figure 2.33: Deviatoric deformation of a material with anisotropic void space.

processes are considered, the porosity can be calculated by the deformation, as presented in section 2.1.7.3. This is the conjunction to stress-permeability and strain-permeability relations.

2.5.3.2 Stress and strain dependent permeability

Scheidegger (1957) reported the dependency of the permeability on external loads. Kranz et al. (1979) supposed the following relation, which includes the definition of effective stresses (chapter 2.1.7.4, equation 2.53)

$$k \propto -(\sigma_{\text{tot}} - \hat{\chi} p_l) \quad (2.148)$$

with a factor $\hat{\chi}$, which equals 1.0 for intact rock and is smaller for fractured rock masses, depending on the stress history and the material. Thus, an increase of effective stresses leads to a decrease of permeability. Bai and Elsworth (1994) and Elsworth (1989) specified this relation and stated a function for the change of permeability in a fractured rock k^{frac} mass and an intact rock mass k^{intact} in the form:

$$k^{\text{intact}} = k_{\text{init}} (1 + \beta_{\text{intact}} (\Delta \varepsilon)^{2/3})^3 \quad (2.149)$$

$$k^{\text{frac}} = k_{\text{init}} (1 + \beta_{\text{frac}} \Delta \varepsilon)^3, \quad (2.150)$$

whereby β_{frac} and β_{intact} depend on material properties of the rock, including the initial fracture geometry for β_{frac} . A similar approach has been given earlier by Gangi (1978). Equation 2.149 for the intact rock mass is based upon the *Hertzian* contact theory (Timošenko and Goodier 1951) and a quadratic relation between permeability and the mean grain diameter R_{mean} ($k \propto R_{\text{mean}}^2$). Equation 2.150 is founded on a parallel plate model (equation 2.144), whereby the strain ε is perpendicular to the considered flow direction. Bai et al. (1999) have expanded this model to the common case, where the principal stresses do not coincide with the principal permeabilities.

Another approach has been published by Wong (2003). He added a strain induced part to the initial permeability. This is determined similar to the linear stress-strain relation (see equation 2.43) by a coefficient tensor \mathbb{C}_h

$$\mathbf{k} = \mathbf{k}_{\text{init}} + \mathbb{C}_h : \boldsymbol{\varepsilon}. \quad (2.151)$$

Analogously to the linear stress-strain relation, at least two parameters are needed for the determination of \mathbb{C}_h , which have to be determined experimentally. Due to the linear setup of this model, no power-law relationship can be considered. Nevertheless, this model has been successfully used for reservoir simulation (Du and Wong 2007).

Many more stress and strain based permeability models can be found in literature (e. g. Zhang et al. 2007; Bruno 1994; Leroueil et al. 1990). Nevertheless, the models as presented in this section demonstrate exemplarily essential characteristics of stress/strain based approaches. Most of them use a kind of power-law for the determination of the permeability and, in contrast to the porosity based models, they have the capacity to consider anisotropy. Both characteristics can be found as well in the model, as developed in section 2.5.4.

2.5.3.3 Further models

There are many more mechanisms that influence the permeability and more methods to describe rock properties. Consequently, more models exist, considering the influence of temperature (Elsworth 1989), damage (Souley et al. 2001; Shao et al. 2005; Zhou et al. 2006), plastic strain, chemical reactions (Min et al. 2009), rock quality (Sen 1996; Liu et al. 1991), grain size distribution, grain orientation, etc. Most of these approaches are restricted to special sites or materials and depend directly on in-situ observations and laboratory tests, respectively. Some of them combine stress with fracture evolution (Simpson et al. 2008; Min et al. 2004) or porosity evolution (Sisavath et al. 2000).

2.5.4 Development of an orthotropic strain based permeability model

2.5.4.1 Approach

In practice, it becomes difficult to determine the parameters for the introduced models. The purpose of the new model, as described in the following, is the estimation of orthotropic permeability depending on the strains without further parameters. It is solely based on the initial permeability (which could be anisotropic), the porosity, the strains, and assumptions concerning the geometry of the pore space. This restriction has to be done due to the fact that no further data are available. In order to allow an unrestricted use of the permeability model in the framework of the coupled model concept, as presented in chapter 1.3.3, it has to deal with shrinkage/swelling and transverse isotropy. Summarizing, the permeability model, developed to investigate the Tournemire site, has to fulfill at least the following requirements:

- ▷ consideration of volumetric and deviatoric deformation (anisotropic stress/strain field),
- ▷ consideration of a transversely isotropic initial permeability,
- ▷ consideration of swelling/shrinkage,
- ▷ preferably independent from the used stress-strain relation,
- ▷ a minimum of additional parameters.

Since no measurement exists which quantifies the strain/stress permeability relation, the results of this model have to be understood as a qualitative estimation. Furthermore, the starting point of the model has to be chosen more elementary. Hence, the approach is founded on simple flow equations (section 2.5.2). The original porous medium is represented by a set of orthogonal fissures or tubes (Liu et al. 1991). In order to describe the flow effective pore space orthotropically, the *void fabric tensor* is introduced. By doing this, it is possible to extent the previously presented volumetric relation between porosity and strain to deviatoric quantities.

The approach is restricted to small changes of the pore space, because otherwise the change of the shape of the pore space and the initiation of new voids had to be taken into account. Thus, the model can be applied in intact rock mass only, otherwise damage has to be considered, as presented as a model extension in section 2.5.5.

2.5.4.2 Void fabric tensor

The permeability is strongly influenced by the packing of particles. But as long as the scalar measure porosity is used for the characterization, the directional nature of void space cannot be captured. Thus, a directional description is introduced by a *void fabric tensor* (Muhunthan and Chameau 1997; Zysset and Curnier 1996). A REV of a porous medium is considered, consisting of solids and voids. A test line, defined by an arbitrary unit vector \mathbf{m} , intersects this domain. The total length of this line is defined as L and the fraction of this test line, which is occupied by voids as $l = \sum l_i$ (figure 2.34). Thus, a directional porosity n_m can be defined as a function of \mathbf{m} by

$$n_m(\mathbf{m}) = \frac{l(\mathbf{m})}{L}. \quad (2.152)$$

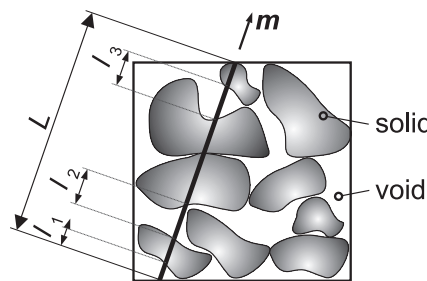


Figure 2.34: Definition of the test line and its void fractions within a REV.

If the length of the test line is in the size of the REV, the directional porosity depends on the orientation of \mathbf{m} solely and can be represented in terms of even ranked symmetric traceless tensors $\Omega_{ij}, \Omega_{ijkl}, \dots$ (Kantani 1984)

$$n_m(\mathbf{m}) = n(1 + \Omega_{ij}v_i v_j + \Omega_{ijkl}v_i v_j v_k v_l + \dots). \quad (2.153)$$

For the sake of simplicity, the used description will be restricted to a second rank tensor, which has been found sufficient for most applications (Kantani 1984). Harrigan and Mann (1984) pointed out the restriction to orthotropic materials, if a symmetric second rank tensor is used. The tensor $\Omega_{ij} = \boldsymbol{\Omega}$ is defined as *void fabric tensor*. The directional porosity can be approximated as

$$n_m(\mathbf{m}) \approx n(1 + \boldsymbol{\Omega} : \mathbf{m}). \quad (2.154)$$

Thus, the void distribution of the medium is described by a scalar valued (mean) porosity n , defining the size of the pore volume in relation to the total volume, and a deviatoric second rank tensor $\boldsymbol{\Omega}$, which characterizes the fabric of the pores. In the case of isotropy, the directional porosity does not depend on the orientation and coincides with the porosity ($n_m(\mathbf{m}) = n$). Consequently, all entries of the void fabric tensor Ω_{ij} become zero. In general, $\boldsymbol{\Omega}$ can be described by five independent variables, due to its symmetry and traceless character. Since the void fabric tensor falls into the general class of second rank tensors, it can be transformed into a principal coordinate system, described by the basic unit vectors ξ, η, ζ , in which the non diagonal entries become zero. A spectral decomposition can be considered

$$\boldsymbol{\Omega} = \hat{\Omega}_{\xi\xi}\xi \otimes \xi + \hat{\Omega}_{\eta\eta}\eta \otimes \eta + \hat{\Omega}_{\zeta\zeta}\zeta \otimes \zeta, \quad (2.155)$$

with the three principal values $\hat{\Omega}_{\xi\xi}, \hat{\Omega}_{\eta\eta}, \hat{\Omega}_{\zeta\zeta}$. An eigenvalue analysis has to be done for the determination of these values. Therefore, the characteristic equation ($\det(\boldsymbol{\Omega} - \lambda \mathbf{1}) = 0$) has to be solved. The arising cubic equation system can be solved for example analytically by the *Cardano's formula* (Bronstein et al. 2008) or numerically by an iterative algorithm, e. g. *Tayler rotation* (Feldmann 1993).

2.5.4.3 Determination of the void fabric tensor in a deformable porous medium

In order to consider anisotropy, a decomposition of the strain tensors in a volumetric and deviatoric part has to be done

$$\boldsymbol{\varepsilon} = \mathbf{1} \varepsilon_{\text{vol}} + \boldsymbol{\varepsilon}_{\text{dev}}, \quad (2.156)$$

$$\varepsilon_{\text{vol}} = \text{tr } \boldsymbol{\varepsilon} = \varepsilon_{xx} + \varepsilon_{yy} + \varepsilon_{zz}, \quad (2.157)$$

$$\boldsymbol{\varepsilon}_{\text{dev}} = \boldsymbol{\varepsilon} - \frac{1}{3} \mathbf{1} \varepsilon_{\text{vol}}. \quad (2.158)$$

The scalar valued porosity is a volumetric measure. It can be determined by the strains (see chapter 2.1.7.3)

$$n = n_{\text{init}} + \varepsilon_{\text{vol}} - \varepsilon_{\text{vol}}^{\text{sw}}. \quad (2.159)$$

The void fabric tensor is a deviatoric measure. It can be determined by

$$\boldsymbol{\Omega} = \boldsymbol{\Omega}_{\text{init}} + \boldsymbol{\varepsilon}_{\text{dev}} - \boldsymbol{\varepsilon}_{\text{dev}}^{\text{sw}}. \quad (2.160)$$

2.5.4.4 Permeability as a function of the void fabric tensor

General description of the approach. For the determination of the permeability it is assumed that the principal axes of the permeability tensor coincide with the principal axes of the void fabric tensor. Thus, one principal coordinate system described by the basic unit vectors ξ, η, ζ can be defined, in which only the diagonal values of the void fabric tensor and the permeability tensor are unequal zero. Furthermore, two different pore space geometries will be considered: a capillary tube model and a fissure model. For both, the permeability can be described as a function of the flow effective area A^{eff} , which is defined perpendicular to the flow direction and can be interpreted as a representation of the pores, which are connected in the direction of flow. The flow effective area in turn can be described by the void fabric tensor and the porosity. Consequently, the general tensor valued problem

$$\mathbf{k} = \mathbf{f}(\Omega, n) \quad (2.161)$$

reduces to three scalar valued functions

$$\hat{k}_{\xi\xi} = f(\hat{A}_{\eta\zeta}^{\text{eff}}) = f(\hat{\Omega}_{\eta\eta}, \hat{\Omega}_{\zeta\zeta}, n), \quad (2.162a)$$

$$\hat{k}_{\eta\eta} = f(\hat{A}_{\xi\zeta}^{\text{eff}}) = f(\hat{\Omega}_{\xi\xi}, \hat{\Omega}_{\zeta\zeta}, n), \quad (2.162b)$$

$$\hat{k}_{\zeta\zeta} = f(\hat{A}_{\xi\eta}^{\text{eff}}) = f(\hat{\Omega}_{\xi\xi}, \hat{\Omega}_{\eta\eta}, n), \quad (2.162c)$$

whereby $\hat{A}_{\eta\zeta}^{\text{eff}}$ represents the flow effective area in the $\eta\zeta$ -plane. In the following, these functions will be covered. Additionally, a procedure for the determination of the initial void fabric tensor (see equation 2.160) will be presented.

Capillary tube model. A unit cube (edge length $a = 1 \text{ m}$) with i equal tubes parallel to the coordinate axes is considered (figure 2.35).

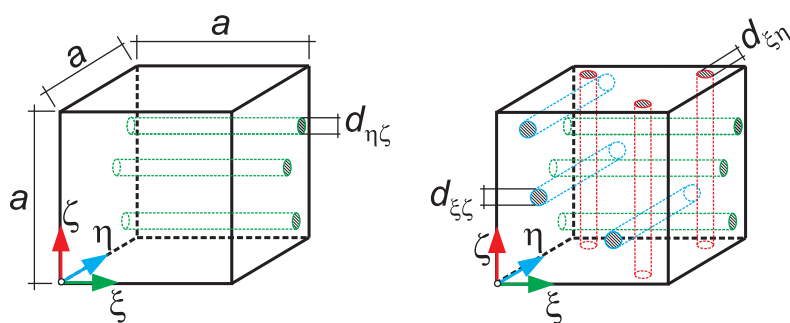


Figure 2.35: Capillary tube model. On the left hand side only the tubes, which are active for a flow in ξ -direction are plotted; here, the shaded area denotes $\hat{A}_{\eta\zeta}^{\text{eff}}$. On the right hand side all tubes representing the total pore space are shown.

Based on equation 2.142, the following relation can be stated, if only small deformations are considered ($a \approx \text{const.}$)

$$\hat{k}_{\xi\xi} = i \frac{\pi d_{\eta\zeta}^4}{128a^2} \propto d_{\eta\zeta}^4. \quad (2.163)$$

A flow effective area $\hat{A}_{\eta\zeta}^{\text{eff}}$ representing a projection of the tubes can be defined as

$$\hat{A}_{\eta\zeta}^{\text{eff}} = i \frac{\pi d_{\eta\zeta}^2}{4} \propto d_{\eta\zeta}^2. \quad (2.164)$$

The flow effective area can also be described by the directional porosity (equation 2.154), whereby the η - and ζ -axis define the directions, which describe the directional porosity in the $\eta\zeta$ -plane

$$\hat{A}_{\eta\zeta}^{\text{eff}} = n_{\eta\zeta} = n + 1/2(\hat{\Omega}_{\eta\eta} + \hat{\Omega}_{\zeta\zeta}) \propto 2n + \hat{\Omega}_{\eta\eta} + \hat{\Omega}_{\zeta\zeta}. \quad (2.165)$$

A comparison of the equations 2.163, 2.164, and 2.165 leads to

$$\hat{k}_{\xi\zeta} \propto (2n + \hat{\Omega}_{\eta\eta} + \hat{\Omega}_{\zeta\zeta})^2. \quad (2.166)$$

On the assumptions that the type and number of tubes are equal in all directions, the shape of the tubes remains unchanged, and there is no interaction between the tubes, equation 2.166 can be extended to a 3-dimensional case. One proportionality coefficient b is sufficient to define the three relations

$$\hat{k}_{\xi\xi} = b(2n + \hat{\Omega}_{\eta\eta} + \hat{\Omega}_{\zeta\zeta})^2, \quad (2.167a)$$

$$\hat{k}_{\eta\eta} = b(2n + \hat{\Omega}_{\xi\xi} + \hat{\Omega}_{\zeta\zeta})^2, \quad (2.167b)$$

$$\hat{k}_{\zeta\zeta} = b(2n + \hat{\Omega}_{\xi\xi} + \hat{\Omega}_{\eta\eta})^2. \quad (2.167c)$$

Fissure model. A unit cube with a network of perpendicular sets of fissures is considered, as depicted in figure 2.36.

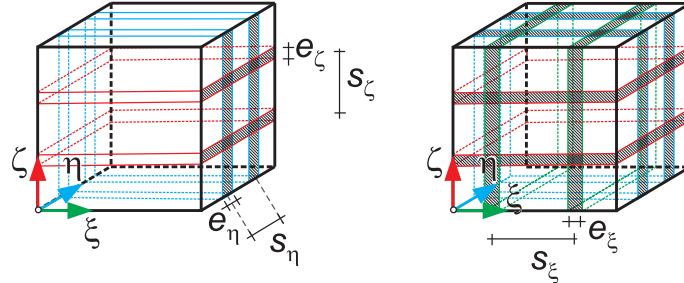


Figure 2.36: Fissure model. On the left hand side only the fissures are plotted, which are active for a flow in ξ -direction; here, the shaded area denotes $\hat{A}_{\eta\zeta}^{\text{eff}}$. On the right hand side all fissures representing the total pore space are shown.

With equation 2.145, the following relation can be stated

$$\hat{k}_{\xi\xi} = \frac{e_{\eta}^3}{12s_{\eta}} + \frac{e_{\zeta}^3}{12s_{\zeta}} \propto \frac{e_{\eta}^3}{s_{\eta}} + \frac{e_{\zeta}^3}{s_{\zeta}}. \quad (2.168)$$

The flow effective area $\hat{A}_{\eta\zeta}^{\text{eff}}$ for the flow in the ξ -direction can be divided into the areas $\hat{A}_{\zeta}^{\text{eff}}$, which is defined by fissures in the $\xi\eta$ -plane, and $\hat{A}_{\eta}^{\text{eff}}$, which is defined by fissures in the $\xi\zeta$ -plane

$$\hat{A}_{\eta\zeta}^{\text{eff}} = \hat{A}_{\zeta}^{\text{eff}} + \hat{A}_{\eta}^{\text{eff}} = \frac{e_{\eta}}{s_{\eta}} + \frac{e_{\zeta}}{s_{\zeta}}. \quad (2.169)$$

The flow effective area can also be described by the directional porosity (equation 2.154), whereby the η - and ζ -axis define the directions, which describe the corresponding directional porosities

$$\hat{A}_{\eta\zeta}^{\text{eff}} = \hat{A}_{\zeta}^{\text{eff}} + \hat{A}_{\eta}^{\text{eff}} = n_{\xi\eta} + n_{\xi\zeta} = n + \hat{\Omega}_{\eta\eta} + n + \hat{\Omega}_{\zeta\zeta} \propto 2n + \hat{\Omega}_{\eta\eta} + \hat{\Omega}_{\zeta\zeta}. \quad (2.170)$$

A comparison of the equations 2.168, 2.169, and 2.170 leads to

$$\hat{k}_{\xi\xi} = c'(n + \hat{\Omega}_{\eta\eta})^3 + c''(n + \hat{\Omega}_{\zeta\zeta})^3 \quad (2.171)$$

with the two independent coefficients c' and c'' .

On the assumptions that the type and number of fissures are equal in all directions ($s_\xi = s_\eta = s_\zeta$), the distance of the fissures remains unchanged and there is no interaction between the fissures in the different directions, one constant factor $c = c' = c''$ is sufficient and the equation 2.171 can be extended to the 3-dimensional case

$$\hat{k}_{\xi\xi} = c \left((n + \hat{\Omega}_{\eta\eta})^3 + (n + \hat{\Omega}_{\zeta\zeta})^3 \right), \quad (2.172a)$$

$$\hat{k}_{\eta\eta} = c \left((n + \hat{\Omega}_{\xi\xi})^3 + (n + \hat{\Omega}_{\zeta\zeta})^3 \right), \quad (2.172b)$$

$$\hat{k}_{\zeta\zeta} = c \left((n + \hat{\Omega}_{\xi\xi})^3 + (n + \hat{\Omega}_{\eta\eta})^3 \right). \quad (2.172c)$$

2.5.4.5 Determination of the initial void fabric tensor

On the assumption that the equations 2.167 and 2.172 are also valid at the initial state, the initial void fabric tensor Ω_{init} and the values for the factors b and c , respectively, can be evaluated by the initial permeability \mathbf{k}_{init} and the initial porosity n_{init} . Once again it is assumed that the principal directions of the permeability and the void fabric tensor coincide. The evaluation of the initial permeability is done in this eigensystem, which is defined by the permeability tensor in the initial state.

Capillary tube model. For the capillary tube model the following four equations can be derived from equation 2.167

$$\hat{k}_{\xi\xi, \text{init}} = b(2n_{\text{init}} + \hat{\Omega}_{\eta\eta, \text{init}} + \hat{\Omega}_{\zeta\zeta, \text{init}})^2 \quad (2.173a)$$

$$\hat{k}_{\eta\eta, \text{init}} = b(2n_{\text{init}} + \hat{\Omega}_{\xi\xi, \text{init}} + \hat{\Omega}_{\zeta\zeta, \text{init}})^2 \quad (2.173b)$$

$$\hat{k}_{\zeta\zeta, \text{init}} = b(2n_{\text{init}} + \hat{\Omega}_{\xi\xi, \text{init}} + \hat{\Omega}_{\eta\eta, \text{init}})^2 \quad (2.173c)$$

$$0 = \hat{\Omega}_{\xi\xi, \text{init}} + \hat{\Omega}_{\eta\eta, \text{init}} + \hat{\Omega}_{\zeta\zeta, \text{init}}. \quad (2.173d)$$

Whereby the last one results from the traceless character of the void fabric tensor ($\text{tr } \boldsymbol{\Omega} = 0$), which originates from its definition (section 2.5.4.2). This equation system can be solved for the four unknowns

$$\hat{\Omega}_{\xi\xi, \text{init}} = 2n_{\text{init}} - \frac{\sqrt{\hat{k}_{\xi\xi, \text{init}}}}{\sqrt{b}}, \quad (2.174\text{a})$$

$$\hat{\Omega}_{\eta\eta, \text{init}} = 2n_{\text{init}} - \frac{\sqrt{\hat{k}_{\eta\eta, \text{init}}}}{\sqrt{b}}, \quad (2.174\text{b})$$

$$\hat{\Omega}_{\zeta\zeta, \text{init}} = 2n_{\text{init}} - \frac{\sqrt{\hat{k}_{\zeta\zeta, \text{init}}}}{\sqrt{b}}, \quad (2.174\text{c})$$

$$\sqrt{b} = \frac{\sqrt{\hat{k}_{\xi\xi, \text{init}}} + \sqrt{\hat{k}_{\eta\eta, \text{init}}} + \sqrt{\hat{k}_{\zeta\zeta, \text{init}}}}{6n_{\text{init}}}. \quad (2.174\text{d})$$

Fissure model. For the fissure model the following four equations can be derived from equation 2.172

$$\hat{k}_{\xi\xi, \text{init}} = c \left((n_{\text{init}} + \hat{\Omega}_{\eta\eta, \text{init}})^3 + (n_{\text{init}} + \hat{\Omega}_{\zeta\zeta, \text{init}})^3 \right), \quad (2.175\text{a})$$

$$\hat{k}_{\eta\eta, \text{init}} = c \left((n_{\text{init}} + \hat{\Omega}_{\xi\xi, \text{init}})^3 + (n_{\text{init}} + \hat{\Omega}_{\zeta\zeta, \text{init}})^3 \right), \quad (2.175\text{b})$$

$$\hat{k}_{\zeta\zeta, \text{init}} = c \left((n_{\text{init}} + \hat{\Omega}_{\xi\xi, \text{init}})^3 + (n_{\text{init}} + \hat{\Omega}_{\eta\eta, \text{init}})^3 \right), \quad (2.175\text{c})$$

$$0 = \hat{\Omega}_{\xi\xi, \text{init}} + \hat{\Omega}_{\eta\eta, \text{init}} + \hat{\Omega}_{\zeta\zeta, \text{init}}. \quad (2.175\text{d})$$

This equation system can be solved for the four unknowns

$$\hat{\Omega}_{\xi\xi, \text{init}} = \frac{\sqrt[3]{-\hat{k}_{\xi\xi, \text{init}} + \hat{k}_{\eta\eta, \text{init}} + \hat{k}_{\zeta\zeta, \text{init}}}}{\sqrt[3]{2c}} - n_{\text{init}}, \quad (2.176\text{a})$$

$$\hat{\Omega}_{\eta\eta, \text{init}} = \frac{\sqrt[3]{+\hat{k}_{\xi\xi, \text{init}} - \hat{k}_{\eta\eta, \text{init}} + \hat{k}_{\zeta\zeta, \text{init}}}}{\sqrt[3]{2c}} - n_{\text{init}}, \quad (2.176\text{b})$$

$$\hat{\Omega}_{\zeta\zeta, \text{init}} = \frac{\sqrt[3]{+\hat{k}_{\xi\xi, \text{init}} + \hat{k}_{\eta\eta, \text{init}} - \hat{k}_{\zeta\zeta, \text{init}}}}{\sqrt[3]{2c}} - n_{\text{init}}, \quad (2.176\text{c})$$

$$\begin{aligned} \sqrt[3]{2c} = \frac{1}{3n_{\text{init}}} & \left(\sqrt[3]{-\hat{k}_{\xi\xi, \text{init}} + \hat{k}_{\eta\eta, \text{init}} + \hat{k}_{\zeta\zeta, \text{init}}} \right. \\ & + \sqrt[3]{+\hat{k}_{\xi\xi, \text{init}} - \hat{k}_{\eta\eta, \text{init}} + \hat{k}_{\zeta\zeta, \text{init}}} \\ & \left. + \sqrt[3]{+\hat{k}_{\xi\xi, \text{init}} + \hat{k}_{\eta\eta, \text{init}} - \hat{k}_{\zeta\zeta, \text{init}}} \right). \end{aligned} \quad (2.176d)$$

2.5.4.6 Algorithm

The permeability model as described above has been implemented in *RockFlow*. The algorithm can be divided into two parts: the initial evaluation of the void fabric tensor Ω_{init} (to be done only once for every finite element) and the calculation of the current permeability in each element (to be done every time the state of strains changes).

Initial evaluation of the void distribution tensor: $\Omega_{\text{init}} = \mathbf{f}(\mathbf{k}_{\text{init}}, n_{\text{init}})$

- ▷ calculation of the eigensystem $(\xi_{\text{init}}, \eta_{\text{init}}, \zeta_{\text{init}})$ of \mathbf{k}_{init} by *Jacobi*-rotation
- ▷ in this system: calculation of $\hat{\Omega}_{\text{init}} = \mathbf{f}(\hat{\mathbf{k}}_{\text{init}}, n_{\text{init}})$ (equations 2.167, 2.172)
- ▷ inverse transformation of $\hat{\Omega}_{\text{init}}$ into the global x - y - z system yields Ω_{init} .

Calculation of the current permeability: $\mathbf{k} = \mathbf{f}(\Omega, n)$:

- ▷ update the porosity $n = n_{\text{init}} + \varepsilon_{\text{vol}} - \varepsilon_{\text{vol}}^{\text{sw}}$ (equation 2.159)
- ▷ update of the void fabric tensor: $\Omega = \Omega_{\text{init}} + \boldsymbol{\varepsilon}_{\text{dev}} - \boldsymbol{\varepsilon}_{\text{dev}}^{\text{sw}}$ (equation 2.160)
- ▷ calculation of the eigensystem (ξ, η, ζ) of the void fabric tensor Ω by *Jacobi*-rotation yields $\hat{\Omega}$
- ▷ in this system: calculation of $\hat{\mathbf{k}} = \mathbf{f}(\hat{\Omega}, n)$ (equations 2.167, 2.172)
- ▷ inverse transformation of $\hat{\mathbf{k}}$ into the global x - y - z system yields \mathbf{k} .

2.5.5 Damage induced permeability

2.5.5.1 Motivation

The above described strain dependent permeability model is based on the assumption of minor changes in the pore geometry. It does not include effects due to the initiation of new fractures. As long as the strain induced change of the porosity in the considered rock is small in relation to the initial porosity, also the change of the permeability is small. Indeed, at the Tournemire site permeability changes up to five orders of magnitudes have been observed in the EDZ around the excavated openings. These changes can be explained by the initiation of new fissures/fractures in a damaged zone.

2.5.5.2 Approach

Two processes can be distinguished: (1) permeability change in intact rock, due to the change of the size of existing pores, and (2) permeability change due to the initiation of new fractures. The latter involves damage. If a damage model is applied (see section 2.4), it is possible to quantify the effect of damage. In a first approach, a separation of the simulated strains in an intact and damaged part is made with the help of the scalar damage variable D

$$\boldsymbol{\varepsilon} = \boldsymbol{\varepsilon}^{\text{frac}} + \boldsymbol{\varepsilon}^{\text{intact}} \quad (2.177\text{a})$$

$$= D\boldsymbol{\varepsilon} + (1 - D)\boldsymbol{\varepsilon}. \quad (2.177\text{b})$$

The determination of permeability in η -direction for the intact and damaged case is presented in figure 2.37 exemplarily. An initially isotropic unit cube is mentioned, which is loaded by a deformation in ζ -direction. At the other boundaries no deformations take place. For the sake of simplicity, no swelling is considered in this example.

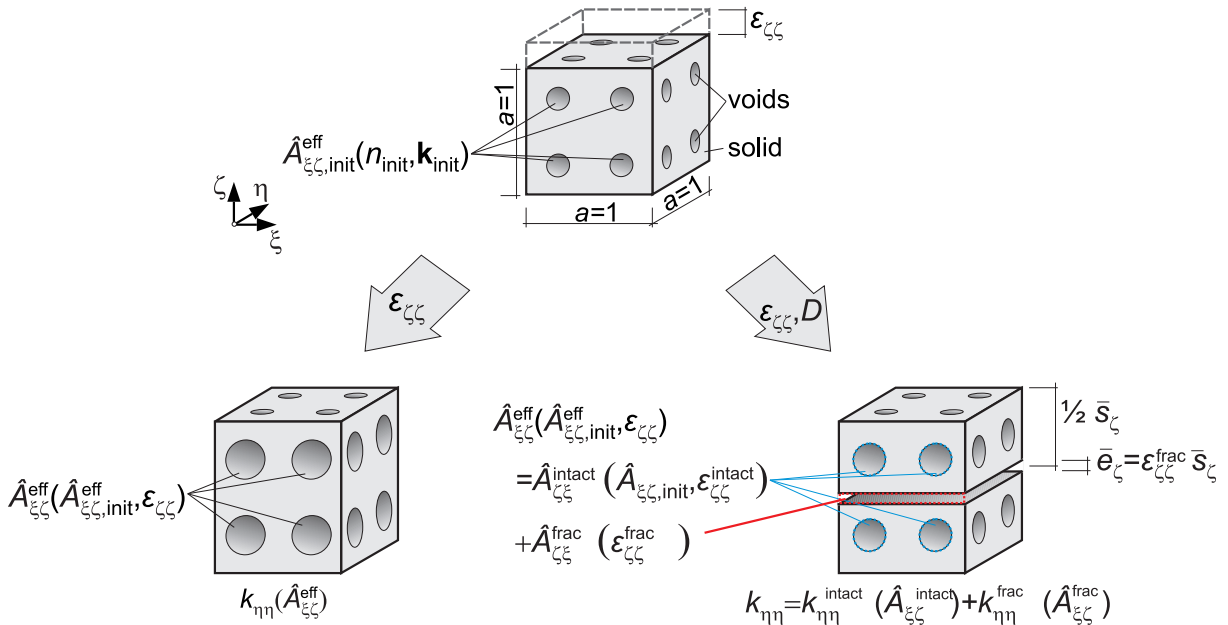


Figure 2.37: Schematic model of the change of voids in a porous media due to deformation. On the left no damage is considered, only the existing pores increase. On the right damage is considered and the flow effective area is separated into pores and one fracture.

In both mentioned cases, the same state of strain is considered. Thus, the flow effective area $\hat{A}_{\xi\xi}^{\text{eff}}$ is the same, but the calculation of permeability differs. In the intact case it is assumed that the initially existing pores become larger. The permeability is determined by the increased flow effective area, using the tube model, as presented in section 2.5.4.4. The cube on the right hand side of figure 2.37 shows a new fracture, oriented perpendicular to the loading direction. In this example, only one fracture is considered. Thus, the averaged distance between two damage induced fractures \bar{s} equals the edge length a of

the cube. The scalar damage variable is used to subdivide the total flow effective area $\hat{A}_{\xi\xi}^{\text{eff}}$ into an intact $\hat{A}_{\xi\xi}^{\text{intact}}$ and a fractured $\hat{A}_{\xi\xi}^{\text{frac}}$ part

$$\hat{A}_{\xi\xi}^{\text{eff}} = \hat{A}_{\xi\xi, \text{init}}^{\text{eff}} + \varepsilon_{\xi\xi} a^2 = \hat{A}_{\xi\xi}^{\text{intact}} + \hat{A}_{\xi\xi}^{\text{frac}} \quad (2.178\text{a})$$

$$= \hat{A}_{\xi\xi, \text{init}}^{\text{eff}} + (1 - D)\varepsilon_{\xi\xi} a^2 + D\varepsilon_{\xi\xi} a^2 \quad (2.178\text{b})$$

$$= \hat{A}_{\xi\xi, \text{init}}^{\text{eff}} + \varepsilon_{\xi\xi}^{\text{intact}} a^2 + \varepsilon_{\xi\xi}^{\text{frac}} a^2. \quad (2.178\text{c})$$

The permeability of the intact and fractured part is determined independently. The total permeability results of the summation of the permeability in the intact rock mass, $\mathbf{k}^{\text{intact}}$ and in the fractured rock mass \mathbf{k}^{frac}

$$\mathbf{k} = \mathbf{k}^{\text{intact}} + \mathbf{k}^{\text{frac}}. \quad (2.179)$$

The permeability in the intact rock mass can be determined as summarized in section 2.5.4.6, whereby the input parameters (n, Ω) have to be exchanged by the following ones

$$n \mapsto n^{\text{intact}} = n_{\text{init}} + \varepsilon_{\text{vol}} - \varepsilon_{\text{vol}}^{\text{sw}} - \varepsilon_{\text{vol}}^{\text{frac}}, \quad (2.180\text{a})$$

$$\Omega \mapsto \Omega^{\text{intact}} = \Omega_{\text{init}} + \boldsymbol{\varepsilon}_{\text{dev}} - \boldsymbol{\varepsilon}_{\text{dev}}^{\text{sw}} - \boldsymbol{\varepsilon}_{\text{dev}}^{\text{frac}}, \quad (2.180\text{b})$$

$$\text{with } \boldsymbol{\varepsilon}^{\text{frac}} = D \mathbb{P}^+(\boldsymbol{\varepsilon} - \boldsymbol{\varepsilon}^{\text{sw}}). \quad (2.180\text{c})$$

In order to consider the fracture initiation only in tension, the positive projection tensor \mathbb{P}^+ is used (see section 2.4.3.7).

The permeability in the damaged rock mass is determined by the cubic law (equation 2.144). As a first approach, it describes the permeability due to the initiations of new fractures. With the assumption of isotropically distributed fractures (the averaged distance between the fractures is the same in all directions), the permeability in the principal directions of $\boldsymbol{\varepsilon}^{\text{frac}}$ can be determined. In the following the permeability in the η -direction will be derived exemplary (compare equation 2.168), whereby \bar{e} denotes aperture of fractures, induced by damage (see figure 2.36).

$$\hat{k}_{\eta\eta}^{\text{frac}} = \frac{\bar{e}_{\xi}^3}{12\bar{s}_{\xi}} + \frac{\bar{e}_{\zeta}^3}{12\bar{s}_{\zeta}} \quad (2.181\text{a})$$

$$= \frac{(\varepsilon_{\xi\xi}^{\text{frac}} \bar{s}_{\xi})^3}{12\bar{s}_{\xi}} + \frac{(\varepsilon_{\zeta\zeta}^{\text{frac}} \bar{s}_{\zeta})^3}{12\bar{s}_{\zeta}} \quad (2.181\text{b})$$

$$= \frac{\varepsilon_{\xi\xi}^{\text{frac}3} \bar{s}_{\xi}^2}{12} + \frac{\varepsilon_{\zeta\zeta}^{\text{frac}3} \bar{s}_{\zeta}^2}{12} \quad (2.181\text{c})$$

$$= \frac{\varepsilon_{\xi\xi}^{\text{frac}3} \bar{s}^2}{12} + \frac{\varepsilon_{\zeta\zeta}^{\text{frac}3} \bar{s}^2}{12}, \text{ with } \bar{s} = \bar{s}_{\xi} = \bar{s}_{\eta} = \bar{s}_{\zeta}. \quad (2.181\text{d})$$

The permeabilities in the other principal directions can be determined analogously

$$\hat{k}_{\xi\xi}^{\text{frac}} = \frac{\varepsilon_{\eta\eta}^{\text{frac}3} \bar{s}^2}{12} + \frac{\varepsilon_{\zeta\zeta}^{\text{frac}3} \bar{s}^2}{12} \quad (2.182)$$

$$\hat{k}_{\zeta\zeta}^{\text{frac}} = \frac{\varepsilon_{\xi\xi}^{\text{frac}3} \bar{s}^2}{12} + \frac{\varepsilon_{\eta\eta}^{\text{frac}3} \bar{s}^2}{12}. \quad (2.183)$$

Only one additional material parameter is needed for this model extension: \bar{s} , the averaged spacing of the damage induced fractures. Several simplifications are underlying with the use of the cubic law. Natural fractures are not smooth and, furthermore, the damaged induced fractures are not passing the whole domain. Nevertheless, this approach has the capacity to predict permeability increase in the damaged zone in the order of some magnitudes. The material parameter \bar{s} quantifies not only the averaged distance between the damaged induced fractures but all additional effects, like roughness and conductivity of the fracture. This parameter has to be fitted against experimental data.

In contrast to the example as presented in figure 2.37 the principal directions of the intact and fractured permeability must not coincide. Furthermore, the initial state can be orthotropic and swelling strain can be considered. Instead of the fissure model, as well the capillary tube model can be applied for the determination of the permeability in the intact rock mass.

2.5.6 Applications

2.5.6.1 Deformation induced anisotropic permeability

The model setup of the first application is presented in figure 2.38. It is a two-dimensional H-M coupled simulation of a rock sample, using the reference material parameters as presented in chapter 1.2.7 (table 1.2, p. 11). A time-dependent antisymmetric displacement boundary condition ($0.0 \leq u \leq 0.1$ m) is applied on two boundaries, without inducing any additional volumetric deformation. The pressure boundary conditions cause a flow diagonal through the domain.

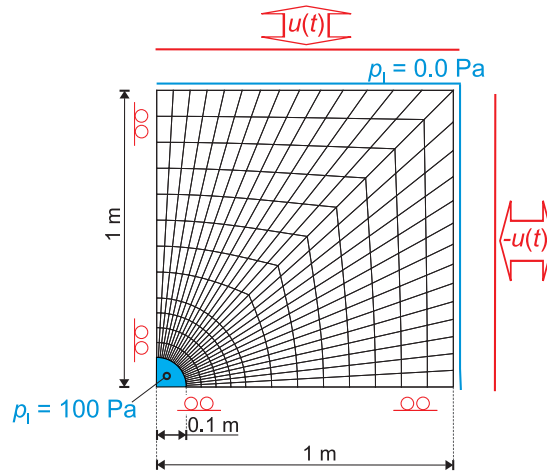


Figure 2.38: Model setup and discretization for an application concerning strain induced change of permeability.

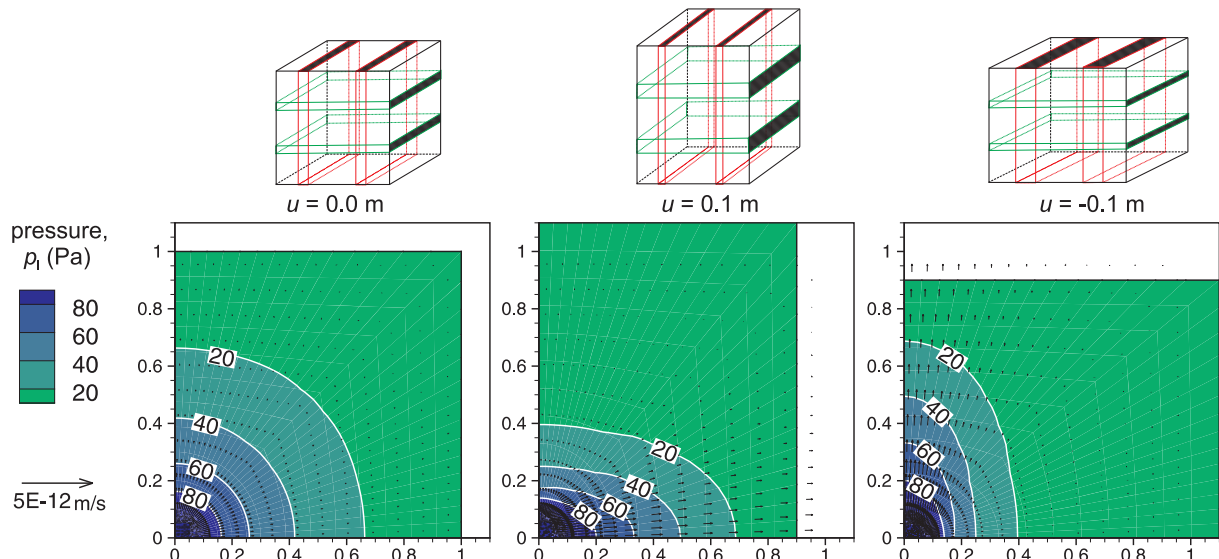


Figure 2.39: Model of pore spaces with fissures (top); resulting pressure field with flow directions (below).

For the permeability calculation the fissure model is used. The resulting pressure field is plotted in figure 2.39 at different states of deformation. Also the corresponding figures of the pore space are shown in order to bring out the mode of action. The figure shows the results at a static, equilibrium state.

The results indicate clearly the influence of the deformation on the pore pressure field and the liquid velocity field. This influence is caused by an anisotropic change of the permeability. The porosity is not changed between the three cases but the directional porosity. The developed model has the capacity to investigate deformation induced anisotropic permeability changes, which would not be possible using standard permeability models solely based on isotropic data.

2.5.6.2 Shrinkage induced anisotropic permeability

In the second application the influence of shrinkage on the permeability is investigated. Therefore, an initially saturated rock sample, as shown in figure 2.40 (left), is considered. The reference material parameters for the isotropic case have been used as presented in chapter 1.2.7 (table 1.2, p. 11). The shrinkage process is induced by a reduced hydraulic saturation at the central hole.

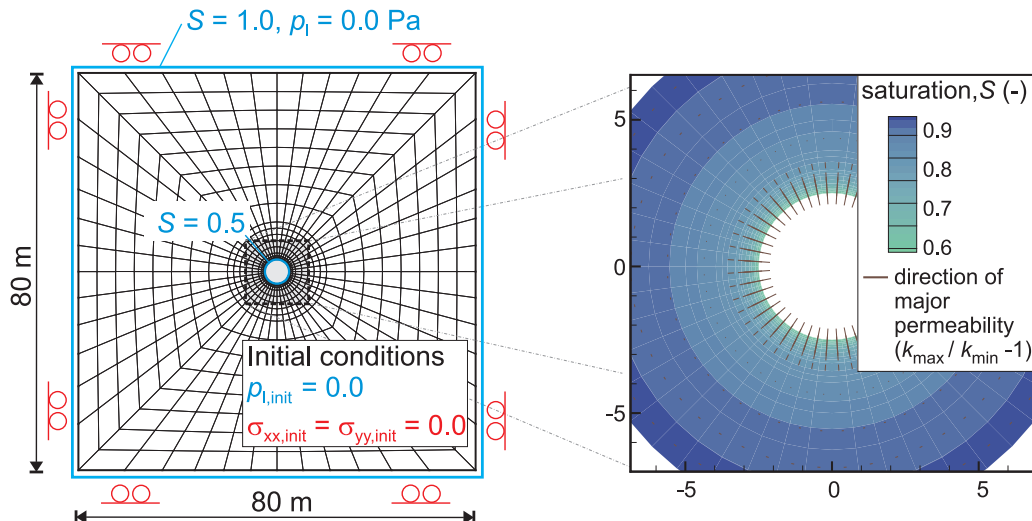


Figure 2.40: Model setup and discretization (left) for an application concerning shrinkage induced change of permeability; saturation field with depiction of the direction of major permeability (right).

The hydraulic boundary condition causes a desaturated zone around the hole, as depicted in figure 2.40 (right). The vectors represent the direction of major permeability and its length corresponds to the magnitude of anisotropy. Thus, if no vector is plotted, the permeability is isotropic as in the initial state. It can be seen that the permeability in the near field of the hole has changed to radial direction. The shrinkage induces strain and the strain induces an anisotropic permeability. This behavior coincides qualitatively with in-situ observations: As presented in chapter 1.2.6 and 2.3.3.2, the shrinkage induces

small radial fractures. This fracturing increases the radial permeability. Hence, the developed model has the capacity to investigate the shrinkage induced anisotropic change of permeability.

2.5.6.3 Excavation induced anisotropic permeability

The third application treats the influence of an excavation process on the permeability. Therefore, a circular excavation is considered as shown in figure 2.41. The results of this study are shown in figure 2.42 in comparison with literature values, as published by Kelsall et al. (1984). Their analytical approach is based on the cubic law and three empirical

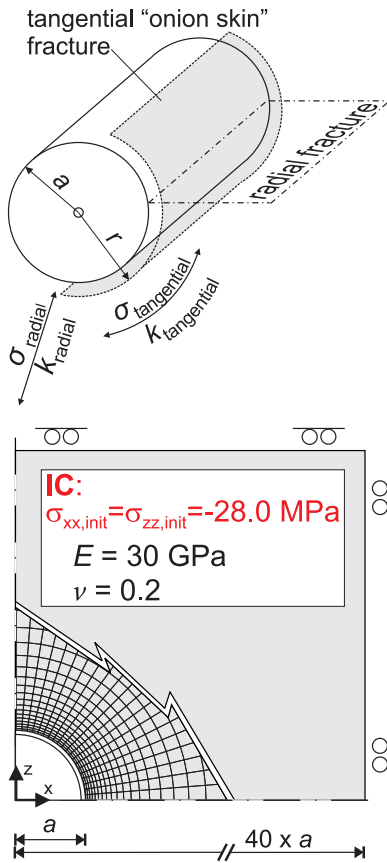


Figure 2.41: Idealized geometry of excavation induced fractures (top) and model setup (beneath).

constants. In spite of the different approaches, a good agreement between the simulated permeabilities and the analytical results of Kelsall et al. (1984) has been obtained.

Two mechanisms can be observed due to the stress redistribution around the excavated opening: on the one hand, the compression mode in tangential direction. Here, the radial permeability is decreased slightly, which can be explained by a closure of radial oriented fractures. On the other hand, the tensile-mode (or at least a reduction of compression) in radial direction. Here, the tangential permeability is increased, caused by a widening of

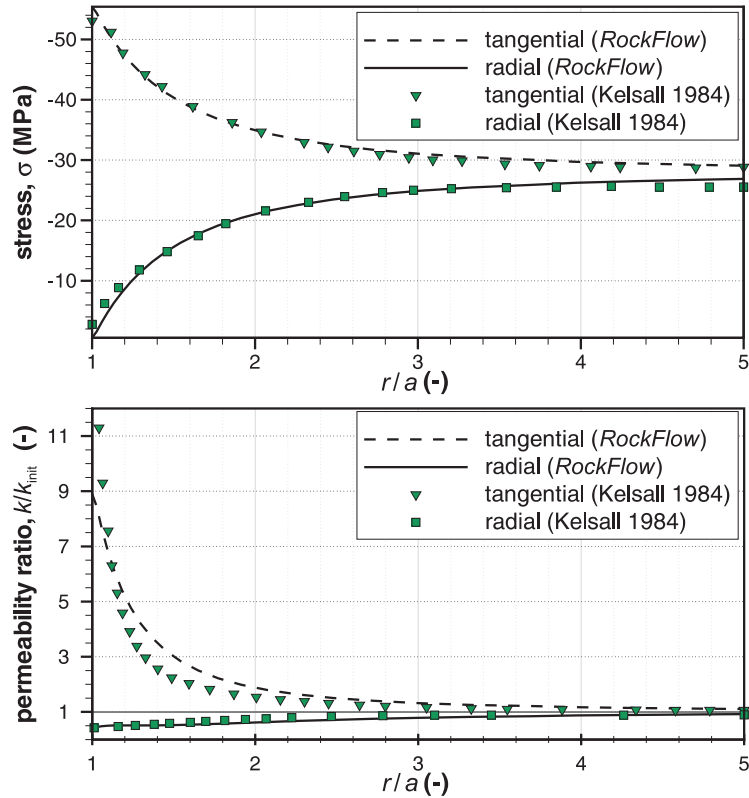


Figure 2.42: Comparison of calculated stresses (top) and permeabilities (beneath) with literature (Kelsall et al. 1984).

the tangential oriented fractures. The calculated values are close to the literature ones, which have been determined analytically by the use of a stress-permeability relation. Zhang et al. (2007) have investigated recently a similar problem and come qualitatively to the same results.

2.5.6.4 Damage induced anisotropic permeability

The following application deals with desaturation, shrinkage, damage, and damage induced permeability. It is founded on the two applications as presented in the sections 2.4.5.3 and 2.5.6.2. The model setup is the same as presented in section 2.5.6.2, figure 2.40, left hand side. Additionally, the damage model (section 2.4.5.3) is applied. Furthermore, damage induced changes in permeability are considered by the approach as specified in section 2.5.5. On the basis of line plots, the mode of action will be illustrated. In figure 2.43 the saturation, permeability, and damage variable along a horizontal line in radial direction are shown. The desaturation process leads to shrinkage and in turn

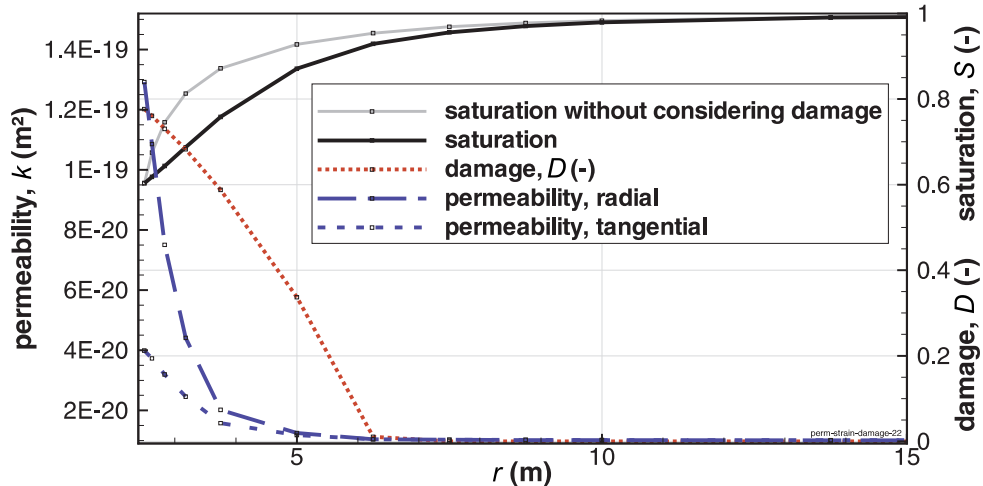


Figure 2.43: Application of the damage induced permeability model. Saturations, damage state and permeability are plotted along a radial oriented line. The initial permeability is isotropic and equals $k_{\text{init}} = 1.0 \times 10^{-20} \text{ m}^2$.

to damage. If the damage process is considered in the determination of the permeability, a largely increased permeability near the opening can be observed. Additionally, the anisotropic behavior can be simulated: the radial permeability is much more increased than the tangential one. This can be explained by the higher impact of shrinkage strain in tangential direction. Due to the change of permeability, the desaturation profile is changed, too. Without considering damage induced permeability, the change in permeability is qualitatively similar but only in the order of a few percent.

Concerning the Tournemire case study, the general change of permeability can be simulated in principle with this model: The observed radial desaturation fractures at the wall of the openings initiate an anisotropic change in permeability.

2.5.7 Conclusions

A permeability model has been developed, implemented and tested. This model has the capacity to investigate an orthotropic change of permeability, induced by elastic and swelling strains. It is based on a tensorial description of the pore space and basic flow models, as the cubic law. The approach leads to similar relationships between porosity/strains and permeability as can be found in literature. A quantitative comparison proves the accuracy of the formulation and implementation.

Furthermore, damage induced permeability change, due to initiation of new fractures, can be simulated. With this approach, the change of permeability in a damaged (fractured) rock mass is much higher than the permeability change in the intact rock mass, even if the same strains are applied. This is a typical behavior of rock.

For the excavation induced change of permeability the shrinkage and the redistribution of stresses leads to contrary effects. While the shrinkage induces an increase of radial permeability, the redistribution of stresses leads to a decrease of radial permeability and an increase of tangential permeability. If fracture initiation due to shrinkage is considered, this effect dominates the change of permeability.

Relating to the Tournemire site, the observation of radial fissures at the sides of the galleries proves that at least in the vertical direction the impact of shrinkage is larger than the impact of stress redistribution.

2.6 Element oriented deactivation of processes

2.6.1 Approach

One aim in the framework of this work is the modeling of an excavation process. A simple but effective modeling approach is provided by the time depending deactivation of the elements in the excavation zone. A general approach has been chosen, that allows the deactivation of multiple or single processes (hydraulics, mechanics, matter and heat transport) in an element, depending on location and/or time. Selecting all processes, a total deactivation of an element is achieved. By deactivating the hydraulic process only, it is also possible to simulate impermeable elements. In figure 2.44 the composition of the coupled equation system is shown with and without considering deactivation.

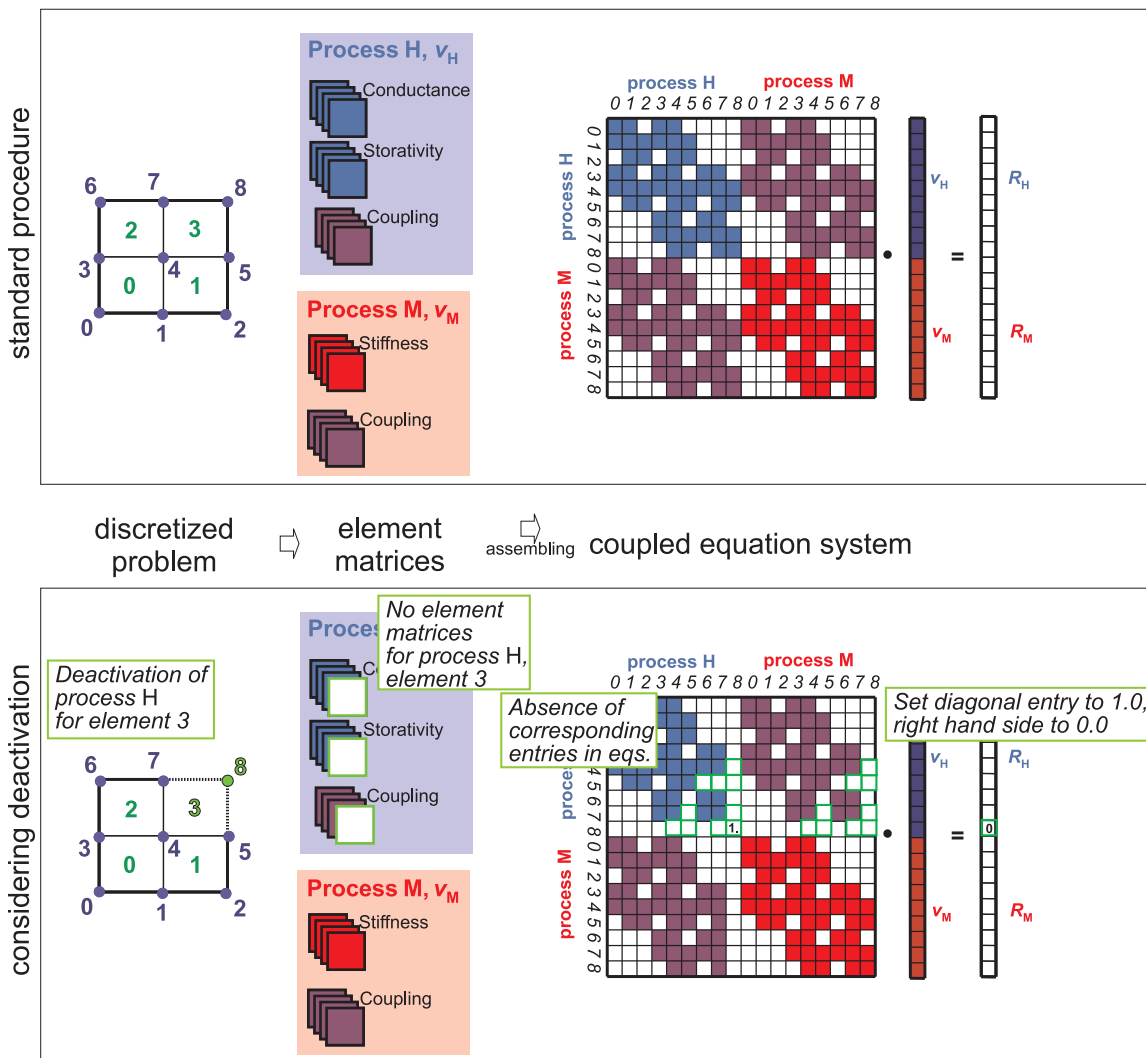


Figure 2.44: Composition of the coupled equation system without (top) and with deactivation of the hydraulic process (H) in element 3 (beneath).

If a process is deactivated, the corresponding element matrices will not be considered. Thus, some entries in the equation system are changed. If all elements around one node are deactivated, non defined diagonal values occur, as presented in the example in figure 2.44. This brings out numerical problems during the solving of the equation system. Therefore, the diagonal value is set to 1.0 and all other entries in the corresponding row and column and the right hand side are set to zero. The last calculated node and element values are saved in the deactivated element or node data, to allow access for a potential reactivation.

2.6.2 Application

Figure 2.45 shows an example for the process deactivation during the simulation. First, the hydraulic process is deactivated in two elements; consequently, the flow field is influenced only. Then, stepwise further deactivations of the hydraulic and mechanical processes are simulated. At the end of the simulation, also the elements 24 and 19 are deactivated. At these elements a pressure boundary condition has been set. Thus, the flow field has changed significantly.

This application shows the capacity of the approach to model an excavation process.

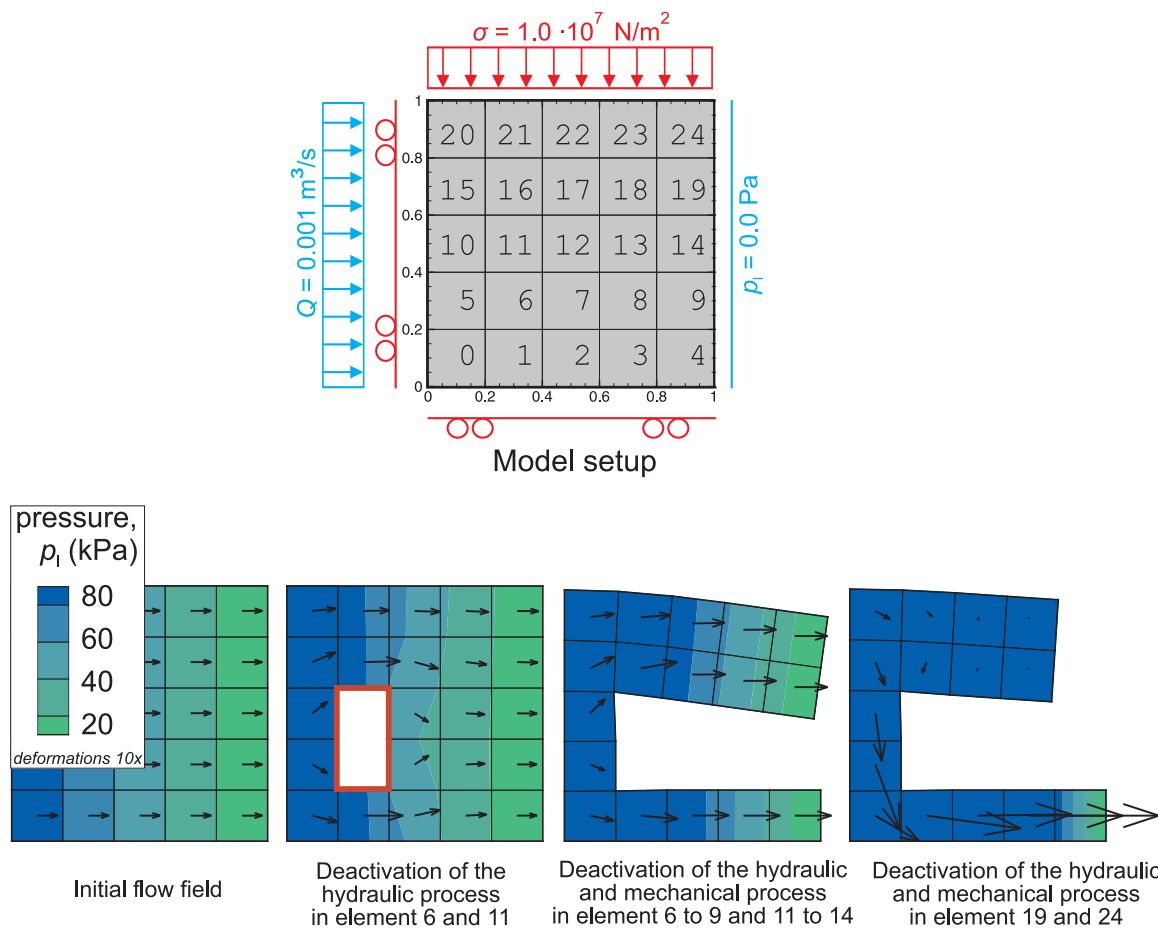


Figure 2.45: Two-dimensional application for process deactivation. The vectors represent the flow field of the liquid.

Chapter 3

Case study

*“In theory there is no difference between theory and practice.
In practice there is.”*

JAN L. A. VAN DE SNEPSCHEUT (Dutch computer scientist, 1953 - 1994)

3.1 Introduction

In chapter 1 the framework of the problem has been presented, including a detailed description of the Tournemire site; in chapter 2 the methods and models have been depicted. Founded on these two, in the current chapter 3 the model will be applied to several simulations concerning the case study Tournemire.

This modeling work has been motivated by the DECOVALEX-THMC project, task C (Rejeb et al. 2008a). This task was led by the *Institute of Radioprotection and Nuclear Safety* (France). Further participants were the *Kyoto University* (Japan), the *Commissariat of Atomic Energy* (France) and the *Federal Institute for Geosciences and Natural Resources* (Germany), who authorized the *Institute of Fluid Mechanics (Leibniz Universität Hannover)* to do the modeling work. In this context, comparative studies between *RockFlow* and two other finite element codes, namely *Cast3M* (CAE 2008) and *THAMES* (Ohnishi et al. 1985), have proved the accuracy of the implementation.

The case study is divided into the following three parts:

Modeling the desaturation process

Observations of seasonally opened fractures at the Tournemire site (Rejeb and Cabrera 2006) as well as laboratory experiments (Valés et al. 2004) have confirmed the importance of the desaturation process on the development of the EDZ in argillaceous rock. Consequently, one focus of the work at hand is the hydraulic-mechanically coupled simulation of the desaturation process around the century old tunnel and the newer galleries. A sensitivity study helps to identify the most important parameters. A comparison of in-situ measured saturations (Rejeb et al. 2008b; Matray et al. 2007) with the prediction of the numerical code ensure the reliability of the study.

This contribution should help to understand and evaluate the hydraulic part of the problem. The hydraulic part is modeled with the *Richards'* approximation for unsaturated one-phase flow. Linear elasticity has been applied for the mechanical part. Furthermore, the influences of coupling and damage have been investigated.

Parts of this study have been discussed on conferences (Maßmann et al. 2006, 2008b; Uehara et al. 2008) and published by the author in Maßmann et al. (2008a).

Modeling the mine-by-test experiment

During and after excavating a gallery in the year 2003, pore water pressures and displacements have been measured (Rejeb et al. 2008b). With a H-M coupled simulation the hydraulic, mechanical and coupling phenomena can be studied and compared with the measurements. The complexity of the applied model will be increased stepwise in order to investigate the influence of the different model approaches. Two- and three-dimensional simulations are applied and will be compared.

Modeling the excavation disturbed zone

Based on the developed models and observations at the three openings at the Tournemire site (excavated in 1881, 1996, and 2003), an analysis of the EDZ will be carried out. Numerical investigations (Rejeb et al. 2006; Rouabhi et al. 2006) have confirmed that

purely mechanical models are not able to predict the observed failure correctly, even if anisotropic plasticity or damage is considered. Thus, failure mechanisms caused by H-M coupled processes will be investigated in the work at hand.

On the basis of the simulation results, potential failure mechanisms will be discussed and compared with in-situ observations.

This numerical study is understood as a contribution to the scientific discussion on this topic. Previous investigations have been done by Millard et al. (2008), Rejeb and Cabrera (2006), Rejeb et al. (2006), Rouabhi et al. (2006), and Uehara et al. (2006), amongst others.

3.2 Modeling the desaturation process

3.2.1 General remarks

In this section a numerical model is applied in order to investigate the transient desaturation process at the Tournemire site. After presenting the model setup, numerical investigations on the basis of the 2003 excavated gallery will be done, to get a first impression. A sensitivity study will follow. At last the simulation results will be compared with saturation measurements at all three openings. The goal of this section is to verify the modeling approach and, where required, an adaption of the model parameters.

3.2.2 Model setup

Two-dimensional hydraulic-mechanically coupled simulations under plane strain and plane flow conditions have been used. The lengths of the galleries permit this reduction of dimension. The domain of the numerical model is 80.0 m times 80.0 m and just represents the argillite. In figure 3.1 the hydraulic and mechanical boundary and initial conditions

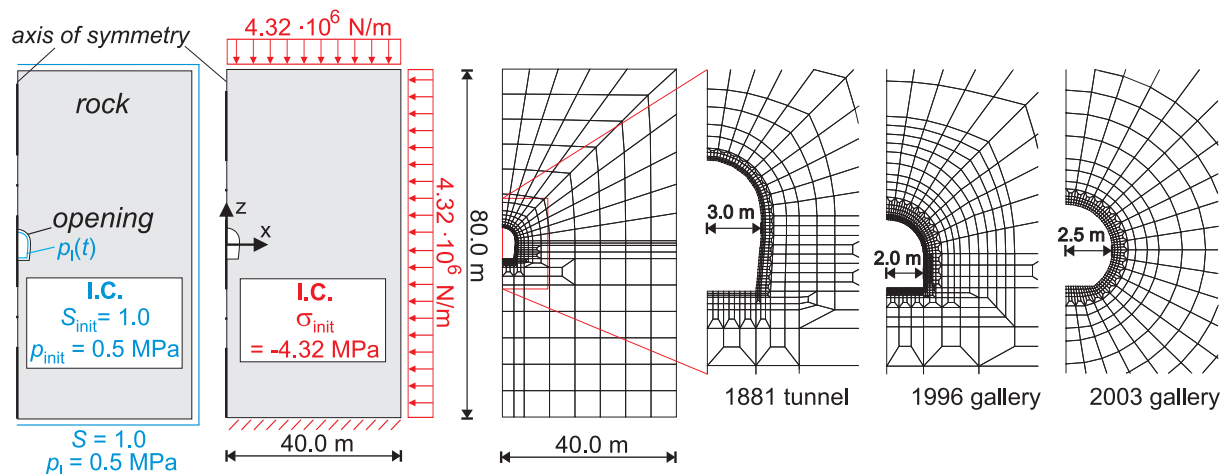


Figure 3.1: Model setup for the simulation of the desaturation process; hydraulic and mechanical boundary and the initial conditions (left) as well as meshes (right).

are shown on one half of the symmetric domain. Furthermore, the meshes for the simulation of the 1881 excavated tunnel and the 1996 and 2003 excavated galleries are depicted. The time-dependent boundary condition of pore water pressure at the opening is calculated with the help of humidities and temperatures. The measured relative humidity h_{rel} and temperature T (Rejeb and Cabrera 2004) can be approximated by sinusoidal functions, as shown in figure 3.2. Based on these functions, the pore water pressure can be calculated by the *Kelvin* equation (equation 2.81, p. 48). Since the *Richards'* approximation (chapter 2.1.7.1) is applied, a direct relation between the pore water pressure and the saturation exists, which is approximated by a *van Genuchten* function (see chapters 1.2.4 and 2.1.7.1).

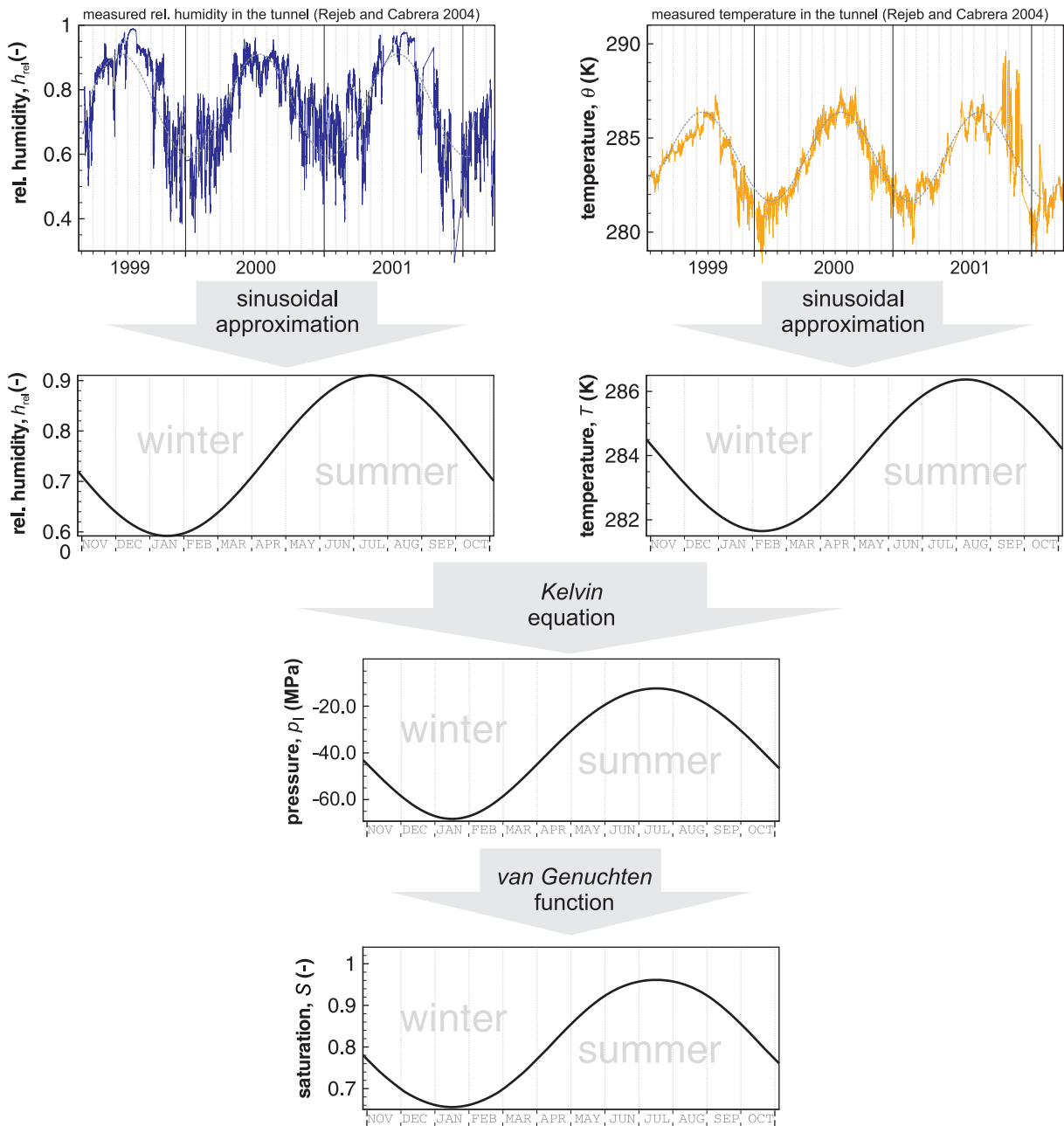


Figure 3.2: Determination of the saturation at the wall of the opening by measured temperature and relative humidity profiles. Measurements by IRSN (Rejeb and Cabrera 2004).

The material properties for the calculation of the reference solution are listed in chapter 1.2.7 (reference parameter set, table 1.2, p. 11). Concerning the galleries, the bedding plane lies in horizontal direction. At the old tunnel, the bedding plane is oriented 4.5° sub-horizontally. The transversely isotropic mechanical and shrinkage properties have been applied here. In the reference solution damage is neglected and a constant intrinsic permeability is used. The excavation is simulated by an instantaneous change in the mechanical boundary conditions at the opening, afterwards the seasonal hydraulic boundary condition is applied at the wall of the opening.

3.2.3 Simulation

Figure 3.3 shows the temporal evolution of the pore water pressure around the 2003 excavated gallery. Due to the mechanical response to the excavation, a pressure increase

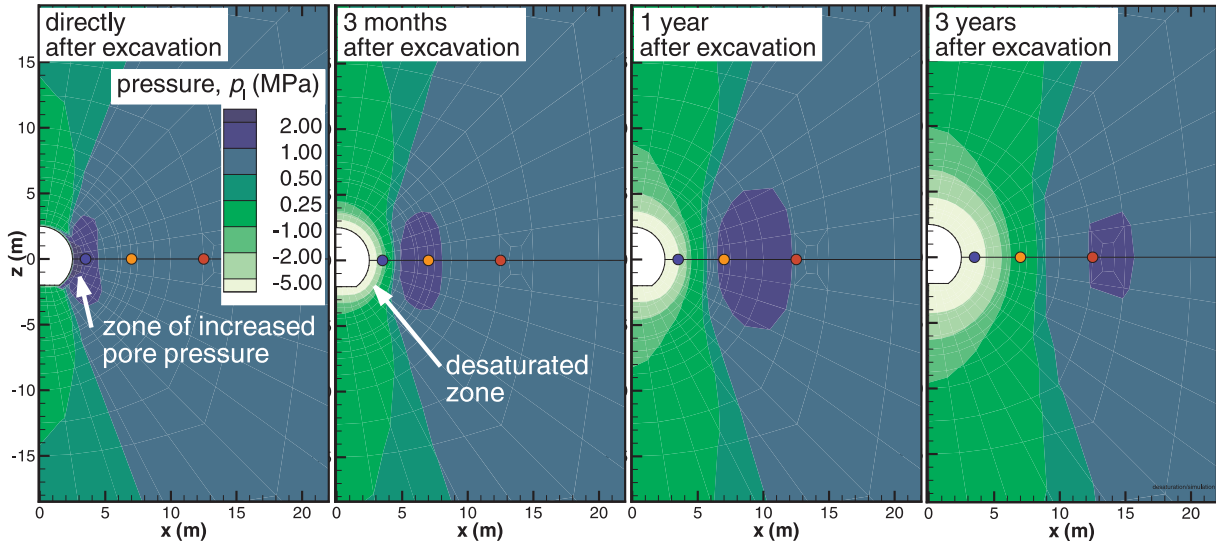


Figure 3.3: Simulated pore water pressure field around the opening in the first three years after the excavation.

next to the opening is predicted directly after excavation, which has also been observed in-situ. After several months the effect of desaturation, due to the contact of the rock with relatively dry air, becomes dominant and leads principally to an increasing desaturated zone around the gallery. The dry climate in winter time leads to a decrease of saturation, while the wet summer months generate a resaturation in the near field of the opening. This leads to the formation of these two zones around the excavated opening: a seasonally influenced zone near the opening, which is characterized by seasonal climatic changes and a long term influenced zone, where a desaturation process without any seasonal effect can be observed. Figure 3.4 shows saturation profiles at different times. The comparison of

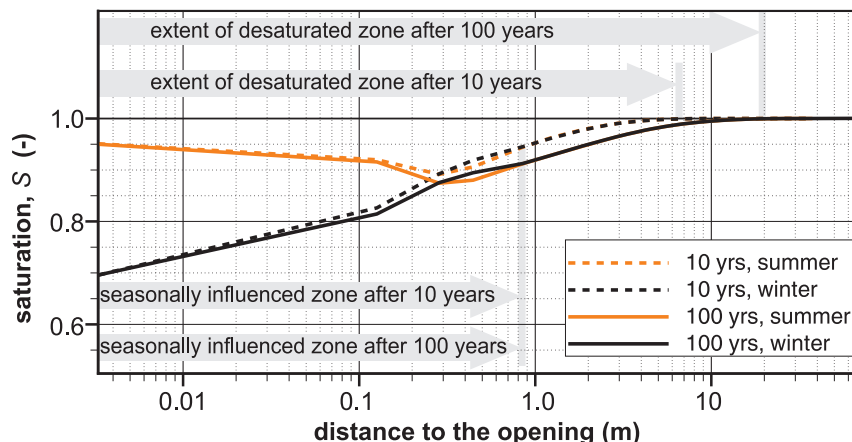


Figure 3.4: Simulated horizontal saturation profiles at different times and seasons.

the saturation profiles in winter and summer time indicates a seasonally influenced zone of about 1 m, whereas the long term influenced zone extends 11.0 m. After several years the size of the seasonally influenced zone remains unchanged but the long term influenced zone still increases slowly. The different characteristic becomes obvious, if the saturation evolutions are plotted, as presented in figure 3.5. Furthermore, a phase shifting can be

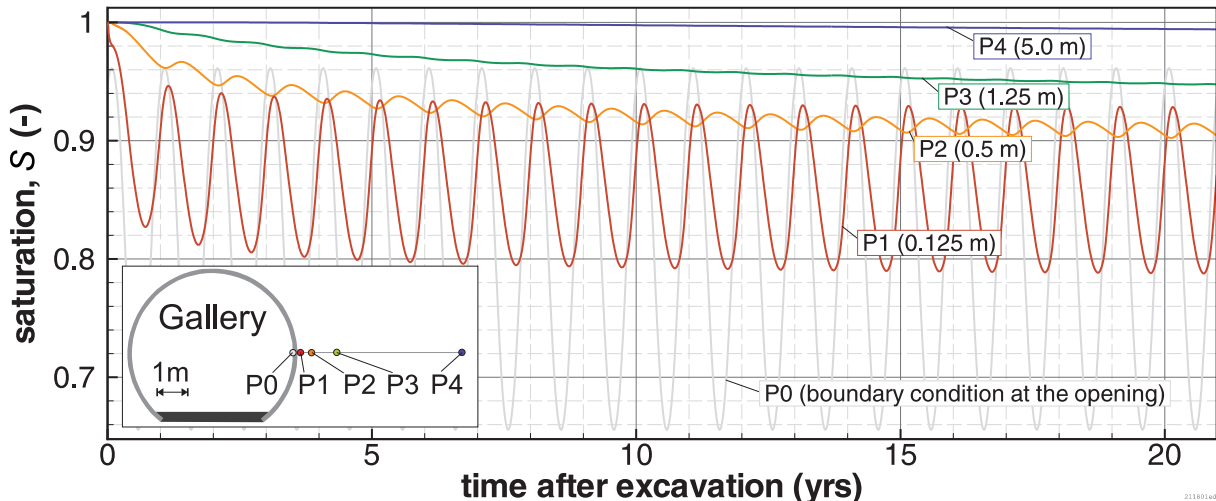


Figure 3.5: Simulated saturation versus time at fixed points. The distance to the opening is denoted directly at the corresponding line.

observed herein, which increases with increasing distance to the opening.

The distinction between these two zones could give assistance in understanding the evolution of the EDZ around the opening, since the desaturation is always combined with shrinkage of the material and the continuous recurring could lead to an irreversible change of material properties.

3.2.4 Sensitivity study

3.2.4.1 General remarks

The simulated size, shape and temporal development of the influenced zones are sensitive to the used model parameters. To get an insight into the effect of these parameters, several simulations have been carried out. In each of these only one parameter differs from the reference parameter set (table 1.2, p. 11).

In order to quantify the extent of the influenced zones, two definitions have been done:
 (1) the rock is labeled as desaturated, if the simulated saturation value is beneath 99.9 %;
 (2) a seasonal influence is denoted, where the simulated value of saturation differs more than 0.01 % between summer and winter time.

The geometry of the 2003 excavated gallery has been used.

In addition, the influence of the tunnel lining at the century old tunnel is investigated.

3.2.4.2 Permeability

The measured values of permeability vary between 10^{-22} and 10^{-17} m^2 . The in-situ permeability is estimated at 10^{-20} m^2 , in laboratory as low as 10^{-22} m^2 (see chapter 1.2.4). In this comparative study permeabilities in three orders of magnitudes have been used. In figure 3.6 the simulated extent of the desaturated zone versus time is shown. The resulting desaturated zone extends between 6 and 27 m after 100 years. With the higher permeability, the extent of the desaturated zone is steady after about 60 years. The extent of the seasonally influenced zone in the steady state is between 0.6 and 2.6 m (figure 3.7). Evidently, the intrinsic permeability has a huge influence on the desaturation process.

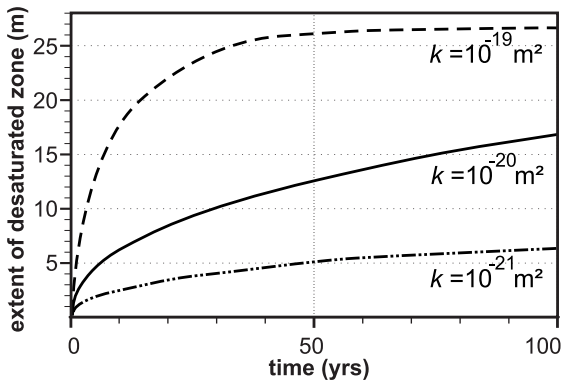


Figure 3.6: Extent of the desaturated zone around the 2003 excavated gallery. Varying intrinsic permeabilities are considered.

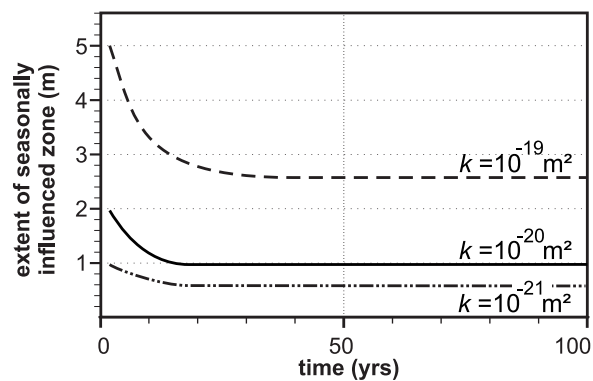


Figure 3.7: Extent of seasonally influenced zone around the 2003 excavated gallery. Varying intrinsic permeabilities are considered.

3.2.4.3 Relative permeability

The relative permeability describes the relation between the permeability and the saturation. In general, the permeability decreases with decreasing saturation. The use of a *van Genuchten* model (equation 2.40, p. 28) has been proved for the Bure¹ argillite by Semete et al. (2008). Since no data exists for the determination of the relative permeability at the Tournemire argillite, the *van Genuchten* model will be used here, too. Figure 3.8 shows a comparison with regard to the relative permeability. In figure 3.9 the used saturation-relative permeability relations are shown. In addition to different *van Genuchten* relations, a cubic function is applied.

Just as much as the intrinsic permeability, the relative permeability has a high impact, but the basic trend of temporal evolution does not change.

¹The French Radioactive Waste Management Agency (ANDRA) is studying the Callovian-Oxfordian argillaceous formation at Bure, East of France, as a potential host formation for underground radioactive waste disposal. The Bure argillite contains about 40 % of clay mineral, 25 to 30 % of quartz and 20 to 30 % of carbonates. The dominant clay minerals are mixed-layered illite-smectite minerals with domination of illite. The porosity is about 14 to 19 %, the laboratory determined permeability amounts to 10^{-21} - 10^{-18} m^2 . (Gaucher et al. 2004; Semete et al. 2008)

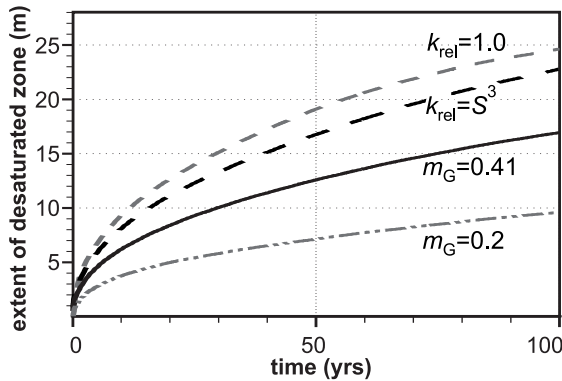


Figure 3.8: Extent of the desaturated zone around the 2003 excavated gallery. Varying relative permeabilities are considered.

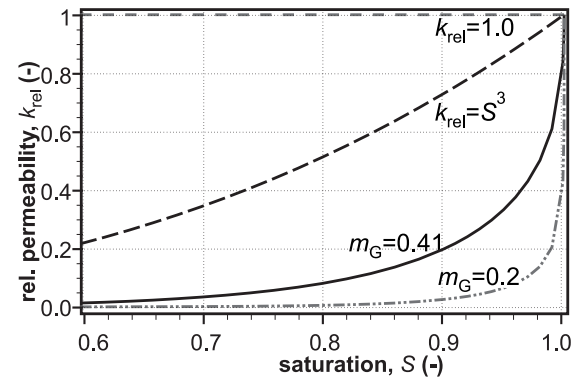


Figure 3.9: Saturation-relative permeability relations, as applied for the simulations presented in figure 3.8.

3.2.4.4 Capillary pressure-saturation relation

Figure 3.11 shows different capillary pressure-saturation relations, based on the *van Genuchten* function (equation 2.41, p. 28), together with measured data (Daupley 1997) and figure 3.10 the corresponding simulation results. The capillarity is the main force for the

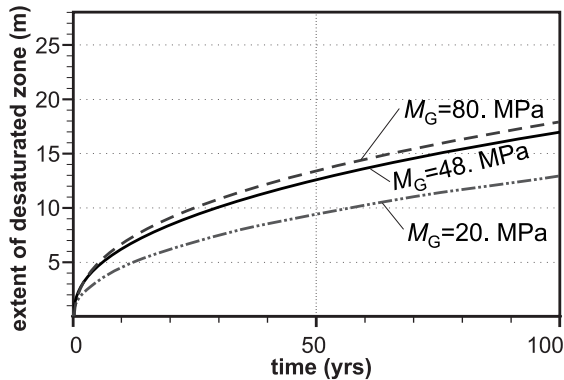


Figure 3.10: Extent of the desaturated zone around the 2003 excavated gallery; varying capillary pressure-saturation relation.

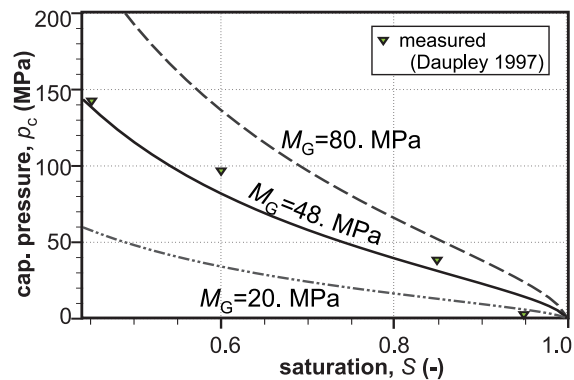


Figure 3.11: Capillary pressure-saturation relations, as applied for simulations as presented in figure 3.10.

desaturation process; thus, it has major influence on the results. But in contrast to the permeability it is less important and the used parameters are better experimentally proved.

3.2.4.5 Seasonal fluctuation of the pressure boundary condition

Figure 3.12 shows the extent of the desaturated zone around the gallery, based on different assumptions of air humidity in the opening, as presented in figure 3.13. The influence on the results is minor. The seasonally influenced zone is slightly enlarged, if the variation of humidity is larger. Thus, the seasonal changes of humidity in the opening have only to be considered, if the seasonally influenced zone is of interest.

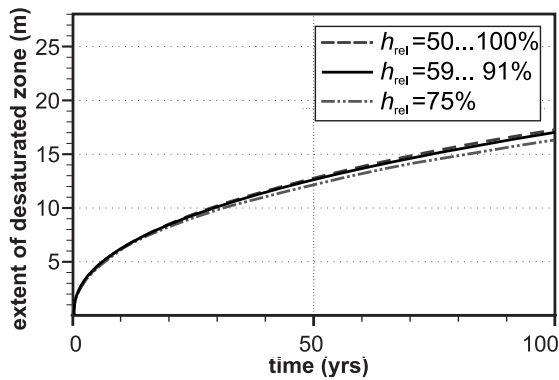


Figure 3.12: Extent of the desaturated zone around the 2003 excavated gallery; varying pressure boundary conditions at the opening.

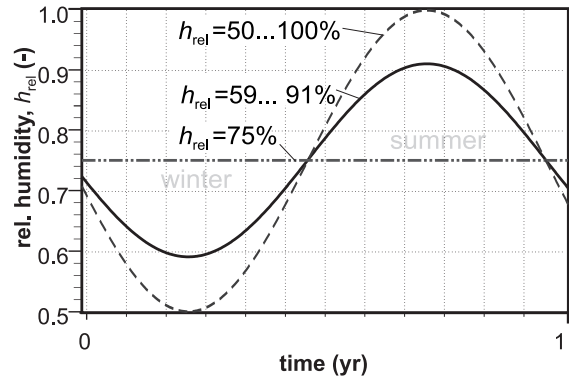


Figure 3.13: Different rel. humidity evolutions, as applied for the simulations as presented in figure 3.12.

A change of temperature in the tunnel is not considered, since its influence on the pore pressure is negligible.

3.2.4.6 Damage and damage induced permeability

In this section the influence of damage and damage induced permeability is investigated. Therefore, two simulations will be compared with the reference solution. In the first one, the damage model will be applied. Therein, the permeability is calculated by the fissure model, as presented in chapter 2.5.4.6. No special emphasis has been put on the damage induced permeability. In the second one, damage induced permeability, as presented in chapter 2.5.6.4, will be considered additionally.

A noticeable influence on the desaturation process is only predicted, if damage induced permeability is considered (see figure 3.14).

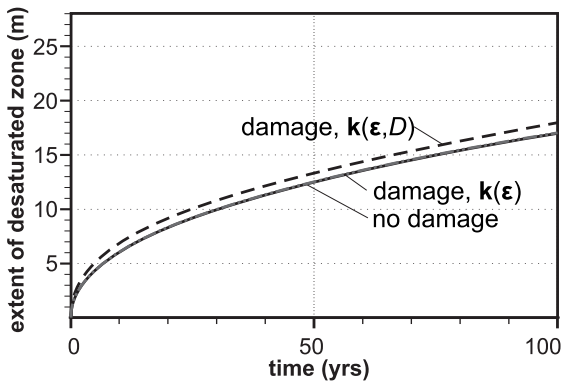


Figure 3.14: Extent of the desaturated zone around the 2003 excavated gallery, considering damage and damage induced permeability.

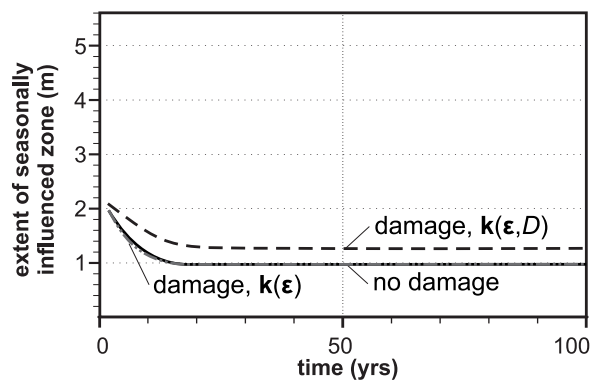


Figure 3.15: Extent of the seasonally influenced zone around the 2003 excavated gallery, considering damage and damage induced permeability.

In figure 3.16 and 3.17 the simulated saturation, damage state and permeability are depicted along a horizontal, radially oriented line. The reference parameters as presented in

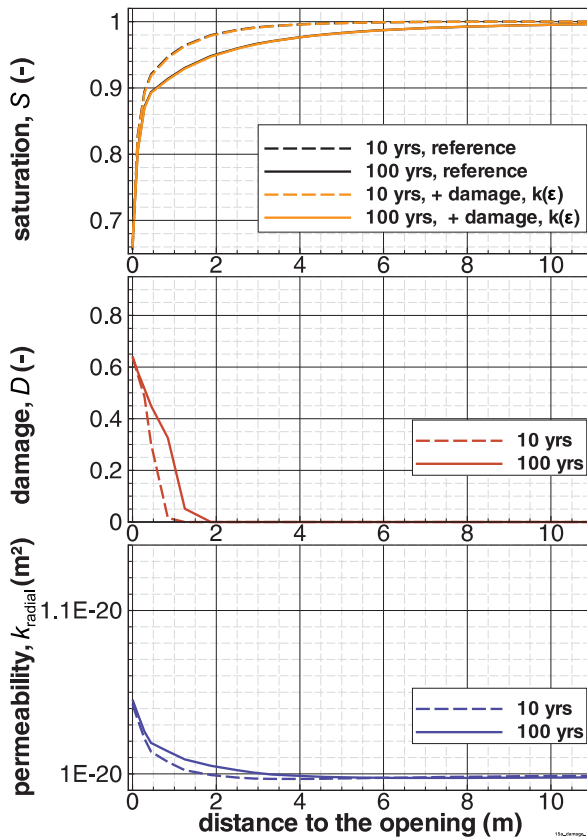


Figure 3.16: Simulation results along a radial line; consideration of damage and deformation induced permeability change.

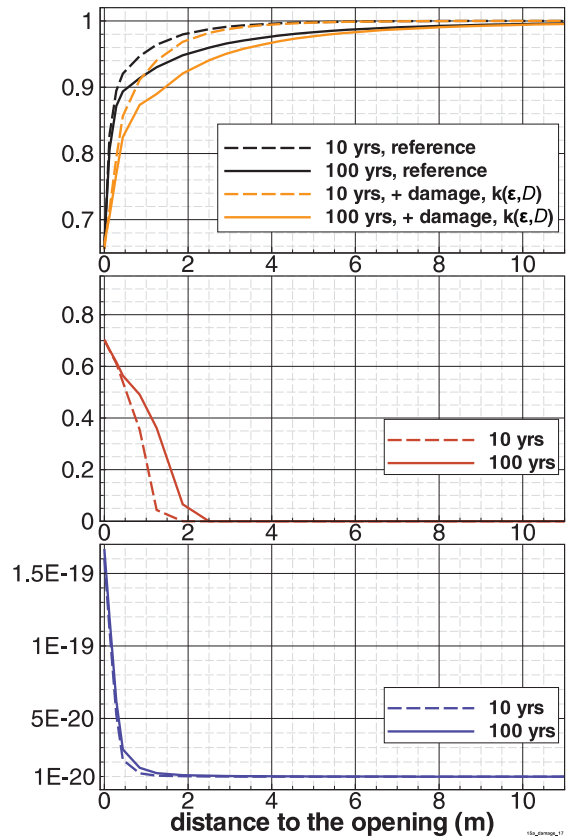


Figure 3.17: Simulation results along a radial line; consideration of damage, and deformation/damage induced permeability change.

chapter 1.2.7 (table 1.2, p. 11) have been used. A discussion of the damage parameters can be found in section 3.4.3.

A distinctly increased permeability can only be observed near the opening (1–2 m). That is why the influence on the extent of the desaturated zone and the seasonally influenced zone (see figure 3.15) is restricted.

3.2.4.7 Further model parameters

Investigations on the initial porosity, swelling parameters, *Young's* modulus, *Biot* coefficient as well as mechanical and hydraulic initial and boundary conditions have been done. Summarizing the results, the desaturation process is only marginally influenced by these parameters, if the variation is in a meaningful magnitude. Also the geometry of the opening has no significant influence.

With the used linear-elastic approach, the main influence of the hydraulic-mechanical coupling on the pore pressure field is restricted to the first weeks after the excavation (see figure 3.3).

3.2.4.8 Influence of the tunnel lining

In contrast to the newer openings, the old tunnel is surrounded by a lining of masonry at the walls and the top. Ballast is located at the bottom. To get an idea of the influence of this different layout on the desaturated zone around the opening, a comparative study has been done. Figure 3.19 presents the mesh around the opening and the tunnel lining. With this model setup for the masonry, the ballast and for the clay different material properties can be used. In this study, all model parameters remain the same except for the permeability of the masonry, which is varying within two orders of magnitude.

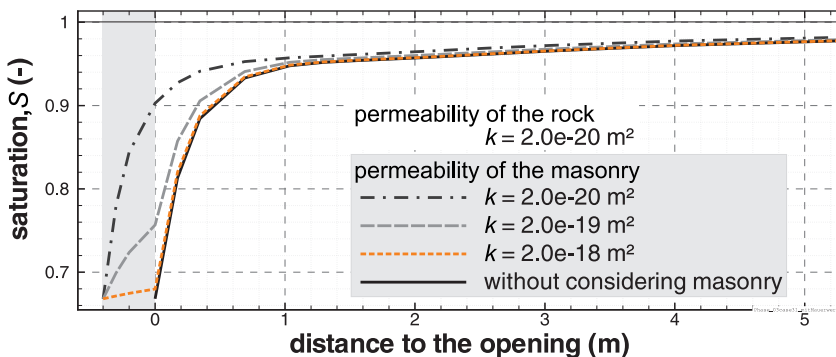


Figure 3.18: Horizontal saturation profiles after 100 yrs simulation time around the old tunnel, considering various permeabilities in the masonry.

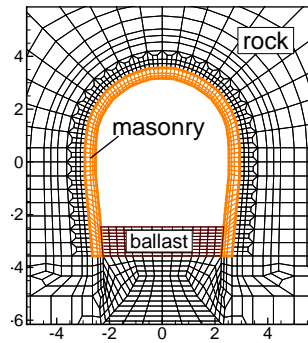


Figure 3.19: Mesh and material groups at the old tunnel.

Figure 3.18 shows the horizontal saturation profiles after 100 years. Above a permeability of $k = 2.0 \times 10^{-18} \text{ m}^2$ the masonry has no influence on the saturation profile. Even with a lower permeability the influence is bounded to the first meters. In fact, the permeability of the masonry should be higher than $k = 2.0 \times 10^{-18} \text{ m}^2$; thus, no significant influence of the masonry on the size of the desaturated zone can be expected.

Nevertheless, the seasonal influence on the desaturation process in the rock could be attenuated. The masonry could even act as a buffer for the moisture transport. There are not enough information available of the hydraulic properties of the masonry in order to quantify these potential effects. Hence, in the following simulations the masonry will not be considered.

3.2.5 Comparison with measurements

3.2.5.1 General remarks

In order to evaluate the used model and its parameters, the simulation results will be compared with measured saturation profiles, as provided by the *IRSN*. Hereby, the permeability will be used to calibrate the simulations, because it is the most influencing parameter and furthermore, the measured permeabilities vary in a wide range. Two different sets of saturation measurements have been realized and provided by the *IRSN*, namely the first and the second campaign.

The hydraulic-mechanically coupled model with the reference model parameters as presented in table 1.2 (p. 11) will be applied. The damage model will not be used here for two reasons: firstly, for the sake of simplicity. The damage model needs additional parameters, which are not experimentally fixed. Secondly, the sensibility study has brought out, that the influence of the damage model on the desaturation process is restricted to a permeability change in the near field. Since the measured saturations vary in a wide range, the consideration of this fine distinction is not meaningful.

The desaturation process is characterized by seasonal and long term influences. Thus, the exact drilling day has been taken into account, if measurements are compared with simulations.

3.2.5.2 First campaign

The saturation measurements within the first campaign has been done along horizontal (MD3, MD6) and diagonal boreholes (MD5, MD7), drilled with a length of about 4.0 m at each opening (Matray et al. 2007). Figure 3.20 shows the location of the boreholes, the shape of the simulated desaturated zone and the comparison between the simulated and measured saturation profiles. The best fit for the 1996 excavated gallery has been reached with a permeability of $k_x = 2.0 \times 10^{-20} \text{ m}^2$ in the bedding plane and $k_z = 0.5 \times 10^{-20} \text{ m}^2$ vertical to the bedding plane. With these values, the desaturation at the tunnel is overestimated, especially at MD7, but at the 1996 excavated gallery the saturation agrees well and also the anisotropic behavior can be simulated. The largest discrepancies can be observed in the near field, which could be explained by influences of the EDZ and the seasonal fluctuation.

The comparison of simulated saturations with the measured ones from the first campaign has brought out no coherent results. It was not possible to predict the desaturated zone at the 1996 excavated gallery and the old tunnel with the same parameters. At both openings, the saturation measurements indicate a higher permeability in bedding plane than perpendicular to it.

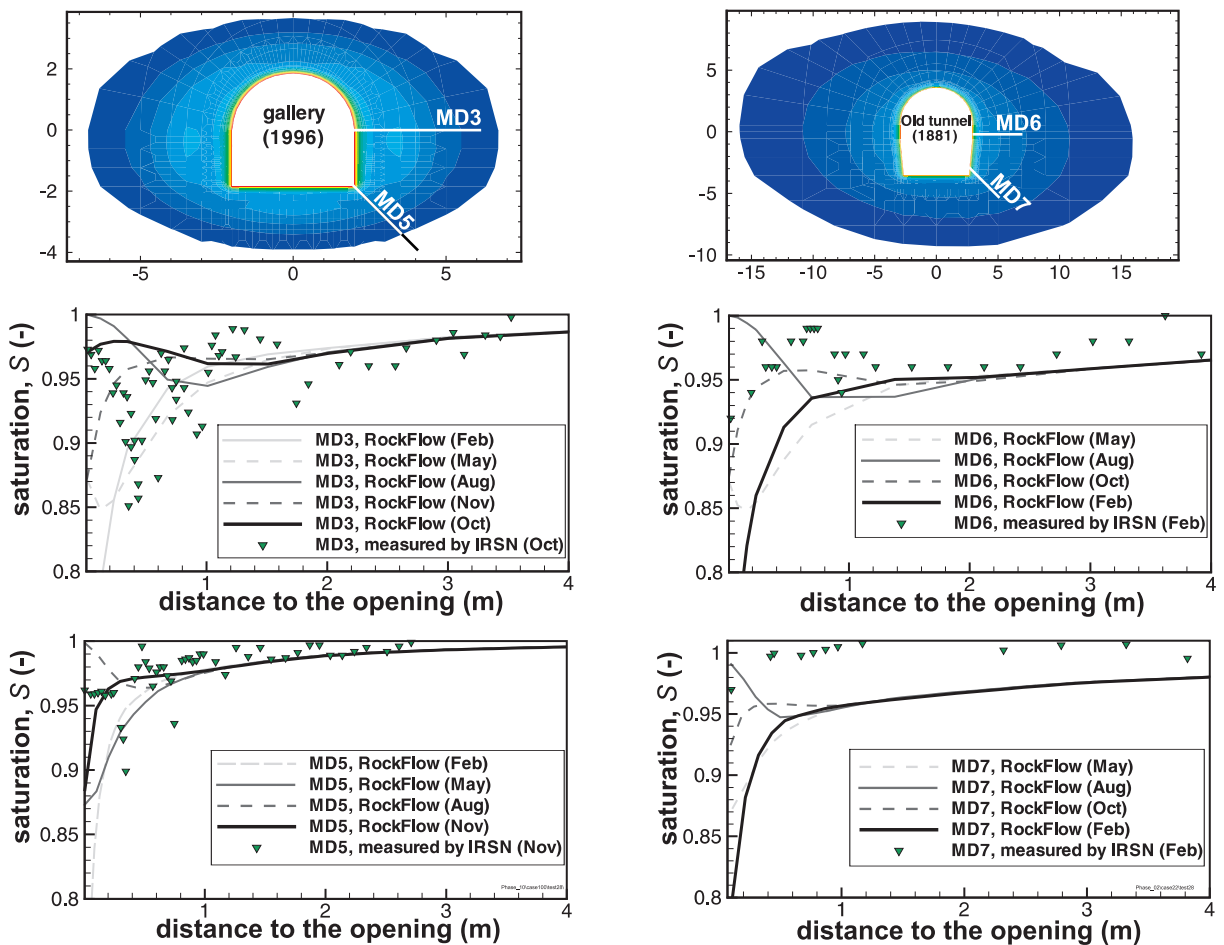


Figure 3.20: Top: simulated desaturated zones and location of the boreholes; beneath: saturation profiles in comparison with measurements of the first campaign (Matray et al. 2007) for the 1996 excavated gallery (left) and the old tunnel (right).

3.2.5.3 Second campaign

The second campaign (also called TM, GEM, and GPM data) consists of eight radial boreholes (with a length between 6.0 and 16.0 m) around each gallery and the tunnel. The location within the Tournemire site is depicted in figure 1.2 on page 6. Figure 3.21 shows all measured saturation profiles around the 2003 excavated gallery and the corresponding simulation results. In order to allow an evaluation of potential anisotropy, the direction of the boreholes has been considered. The corresponding plots for the other two openings are presented in appendix A.1.1 (p. 170 et seq.). For every borehole the measured saturation profile has been compared with the simulation results and evaluated. The comparison between measured and simulated saturation profiles proves difficult because the measurements show a broad spread. Not at every borehole the profiles are comparable, e. g. at GPM 135 the trend is completely different or at GPM 225 there is not enough data available for a reasonable comparison.

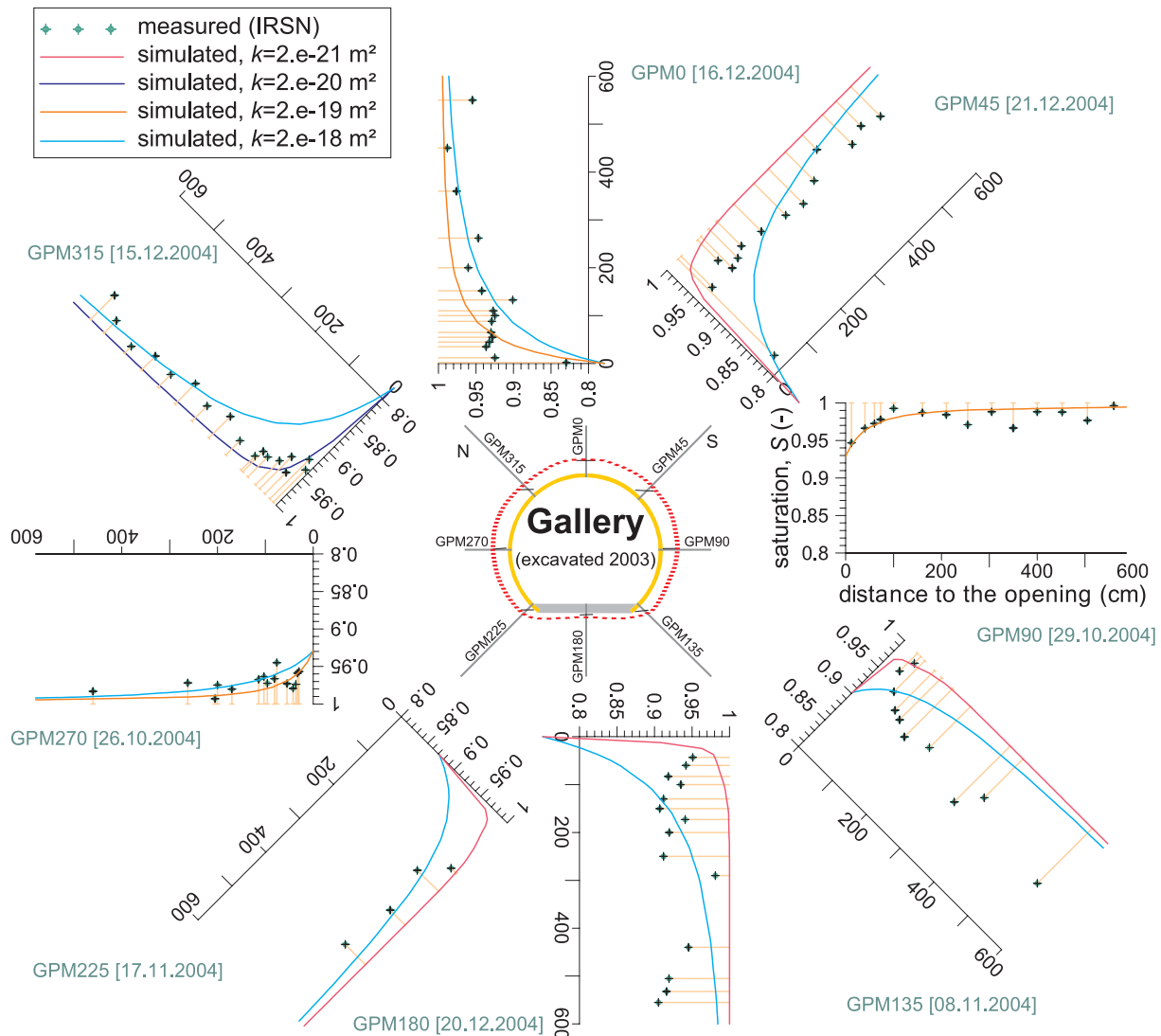


Figure 3.21: Direction dependent visualization of measured (IRSN) and calculated saturation profiles at the 2003 excavated gallery (second campaign).

3.2.5.4 Determination of permeability

One goal of the investigation on the desaturated zone was the determination of permeability. However, the comparison between measurements and simulations has not brought out a clear result, despite the fact that measurements at 28 boreholes have been analyzed (cf. table 3.1). At some boreholes the simulated saturation profiles fit the measurements, but it was not possible to find an unique parameter set, which can predict all measurements. The measurement of saturation is very difficult so that uncertainties have to be considered. An anisotropic tendency is only observable in the measurements of the first campaign. The influence of the seasonal effects of humidity could neither be verified nor ruled out.

Table 3.1: Comparison between measured and calculated saturation profiles (first and second campaign).

		Permeability with the best fit (m^2)				Not comparable
		2.0×10^{-21}	2.0×10^{-20}	2.0×10^{-19}	2.0×10^{-18}	
Tunnel (1881 excavated)	MD6	★				
	MD7	★				
	TM 0			★		
	TM 45			★		
	TM 90	★ (*4)			★ (*4)	
	TM 135					★ (*1)
	TM 180		★			
	TM 225					★ (*1)
	TM 270	★ (*4)			★ (*4)	
	TM 315					★ (*2)
East gallery (1996 excavated)	MD3		★			
	MD5	★ (*5)				
	GEM 0			★		
	GEM 45		★			
	GEM 90		★			
	GEM 135					★ (*2)
	GEM 180					★ (*2)
	GEM 225					★ (*2)
	GEM 270		★			
	GEM 315		★ (*3)			
Main gallery (2003 excavated)	GPM 0			★	★	
	GPM 45					★ (*2)
	GPM 90			★		
	GPM 135					★ (*2)
	GPM 180					★ (*2)
	GPM 225					★ (*1)
	GPM 270		★ (*4)	★ (*4)		
	GPM 315		★ (*4)		★ (*4)	

*1) lack of data

*2) different trend

*3) values only partly comparable

*4) in the near field the lower permeability fits better, in the far field the higher one

*5) $5.0 \times 10^{-21} \text{ m}^2$

Considering the measurements of both campaigns the desaturation process can be simulated in principle with a permeability in the range between 2.0×10^{-21} and $0.5 \times 10^{-18} \text{ m}^2$.

Exemplarily, all measured saturations are plotted together with simulation results in figure 3.22 for the 2003 excavated gallery. The depicted simulation results cover the wide

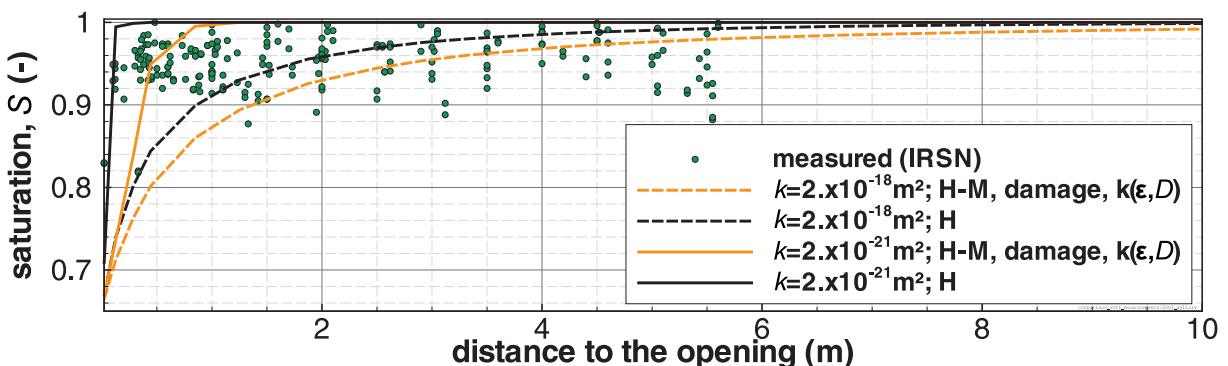


Figure 3.22: Comparison between measured and simulated saturations. The simulations differ in the value of permeability and the considered process.

range of permeability. Additionally, the influence of the mechanical model, considering damage and damage induced permeability, can be observed. Without considering the damage induced permeability, no differences would occur between the hydraulic (H) and the hydraulic-mechanically coupled (H-M) approach. The used damage induced permeability model has a distinctive influence on the simulation result in the near field of the gallery. Here, the permeability is increased more than one order of magnitude (see figure 3.17). This leads to a shift of the saturation profile of about 1 – 2 m insight the rock. It is not possible to limit the range of permeability or to confirm the use of the damage induced permeability model with these measurements. Nevertheless, the range of measured saturation profiles can be simulated with the used model parameters.

3.2.6 Conclusions

In order to investigate the extent and development of the unsaturated zones around the excavated openings, fully hydraulic-mechanically coupled simulations with consideration of anisotropy, damage and deformation induced permeability have been performed.

Concerning the affected area around the excavation, two zones can be distinguished: one zone near the opening, showing a seasonally affected saturation and a second zone, where the saturation is decreased, but changes take place only slowly. The first zone extents about 1 – 2 m, the extent of the second zone depends on the time and also strongly on the material properties. The parameters of main interest should be the intrinsic permeability and the relative permeability. Thus, also the processes which exhibit a strong impact on the permeability are of interest, such as damage. Regarding the range of intrinsic permeability measurements, the simulated desaturated zone varies between 2 and 27 m after 100 years. The relative permeability also has a large influence but is not even experimentally confirmed. Thus, its use is conducted with uncertainties.

In-situ investigations have shown that a damage induced permeability change around the excavation is restricted to the near field. The used permeability model has been adapted accordingly. Consequently, the influence on the extent of the desaturated zone is restricted, but the impact on the near field is significant. It leads to a faster desaturation process, especially in the short term behavior. This could be an explanation for the low differences between the desaturated zones around the openings of different ages.

A comparison with measured saturation profiles has indicated that the developed model has the capacity to simulate the desaturation process only partly. The wide spread of measured saturation profiles at the three openings can be covered only by simulations with a wide range of permeability ($k = 2. \times 10^{-21} \dots 2. \times 10^{-18} \text{ m}^2$). In this context, a consideration of minor significant effects, such as the hydraulic-mechanically coupling or the tunnel lining, is not meaningful.

Most of the measurements have not confirmed any hydraulic anisotropy. Thus, the problem can be treated by a one-dimensional approach. Even the seasonal changes of air humidity in the tunnel and galleries can be neglected, if only the extent of the unsaturated zone is of interest.

The wide spread of measured saturations could be caused by an inhomogeneous dis-

tribution of permeability. Even if the rock is nearly homogeneous in the undisturbed configuration, the desaturation fissures could lead to preferential flow paths. Along these fissures the desaturation process would take place much faster than in the undisturbed matrix material. Thus, the in-situ measured permeability is not sufficient to characterize the desaturation process in the fractured zones.

3.3 Modeling the mine-by-test experiment

3.3.1 The mine-by-test experiment

In order to allow a more precise analysis of the argillite at the Tournemire site, a new

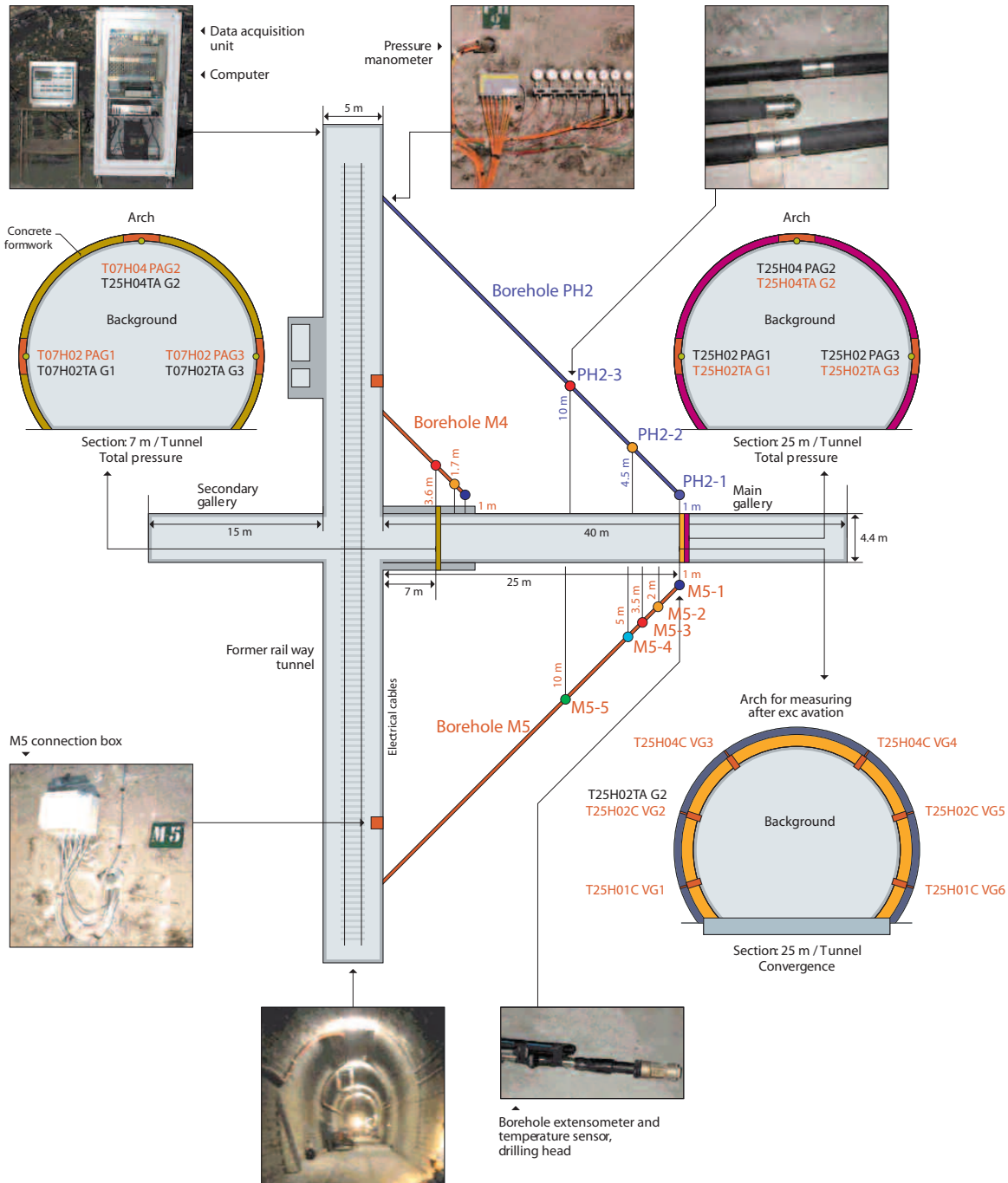


Figure 3.23: Layout of the hydraulic and mechanical instrumentation of the mine-by-test experiment (Rejeb 2005).

gallery has been excavated in 2003. For the long term study of the hydraulic-mechanical response of the rock mass due to the excavation process, instrumentation has been done by the IRSN as shown in figure 3.23. The location within the Tournemire underground laboratory is presented in figure 1.2 (p. 6). More information concerning the excavation process and the instrumentation can be found in Rejeb et al. (2008b) and Rejeb (2005). The object of investigation is the rock mass response to the excavation of the 40 m long main gallery. The zone with concrete lining close to the tunnel (cf. figure 3.23) will not be considered. The support and the closeness to the old tunnel could involve complex interactions which will not be a subject of the current study.

Accordingly, the pressure measurements along the borehole PH2 and the horizontal displacement measurements in the borehole M5 are in the center of interest.

3.3.2 Interpretation of the measured data

Figures 3.24 and 3.25 show measured displacements and pressures along borehole M5 and PH2, respectively. Each color corresponds to one monitoring point. Additionally, the distance to the gallery is depicted. The data have been continuously measured during and after the excavation phase. Figure 3.25 shows the measured displacements during the excavation phase together with the temporal evolution of the excavation. The measured

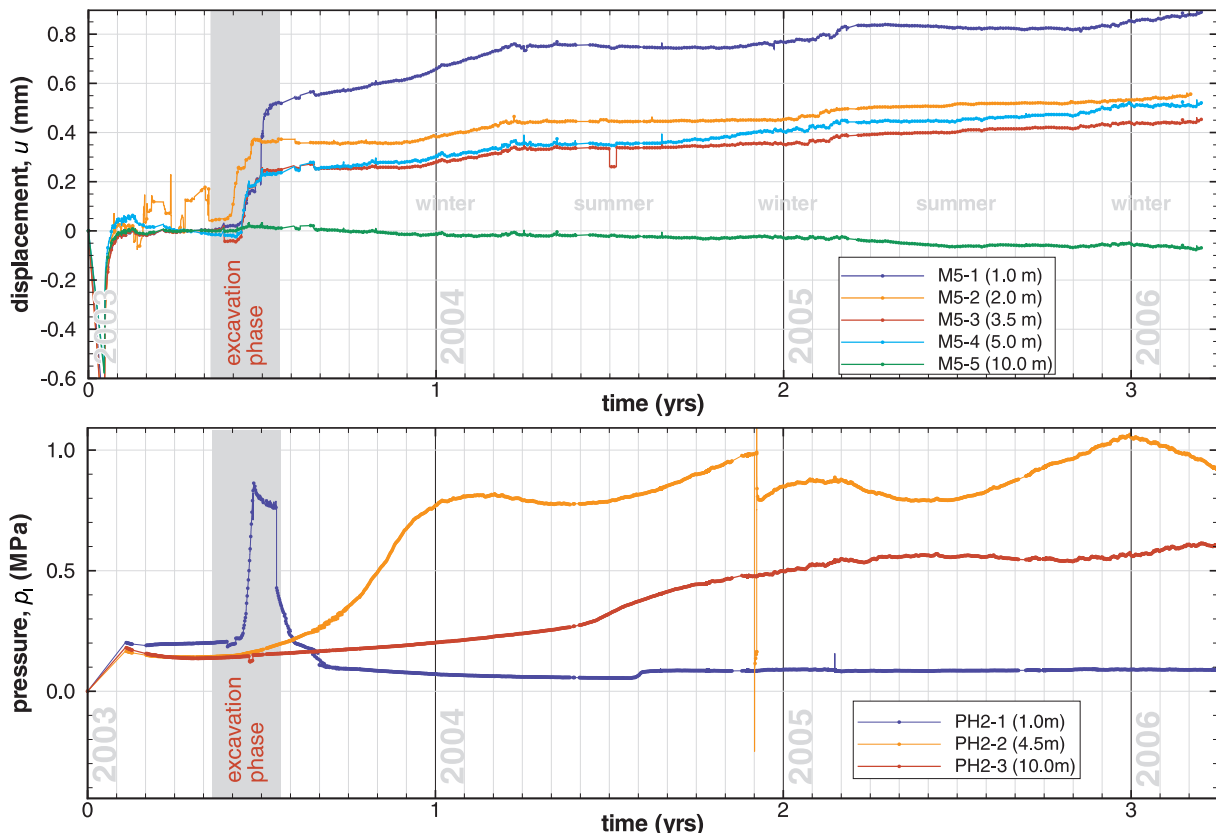


Figure 3.24: Mine-by-test experiment, measured displacements (top) and pore water pressures (beneath) during and after the excavation of the main gallery. All measurement data are provided by the IRSN.

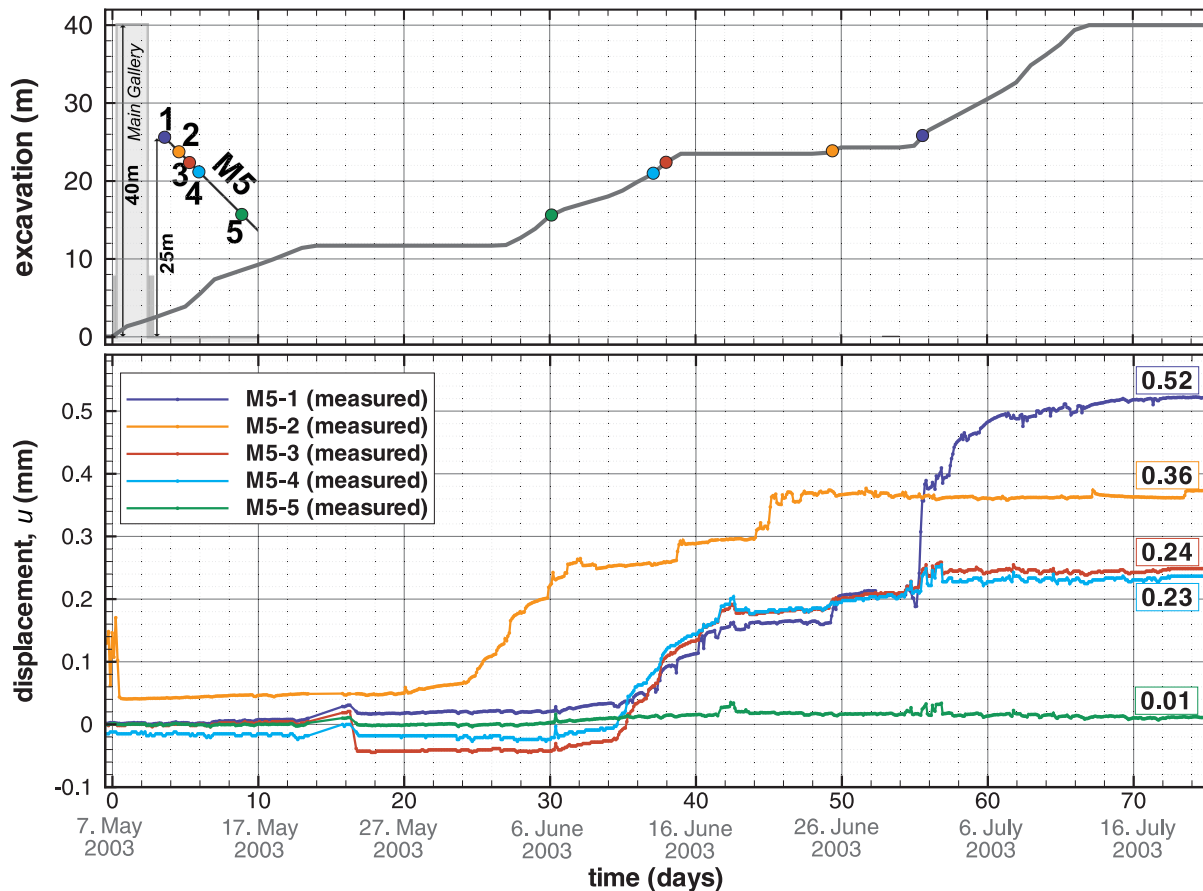


Figure 3.25: Mine-by-test experiment, evolution of the excavation front (top) and measured displacements (beneath) during the excavation of the main gallery. All measurement data are provided by the IRSN (Rejeb 2005). The dots mark the point in time, when the excavation front passes by a monitoring point.

displacements directly after the excavation phase are plotted for each monitoring point on the right hand side. During the excavation, the major change of displacements can be observed. This can be interpreted as an elastic and maybe plastic deformation as a direct reaction to stress rearrangement due to the excavation. A closer look at the excavation phase (figure 3.25) reveals a nearly equal amount of displacement at M5-1, M5-3, and M5-4 between the 35th and 55th day, even if the excavation front passes the monitoring point one after another.

After the excavation, the displacements close to the tunnel continue increasing. This may be caused by a desaturation process due to the contact with air, consolidation and/or a viscous material behavior. The change of displacement is getting smaller with time. Half a year after excavation, only in winter months changes are observed. This could be an indicator of a seasonal effect on displacement and pressure: shrinkage of the rock in the dry winter time.

As expected, the displacements are directed towards the opening and decrease with increasing distance to the excavation. Indeed, two exceptions are observable: (1) The displacement sensor M5-5 shows a slightly increasing displacement contrary to the excavated tunnel, (2) two months after the excavation, the sensor M5-4 recorded higher

displacements than M5-3, even though M5-4 is 1.5 m farther away from the gallery. Both observations are hard to explain and could be caused by local inhomogeneities or inaccuracies in the measurements.

The pore water pressure is influenced by the excavation process, too. A jump in pore water pressure is recorded close to the opening (blue line). The fast reduction could be caused by the desaturation process at the opening. Further away from the opening the pore water pressure increases more gently, this may be caused by a rearrangement of stresses in combination with a consolidation process of the rock. Seasonal influences can be observed at PH2.

Experimental uncertainties have been reported: at PH2-1 after the peak in July 2003 and at PH2-2 after the second peak in December 2004. Consequently, these measurements will not be considered for comparison with simulation results.

3.3.3 Model setup

3.3.3.1 Two-dimensional

For the two-dimensional model, a plane normal to the gallery axis is simulated as shown in figure 3.26. The monitoring points of displacement and pore water pressure are projected

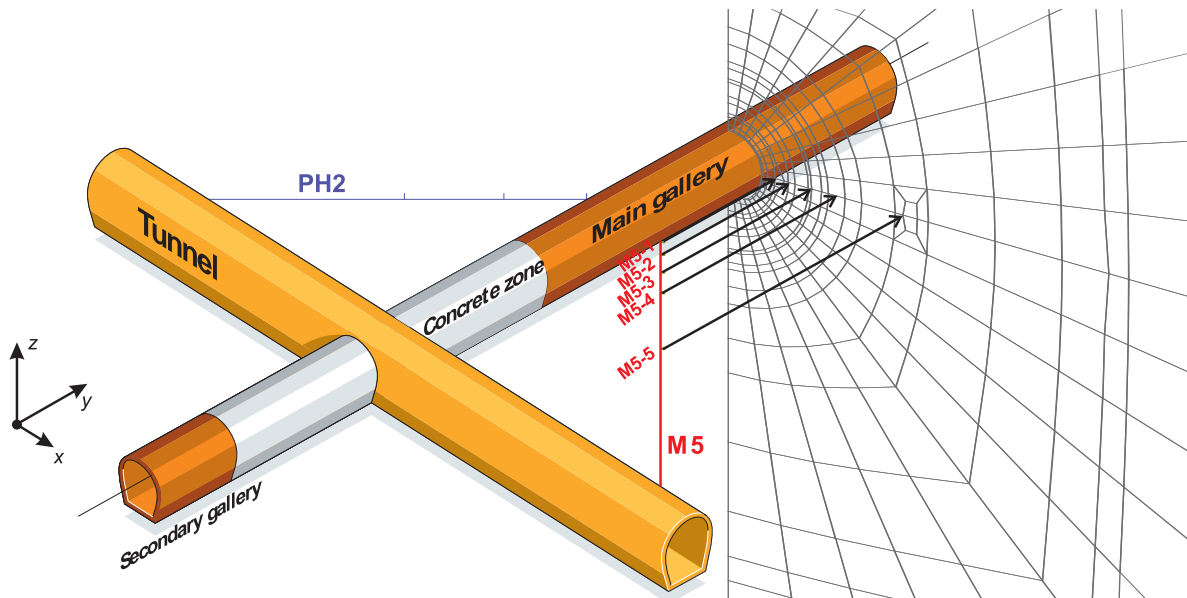


Figure 3.26: Two-dimensional discretization of the domain and projection of monitoring points. Three-dimensional plot of the gallery/tunnel based on Rejeb (2005).

into this plane, figured as arrows in figure 3.26. The initial and boundary conditions are presented together with the mesh, consisting of 594 nodes and 546 quadrangular elements, in figure 3.27.

The model setup equals the previous one, as presented in figure 3.1, except for the initial pore water pressure, which has been set to 0.2 MPa in adaption to the measured values at the monitoring points (see figure 3.24). The simulation domain measures 260 m ×

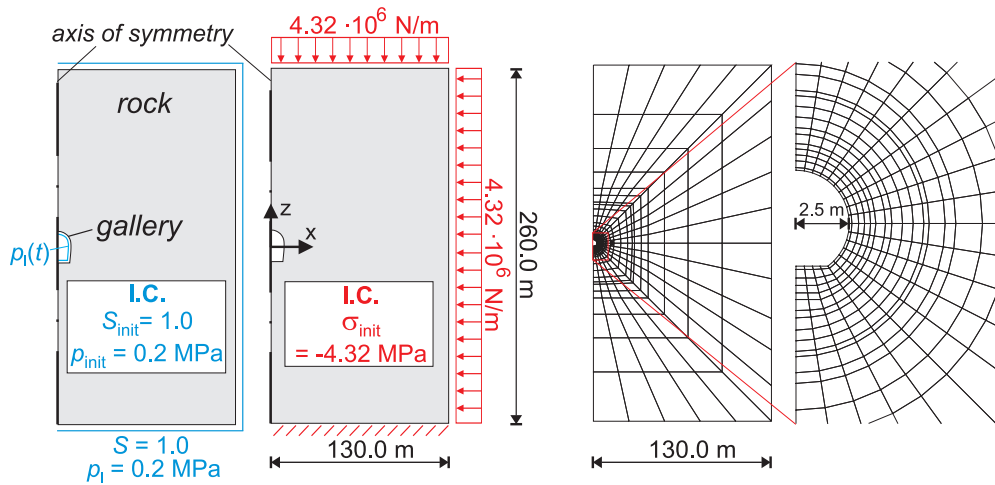


Figure 3.27: Initial and boundary conditions (left) as well as the finite element mesh (right) for the two-dimensional simulation of the mine-by-test experiment.

260 m. The excavation process is simulated by an instantaneous change in the boundary conditions at the opening.

With a plane strain and plane flow model the time-dependent excavation progress cannot be simulated and inaccuracies have to be expected. But the advantages are a short computing time and a simpler model setup.

The displacement sensors measure the relative displacement of the monitoring point with respect to the reference point, which is located at the old tunnel. In order to allow a comparison of the simulated displacements of the two-dimensional model Δl_{2d} with the measured data Δr , the following conversion is used (see figure 3.28):

$$\Delta r = \sqrt{a^2 + (a + \Delta l_{2d})^2} - \sqrt{2} a \quad (3.1)$$

The basis for this conversion is the assumption of a rock displacement perpendicular towards the excavation, as shown in figure 3.28. Because $a \gg \Delta l_{2d}$, the conversion can be simplified to

$$\Delta r \approx \frac{1}{2} \sqrt{2} \Delta l_{2d}. \quad (3.2)$$

In general, the reference parameter set as presented in table 1.2 (p. 11) is used, variations will be mentioned. With the used parameters, coupling due to the effective stress approach will be neglected in unsaturated areas. Therefore, the effect of suction is modeled only by the shrinkage model (cf. chapter 2.3).

In order to consider the gravity forces, the hydraulic and mechanical boundary and initial conditions have to be given as a function of depth. Indeed, comparative investigations have shown that the influence of gravity can be neglected, if only the processes near the excavation are of interest.

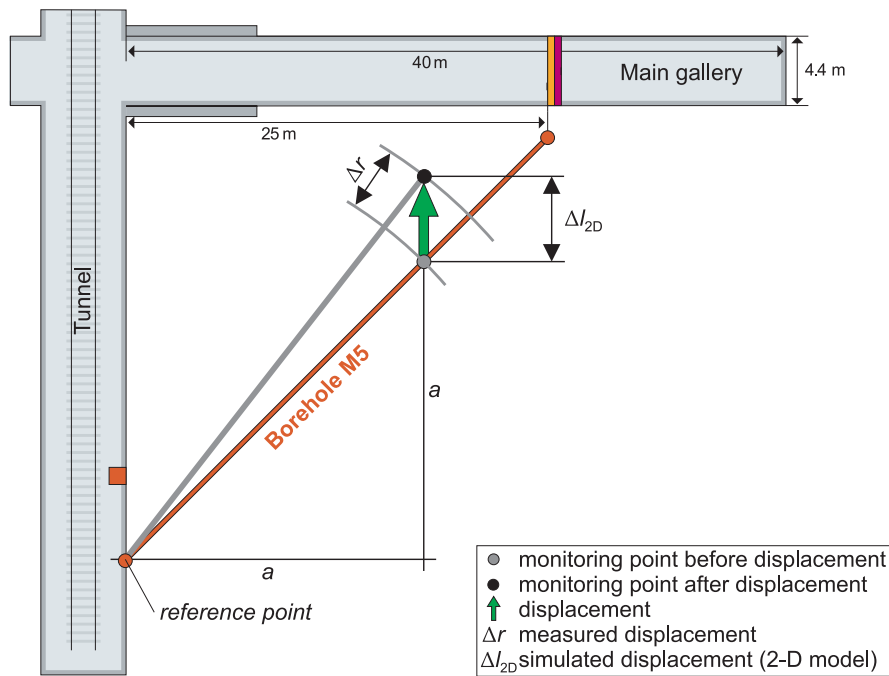


Figure 3.28: Measured and simulated displacements during and after the excavation of the main gallery, applying the two-dimensional model.

3.3.3.2 Three-dimensional

The mesh for the three-dimensional discretization is plotted in figure 3.29. It consists of 18,585 nodes and 16,524 hexagonal elements. The old tunnel is not considered in the simulation. For the three-dimensional simulations, the same initial conditions as in the two-dimensional simulations have been used; the boundary conditions have been adapted accordingly. The excavation process is simulated by a time-dependent deactivation of the elements in the excavation zone, as presented in chapter 2.6. In this way, the excavation progress including interruptions can be considered.

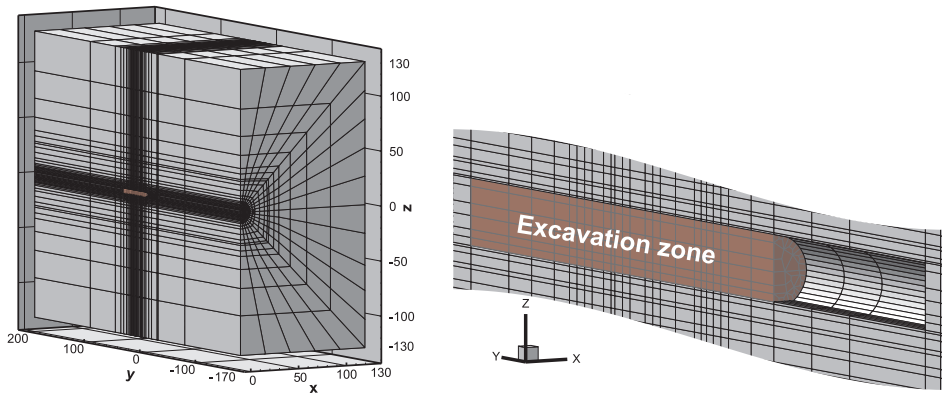


Figure 3.29: Three-dimensional finite element mesh as applied for the simulation of the mine-by-test experiment.

3.3.4 Simulation and comparison with measurements

3.3.4.1 General remarks

In the following sections several simulation results will be presented and compared with the measured data. In a first step, the accuracy of the model will be verified by comparing numerical results of a three-dimensional model with a two-dimensional approach, applying a two-dimensional problem. Furthermore, the mechanical input parameters will be checked and adjusted in the range of the measurements, if needed.

The study on the measurements (section 3.3.2) has brought out a distinction between two time periods concerning the response of the rock mass to the excavation: (1) short term response (during and directly after the excavation); (2) long term behavior (two years and more). The major amount of displacements is observed during and directly after the excavation. During this time period neither failure nor damage are observed. The long term behavior is influenced by a seasonal desaturation process and a failure or damage mechanism. In both time periods H-M coupling phenomena take place. Both, the long term behavior and the short term behavior, will be investigated by the comparison of measured displacements and pore water pressures with simulation results.

3.3.4.2 Determination of the mechanical parameters

Directly after the excavation phase all monitoring points show a constant displacement (see figure 3.25). This amount of displacement seems to originate from the redistribution of stresses only. Other effects, like shrinkage or viscosity, should need more time to have a notable effect on the displacement in the rock. In order to investigate this assumption, the excavation has been simulated by a two-dimensional linear-elastic model. The lines in figure 3.30 represent the simulated displacement versus the distance to the opening

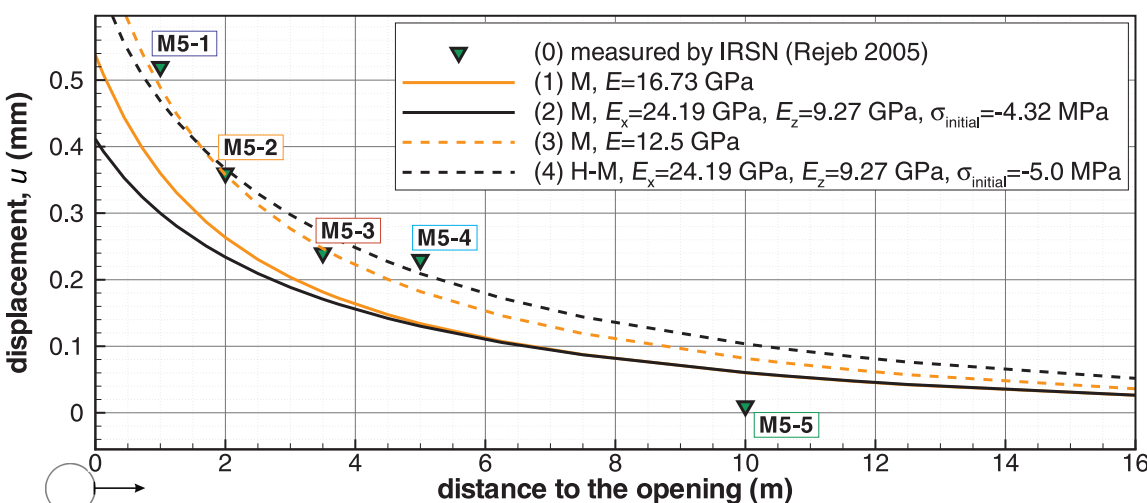


Figure 3.30: Comparison between measured and simulated displacements, directed towards an excavated opening.

along a horizontal line in comparison with the measurements. The solid lines correspond to the isotropic (1) and anisotropic (2) reference parameter set (table 1.2, p. 11). With these parameters, the displacements are underestimated. A better fit can be reached, if the *Young's* modulus is reduced about a quarter to 12.5 GPa (3). This value is still within the range of measurements (see chapter 1.2.5). Since the hydraulic-mechanical coupling also influences the displacement, an additional simulation considering the hydraulic process has been done (4). Herein, the transversely isotropic mechanical properties (table 1.2) have been used and the initial stress in the rock mass has been increased to -5.0 MPa. With this parameter set a good agreement with the measurements can be reached. The increased value for the initial stress is still within the range of measurements (chapter 1.2.5). It seems to be more meaningful to vary the initial stress field than the mechanical properties, since the measurements of the in-situ stresses come along with higher uncertainties than the mechanical properties, which have been determined by many laboratory tests. This procedure differs from Millard and Rejeb (2008), who used a decreased mechanical stiffness in order to obtain a better accordance with measurements.

Except for the monitoring point M5-5, directly after excavation all measured displacements can be simulated well with linear-elastic models using one single parameter set. All used parameters are within the range of measurements. The parameter set corresponding to line (4) will be used in the following simulations.

3.3.4.3 Comparison of the two-dimensional and three-dimensional approach

In order to verify the numerical model, the excavation process is modeled as a two-dimensional problem. The simulation results of a three-dimensional and a two-dimensional approach will be compared. Transversely isotropic elasticity and H-M coupling is considered. Furthermore, the desaturation, as initiated by a hydraulic boundary condition at the opening, induces anisotropic shrinkage in the near field. The hydraulic and mechanical response four months after excavation are presented in figure 3.31 and 3.32, respectively. A good agreement between the approaches can be observed, although different meshes have been used.

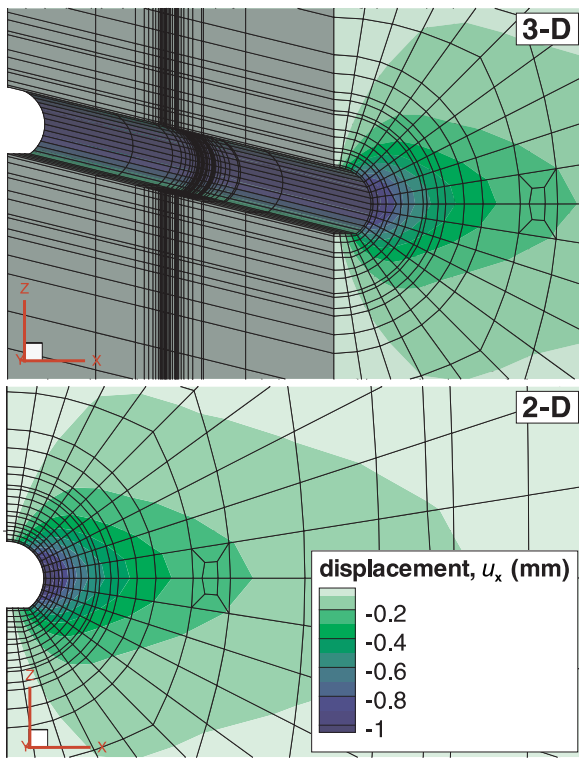


Figure 3.31: Displacement field four months after the excavation, simulated by a three-dimensional (top) and two-dimensional (beneath) approach.

3.3.4.4 Short term response

Mechanical response

To get a first impression of the modeling results, the displacements around the gallery at the beginning of the excavation process are shown in figure 3.33. The influenced displacement field moves with the excavation front in the direction of the y -axis (to the left). In figure 3.34 simulated displacements with the corresponding measurements for

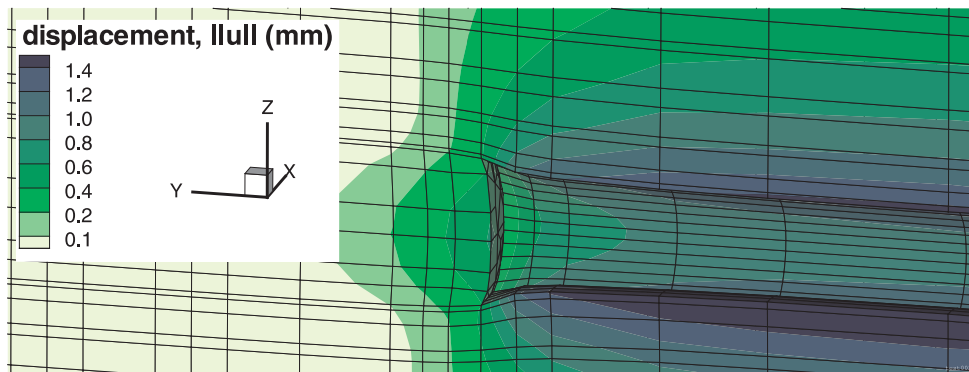


Figure 3.33: Short term response to the excavation calculated by three-dimensional model; simulated displacements around excavated opening on May, 15th. The displacement field, which is projected on the mesh, is scaled by the factor 500.

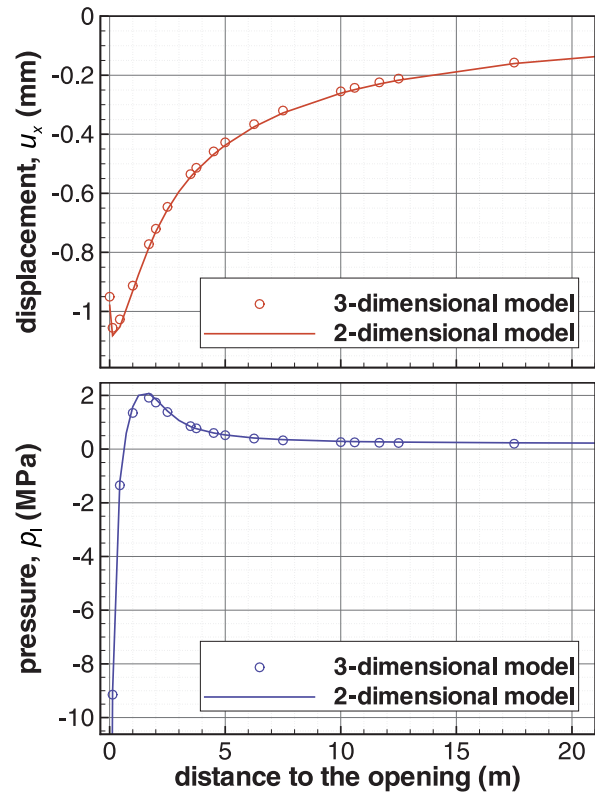


Figure 3.32: Comparison of two-dimensional and three-dimensional model approach. The results along the direction of the x -axis are plotted.

the short term predictions are plotted for the monitoring point M5-1. The results at the other monitoring points can be found in the appendix A.2.1.1 (p. 173). In these figures,

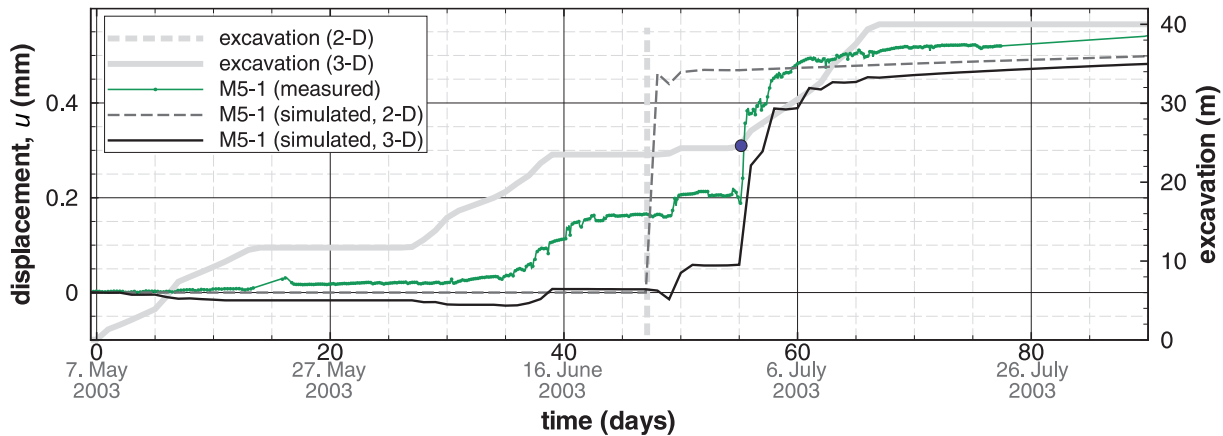


Figure 3.34: Measured (IRSN) and simulated displacements at the monitoring point M5-1 during and directly after the excavation phase.

the excavation process is shown as a bold line. Exactly at the point in time, when the excavation front passes the corresponding monitoring point, the gray line is marked with a dot. Additionally, the point in time when the instantaneous excavation takes place in the two-dimensional model is marked by a vertical dashed line.

In the two-dimensional model the excavation is simulated by an instantaneous change in the boundary condition at the opening, in the three-dimensional model by a time-dependent deactivation of elements. Therefore, the displacement evolution during the excavation phase can only be reproduced by the three-dimensional model. After the excavation has been finished, the two- and the three dimensional model show the same displacements. This behavior can be observed at all monitoring points. The distinctions between the two- and three-dimensional approach can be explained by the desaturation process. Due to the restriction of the two-dimensional approach, the impact of the desaturation process starts for all monitoring points at the same point in time. In the three-dimensional model, the desaturation starts with the deactivation of elements; it depends on the location of the excavation front with respect to the monitoring point.

The major displacements can be observed approximately in an area of 10 m in front and behind the monitoring point, when the excavation front passes by. This trend is the same in the measured and calculated data, but the evolution of displacement looks different. In most cases the simulations underestimate the displacements. After the excavation, the simulated values of the two- and three-dimensional model equal nearly the measurements. Thus, the two-dimensional approach seems to be adequate after the excavation phase.

All displacements are referred to a reference point at the old tunnel (see figure 3.26). Caused by the displacement of this point toward the gallery at the beginning of the excavation phase, all simulated displacements show a decrease. In the measured data this effect cannot be observed; the point at the old tunnel seems to be fixed. The difference could be explained by influences of the old tunnel, its EDZ, and the concrete zone of the gallery, which are not considered in the model.

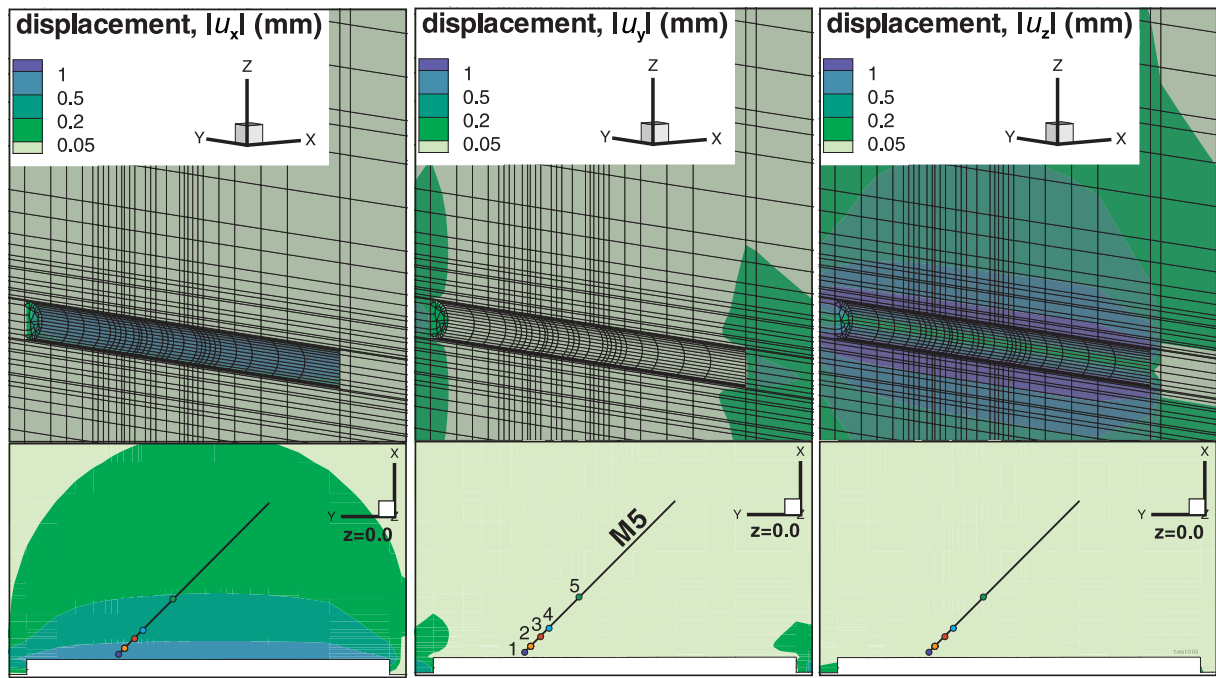


Figure 3.35: Displacements around the completely excavated gallery, calculated with the three-dimensional model (simulated day: 90th; August, 5th, 2003). Top: three-dimensional view; bottom: slices in the xy -plane at $z = 0.0$.

In figure 3.35 the displacements in all three directions are plotted, evaluated approximately three weeks after the excavation phase has been finished (simulated date: August, 5th, 2003). Especially in the investigated area of the borehole M5, the displacements in y -direction play only a minor part. The borders of the gallery seem to be far enough from the boreholes, so that the process after the excavation phase can be modeled approximately by a two-dimensional model.

Hydraulic response

In figure 3.36 the pore water pressure evolution around the opening is plotted, as simulated by the two-dimensional and the three-dimensional model, respectively. In the first phase the consolidation process dominates, caused by the excavation. This leads to a pressure increase beside the opening and a decrease above and beneath the opening (see also figure 3.3). Since the excavation is modeled by a time-dependent deactivation of elements, a passing excavation front can be observed: At day 30 the excavation front passes the first monitoring point (PH2-3, $y = 16.0$ m), at day 38 the second (PH2-2, $y = 21.5$ m) and at day 50 the last one (PH2-1, $y = 25.0$ m).

Nearly no differences between the slices can be observed after the excavation process has been completed (day 90). It seems that the three-dimensional process during the excavation converts into a two-dimensional one, just a few days after the excavation front has passed by. A comparison between the three-dimensional and the two-dimensional model results reveals that the simulated pressure field is nearly the same.

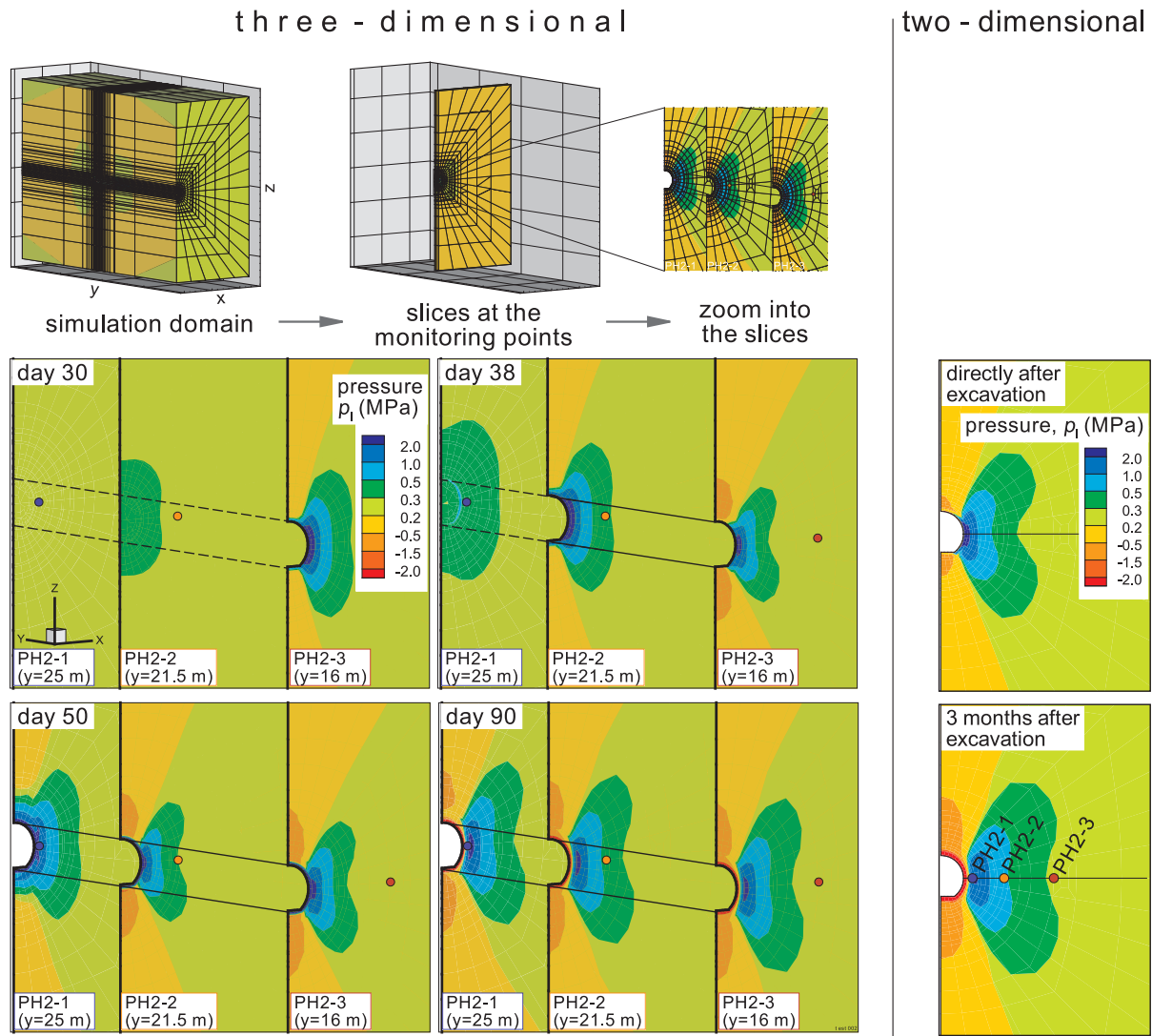


Figure 3.36: Evolution of the pore water pressure during and after the excavation phase, simulated by a three-dimensional (left) and two-dimensional approach (right).

The hydraulic simulation results and the measured data for the short term predictions are plotted in figure 3.37 for the monitoring point PH2-1. The results at the other monitoring points can be found in the appendix A.2.1.2 (p. 175). Although the simulation period is short, the trend of the arising pore water pressure can be observed in the simulation results. Furthermore, the results of the two-dimensional and three-dimensional approach show a good agreement. However, the comparison with the measurements bear some difficulties. At the monitoring point PH2-1, only a few days are available and at PH2-2 and PH2-3 only minor changes can be observed during the excavation phase.

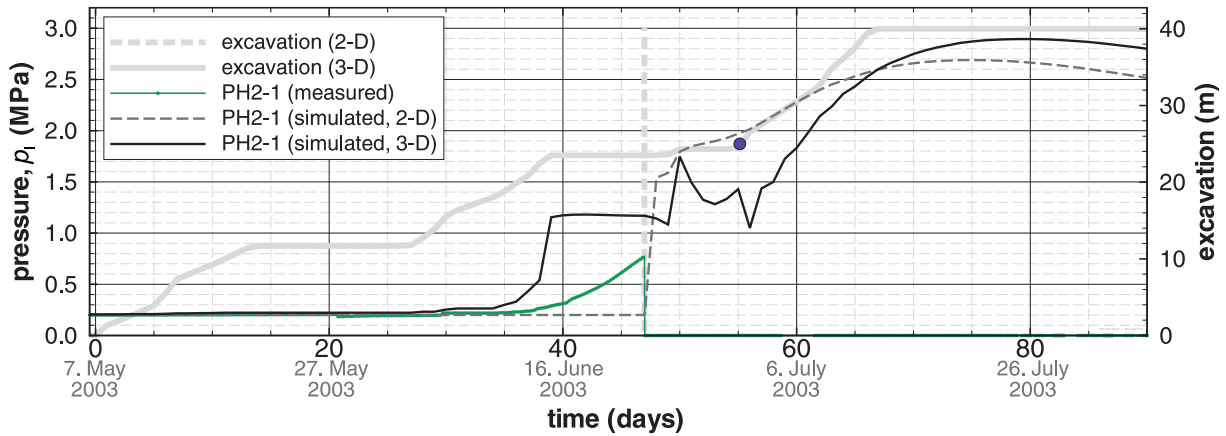


Figure 3.37: Measured (IRSN) and simulated pore water pressure at the monitoring point PH2-1 during and directly after the excavation phase.

3.3.4.5 Long term response

General remarks

In this section the mechanical and hydraulic response during the first three years after the excavation of the gallery is considered. As mentioned before, several processes influence the long term behavior of the rock. In order to investigate the effect of the different processes, several simulations will be presented, with increasing level of complexity. The simulation results will be compared with measurements at the monitoring points along borehole M5 and PH2.

M5-5 and M5-4 will not be mentioned. The displacement device M5-5 shows nearly no displacement in contrast to all simulations. No further insight could be received by comparison of the displacements at this point. The monitoring point M5-4 shows directly after excavation nearly the same displacements as M5-3, which is 1.5 m closer to the gallery. Even in the first year after excavation these two monitoring points show very similar displacements. Consequently M5-4 will be neglected.

Purely mechanical

As already presented in section 3.3.4.2, the displacements directly after excavation at M5-1, M5-2, and M5-3 can be modeled well with a linear-elastic model. The simulated and measured displacements at the monitoring points are presented in figure 3.38. In this simulation a isotropically linear-elastic model with a *Young's* modulus of $E = 12.5$ GPa has been applied. As long as no time-dependent process is involved, no changes in the long term behavior can be predicted. Thus, the simulation results show discrepancies, which increase with time. As a matter of course, no prediction about the pore water pressure can be given by this model approach.

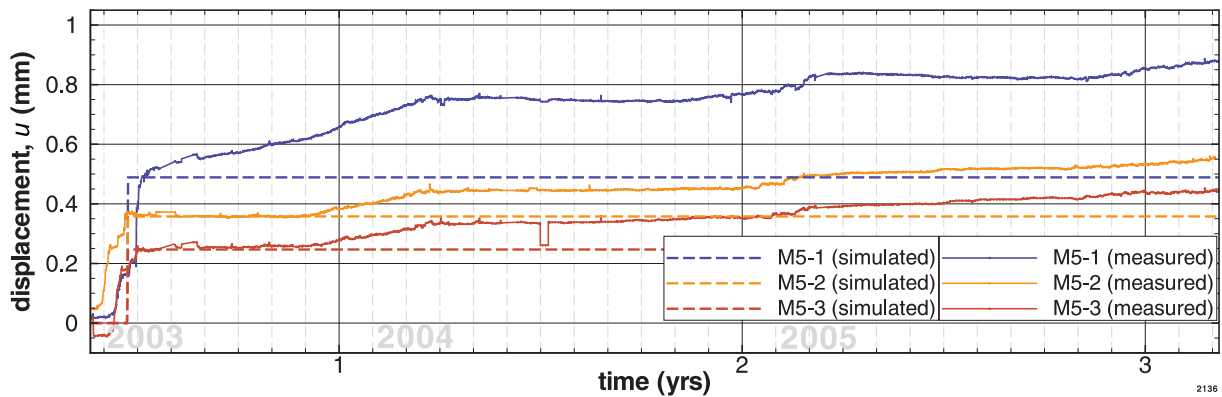


Figure 3.38: Comparison between measured (solid lines) and simulated (dashed lines) displacements in borehole M5. Only the mechanical process is considered using an isotropically linear-elastic model.

Hydraulic-mechanical coupling and anisotropy (saturated conditions)

In a next step, hydraulic-mechanical coupling is investigated under saturated conditions. Here, the hydraulic boundary condition at the opening is set to 0.0 Pa after the excavation. Two cases are mentioned: isotropically mechanical properties and transversely isotropically mechanical properties. With the isotropic setup, only minor changes of the pressures can be simulated, which are not in the order of magnitude of the measurements. The comparison between measured and simulated values for the transversely isotropic case is presented in figure 3.39. In order to reach a better agreement with the measurements, the initial stress has been increased to $\sigma_{\text{init}} = -5.0$ MPa (see section 3.3.4.2) and the permeability reduced to $k = 0.2 \times 10^{-20}$ m² in comparison with the reference values as presented in chapter 1.2.7. Both values are still in the range of measurements. The same value of permeability has been used by Millard and Rejeb (2008) in bedding plane. The change of initial stress influences mainly the mechanical response. Although the pressure increase is still underestimated, the trend can be modeled in principle with the transversely isotropic setup. In comparison with the purely mechanical approach, the mechanical response has changed only slightly. No significant transient behavior can be observed in the simulated displacements.

As an important result of this study, a strong connection between mechanical anisotropy and pressure response has been determined. In order to explain this phenomenon, in figure 3.40 the strains are plotted for two purely mechanical calculations, one with isotropic ($E_x = E_y = E_z$) and one with transversely isotropic stiffness ($E_x = E_y > E_z$). In the anisotropic simulation, the absolute values of volumetric strain next to the opening are substantially higher. This leads to the observed pressure increase in this area. This effect is discussed in detail in chapter 2.2.5.3.

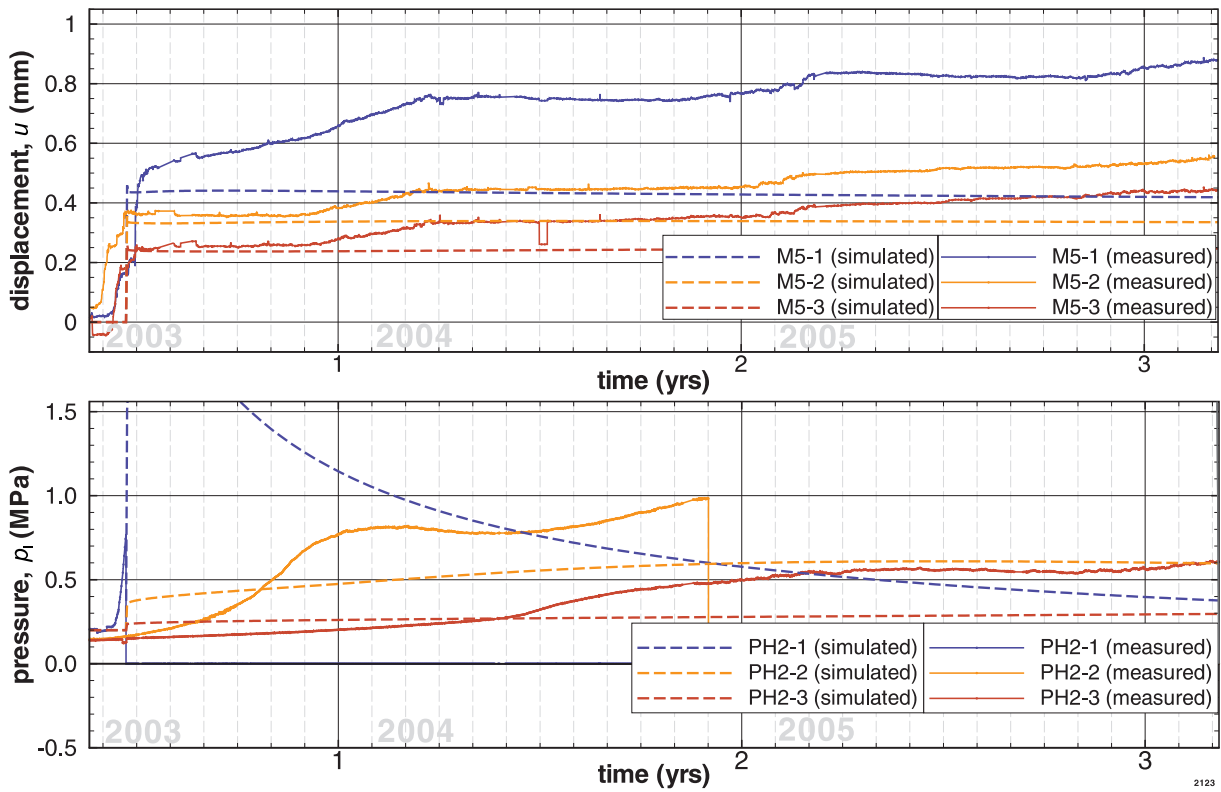


Figure 3.39: Comparison between measured (solid lines) and simulated (dashed lines) displacements in borehole M5 and pore water pressures at borehole PH2. A hydraulic-mechanically coupled model is applied, using a transversely isotropic linear-elastic model under saturated conditions.

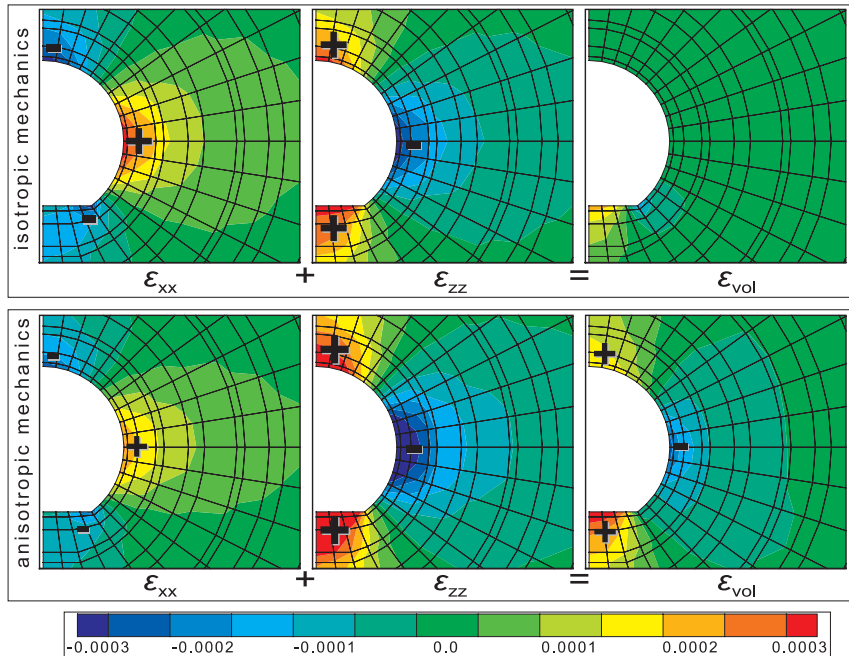


Figure 3.40: Calculated strains in the isotropic (top) and anisotropic (beneath) case. Positive values signify extension.

Considering anisotropic shrinkage

If the claystone is exposed to unsaturated conditions, it shrinks. This behavior is simulated by an shrinkage/swelling model, as presented in chapter 2.3. In figure 3.41 a

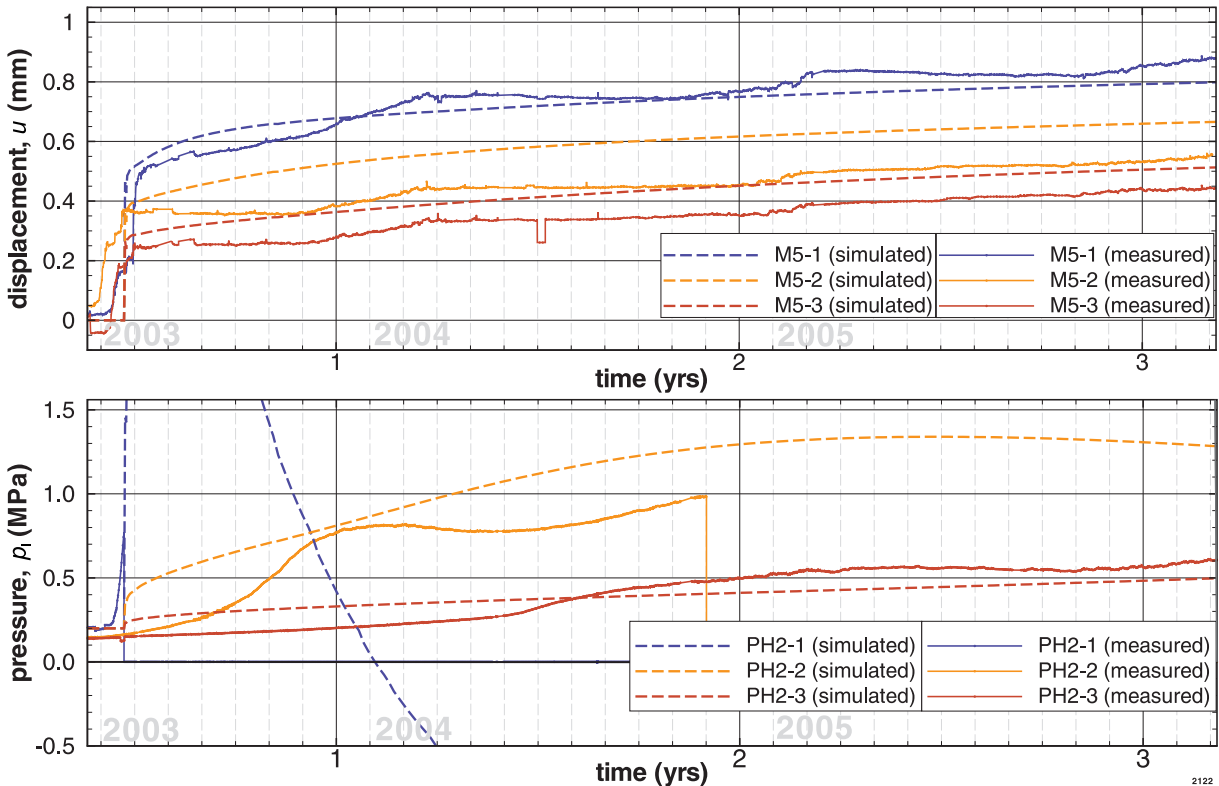


Figure 3.41: Comparison between measured (solid lines) and simulated (dashed lines) displacements in borehole M5 and pore water pressures at borehole PH2. A hydraulic-mechanically coupled model is applied, using a transversely isotropic linear-elastic model under unsaturated conditions, considering transversely isotropic shrinkage.

comparison between measurements and simulations is shown, considering a desaturation of the rock. The desaturation process is initiated by a constant hydraulic boundary condition at the walls of the gallery, which corresponds to the mean value of the measured humidity in the gallery ($h_{\text{rel,mean}} = 75.12\% \xrightarrow{\text{Kelvin}} p_c = 37.53 \text{ MPa} \xrightarrow{\text{van Genuchten}} S = 80.0\%$).

Increasing displacements at all monitoring points can be observed. Even if the transient behavior of the displacements can be modeled by this approach, the displacements at M5-2 and M5-3 are overestimated. Furthermore, the observed seasonal trend cannot be reproduced. Concerning the hydraulic results, the simulated pressures are increased and are more adequate in comparison with the simulation without considering shrinkage. The monitoring point PH-1, which is located close to the gallery, shows negative pressures about seven months after the excavation. This negative pore water pressure signifies unsaturated conditions. Thus, the increasing desaturated zone around the opening has reached the monitoring point PH-1 at this point in time.

Seasonal influence

In order to consider the seasonal change of humidity in the gallery, a transient hydraulic boundary condition is applied at the gallery wall (see figure 3.2 in section 3.2.2). In figure 3.42 the simulation results are depicted in comparison with measurements. The

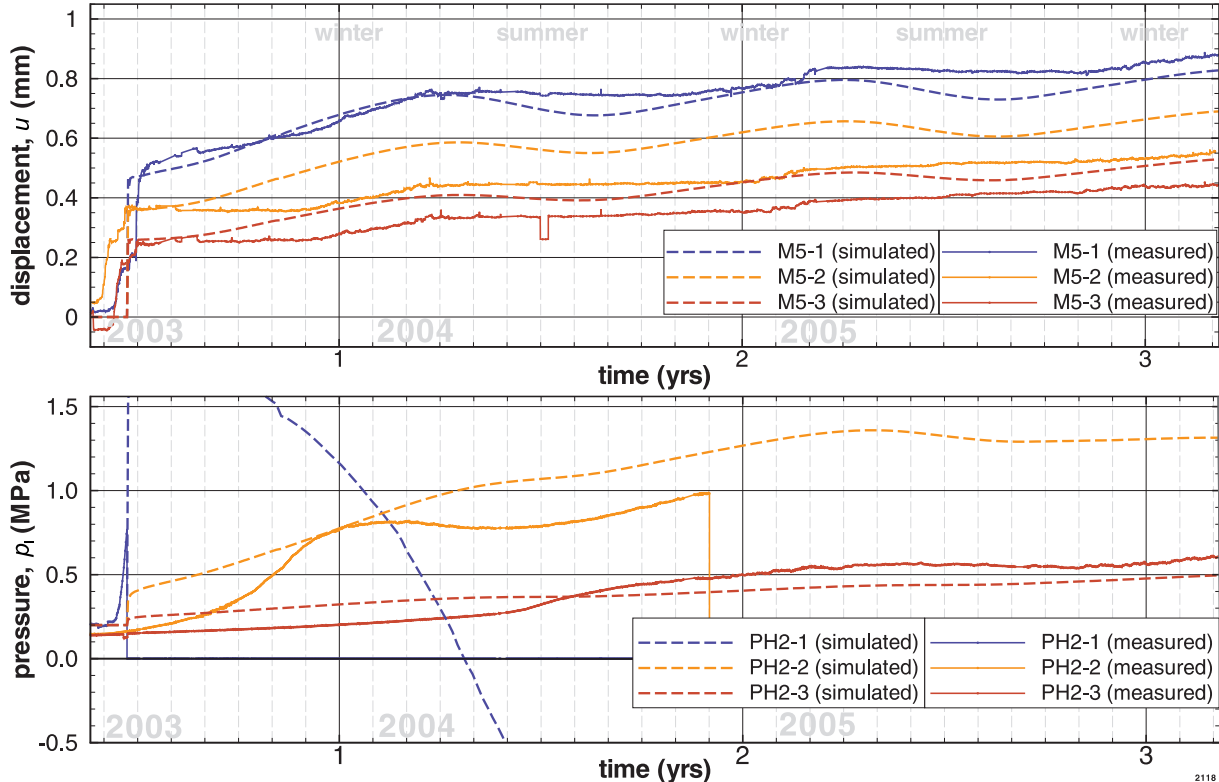


Figure 3.42: Comparison between measured (solid lines) and simulated (dashed lines) displacements in borehole M5 and pore water pressures at borehole PH2. A hydraulic-mechanically coupled model is applied, using a transversely isotropic linear-elastic model, considering transversely isotropic shrinkage and seasonally influenced desaturation.

seasonal fluctuations of the displacements coincide with the measured ones. Thus, the seasonal desaturation process could be an explanation for the measured increase of displacements in the winter months. However, the simulated decrease of displacements in the summer months can be observed in the measurements only marginally.

Concerning the hydraulic part, measurements and simulations indicate a seasonal influence at PH-2.

Considering damage

In a last step, damage is considered additionally. A brittle damage model is applied, as presented in detail in chapter 2.4. The parameters as presented in table 1.2 (p. 11, column “mine-by-test”) have been used. Herewith, the permeability is increased close to the opening. A detailed discussion of the processes in the near field follows in section 3.4. The simulated and measured values are depicted in figure 3.43. The consideration of the

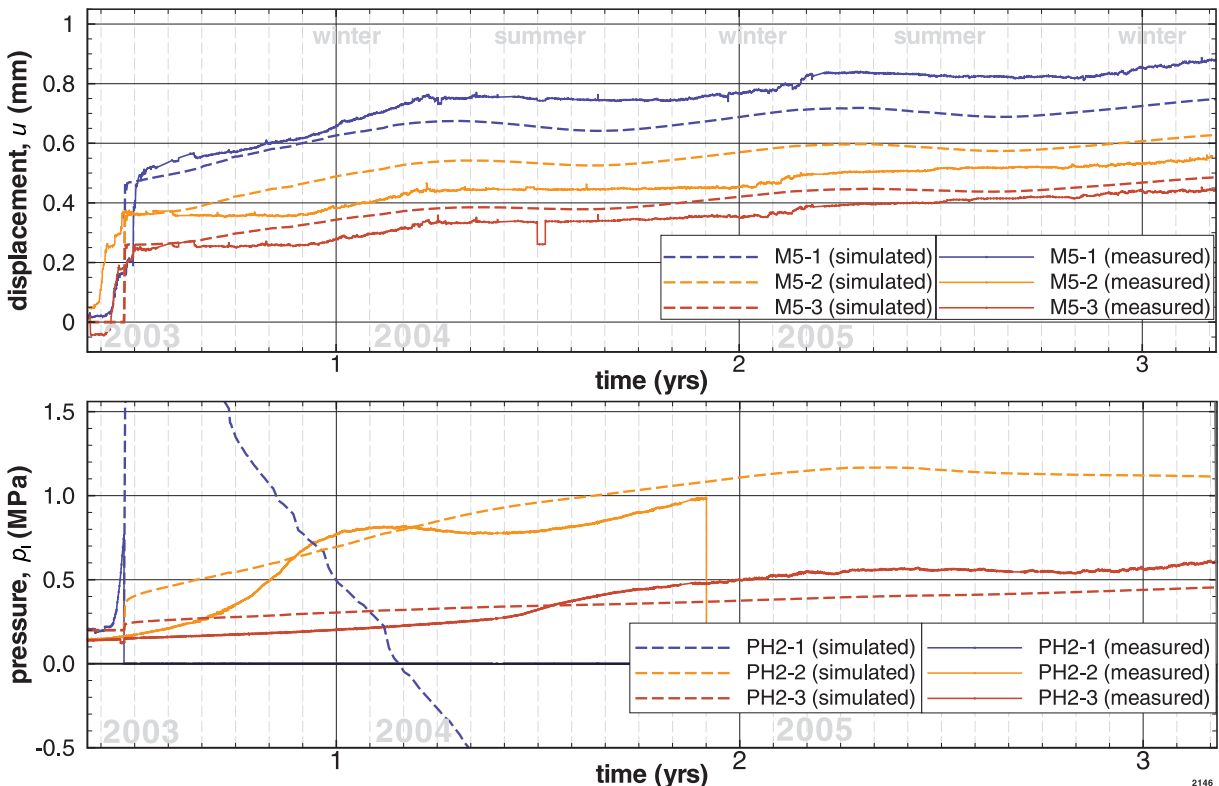


Figure 3.43: Comparison between measured (solid lines) and simulated (dashed lines) displacements in borehole M5 and pore water pressures at borehole PH2. A hydraulic-mechanically coupled model is applied, using a transversely isotropic linear-elastic model, considering damage, transversely isotropic shrinkage, and seasonally influenced desaturation. An initial permeability of $k_{\text{init}} = 0.2 \times 10^{-20} \text{ m}^2$ is used.

damage model has a significant influence on the simulation result. In contrast to the previous simulation (figure 3.42) the decrease of displacements in the summer months is reduced and the main trend of displacement fits better the measurements. Nevertheless, the absolute amount of displacement is overestimated at M5-2 and underestimated at M5-1. The simulated pressures have not changed essentially in comparison to the simulation without considering damage.

Comparative studies have shown that the influence of the microcrack opening-closing mechanism on the results is negligible for this problem.

Impact of permeability. In order to demonstrate the strong influence of the permeability on the simulation results, an additional simulation with the reference permeability ($k_{\text{init}} = 1.0 \times 10^{-20} \text{ m}^2$) instead of the fitted one ($k_{\text{init}} = 0.2 \times 10^{-20} \text{ m}^2$) has been done. All other input parameters remain unchanged. In figure 3.44 the simulation results are plotted.

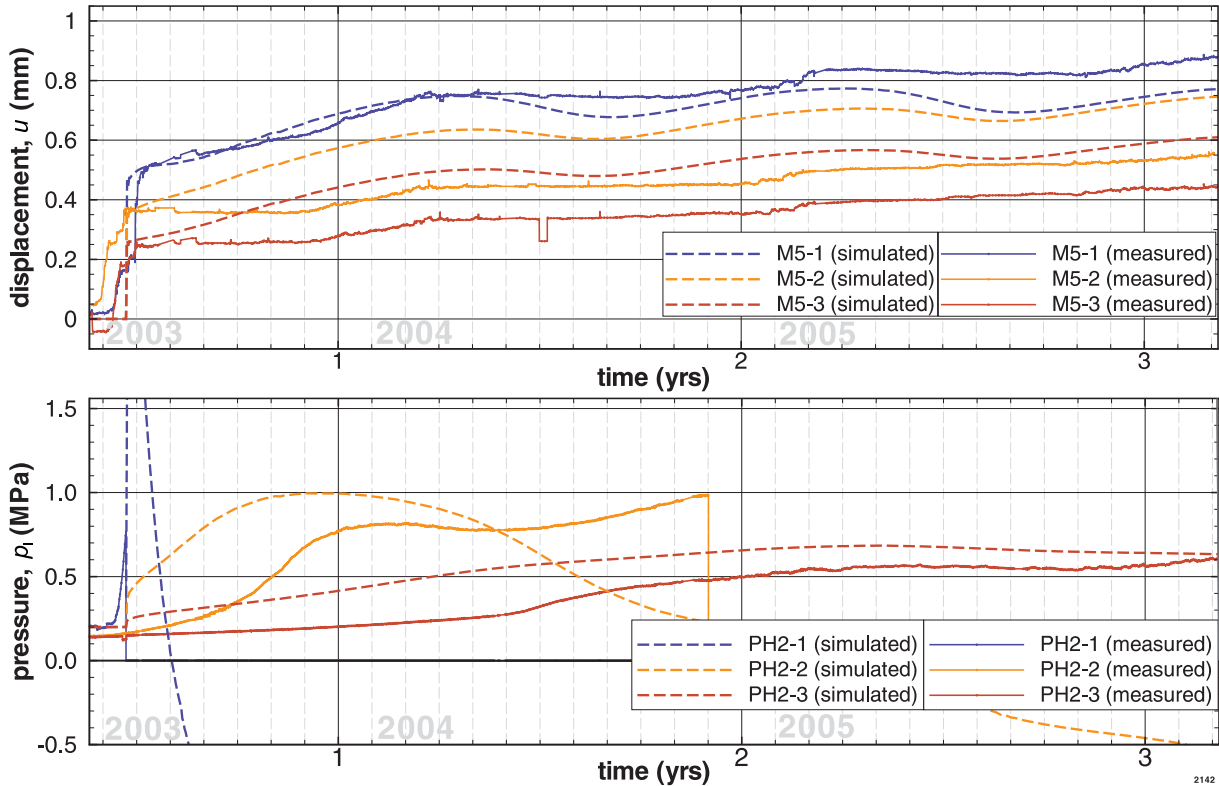


Figure 3.44: Comparison between measured (solid lines) and simulated (dashed lines) displacements in borehole M5 and pore water pressures at borehole PH2. A hydraulic-mechanically coupled model is applied, using a transversely isotropic linear-elastic model, considering damage, transversely isotropic shrinkage, and seasonally influenced desaturation. In contrast to figure 3.43, the reference permeability of $k_{\text{init}} = 1.0 \times 10^{-20} \text{ m}^2$ is used.

Due to the higher permeability, the desaturation process takes place faster and consequently a higher amount of seasonal shrinkage can be observed. Furthermore, the pressure evolution takes place faster, in particular the phase of pressure decrease is reached earlier.

3.3.5 Conclusions

The analysis of the measurements from experiments and in-situ observations shows that the response of the Tournemire argillite to excavation occurs in two phases: First, the main hydraulic-mechanical response is governed by the rearrangement of stresses in the rock mass, inducing linked variations in deformation and pore water pressure. During this phase, neither failure nor damage is observed around the openings. The second phase

begins some time after excavation with the desaturation/resaturation process at the uncovered walls of the openings and an initiation of microcracks.

This general response of the argillite can be simulated well by the applied model: Directly after the excavation, the stress field around the excavation changes, which initiates deformations towards the opening and a pressure increase close to the opening; after approximately three months, the desaturation process, simulated by a seasonally hydraulic boundary condition, dominates the pressure field. Shrinkage and damage is predicted in the near field of the opening.

The quantitative comparison of the measured data from the mine-by-test experiment with the simulations indicates that the developed coupled model can be used to simulate the general behavior of the argillaceous rock due to mechanical excavation. The measured displacements directly after the excavation can be predicted by linear elasticity, using material properties as determined in laboratory. The measured increasing pore water pressure can be simulated with a H-M coupled model considering transversely isotropic linear elasticity.

Seasonal shrinkage could be an explanation for the measured seasonal variation of the displacements. With the transversely isotropic shrinkage parameters, as determined in laboratory, the seasonal influence is overestimated, but in combination with continuum damage mechanics, a good agreement can be reached.

In the long term behavior (3 years), the main trends of the measurements can be predicted. The aberrations could be explained by several reasons. Inhomogeneity may be one reason. The monitoring points are not arranged perpendicular to the gallery axis; thus, the measured displacements are referred to different areas of the rock. Even if the rock was initially homogeneous, the desaturation could induce inhomogeneities due to fracturing. Another reason for the aberrations may be given by additional processes, which are not considered in the applied model. This could be for instance non-linear elasticity, visco-plasticity, material hardening due to desaturation, fatigue due to recurring desaturation/resaturation cycles, and discrete fracture propagation.

In order to reach a better agreement with the measurements, the material parameters have been slightly adjusted in comparison with the reference parameter set (table 1.2, p. 11): The intrinsic permeability has been reduced, the initial stress state increased. All used parameters are in the range of measurements.

A three-dimensional model has been applied to study the unsteady excavation progress. During the excavation phase, this model overestimates the displacements, but directly after the excavation phase, the three-dimensional and the two-dimensional simulations show good agreement with the measurements. Thus, a two-dimensional plane strain, plain flow model seems to be sufficient to model the response of the rock mass after the excavation phase.

The good agreement of the linear mechanical model with the displacement measurements directly after excavation indicates that non-linear material behavior becomes accountable in the long term behavior only.

The simulation results are very sensitive to the used permeability.

3.4 Modeling the excavation disturbed zone

3.4.1 General remarks

In order to evaluate the EDZ, hydraulic-mechanically coupled simulations under plane strain and plane flow conditions have been investigated. The same model setup as described in section 3.3 and the parameters as listed in table 1.2 (p. 11, column “mine-by-test”) have been used. Previous studies concerning the desaturation process (section 3.2) and the mine-by-test (section 3.3) have verified, that this model has the capacity to predict the main trends of the hydraulic and mechanical behavior of the rock due to the excavation.

The state of stresses around the excavated opening will be analyzed to investigate potential failure mechanisms. Therefore, a *Mohr-Coulomb* criterion is used. Furthermore, a continuum damage model is applied. Consequently, this section starts with a description of the *Mohr-Coulomb* criterion and the damage model. After studying the evolution of stresses, permeability, damage, and desaturation a comparison between the model results and observations at the Tournemire site, as done by the *IRSN*, will be presented.

3.4.2 *Mohr-Coulomb* criterion

Extensive experiments have been carried out on the mechanical behavior of the Tournemire argillite. The main mechanisms of failure are the extension and sliding of the bedding planes in the argillite matrix (Niandou et al. 1997). Even if the material shows anisotropic properties, a *Mohr-Coulomb* criterion has been considered in order to investigate the failure mechanism in a first approach. The following values have been determined experimentally by Rejeb and Cabrera (2004): friction angle $\phi = 20^\circ$ and a cohesion c in the range between 6.6 and 10.9 MPa.

An estimation of possible failure for the prediction of the EDZ is performed by evaluating the simulated state of stresses with the *Mohr-Coulomb* criterion.

This criterion is a generalization of the friction failure law, as introduced by *Coulomb* in 1773 (Davis and Selvadurai 2002; Khan and Huang 1995)

$$\tau = c - \sigma_n \tan \phi. \quad (3.3)$$

It describes a linear relationship between the limiting shear stress τ in a plane and the normal stress σ_n on that plane. Reformulation in the terms of principal stresses, by referring to *Mohr*’s circle, yields (Khan and Huang 1995):

$$\hat{\sigma}_1 - \hat{\sigma}_3 = 2c \cos \phi - (\hat{\sigma}_1 + \hat{\sigma}_3) \sin \phi \quad (3.4)$$

with the definition of the principal stresses $\hat{\sigma}_1 \geq \hat{\sigma}_2 \geq \hat{\sigma}_3$ as the eigenvalues of the stress tensor σ . Obviously, the intermediate principal stress is neglected. A yield function f_y describing the failure surface can be defined as follows

$$f_y(\hat{\sigma}_1, \hat{\sigma}_3) = \hat{\sigma}_1 - \hat{\sigma}_3 + (\hat{\sigma}_1 + \hat{\sigma}_3) \sin \phi - 2c \cos \phi. \quad (3.5)$$

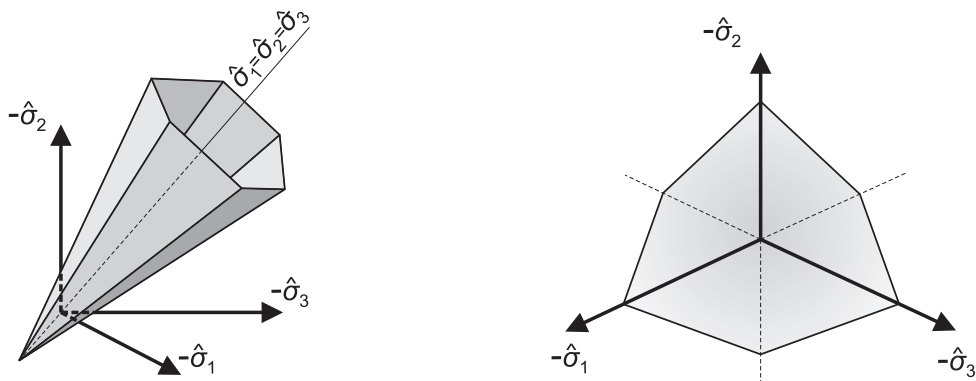


Figure 3.45: *Mohr-Coulomb* yield surface; perspective view in the principal stress space (left) and plot in the π -plane (right).

A graphical representation of the yield surface is given in figure 3.45 as a perspective view in the principal stress space and as a plot in the π -plane, which is perpendicular to the space diagonal ($\hat{\sigma}_1 = \hat{\sigma}_2 = \hat{\sigma}_3$). For all states of stresses, which are within this envelope, the criterion ($f_y < 0$) is hold and no failure is predicted. The size of the shape in the π -plane varies along the space diagonal: The yield surface grows as the mean stress increases, i. e. the *Mohr-Coulomb* criterion is pressure sensitive. In elastic-plastic models, this function is used to distinguish between elastic and plastic material behavior. The validity of the *Mohr-Coulomb* criterion is well established for many soils (Chen and Baladi 1985).

3.4.3 Continuum damage model

Continuum damage mechanics (cf. chapter 2.4) is applied in order to simulate the material degradation in tension. The damage criterion is a function of strain energy, considering tensile strains only. A continuum approach remains valid solely as long as no mesocrack initiation and localization effects, respectively, take place. In the context of the simulation of the shrinkage of the Tournemire clay, the limit of validity is reached, especially directly at the wall of the openings. Here, crack apertures in the order of millimeter are observed, but they are still evenly spread. Due to these cracks, the material loses its integrity locally, which cannot be modeled by the damage model. Nevertheless, CDM has the capacity to simulate the reduced stiffness of the material, which leads to a more realistic prediction of the state of stresses around the excavation. For reasons of numerical stability, a smooth damage evolution function is needed and the state of damage has to be limited. Thus, even in the damaged configuration a residual stiffness could lead to stresses, which exceed the strength of the material.

Unfortunately, measurements on the damage behavior in tension and deformation induced permeability do not exist. A verification of the used parameters has to be done by comparing the simulation results with in-situ measurements and observations. The observations of desaturation fissures at the excavated openings confirm the assumption of an increased permeability in the near field, especially in radial direction. In-situ measurements of per-

meability have indicated that these effects are restricted to a distance of 1 to 2 m around the opening (Rejeb and Cabrera 2006). Matray et al. (2007) pointed out the strong correlation between the EDZ extension and the zone of increased permeability. Furthermore, the observation of fissures in the near field indicates a damage process. Obviously, the shrinkage process leads to tensile stresses exceeding the tensile strength of the material, which is about $R_{\text{ten}} = 3.6$ MPa. The size of this zone is about 0.5 m at the two galleries. A brittle damage model has been applied, as presented in detail in chapter 2.4. A *Marigo* damage evolution model has been chosen (see chapter 2.4.3.4) combined with an equivalent stress definition after Ju (1989) (equation 2.108d). The damage state is described by a scalar damage variable D , microcrack opening-closing mechanism is considered. Furthermore, damage induced permeability is calculated as presented in chapter 2.5.5. Applying the parameters as listed in table 1.2 (column “mine-by-test”, p. 11), the calculated damage state is in a reasonable range, as presented in figure 3.46. The tensional

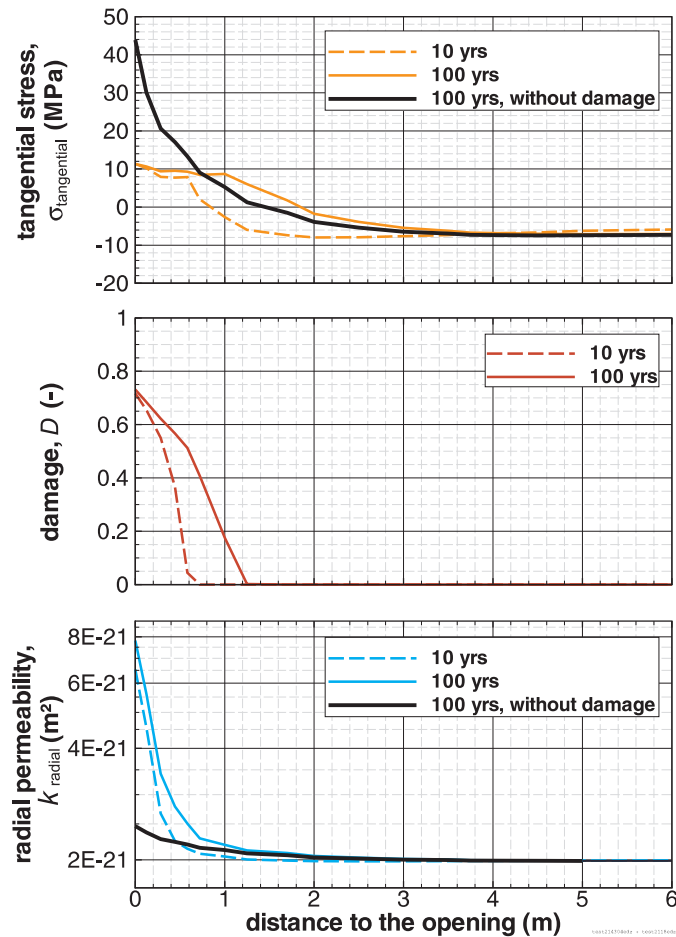


Figure 3.46: Simulated tangential stress, damage state, and radial permeability along a radial line, considering deformation and damage induced permeability.

stresses at the opening are reduced strongly in comparison with the simulation results without considering damage. Indeed, the tensional strength is still exceeded in the tangential direction.

The damage-permeability model leads to a feedback on the damage. Due to the increased permeability, saturation decreases faster and as a consequence shrinkage occurs. This shrinkage effects a higher state of damage. At this point, a weakness of the model approach appears: The increased permeability is caused by the initiation of new fissures but the permeability in the intact areas of the rock matrix remains nearly unchanged. Thus, in reality at least two permeabilities characterize the rock. The desaturation process is governed by both: the permeability due to the fissures and the permeability in the intact matrix. Measurements show an increase of permeability in several orders of magnitudes, but this permeability is highly influenced by preferential flow paths and does not represent a mean permeability, which can be used to calculate the desaturation process with a single permeability model. Consequently, the permeability change in the applied model has to be more moderate than the measured one. In this context, a simulated increase of permeability at the opening by the factor four seems to be meaningful.

3.4.4 Evaluation of stresses

3.4.4.1 The 2003 excavated gallery

In order to analyze potential failure mechanisms around the excavated opening, the evolution of the stress field around the excavation is investigated. Therefore, a H-M coupled model considering shrinkage, damage, strain and damage induced permeability as well as anisotropy is applied. The model setup is presented in detail in section 3.3.3. The principal stresses in the xz -plane are presented in figure 3.47 taking into account the directions and values. Additionally, the extent of the desaturated and damaged zones as well as an evaluation of the *Mohr-Coulomb* criterion are depicted. A cohesion at the lower bound ($c = 6.6$ MPa) of the measurements has been used. Thus, the colored zone illustrates the maximum extent of the zone, where the *Mohr-Coulomb* criterion predicts a failure ($f_y > 0.0$). The different colors depict the value of the yield function f_y and illustrate, how far the calculated stresses are off the yield surface. This is a post-processing analysis of the damage effective stresses $\bar{\sigma}$ (cf. chapter 2.4.2.3), no plasticity is considered.

Directly after excavating the gallery, neither the damage model nor the *Mohr-Coulomb* criterion predict any non-linear mechanical behavior. The measured rock strength is not exceeded. This finding is in accordance with in-situ observations (cf. chapter 1.2.6) and simulation results, which can be found in literature (Millard et al. 2008; Rejeb et al. 2006; Rouabhi et al. 2005). Millard et al. (2008) have shown, that even by the use of damage, viscosity or anisotropic plasticity directly after the excavation no failure can be predicted. A few months after the excavation, the desaturation process becomes important. It leads to shrinkage and thus tensile stresses occur, which exceed the tensile strength of the material. The damage criterion and the *Mohr-Coulomb* criterion predict material failure. An area of tensile stresses is formed around the opening. In the wet summer the amount of tensile stresses decreases distinctly at the wall of the opening and low compressive stresses are predicted at the bottom. The observation of just partly existent low compressive stresses could explain the negligible influence of the crack opening-closing mechanism on the simulation results (cf. section 3.3.4.5). The principal stresses around the opening are oriented tangentially.

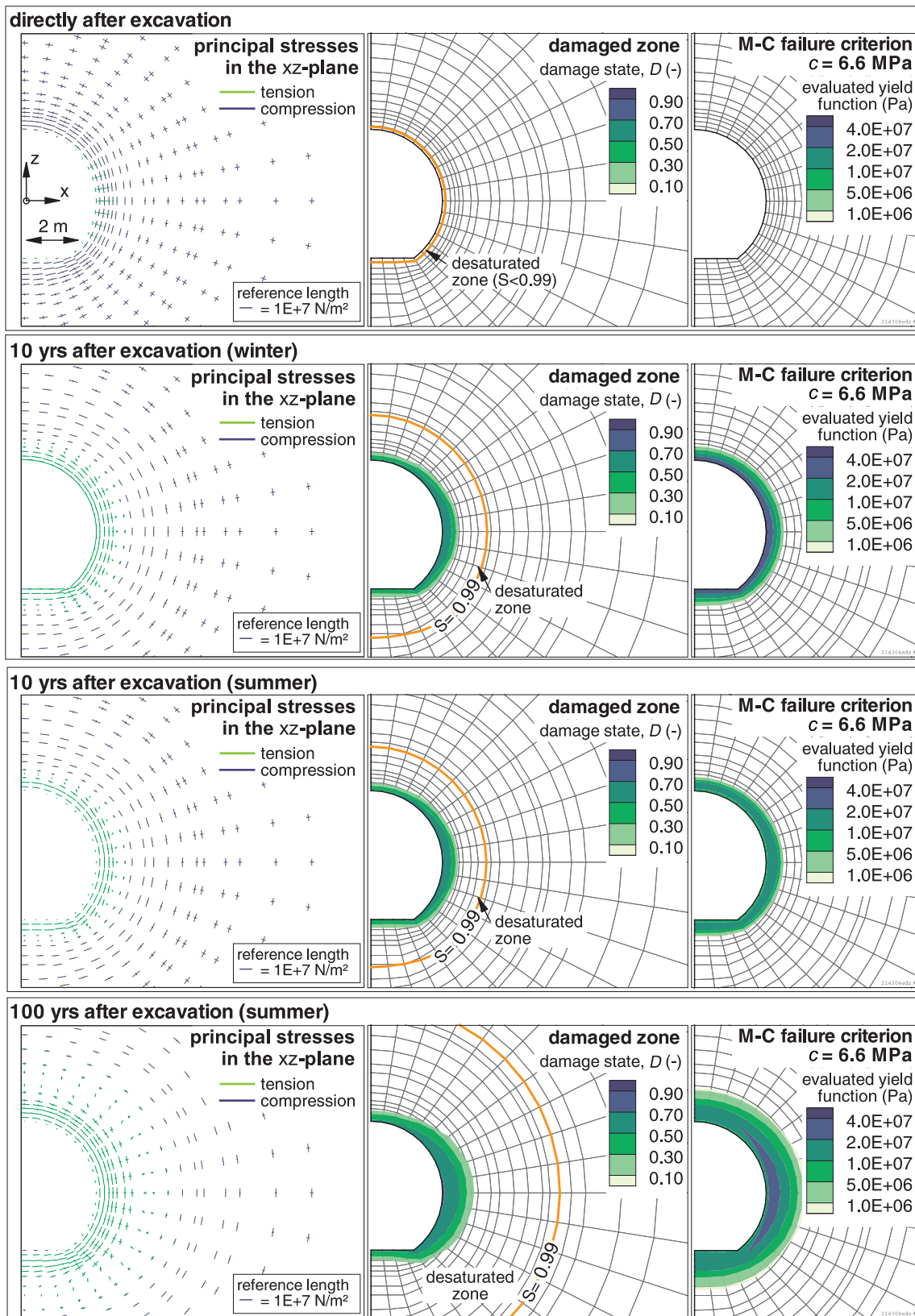


Figure 3.47: Evolution of the excavation induced stresses in the near field of the 2003 excavated gallery (left), damaged and desaturated zones (center), evaluation of the *Mohr-Coulomb* criterion (right).

Regarding the stress field around the excavation two types of disturbances can be distinguished: (1) a zone of increased tangential compressive stresses, due to a rearrangement of the initial stresses; (2) a zone of tangentially oriented tensile stresses, due to shrinkage. Both show a nearly circular shape. The first one moves with time from the opening into the rock and increases. The second one occurs a few months after excavation directly at the opening and increases slightly. In between these two zones, low amounts of stresses are present. Only in this small transition area radially oriented tensile stresses are predicted, partly in combination with tangentially oriented compressive stresses.

After 100 years of simulation time the damaged zone has a higher extent in horizontal than in vertical direction. The zone, where the *Mohr-Coulomb* criterion is exceeded, also shows this anisotropic shape, but less marked. This effect is caused by the anisotropic shrinkage and the consequential higher horizontal permeability.

In Figure 3.48 an evolution of the principal stresses at three points is depicted. Figure 3.49 shows the same, but no damage is considered here. Directly after the excavation, at all

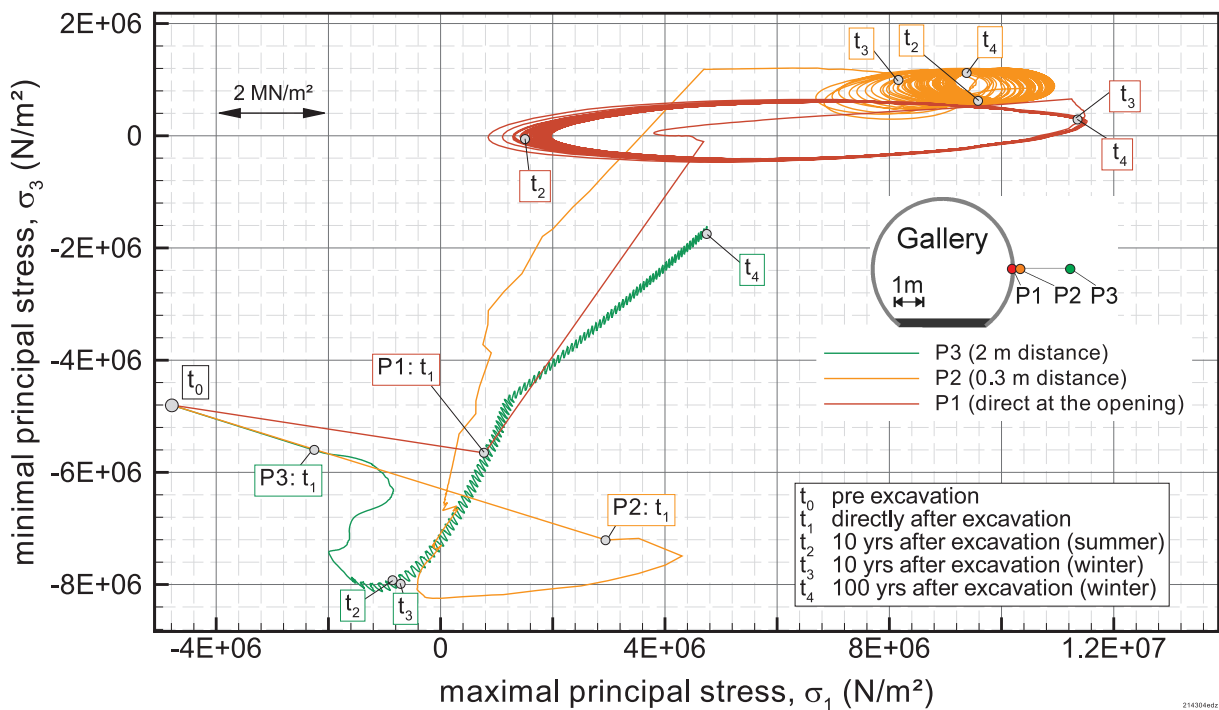


Figure 3.48: Simulated evolution of the principal stresses at three points during a time period of 100 years, considering damage.

points an increase of one principal stress can be observed: The rearrangement of stresses leads to an increase of compressive stresses. At the points P1 and P2 shortly after the excavation the state of stresses is dominated by the cyclic swelling-shrinkage process. Only directly at the opening (P1), compressive stresses are predicted in summer. These compressive stresses are oriented radially. Further away from the excavation (P3), the seasonal process becomes less important. It takes about 20 years until tensional stresses are predicted at P3. At this point in time, the compressive stresses are still increased in comparison with the initial stress.

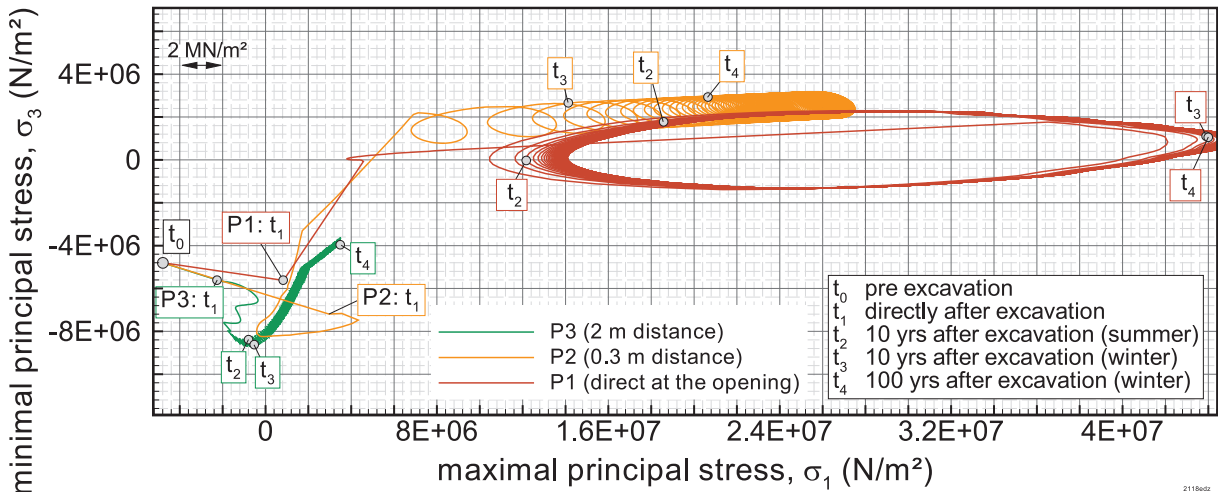


Figure 3.49: Simulated evolution of the principal stresses at three points during a time period of 100 years, considering no damage.

The damage process initiates some kinks in the temporal evolution of the stresses, which can be explained by the exceeding of the damage threshold in some elements. In contrast to the simulation without considering damage, the stresses are lower, due to the degradation of the mechanical stiffness. The damage model reduces the maximal tensional stresses directly at the opening by the factor four.

The compressive strength of the material ($R_{\text{comp}} = 13. \dots 32. \times 10^6 \text{ N/m}^2$) is never exceeded at any point. The tensional strength ($R_{\text{ten}} \approx 3.6 \times 10^6 \text{ N/m}^2$) is exceeded at the points P1 and P2, which are located close to the excavation.

3.4.4.2 The 1996 excavated gallery

Figure 3.50 shows the simulated stress evolution around the 1996 excavated gallery. The

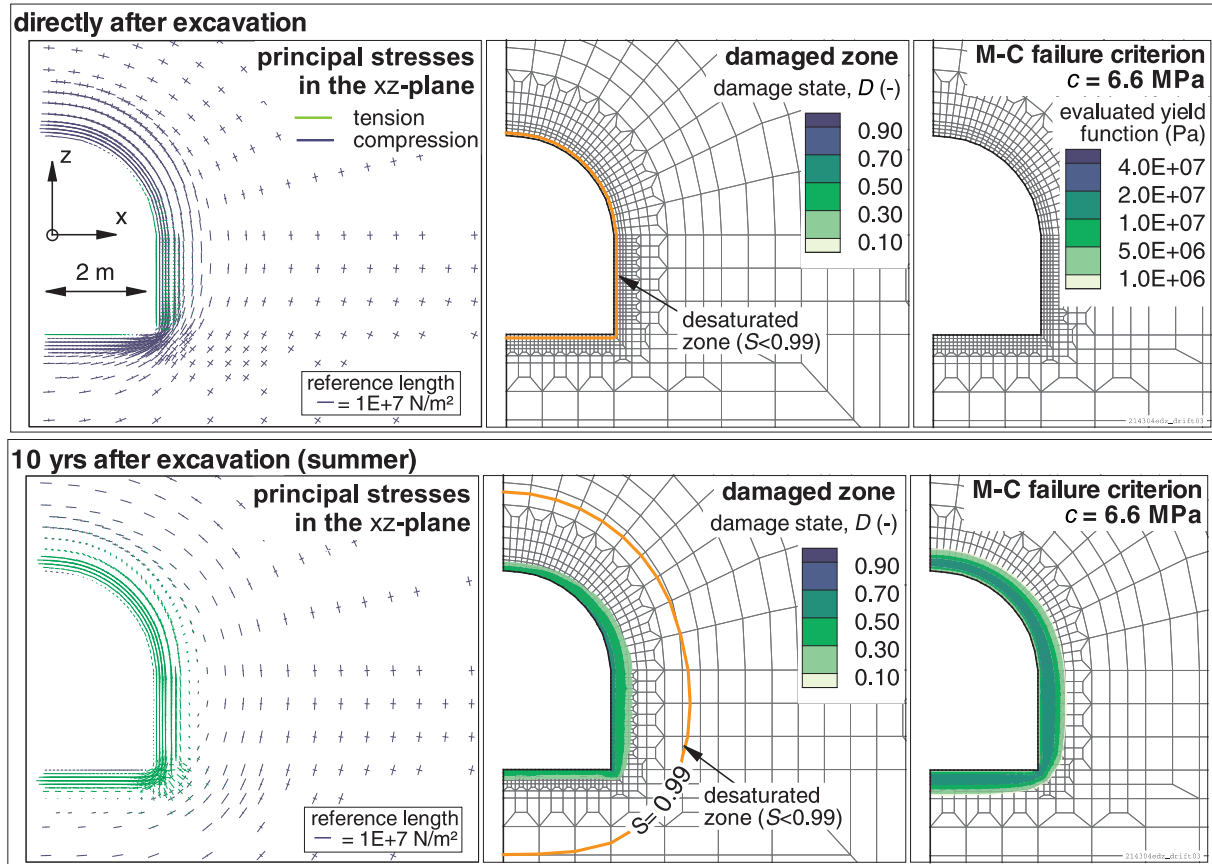


Figure 3.50: Evolution of the excavation induced stresses in the near field of the 1996 excavated gallery (left), damaged and desaturated zone (center), as well as evaluation of the Mohr-Coulomb criterion (right).

same model setup as for the previous simulation has been applied, except for the geometry. Basically, the same evolution as depicted in figure 3.47 can be observed: no exceeding of the rock strength directly after the excavation and a failure mechanism due to shrinkage three months after excavation. Small compressive stresses are predicted at the top and the bottom of the opening in the summer, when a resaturation takes place. In the corner of the opening, at a distance of approximately 10 cm, radially oriented tensile stresses and tangentially oriented compressive stresses are predicted.

3.4.4.3 The 1881 excavated tunnel

Figure 3.51 shows the simulated stress evolution around the old tunnel. The same model

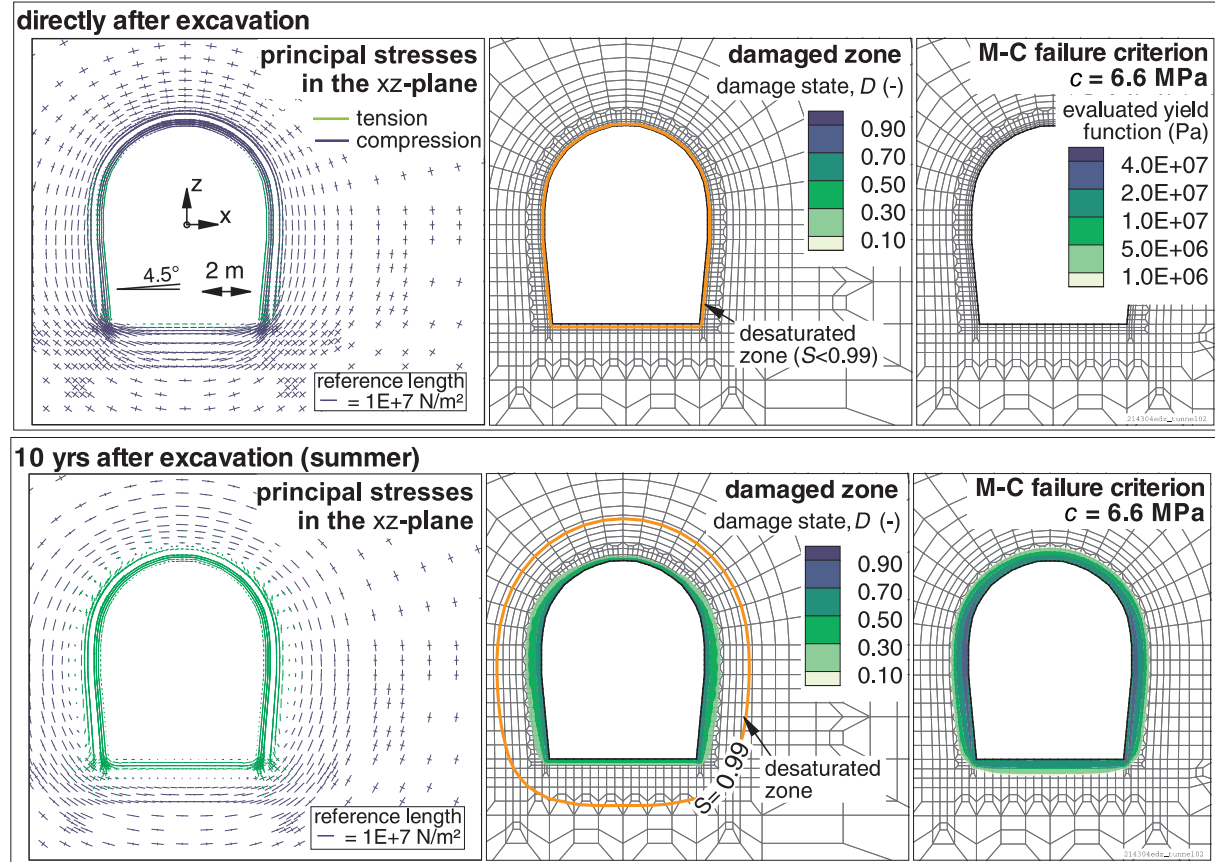


Figure 3.51: Evolution of the excavation induced stresses in the near field of the old tunnel (left), damaged and desaturated zone (center), evaluation of the *Mohr-Coulomb* criterion (right).

setup as for the previous simulation has been applied, except for the geometry. The plane of isotropy has been defined with respect to the bedding plane, which is oriented 4.5° subhorizontal. Thus, the problem is not any longer symmetric with respect to the yz -plane and the whole system has to be modeled.

Again, the same behavior as depicted in figure 3.47 can be observed. The stress distribution at the corner of the opening is similar to the 1996 excavated gallery.

With the exception of the stress distribution at the sharp corner, the influence of the shape seems to be of secondary importance.

3.4.5 Evaluation of permeability

The strain based permeability model with consideration of the state of damage (cf. chapter 2.5) has been used. In figure 3.52 the permeability tensor is figured with its principal

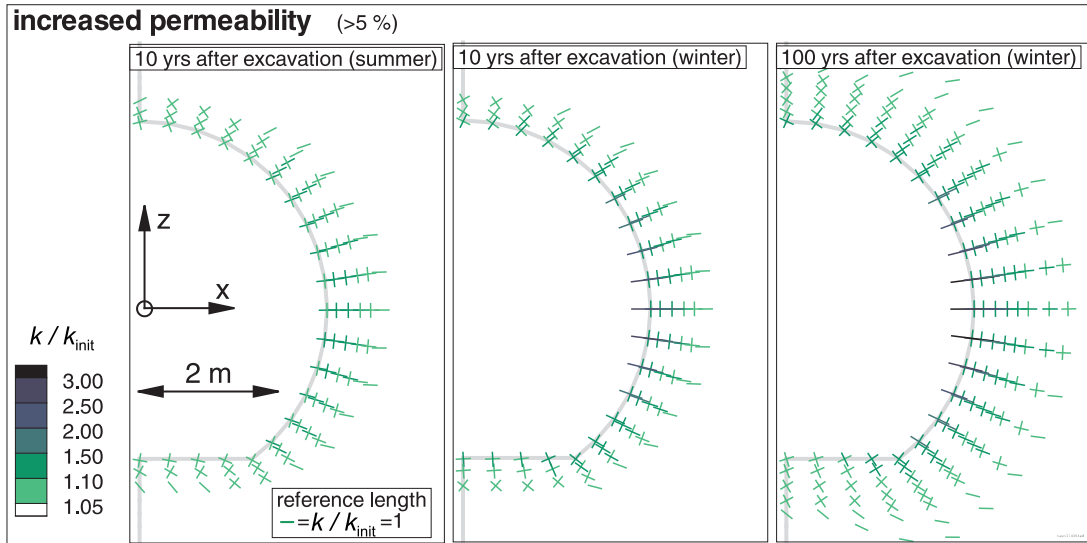


Figure 3.52: Simulated changes of permeability around the 2003 excavated gallery. The principal directions of the permeability tensor \mathbf{k} are plotted, if the corresponding eigenvalue is increased more than 5 % compared to the initial value.

directions and the corresponding minimal and maximal permeabilities. Only the area where the permeability is increased more than 5 % is considered. This area enlarges slightly with time. An anisotropic change of permeability is predicted. The highest permeability can be observed in radial direction, at the side of the opening in winter time. In this region, the permeability depends stronger on the season, than on time. Furthermore, here the highest amount of anisotropy can be noted. This phenomenon is caused by the anisotropic shrinkage. Only in this region, the highest amount of shrinkage strain is directed parallel to the surface of the opening.

3.4.6 Comparison with observations and discussion of potential failure mechanisms

Several excavation induced processes have been mentioned so far. They act on different scales of time and space. For a general classification and in order to compare the simulated magnitudes with the observed ones, in figure 3.53 a comprehensive view of some selected quantities is given. Each calculated criterion is plotted at three points in time. These times correspond approximately to the age of the three openings, when the in-situ investigations have been carried out. This plot can be understood as a summary of the foregoing analysis. The simulated extents are deduced from modeling the 2003 gallery (section 3.4.4.1). The simulation predicts an EDZ, which is characterized by tension induced damage and an increased permeability. Its extent increases slowly with time and equals approximately the observed one. The simulated strong anisotropic shape of the damaged zone is not coherent

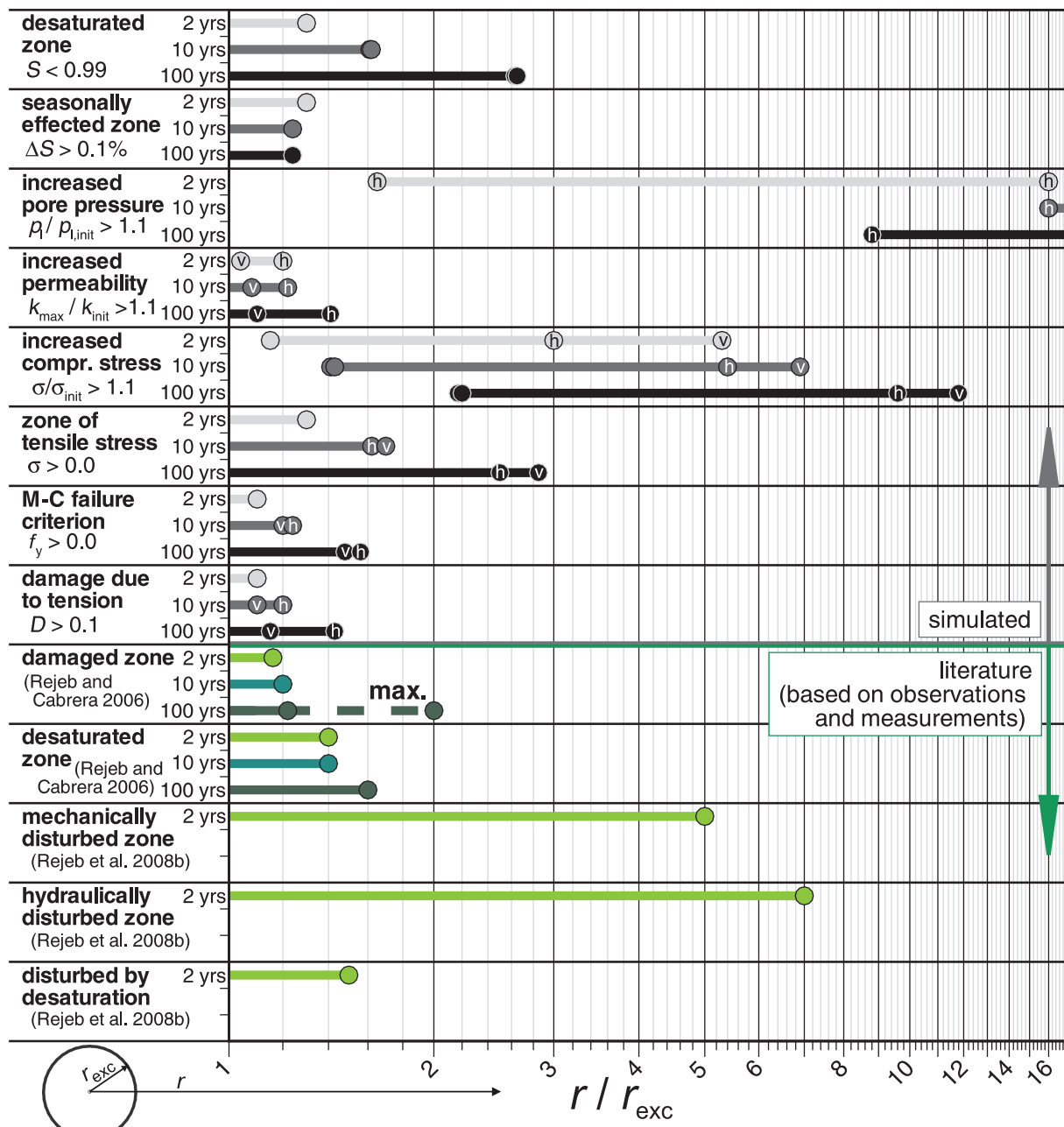


Figure 3.53: Excavation disturbed zones, simulations, and observations. The zones have been evaluated 2, 10 and 100 years after the excavation. The literature values correspond to the 2003 excavated gallery (2 yrs.), the 1996 excavated gallery (10 yrs.) and the old tunnel (100 yrs.). Some simulated quantities show an anisotropic behavior; consequently, v and h denotes the corresponding value in vertical and horizontal direction, respectively.

to the *Mohr-Coulomb* failure criterion and is also not observed. The interaction between anisotropic shrinkage, permeability and damage could lead to this overestimation. The simulated and observed size of the desaturated zone is also similar, solely the simulated extent after 100 years seems to be overestimated. The extent of the mechanically disturbed zone, as postulated by Rejeb and Cabrera (2006), accords well with the zone of increased compressive stresses.

It is interesting to observe that the expansion of the tensile zone leads to a shift and an increase of the zone of increased compressive stresses. There exists a transition zone, where both tension and compression take place.

In order to enable a comparison of the EDZ around the three openings, Rejeb and Cabrera (2006) describe the disturbed/damaged zones in dependency on the mean radius of the corresponding opening, as plotted in figure 3.53. Since not all processes are known and have to depend linearly on the radius of the opening, this illustration is connected with some uncertainties. As a consequence, in the following the simulation results will be directly compared with the observations. As a last plot, in figure 3.54 a comparison of

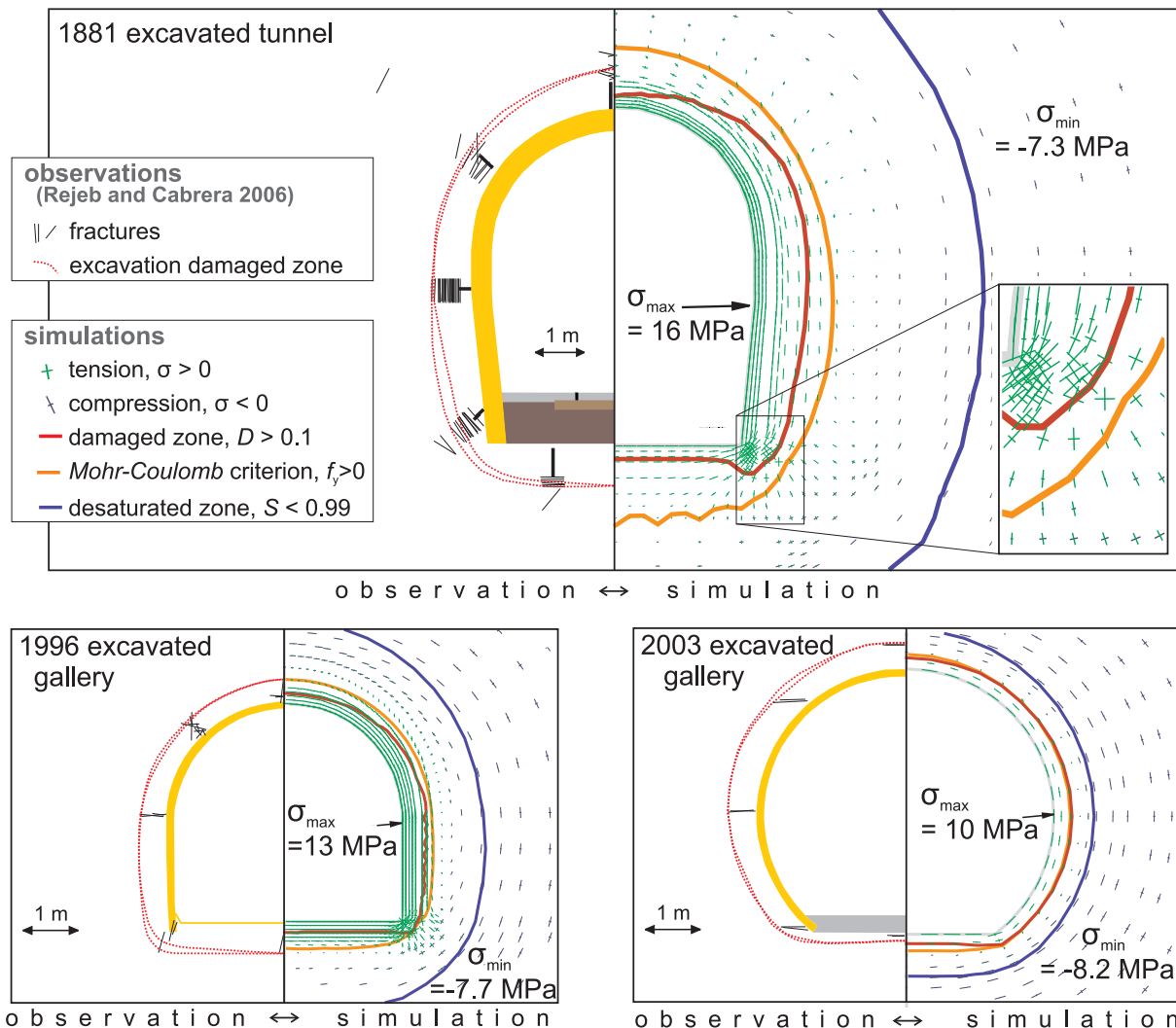


Figure 3.54: Comparison of the observed fractured zones (Rejeb and Cabrera 2006) with simulation results (cf. chapter 1.2.6). The simulated time corresponds to the time period between excavation and core drilling at each opening (tunnel: 124 years; 1996 gallery: 9 years; 2003 gallery: 1.5 years). Since the measurements are approximately isotropic, the right hand side has been flipped horizontal.

the observed fractured zone (Rejeb and Cabrera 2006) with simulation results is depicted. The observed fractures are in the same region, where the *Mohr-Coulomb* criterion predicts a failure. The simulated damaged zone is smaller and characterized by anisotropy.

Attention has to be paid on the direction of fracturing and the simulated stresses. All observed radial oriented fractures can be explained by the shrinkage process. The tensional strength of the material is largely exceeded, as described priorly in detail in section 3.4.4. The maximal tensional stresses are tangentially oriented and the classical tensional crack (mode 1, cf. chapter 2.4.3.7) is oriented perpendicular to it, consequently radially.

Another mechanism seems to take place around the century old tunnel, where tangentially oriented fractures have been observed. The evaluation of stresses indicates only two potential zones: one is located at the sharp edges, but this zone is small and cannot explain a failure around the whole excavation. The other one is the transition area, located at the desaturation front. Here, compressive stresses are increased in comparison with the initial state and additionally, the shrinkage induces small tensional stress. In this area a potential failure mechanism is governed by compression and could lead to tangential cracks. However, the simulated stresses in this zone are still within the *Mohr-Coulomb* yield surface and a degradation of strength seems to be improbable, since the saturation is decreased only sparsely and no seasonally effects take place.

Thus, another mechanism, which has not been mentioned so far, could proceed and may influences the long term behavior. A determination is difficult, because information about the long term behavior of the Tournemire argillite are scarce. Nevertheless, one presumption will be mentioned:

The desaturation of the argillite could lead to a total loss of integrity. The recurring shrinkage and swelling may intensify this process. Thus, small loads could cause material failure and fracturing. Even the dead load could be strong enough for it.

In this case, tangential fracturing is explainable, since the only possible stress free direction of motion is directed towards the opening. Observations of spalling at the walls of the uncovered galleries (figure 3.55) and the slight degradation of an uncovered rock sample, lying for years in a niche of the old tunnel (figure 3.56), could confirm this presumption.



Figure 3.55: Spalling at the wall of the gallery. The darker area signifies the rock surface with higher water content, which has been exposed to the atmosphere quite recently.



Figure 3.56: Disintegrating rock sample. This rock with an extent of approximately 1.5 m is located uncovered since over ten years in a niche of the old tunnel.

3.4.7 Conclusions

As mentioned before (cf. section 3.3.5), the hydraulic and mechanical response of the rock mass to the excavation process can be distinguished in two phases.

Directly after the excavation, the mechanical process is dominant. The rearrangement of stresses leads in general to an increase of the compressive stresses around the opening. During this phase, the stress field around the opening is mainly influenced by the initial stress, the geometry of the opening, and the mechanical material properties. The numerical model predicts no damage and the evaluation of the *Mohr-Coulomb* criterion indicates no failure at any opening. This simulation result is coherent with in-situ observations and other studies as can be found in literature.

In the second phase, the hydraulic process becomes dominant. The desaturation process causes material shrinkage and subsequently contraction. Tensile stresses initiate damage and an anisotropic increased permeability. The evaluation of the *Mohr-Coulomb* criterion indicates almost equidistant failure zones around each opening, which measure nearly the same as the fractured zones, observed in-situ. Thus, the radially oriented tensile cracks at the openings can be well predicted with the used model.

Around the century old tunnel, observations suggest the assumption of a second failure mechanism, which is not predicted by the model. An explanation of the observed tangentially oriented fractures could be given by the presumption of a loss of integrity in the long term as a consequence of the desaturation induced shrinkage. This process is not proved so far.

All in all, the shrinkage seems to be the governing process for the development of the EDZ and consequently coupled modeling is indispensable.

Chapter 4

Summary and conclusions

4.1 Summary

This thesis is focused on the development of numerical methods and their application to modeling clay materials. The study has been motivated by the international discussion on the adequacy of claystone as a potential host rock for a final repository of radioactive waste. The involved processes, which could impact the safety of such a repository, are manifold and strongly interacting. Coupled modeling can support the performance assessment. The processes under consideration are from different disciplines, mainly solid mechanics and fluid mechanics, as applied to geological problems.

The investigation can be divided into three main parts: At first, the modeling approach is presented (chapter 1). Subsequently, the developed methods are discussed in detail (chapter 2). In the third part, these methods are applied to a case study for which field data are available, namely the Tournemire underground laboratory of the *IRSN* (chapter 3).

The modeling approach. In the first part, the concept for the numerical model is developed. It is founded on observations and measurements at three openings at the argillaceous Tournemire site (a century old tunnel and two galleries, excavated in 1996 and 2003). The delayed failure mechanism around the excavations and the seasonally influenced fracture apertures are of particular interest. Two main processes constitute the basis of the applied model: deformation (mechanics) and fluid flow (hydraulics). The mechanical problem is stated as an elastic-damage model, the hydraulic problem as a *Darcy* type flow, considering unsaturated conditions by the *Richards'* approximation. Several coupling phenomena are taken into account: *Terzaghi*'s effective stress concept, mass conservation of the liquid in deformable porous media, drying induced shrinkage, and a deformation and damage dependent permeability. Additionally, transverse isotropy is considered in the material properties of elasticity, shrinkage/swelling, and fluid flow.

The methods. The second part focuses on those methods, which are investigated, newly developed, implemented into the finite element code *RockFlow*, and tested. The theory of porous media including balance equations of mass, energy and linear momentum are the foundation. Applications demonstrate the capacity of the models and their impact within simulations of excavation processes.

Anisotropy is investigated in the framework of hydraulic-mechanical coupling. Systematically selected numerical examples verify the implementation. A more detailed application to an excavation problem demonstrates the strong impact of anisotropy on the results and emphasizes its importance.

The developed strain based shrinkage model allows the modeling of transversely isotropic shrinkage/swelling behavior. A power-law is used to calculate the shrinkage strain by the saturation of the liquid phase. Herewith, a good agreement to laboratory tests and in-situ observations can be reached.

Based on a literature review, a continuum damage model is implemented and adapted to the hydraulic-mechanically coupled problem. For the sake of simplicity, an isotropic approach is chosen. Different material behaviors in tension and compression as well as the crack opening-closing mechanism are considered. A numerical application proves the potential of the model to predict shrinkage induced damage.

The permeability of the host rock is a key issue for the safety assessment of a repository.

Thus, the analysis of processes, which could have an impact on the rock permeability, is one focal point of the present study. Based on a tensorial description of the pore space and simple flow models, an orthotropic permeability model is developed. Hereby, the strains and optionally the state of damage are considered. A quantitative comparison with results from literature confirms the accuracy of the formulation and implementation.

The case study. In the third and last part of this work, the newly developed model is applied to study three issues related to the excavations at the Tournemire site: the desaturation process, the mine-by-test experiment, and the excavation disturbed zone.

The contact of the claystone with ambient air creates a desaturated area of nearly circular shape around each excavation. The modeling work brings out a distinction of two zones: The first zone near the opening (1 – 2 m) is characterized by a seasonally affected saturation. In the second zone the saturation is decreased, but changes take place more slowly. The size of both zones strongly depends on the material properties. The most significant parameters are the intrinsic permeability and the relative permeability.

When applying permeabilities within a range of three orders of magnitude, the wide spread of measured saturations can be covered by the simulations. A visualization of the measured saturation profiles, considering the direction of drilling, does not show an anisotropic tendency. Further model simplifications are possible, if only an estimation of the desaturated zone is of interest: A one-dimensional hydraulic model, without consideration of any seasonal effect, should be sufficient.

The mine-by-test was carried out by the *IRSN*, in order to study excavation induced processes. A comparison between measured and simulated displacements and pore water pressures proves the capacity of the model to predict the response of the rock. Two temporal phases can be distinguished: In the first one, the mechanical process is dominant. The rearrangement of stresses leads to displacements towards the opening. This causes an increase in the pore water pressure next to the opening. A few months after the excavation, the second phase begins: The hydraulic process becomes dominant. The seasonal desaturation causes seasonally influenced displacements and decreasing pore water pressures.

These two phases can be simulated well with the developed two-dimensional model, applying material properties as determined in laboratory.

In order to evaluate the state of stresses in the excavation disturbed zone, the *Mohr-Coulomb* criterion is applied as post-processing failure analysis. Herewith, an excavation damaged zone around the three openings is predicted solely in the second phase, when the desaturation process takes place. This result is coherent with the observed delayed failure mechanism. The extent and shape of the simulated failure zones are similar to the observed fractured zones. In measurements and simulations these zones are characterized by an increased permeability. The continuum damage model is applied to simulate the material degradation in this zone.

An analyses of the simulated stress field yields radial desaturation cracks, which are also observed in-situ. The tangentially oriented cracks at the century old tunnel cannot be predicted with the developed model and the material properties from laboratory. Here, a secondary failure mechanism seems to take place, which could possibly be a further degradation of material strength, caused by the desaturation.

4.2 Conclusions

The developed methods presented in this thesis are a necessary advancement of the coupled hydraulic-mechanical modeling considering damage caused by desaturation. With their implementation into the computer code *RockFlow* new possibilities of analysis and prediction have been provided. In particular, the main trends of the excavation induced hydraulic and mechanical response of argillite can be modeled.

The delayed development of an excavation damaged zone can be predicted correctly for a time period of at least ten years. Even for longer periods, a good estimation of the EDZ can be given, though not all observed failure mechanisms are understood so far.

Further investigations on the long term material behavior, especially under unsaturated conditions, are needed in order to improve the understanding and in consequence the further numerical modeling. Of special interest are the coupling between shrinkage, damage and permeability, considering transverse isotropy.

In the context of the performance assessment of a repository in argillite a number of lessons have been learned. The most important one is, that it is not sufficient to consider the mechanical properties on its own, since the key process for the long term behavior is a hydraulic one: the dehydration.

Bibliography

M. Bai and D. Elsworth. Modeling of subsidence and stress-dependent hydraulic conductivity for intact and fractured porous media. *Rock Mechanics and Rock Engineering*, 27(4):209–234, 1994.

M. Bai, F. Meng, D. Elsworth, and J.-C. Roegiers. Analysis of stress-dependent permeability in nonorthogonal flow and deformation fields. *Rock Mechanics and Rock Engineering*, 32(3):195–219, 1999.

J. Barescut and J. Michelot. Constraints on transport in the Tournemire clay site. *Journal of Contaminant Hydrology*, 26:71–79, 1997.

C. Barlag. *Adaptive Methoden zur Modellierung von Stofftransport im Kluftgestein*. PhD thesis, Institut für Strömungsmechanik und Elektronisches Rechnen im Bauwesen, Universität Hannover, report no. 52, 1997.

Z. P. Bazant, editor. *Mathematical Modelling of Creep and Shrinkage of Concrete*. John Wiley & Sons, 1989.

J. Bear. *Dynamic of Fluids in Porous Media*. Elsevier, New York, 1972.

J. Bear and Bachmat. *Introduction to Modeling of Transport Phenomena in Porous Media*. Kluwer Academic Publishers, Dordrecht, 1990.

F. Benboudjema, F. Meftah, and J. M. Torrenti. Interaction between drying, shrinkage, creep and cracking phenomena in concrete. *Journal of Engineering Structures*, 27: 239–250, 2005.

D. G. Bennett and R. Gens. Overview of european concepts for high-level waste and spent fuel disposal with special reference waste container corrosion. *Journal of Nuclear Materials*, 379:1–8, 2008.

Y. Bernabé, U. Mok, and B. Evans. Permeability-porosity relationships in rocks subjected to various evolution processes. *Pure and Applied Geophysics*, 160:937–960, 2003.

BfS. Endlagerung radioaktiver Abfälle als nationale Aufgabe. Technical report, Bundesamt für Strahlenschutz, Salzgitter, Germany, 2005.

BfS. Jahresbericht 2006. Technical report, Bundesamt für Strahlenschutz, Salzgitter, Germany, 2007.

BGR. Endlagerung radioaktiver Abfälle in Deutschland. Untersuchung und Bewertung von Regionen mit potenziell geeigneten Wirtsgesteinsformationen. Technical report, Federal Institute for Geosciences and Natural Resources (BGR), April 2007a.

BGR. Tätigkeitsbericht 2005/2006. Technical report, Federal Institute for Geosciences and Natural Resources (BGR), May 2007b.

BGR. 50 Jahre BGR, ein Tätigkeitsbericht der Bundesanstalt für Geowissenschaften und Rohstoffe 1958-2008. Technical report, Federal Institute for Geosciences and Natural Resources (BGR), November 2008.

M. A. Biot. General theory of three-dimensional consolidation. *Journal of Applied Physics*, 12:155–164, 1941.

M. A. Biot. General solution of the equations of elasticity and consolidation for a porous material. *Journal of Applied Mechanics*, 23:91–96, 1956.

J. T. Birkholzer, J. Rutqvist, E. L. Sonnenthal, D. Barr, M. Chijimatsu, O. Kolditz, Q. Liu, Y. Oda, W. Wang, M. Xie, and C. Zhang. Geomechanical/geochemical modeling studies conducted within the international DECOVALEX project. paper LBNL 59050, Lawrence Berkeley National Laboratory (University of California), 2005.

A. W. Bishop and G. E. Blight. Some aspects of effective stress in saturated and partly saturated soils. *Géotechnique*, 13:177–197, 1963.

L. Bjerrum, A. Casagrande, R. B. Peck, and A. W. Skempton, editors. *From Theory to Practice in Soil Mechanics. Selections from the Writings of Karl Terzaghi*. John Wiley & Sons, New York, 1960.

P. Blümling, F. Bernier, P. Lebon, and C. D. Martin. The excavation damaged zone in clay formations time-dependent behaviour and influence on performance assessment. *Physics and Chemistry of the Earth*, 32:588–599, 2007.

J. Boisson, L. Bertrand, J. Heitz, and Y. M. Golvan. In situ and laboratory investigations of fluid flow through an argillaceous formation at different scales of space and time, Tournemire tunnel, southern France. *Hydrogeology Journal*, 9:108–123, 2001.

B. Bonin. Deep geological disposal in argillaceous formations: studies at the Tournemire test site. *Journal of Contaminant Hydrology*, 35:315–330, 1998.

R. M. Bowen. Incompressible porous media models by use of theory of mixtures. *International Journal of Engineering Science*, 18:1129–1148, 1980.

V. Bräuer, M. Reh, P. Schulz, P. Schuster, and K. H. Sprado. Endlagerung stark wärmeentwickelnder radioaktiver Abfälle in tiefen geologischen Formationen Deutschlands - Untersuchung und Bewertung von Regionen in nichtsalinaren Formationen. Technical report, Federal Institute for Geosciences and Natural Resources (BGR), Hannover/Berlin, Germany, 1994.

I. N. Bronstein, K. A. Semenjajew, G. Musiol, and H. Mühlig. *Taschenbuch der Mathematik*. Harri Deutsch, Frankfurt a. M., 7th edition, 2008.

M.S. Bruno. Micromechanics of stress-induced permeability anisotropy and damage in sedimentary rock. *Mechanics of Materials*, 9:108–123, 1994.

J. Cabrera. Caractérisation des discontinuités en milieu argileux (station expérimentale de Tournemire). Scientific and technical report, Institute of Radioprotection and Nuclear Safety (IRSN), France, 2002.

CAE. Commissariat of Atomic Energy: Cast3M. <http://www-cast3m.cea.fr>, 2008. Accessed 9 April 2009.

R. W. Carlson. Drying shrinkage of large concrete members. *Journal of the American Concrete Institute*, 33:327–336, 1937.

P. C. Carman. Fluid flow through granular beds. *Trans. Inst. Chem. Eng.*, 15:150–156, 1937.

J.-L. Chaboche. Continuum damage mechanics - present state and future trends. *Nuclear Engineering and Design*, 105:19–33, 1981a.

J.-L. Chaboche. Continuous damage mechanics - a tool to describe phenomena before crack initiation. *Nuclear Engineering and Design*, 64:233–247, 1981b.

J.-L. Chaboche. Damage induced anisotropy: On the difficulties associated with the active/passive unilateral conditions. *International Journal of Damage Mechanics*, 1:148–171, 1992.

J.-L. Chaboche. Development of continuum damage mechanics for elastic solids sustaining anisotropic and unilateral damage. *International Journal of Damage Mechanics*, 2:311–329, 1993.

J.-L. Chaboche, P. M. Lesne, and J. F. Maire. Continuum damage mechanics, anisotropy and damage deactivation for brittle materials like concrete and ceramic composites. *International Journal of Damage Mechanics*, 4:5–22, 1995.

D. Charpentier, D. Tessier, and M. Cathelineau. Shale microstructure evolution due to tunnel excavation after 100 years and impact of tectonic paleo-fracturing. Case of Tournemire, France. *Engineering Geology*, 70:55–69, 2003.

W. F. Chen and G. Y. Baladi. *Soil Plasticity, Theory and Implementation*. Number 38 in Developments in Geotechnical Engineering. Elsevier, Amsterdam, 1985.

A. S. Chiarelli, J. F. Shao, and N. Hoteit. Modeling of elastoplastic damage behavior of a claystone. *International Journal of Plasticity*, 19:23–45, 2003.

C. L. Chow and T. J. Lu. An analytical and experimental study of mixed-mode ductile fracture under nonproportional loading. *International Journal of Damage Mechanics*, 1(2):191–236, 1992.

N. Conil, I. Djeran-Maigre, R. Cabrillac, and K. Su. Poroelastic damage model for claystones. *Applied Clay Science*, 26:473–487, 2004.

J. Constantin, J. B. Peyaud, P. Vergély, M. Pagel, and J. Cabrera. Evolution of the structural fault permeability in argillaceous rocks in a polyphased tectonic context. *Physics and Chemistry of the Earth*, 29:25–41, 2004.

J. P. Cordebois and F. Sidoroff. Damage induced elastic anisotropy. *Mechanical Behavior of Anisotropic Solids*, pages 761–774, 1983. Colloques internationaux du CNRS, No295.

F. H. Cornet. The HTPF and integrated stress determination methods. In J. A. Hudson, editor, *Comprehensive Rock Engineering. Principles, Practice & Projects*, volume 3: Rock testing and site characterization, chapter 15, pages 413–432. Pergamon Press, Oxford, 1st edition, 1993.

F. H. Cornet and B. Valette. In situ stress determination from hydraulic injection test data. *Journal of Geophysical Research*, 89(B13):11,527–11,537, December 1984.

P. Cosenza, A. Ghorbani, N. Florsch, and A. Revil. Effects of drying on the low-frequency electrical properties of Tournemire argillites. *Pure and Applied Geophysics*, 164:2043–2066, 2007.

X. Daupley. *Etude du potentiel de l'eau interstitielle d'une roche argileuse et de relations entre ses propriétés hydriques et mécaniques - application aux argilites du Toarcien dans la région de Tournemire (Aveyron)*. PhD thesis, Paris School of Mines, 1997.

R. O. Davis and A. P. S. Selvadurai. *Plasticity and Geomechanics*. Cambridge University Press, Cambridge, UK, 2002.

R. de Boer. Development of porous media theories - a brief historical review. *Transport in Porous Media*, 9:155–164, 1992.

R. de Boer and W. Ehlers. The development of the concept of effective stresses. *Acta Mechanica*, 83:77–92, 1990.

I. Deniau, I. Devol-Brown, S. Derenne, F. Behar, and C. Largeau. Comparison of the bulk geochemical features and thermal reactivity of kerogens from Mol (boom clay), Bure (callovoxfordian argillite) and Tournemire (toarcian shales) underground research laboratories. *Science of the Total Environment*, 389:475–485, 2008.

H. Ding, W. Chen, and L. Zhang. *Elasticity of Transversely Isotropic Materials*, volume 126 of *Solid mechanics and its applications*. Springer, Dordrecht, 2006.

P. A. Domenico and F. W. Schwartz. *Physical and Chemical Hydrogeology*. John Wiley & Sons, New York, 1990.

J. Du and R. C. K. Wong. Application of strain-induced permeability model in a coupled geomechanics-reservoir simulator. *Journal of Canadian Petroleum Technology*, 46(12):55–61, 2007.

W. B. Durham. Laboratory observations of the hydraulic behavior of a permeable fracture from 3800 m depth in the KTB pilot hole. *Journal of Geophysical Research*, 102(8): 18405–18416, 1997.

W. Ehlers. Foundations of multiphasic and porous materials. In W. Ehlers and J. Bluhm, editors, *Porous Media*. Springer, Berlin, 2002.

W. Ehlers and J. Bluhm, editors. *Porous Media*. Springer, Berlin, 2002.

W. Ehlers and T. Graf. On partially saturated soil as a triphasic material. Technical Report 2003/12, Universität Stuttgart, Sonderforschungsbereich 404, 2003.

W. Ehlers, B. Markert, and A. Acartürk. A continuum approach for 3-d finite viscoelastic swelling of charged tissues and gels. Technical Report 2003/13, Universität Stuttgart, Sonderforschungsbereich 404, 2003.

D. Elsworth. Thermal permeability enhancement of blocky rocks: One-dimensional flows. *International Journal of Rock Mechanics and Mining Science & Geomechanics Abstracts*, 26:329–339, 1989.

D. Feldmann. *Repetitorium der Ingenieurmathematik, Teil 2 Numerische Mathematik*. Bino, Springer, 4th edition, 1993.

P. Fillunger. Der Auftrieb in Talsperren. *Österr. Wochenschrift für den öffentlichen Baudienst*, 19:532–570, 1913.

L. R. Fisher and J. N. Israelachvili. Direct experimental verification of the Kelvin equation for capillary condensation. *Nature*, 277:548–549, 1979.

S. Flügge, editor. *Die nicht-linearen Feldtheorien der Mechanik*, volume III/3 of *Handbuch der Physik*. Springer, Berlin, 1965.

D. G. Fredlund and H. Rahardjo. *Soil Mechanics for Unsaturated Soils*. John Wiley & Sons, New York, 1998.

A. F. Gangi. Variation of whole and fractured porous rock permeability with confining pressure. *International Journal of Rock Mechanics and Mining Science*, 15:249–257, 1978.

E. Gaucher, C. Robelin, J. M. Matray, G. Négrel, Y. Gros, J. F. Heitz, A. Vinsot, H. Rebour, A. Cassagnabère, and A. Bouchet. ANDRA underground research laboratory: interpretation of the mineralogical and geochemical data acquired in the CallovianOxfordian formation by investigative drilling. *Physics and Chemistry of the Earth*, 29: 55–77, 2004.

D. Gawin, F. Pesavento, and B. A. Schrefler. Hygro-thermo-chemo-mechanical modelling of concrete at early ages and beyond. Part I: Hydration and hygro-thermal phenomena. *Int. J. Numer. Meth. Engng.*, 67:299–331, 2006.

A. Gens. *Modern issues in non-saturated soils: advanced school lectures given at the International Centre for Mechanical Sciences in Udine, 1994*. CISM courses and lectures. Springer, Wien, 1995.

A. Gens and E. E. Alonso. A framework for the behaviour of unsaturated expansive clay. *Canadian Geotechnical Journal*, 29:1013–1032, 1992.

A. Giacomini, O. Buzzi, A. M. Ferrero, M. Migliazza, and G. P. Giani. Numerical study of flow anisotropy within a single natural rock joint. *International Journal of Rock Mechanics and Mining Science*, 45:47–58, 2008.

R. E. Goodman. *Introduction to Rock Mechanics*. John Wiley & Sons, New York, 2nd edition, 1996.

D. Gross and T. Seelig. *Fracture Mechanics. With an Introduction to Micromechanics*. Springer, Berlin, 2006.

A. Habbar. *Direkte und Inverse Modellierung reaktiver Transportprozesse in klüftig-porösen Medien*. PhD thesis, Institut für Strömungsmechanik und Elektronisches Rechnen im Bauwesen, Universität Hannover, report no. 65, 2001.

T. P. Harrigan and R. W. Mann. Characterization of microstructural anisotropy in orthotropic materials using a second rank tensor. *Journal of Materials Science*, 19:761–767, 1984.

P. Haupt. *Continuum Mechanics and Theory of Materials*. Springer, Berlin, 2nd edition, 2002.

U. Häußler-Combe. Zur Verwendung von Stoffgesetzen mit Entfestigung in numerischen Rechenverfahren. *Bauingenieur*, 82:286–298, June 2007.

R. Helmig. *Theorie und Numerik der Mehrphasenströmungen in geklüftet-porösen Medien*. PhD thesis, Institut für Strömungsmechanik und Elektronisches Rechnen im Bauwesen, Universität Hannover, report no. 34, 1993.

P. Hoth, H. Wirth, K. Reinhold, V. Bräuer, P. Krull, and H. Feldrappe. Endlagerung radioaktiver Abfälle in tiefen geologischen Formationen Deutschlands. Untersuchung und Bewertung von Tongesteinsformationen. Technical report, Federal Institute for Geosciences and Natural Resources (BGR), Berlin/Hannover, Germany, 2007.

J. A. Hudson, O. Stephansson, J. Andersson, C.-F. Tsang, and L. Jing. Coupled T-H-M issues relating to radioactive waste repository design and performance. *International Journal of Rock Mechanics and Mining Science*, 38:143–161, 2001.

IAEA. Geological disposal of radioactive waste: Safety requirements. Technical Report WS-R-4, International Atomic Energy Agency (IAEA), Vienna, 2006.

IAEA. Estimation of global inventories of radioactive waste and other radioactive materials. Technical Report IAEA-TECDOC-1591, International Atomic Energy Agency (IAEA), Vienna, 2008.

ISU. Software package rockflow, web-page. web-page of the Institut für Strömungsmechanik und Umweltphysik im Bauwesen, Leibniz Universität Hannover, 2009. <http://www.hydromech.uni-hannover.de>, <http://www.rockflow.de>.

K. Iwai. *Fundamental studies of fluid flow through a single fracture*. PhD thesis, University of California, Berkeley, 1976.

L. Jing. A review of techniques, advances and outstanding issues in numerical modelling for rock mechanics and rock engineering. *International Journal of Rock Mechanics and Mining Science*, 40:283–353, 2003.

L. Jing, F. Kautsky, O. Stephansson, and C.-F. Tsang. DECOVALEX-THMC Project. Executive summary. Technical Report SKI 2008:40, Swedish Nuclear Power Inspectorate, June 2008.

J. W. Ju. On energy-based coupled elastoplastic damage theories: constitutive modeling and computational aspects. *International Journal of Solids and Structures*, 25(7):803–833, 1989.

J. W. Ju. Isotropic and anisotropic damage variables in continuum damage mechanics. *Journal of Engineering Mechanics*, 116(12):2764–2770, 1990.

L. M. Kachanov. Time of the rupture process under creep conditions. *Izv. Akad. Nauk. S.R.S. Otd. Tekh. Nauk*, 8:26–31, 1958.

L. M. Kachanov. *Introduction to continuum damage mechanics*. Martinus Nijhoff, Dordrecht, 1986.

R. Kaiser. *Gitteradaption für die Finite-Elemente-Modellierung gekoppelter Prozesse in geklüftet porösen Medien*. PhD thesis, Institut für Strömungsmechanik und Elektromechanik im Bauwesen, Universität Hannover, report no. 63, 2001.

K.-I. Kantani. Stereological determination of structural anisotropy. *Int. J. Engng. Sci.*, 22(5):531–546, 1984.

P. I. Kattan and G. Z. Voyatzis. *Damage mechanics with finite elements. Practical application with computer tools*. Springer, Berlin, 2002.

P. C. Kelsall, J. B. Case, and C. R. Chabannes. Evaluation of excavation-induced changes in rock permeability. *International Journal of Rock Mechanics and Mining Science*, 21 (3):123–135, 1984.

A. S. Khan and S. Huang. *Continuum Theory of Plasticity*. John Wiley & Sons, New York, 1995.

F. Kockel and P. Krull. Endlagerung stark wärmeentwickelnder radioaktiver Abfälle in tiefen geologischen Formationen Deutschlands - Untersuchung und Bewertung von Salzformationen. Technical report, Federal Institute for Geosciences and Natural Resources (BGR), Hannover/Berlin, Germany, 1995.

M. Kohlmeier. *Coupling of thermal, hydraulic and mechanical processes for geotechnical simulations of partially saturated porous media*. PhD thesis, Institut für Strömungsmechanik und Elektronisches Rechnen im Bauwesen, Leibniz Universität Hannover, report no. 72, 2006.

M. Kohlmeier, J. Maßmann, M. Wulkau, and G. Zieflle. *RockFlow 5 User's Manual. Keyword Description*. Institut für Strömungsmechanik und Umweltphysik im Bauwesen, Leibniz Universität Hannover, 5.1.10 edition, January 2009. <http://www.rockflow.de>.

K. Kolari. *Damage mechanics model for brittle failure of transversely isotropic solids*. PhD thesis, Department of Mechanical Engineering of Helsinki University of Technology, 2007.

O. Kolditz. *Stoff- und Wärmetransport im Kluftgestein*. Habilitation, Institut für Strömungsmechanik und Elektronisches Rechnen im Bauwesen, Universität Hannover, report no. 47, 1996.

O. Kolditz, M. Kohlmeier, C. Thorenz, and H. Shao. Numerical modelling of moisture swelling in unsaturated porous media. *Developments in Water Science*, 47:1–8, 2002.

H. Komine and N. Ogata. New equations for swelling characteristics of bentonite-based buffer materials. *Canadian Geotechnical Journal*, 40:460–475, 2003.

J. Kozeny. Über kapillare Leitung des Wassers im Boden. *Sitzungsber. Akad. Wiss.*, 136: 271–306, 1927.

R. L. Kranz, A. D. Frankel, T. Engelder, and C. H. Scholz. The permeability of whole and jointed barre granite. *International Journal of Rock Mechanics and Mining Science*, 16 (4):225–234, 1979.

K.-P. Kröhn. *Simulation von Transportvorgängen im klüftigen Gestein mit der Methode der Finiten Elemente*. PhD thesis, Institut für Strömungsmechanik und Elektronisches Rechnen im Bauwesen, Universität Hannover, report no. 29, 1991.

K. Kühn. Field experiments in salt formations. *Philosophical Transactions of the Royal Society of London*, Series A, Mathematical and Physical Sciences, 319(1545):157–161, 1986.

T. Lege. *Modellierung des Kluftgesteins als geologische Barriere für Deponien*. PhD thesis, Institut für Strömungsmechanik und Elektronisches Rechnen im Bauwesen, Universität Hannover, report no. 45, 1995.

J. Lemaitre. *A Course on Damage Mechanics*. Springer, Berlin, 1992.

J. Lemaitre and R. Desmorat. *Engineering Damage Mechanics. Ductile, Creep and Brittle Failures*. Springer, Berlin, 2005.

S. Leroueil, G. Bouclin, F. Tavenas, L. Bergeron, and P. La Rochelle. Permeability anisotropy of natural clays as a function of strain. *Canadian Geotechnical Journal*, 27: 568–579, 1990.

R. W. Lewis and B. A. Schrefler. *The Finite Element Method in Deformation and Consolidation of Porous Media*. John Wiley & Sons, Chichester, 1987.

R. W. Lewis and B. A. Schrefler. *The Finite Element Method in the Static and Dynamic Deformation and Consolidation of Porous Media*. John Wiley & Sons, Chichester, 1998.

J. Liu, D. Elsworth, and B. H. Brady. Linking stress-dependent effective porosity and hydraulic conductivity fields to RMR. *International Journal of Rock Mechanics and Mining Science*, 36:581–596, 1991.

N. Lu and W. J. Likos. *Unsaturated Soil Mechanics*. John Wiley & Sons, New Jersey, 2004.

V. A. Lubarda and D. Krajcinovic. Damage tensors and the crack density distribution. *International Journal of Solids and Structures*, 30(20):2859–2877, 1993.

J. Maßmann and A. Ahmari. *RockFlow Tutorial*. Institut für Strömungsmechanik und Elektronisches Rechnen im Bauwesen, Universität Hannover, 2006. <http://www.rockflow.de>.

J. Maßmann, G. Zieffle, M. Kohlmeier, W. Zielke, and H. Shao. Coupled hydro-mechanical modeling of seasonally affected unsaturated claystone. In Weiya Xu, editor, *Proc. of the 2nd International Conference on Coupled T-H-M-C Processes in Geosystems and Engineering (GeoProc2006)*, Nanjing, P. R. China, 2006. HoHai University.

J. Maßmann, S. Uehara, A. Rejeb, and A. Millard. Investigation of desaturation in an old tunnel and new galleries at an argillaceous site. *Environmental Geology*, special issue, June 2008a. online available: <http://dx.doi.org/10.1007/s00254-008-1438-2>, to be printed.

J. Maßmann, G. Zieffle, M. Kohlmeier, W. Zielke, H. Shao, and A. Rejeb. Numerical Analysis of the Desaturation Process at the Argillaceous Tournemire Site (France). In J. F. Shao and N. Burlion, editors, *Thermo-Hydromechanical and Chemical Coupling in Geomaterials and Applications: Proceedings of the 3rd International Symposium Geo-Proc'2008*, pages 355–362. John Wiley & Sons, June 2008b.

J. M. Matray, S. Savoye, and J. Cabrera. Desaturation and structure relationships around drifts excavated in the well-compacted Tournemire's argillite (Aveyron, France). *Engineering Geology*, 90:1–16, 2007.

J. Mazars. A description of micro- and macroscale damage of concrete structures. *Engineering Fracture Mechanics*, 25(5-6):729–737, 1986.

M. Mazurek, F. J. Pearson, G. Volckaert, and H. Bock. Features, events and processes evaluation catalogue for argillaceous media. Technical report, Nuclear Energy Agency, Organization for Economic Co-Operation and Development, Paris, France, 2003.

A. Meister. *Numerik linearer Gleichungssysteme. Eine Einführung in moderne Verfahren. Numerische Mathematik*. Vieweg, Germany, 3rd edition, 2008.

A. Meunier. *Clays*. Springer, Berlin, 2005.

A. Millard and A. Rejeb. Identification of the Hydro-Mechanical in-Situ Properties of Tournemire Argillite from Mine-by-test Experiment. In J. F. Shao and N. Burlion, editors, *Thermo-Hydromechanical and Chemical Coupling in Geomaterials and Applications: Proceedings of the 3rd International Symposium GeoProc'2008*, pages 313–320. John Wiley & Sons, June 2008.

A. Millard, J. Maßmann, A. Rejeb, and S. Uehara. Study of the initiation and propagation of excavation damaged zones around openings in argillaceous rock. *Environmental Geology*, special issue, August 2008. online available: <http://dx.doi.org/10.1007/s00254-008-1518-3>, to be printed.

K.-B. Min, J. Rutqvist, C.-F. Tsang, and L. Jing. Stress-dependent permeability of fractured rock masses: a numerical study. *International Journal of Rock Mechanics and Mining Science*, 41:1191–1210, 2004.

K.-B. Min, J. Rutqvist, and D. Elsworth. Chemically and mechanically mediated influences on the transport and mechanical characteristics of rock fractures. *International Journal of Rock Mechanics and Mining Science*, 46:80–89, 2009.

S. Moenckes. *Grid Generation for Simulation of Flow and Transport Processes in Fractured-Porous Media*. PhD thesis, Institut für Strömungsmechanik und Elektromechanisches Rechnen im Bauwesen, Universität Hannover, report no. 68, 2004.

B. Muhunthan and J. L. Chameau. Void fabric tensor and ultimate state surface of soils. *Journal of Geotechnical and Geoenvironmental Engineering*, 123(2):173–181, 1997.

S. Murakami. Mechanical modeling of material damage. *Applied Mechanics*, 55:280–286, June 1988.

S. Murakami and K. Kamiya. Constitutive and damage evolution equations of elastic-brittle materials based on irreversible thermodynamics. *Int. J. Mech. Sci.*, 39(4):473–486, 1997.

NAGRA, Colenco Power Engineering AG, and GRS. Auswertung von Langzeitsicherheitsanalysen hinsichtlich Kriterien für die Auswahl von Endlagerstandorten - Schlussbericht. Technical Report PSP Nr. WS 0008, Nationale Genossenschaft für die Lagerung radioaktiver Abfälle (NAGRA), Colenco Power Engineering AG, Gesellschaft für Anlagen- und Reaktorsicherheit (GRS), beauftragt vom Bundesamt für Strahlenschutz (BfS), Wettingen, Germany, 2002.

J. A. Nelder and R. Mead. A simplex method for function minimization. *The Computer Journal*, 7:308–313, 1965.

H. Niandou, J. F. Shao, J. P. Henry, and D. Fourmaintraux. Laboratory investigation of the mechanical behaviour of Tournemire shale. *International Journal of Rock Mechanics and Mining Science*, 34(1):3–16, 1997.

J. Niechcial. *A Particle of Clay: The Biography of Alec Skempton, Civil Engineer*. Whittles, Latheronwheel, 2002.

Y. Ohnishi, H. Shibata, and A. Kobayashi. Development of finite element code for the analysis of coupled thermo-hydro-mechanical behaviors of a saturated-unsaturated medium. In *Proc. of Int. Symp. on Coupled Process Affecting the Performance of a Nuclear Waste Repository*, pages 263–268, Berkeley, U.S.A., 1985.

M. Ortiz. A constitutive theory for the inelastic behaviour of concrete. *Mechanics of Material*, 4:67–93, 1985.

M. Ortiz. An analytical study of the localized failure modes of concrete. *Mechanics of Material*, 6:159–174, 1987.

D. Patriarche, E. Ledouxa, R. Simon-Coincon, J. Michelot, and J. Cabrera. Characterization and modeling of diffusion process for mass transport through the Tournemire argillites (Aveyron, France). *Applied Clay Science*, 26:109–122, 2004.

P. Przyna. Fundamental problems in viscoplasticity. *Adv. Appl. Mech.*, 9:244–386, 1966.

R. Pusch. Alteration of the hydraulic conductivity of rock by tunnel excavation. *International Journal of Rock Mechanics and Mining Science*, 26(1):79–83, 1989.

R. Pusch and R. N. Yong. *Microstructure of Smectite Clays and Engineering Performance*. Taylor & Francis, 2006.

R. Ratke, O. Kolditz, and W. Zielke. ROCKFLOW-DM2 - 3-D Dichteströmungsmodell. Technical report, Institut für Strömungsmechanik und Elektronisches Rechnen im Bauwesen, Universität Hannover, 1996.

A. Rejeb. Time-dependent behaviour of Tournemire argillites (France). In South African Institute of Mining and Metallurgy, editor, *Proc. of ISRM 2003-Technology Roadmap for Rock Mechanics*, Johannesburg, South Africa, 2003.

A. Rejeb. Disturbances caused by the excavation of a gallery in the Tournemire site in 2003. In: Safety of the Geological Disposal of Radioactive Waste. Scientific and technical report, Institute of Radioprotection and Nuclear Safety (IRSN), France, 2005.

A. Rejeb and J. Cabrera. Description for Task C, Excavation Disturbed Zone (EDZ) in the argillaceous Tournemire site (France). Technical report, Institute of Radioprotection and Nuclear Safety (IRSN), France, 2004.

A. Rejeb and J. Cabrera. Time-dependent evolution of the excavation damaged zone in the argillaceous Tournemire site (France). In Weiya Xu, editor, *Proc. of the 2nd International Conference on Coupled T-H-M-C Processes in Geosystems and Engineering (GeoProc2006)*, Nanjing, P. R. China, 2006. HoHai University.

A. Rejeb, A. Millard, A. Rouabhi, and M. Tijani. Modelling approaches of the excavation damaged zone (EDZ) around the old tunnel at the argillaceous Tournemire site. In Weiya Xu, editor, *Proc. of the 2nd International Conference on Coupled T-H-M-C*

Processes in Geosystems and Engineering (GeoProc2006), Nanjing, P. R. China, 2006. HoHai University.

A. Rejeb, A. Rouabhi, A. Millard, J. Maßmann, and S. Uehara. DECOVALEX-THMC Project. Task C: Hydro-mechanical response of the Tournemire argillite to the underground openings excavation: unsaturated zones and mine-by-test experiment. Technical Report SKI 2008:44, Swedish Nuclear Power Inspectorate, June 2008a.

A. Rejeb, K. B. Slimane, J. Cabrera, J. M. Matray, and S. Savoye. Hydro-mechanical response of the Tournemire argillite to the excavation of underground openings: Un-saturated zones and mine-by-test experiment. In J. F. Shao and N. Burlion, editors, *Thermo-Hydromechanical and Chemical Coupling in Geomaterials and Applications: Proceedings of the 3rd International Symposium GeoProc'2008*, pages 649–656. John Wiley & Sons, June 2008b.

L. A. Richards. Capillary conduction of liquids through porous media. *Physics*, 1:318–333, 1931.

T. Rother. *Geometric Modelling of Geo-Systems*. PhD thesis, Institut für Strömungsmechanik und Elektronisches Rechnen im Bauwesen, Universität Hannover, report no. 64, 2001.

A. Rouabhi, M. Tijani, and A. Rejeb. Projet Tournemire: Études Expérimentale et Théorique du Comportement des Argilites en de la Compréhension des Zones Endomagées autour des Ouvrages Souterrains du site de Tournemire. Technical Report R051216AROU, École des Mines de Paris Centre de Géotechnique et d'Exploration du Sous-sol, Institute of Radioprotection and Nuclear Safety (IRSN), December 2005.

A. Rouabhi, M. Tijani, and A. Rejeb. Triaxial behaviour of transversely isotropic materials application to sedimentary rocks. *International Journal for Numerical and Analytical Methods in Geomechanics*, 2006.

J. Rutqvist, L. Börgesson, M. Chijimatsu, A. Kobayashi, L. Jing, T. S. Nguyen, J. Noorishad, and C.-F. Tsang. Thermohydromechanics of partially saturated geological media: governing equations and formulation of four nite element models. *International Journal of Rock Mechanics and Mining Science*, 38:105–127, 2001.

M. R. Salari, S. Saeb, K. J. Willam, S. J. Patchet, and R. C. Carrasco. A coupled elastoplastic damage model for geomaterials. *Computer Methods in Applied Mechanics and Engineering*, 193(27-29):2625–2643, 2004.

T. Schanz, editor. *Theoretical and Numerical Unsaturated Soil Mechanics*, volume 113 of *Springer Proceedings in Physics*. Springer, Berlin, 2007.

A. E. Scheidegger. *The Physics of Flow Through Porous Media*. University of Toronto Press, 1957. reprint 1958.

J. Schröder. *Theoretische und algorithmische Konzepte zur phänomenologischen Beschreibung anisotropen Materialverhaltens*. PhD thesis, Institut für Baumechanik und Numerische Mechanik, Universität Hannover, 1996.

P. Semete, C. Imbert, P. Desgree, B. Février, A. Courtois, and G. Touzé. Experimental study of the water permeability of partially saturated argillite. In J. F. Shao and N. Burlion, editors, *Thermo-Hydromechanical and Chemical Coupling in Geomaterials and Applications: Proceedings of the 3rd International Symposium GeoProc'2008*, pages 220–230. John Wiley & Sons, June 2008.

Z. Sen. Theoretical RQD-porosity-conductivity-aperture charts. *International Journal of Rock Mechanics and Mining Science*, 33(2):173–177, 1996.

H. Shao. *Simulation von Strömungs- und Transportvorgängen in geklüftet porösen Medien mit gekoppelten Finite-Elemente- und Rand-Element-Methoden*. PhD thesis, Institut für Strömungsmechanik und Elektronisches Rechnen im Bauwesen, Universität Hannover, report no. 37, 1994.

H. Shao, T. Nowak, Ch. Lege, H. Kunz, and V. Bräuer. Hydro-Mechanical Behaviour of Saturated-Unsaturated Clay Materials - Experimental and Numerical Investigations of Gas Migration. In Weiya Xu, editor, *Proc. of the 2nd International Conference on Coupled T-H-M-C Processes in Geosystems and Engineering (GeoProc2006)*, Nanjing, P. R. China, 2006a. HoHai University.

J. F. Shao and N. Burlion, editors. *Thermo-Hydromechanical and Chemical Coupling in Geomaterials and Applications: Proceedings of the 3rd International Symposium GeoProc'2008*, Lille, France, June 2008. Polytech Lille, John Wiley & Sons.

J. F. Shao, H. Zhou, and K. T. Chau. Coupling between anisotropic damage and permeability variation in brittle rocks. *Int. J. Numer. Anal. Meth. Geomech.*, 29:1231–1247, 2005.

J. F. Shao, K. T. Chau, and X. T. Feng. Modeling of anisotropic damage and creep deformation in brittle rocks. *International Journal of Rock Mechanics and Mining Science*, 43:582–592, 2006b.

J. F. Shao, Y. Jia, D. Kondo, and A. S. Chiarelli. A coupled elastoplastic damage model for semi-brittle materials and extensions to unsaturated conditions. *Mechanics of Material*, 38:218–232, 2006c.

J. C. Simo and J. W. Ju. Strain- and stress-based continuum damage models—i. formulation. *Int. J. Solids Structures*, 23(7):821–840, 1987a.

J. C. Simo and J. W. Ju. Strain- and stress-based continuum damage models—ii. computational aspects. *Int. J. Solids Structures*, 23(8):840–869, 1987b.

G. D. H. Simpson, Y. Guéguen, and F. Schneider. Analytical model for permeability evolution in microcracking rock. *Pure and Applied Geophysics*, 160:999–1008, 2008.

S. Sisavath, X. D. Jing, and R. W. Zimmerman. Effect of stress on the hydraulic conductivity of rock pores. *Phys. Chem. Earth (A)*, 25(2):163–168, 2000.

A. W. Skempton. Terzaghi's discovery of effective stress. In L. Bjerrum, editor, *From Theory to Practice in Soil Mechanics. Selections from the Writings of Karl Terzaghi*, pages 42–53. John Wiley & Sons, 1960.

A. W. Skempton. Effective stress in soils, concrete and rocks. In *Proc. of the Conference on Pore Pressure and Suction in Soils*, pages 4–16, London, 1961. British National Society of the Internat. Society of Soil Mechanics and Foundation Engineering at the Institution of Civil Engineers, Butterworth.

J. Skrzypek and A. Ganczarski. *Modeling of Material Damage and Failure of Structures: Theory and Applications*. Springer, Berlin, 1999.

D. T. Snow. *Parallel plate model of fractured permeable media*. PhD thesis, University of California, Berkeley, 1965.

D. T. Snow. Anisotropic permeability of fractured media. *Water Resources Research*, 5 (6):1273–1289, 1969.

M. Souley, F. Homand, S. Pepa, and D. Hoxha. Damage-induced permeability changes in granite: a case example at the URL in Canada. *International Journal of Rock Mechanics and Mining Science*, 38:297–310, 2001.

E. Stein and F.-J. Barthold. Elastizitätstheorie. In G. Mehlhorn, editor, *Der Ingenieurbau, Grundwissen: Werkstoffe, Elastizitätstheorie*, pages 165–428. Ernst & Sohn, Berlin, 1996.

O. Stephansson, J. A. Hudson, and L. Jing, editors. *International Conference on Coupled T-H-M-C Processes in Geosystems: Fundamentals, Modelling, Experiments & Applications (GeoProc2003)*, Stockholm, Schweden, October 2003. Department of Land and Water Resources Engineering (LWR), Royal Institute of Technology (KTH).

O. Stephansson, C.-F. Tsang, L. Jing, and F. Kautsky. DECOVALEX project 1992 - 2006: Purpose, tasks and main achievements. In Weiya Xu, editor, *Proc. of the 2nd International Conference on Coupled T-H-M-C Processes in Geosystems and Engineering (GeoProc2006)*, Nanjing, P. R. China, 2006. HoHai University.

S. P. Sutera. The History of Poiseuille's law. *Annu. Rev. Fluid Mechanics*, 25:1–19, 1993.

G. Swoboda and Q. Yang. An energy based damage model of geomaterials - i. formulation and numerical results. *International Journal of Solids and Structures*, 36:1719–1734, 1999a.

G. Swoboda and Q. Yang. An energy based damage model of geomaterials - ii. deduction of damage evolution laws. *International Journal of Solids and Structures*, 36:1735–1755, 1999b.

S. Takashima and K. Kurita. Permeability of granular aggregate of soft gel: Application to the partially molten system. *Earth and Planetary Science Letters*, 267:83–92, 2008.

H. R. Thomas and P. J. Cleall. Inclusion of expansive clay behaviour in coupled thermo hydraulic mechanical models. *Engineering Geology*, 54:93–108, 1999.

C. Thorenz. *Model Adaptive Simulation of Multiphase and Density Driven Flow in Fractured and Porous Media*. PhD thesis, Institut für Strömungsmechanik und Elektromechanisches Rechnen im Bauwesen, Universität Hannover, report no. 62, 2001.

D. Tikhomirov. *Theorie und Finite-Element-Methode für die Schädigungsbeschreibung in Beton und Stahlbeton*. PhD thesis, Institut für Baumechanik und Numerische Mechanik, Universität Hannover, 2000.

S. P. Timošenko and J. N. Goodier. *Theory of Elasticity*. Engineering societies monographs. McGraw-Hill, New York, 2nd edition, 1951.

C. Truesdell and R. A. Toupin. The classical field theories. In S. Flügge, editor, *Handbuch der Physik*, volume III/1, pages 226–902. Springer, Berlin, 1960.

C.-F. Tsang, F. Bernier, and C. Davies. Geohydromechanical processes in the excavation damaged zone in crystalline rock, rock salt, and indurated and plastic clays - in the context of radioactive waste disposal. *International Journal of Rock Mechanics and Mining Science*, 42:109–125, 2005.

C.-F. Tsang, O. Stephansson, L. Jing, and F. Kautsky. DECOVALEX Project: from 1992 to 2007. *Environmental Geology*, special issue, October 2008. online available: <http://dx.doi.org/10.1007/s00254-008-1625-1>, to be printed.

S. Uehara, A. Kobayashi, M. Chijimatsu, Y. Ohnishi, and T. Fujita. Development of stress conditions around a tunnel excavated in argillaceous rock related to change of saturation conditions. In Weiya Xu, editor, *Proc. of the 2nd International Conference on Coupled T-H-M-C Processes in Geosystems and Engineering (GeoProc2006)*, Nanjing, P. R. China, 2006. HoHai University.

S. Uehara, A. Kobayashi, M. Chijimatsu, Y. Ohnishi, T. Fujita, and A. Rejeb. Hydraulic Modeling of Unsaturated Zones around Three Openings at the Argillaceous Tournemire Site (France). In J. F. Shao and N. Burlion, editors, *Thermo-Hydromechanical and Chemical Coupling in Geomaterials and Applications: Proceedings of the 3rd International Symposium GeoProc'2008*, pages 419–425. John Wiley & Sons, June 2008.

F. Valés, D. Nguyen Minh, H. Gharbi, and A. Rejeb. Experimental study of the influence of the degree of saturation on physical and mechanical properties in Tournemire shale (France). *Appl. Clay Sci.*, 26:197–207, 2004.

H. A. van der Vorst. BI-CGSTAB: A fast and smoothly converging variant of BI-CG for the solution of nonsymmetric linear systems. *SIAM Journal on Scientific Computing*, 13(2):631–644, 1992.

M. Th. van Genuchten. A closed-form equation for predicting the hydraulic conductivity of unsaturated soils. *Soil Sci. Soc. Am.*, 44:892–898, 1980.

K. von Terzaghi. The shear resistance of saturated soils. In *Proc. 1st Int. Conf. Soil Mech. Found. Eng*, volume 1, pages 54–56, Cambridge, MA, 1936.

K. von Terzaghi. *Theoretical Soil Mechanics*. John Wiley & Sons, New York, 7th edition, 1954.

K. von Terzaghi and O. K. Fröhlich. *Theorie der Setzung von Tonschichten. Eine Einführung in die analytische Tonmechanik*. Franz Deuticke, Wien, 1936.

G. Z. Voyatzis and P. I. Kattan. *Damage Mechanics*. CRC Press, Boca Raton, 2005.

G. Z. Voyatzis and C. R. Song. *The Coupled Theory of Mixtures in Geomechanics with Applications*. Springer, Berlin, 2006.

R. Walsh, C. McDermott, and O. Kolditz. Numerical modeling of stress-permeability coupling in rough fractures. *Hydrogeology Journal*, 16:613–627, 2008.

S. Weßling. *The investigation of underground coal fires - towards a numerical approach for thermally, hydraulically, and chemically coupled processes*. PhD thesis, Fachbereich Physik der Mathematisch-Naturwissenschaftlichen Fakultät der Westfälischen Wilhelms-Universität, 2007.

P. A. Witherspoon, J. S. Y. Wang, K. Iwai, and J. E. Gale. Validity of cubic law for fluid flow in a deformable rock fracture. *Water Resources Research*, 16(6):1016–1024, 1980.

W. Wittke. *Felsmechanik. Grundlagen für wirtschaftliches Bauen im Fels*. Springer, Berlin, 1984.

J. Wollrath. *Ein Strömungs- und Transportmodell für klüftiges Gestein und Untersuchungen zu homogenen Ersatzsystemen*. PhD thesis, Institut für Strömungsmechanik und Elektronisches Rechnen im Bauwesen, Universität Hannover, report no. 28, 1990.

R. C. K. Wong. A model for strain-induced permeability anisotropy in deformable granular media. *Can. Geotech. J.*, 40:95–106, 2003.

P. Wriggers. *Nichtlineare Finite-Element-Methoden*. Springer, Berlin, 2001.

M. Wulkau. Entwicklung einer Struktur- und Datenverwaltung zur objektorientierten Umsetzung eines flexiblen Konzepts der Dateneingabe im FE-Programm RockFlow. Studienarbeit 2005/4, Institut für Strömungsmechanik und Elektronisches Rechnen im Bauwesen, Universität Hannover, 2005.

M. Xie, H. C. Moog, and O. Kolditz. Geochemical effects on swelling pressure of highly compacted bentonite: Experiments and model analysis. In T. Schanz, editor, *Theoretical and Numerical Unsaturated Soil Mechanics*, volume 113 of *Springer Proceedings in Physics*, pages 93–100. Springer, Berlin, 2007.

P. Xu and B. Yu. Developing a new form of permeability and Kozeny-Carman constant for homogeneous porous media by means of fractal geometry. *Advances in Water Resources*, 31:74–81, 2008.

W. Xu, editor. *2nd International Conference on Coupled T-H-M-C Processes in Geosystems and Engineering: Advances on Coupled Thermo-Hydro-Mechanical-Chemical Processes in Geosystems and Engineering (GeoProc2006)*, Nanjing, China, May 2006. Ho-Hai University.

C.-L. Zhang, T. Rothfuchs, H. Moog, J. Dittrich, and J. Müller. Thermo-Hydro-Mechanical and Geochemical Behaviour of the Callovo-Oxfordian Argillite and the Opalinus Clay. Technical report, Gesellschaft für Anlagen- und Reaktorsicherheit (GRS) mbH, 2004.

J. Zhang, W. B. Standifird, J.-C. Roegiers, and Y. Zhang. Stress-dependent fluid flow and permeability in fractured media: from lab experiments to engineering applications. *Rock Mechanics and Rock Engineering*, 40(1):3–21, 2007.

J. J. Zhou, J. F. Shao, and W. Y. Xu. Coupled modeling of damage growth and permeability variation in brittle rocks. *Mechanics Research Communications*, 33:450–459, 2006.

G. Zieffle. *Modeling aspects of coupled hydraulic-mechanical processes in clay material*. PhD thesis, Institut für Strömungsmechanik und Elektronisches Rechnen im Bauwesen, Leibniz Universität Hannover, report no. 74, 2008.

O. C. Zienkiewicz and R. L. Taylor. *The Finite Element Method*, volume 1: The Basis. Butterworth-Heinemann, Oxford, 5th edition, 2000.

O. C. Zienkiewicz and R. L. Taylor. *The Finite Element Method for Solid and Structural Mechanics*. Elsevier, 6th edition, 2005.

O. C. Zienkiewicz, A. H. C. Chan, M. Pastor, B. A. Schrefler, and T. Shiomi. *Computational Geomechanics with Special Reference to Earthquake Engineering*. John Wiley & Sons, Chichester, 1999.

B. Zinszner, P. Meynier, J. Cabrera, and P. Volant. Vitesse des ondes ultrasonores, soniques et sismiques dans les argilites du tunnel de Tournemire. Effet de l'anisotropie et de la fracturation naturelle. *Oil & Gas Science and Technology - Revue de l'IFP*, 57(4):341–353, 2002.

P. K. Zysset and A. Curnier. A 3d damage model for trabecular bone based on fabric tensors. *J. Biomechanics*, 29:1549–1558, 1996.

Appendix A

Additional simulation results

A.1 Desaturation process

A.1.1 Comparison of simulation results with measurements of the 2nd campaign

Figures A.1 - A.3 show all measured saturation profiles of the second campaign, as provided by the IRSN, and the corresponding simulations with variations of the permeability. In figure A.3 all simulation results are plotted, in the other ones only the simulation results with the best fit are depicted.

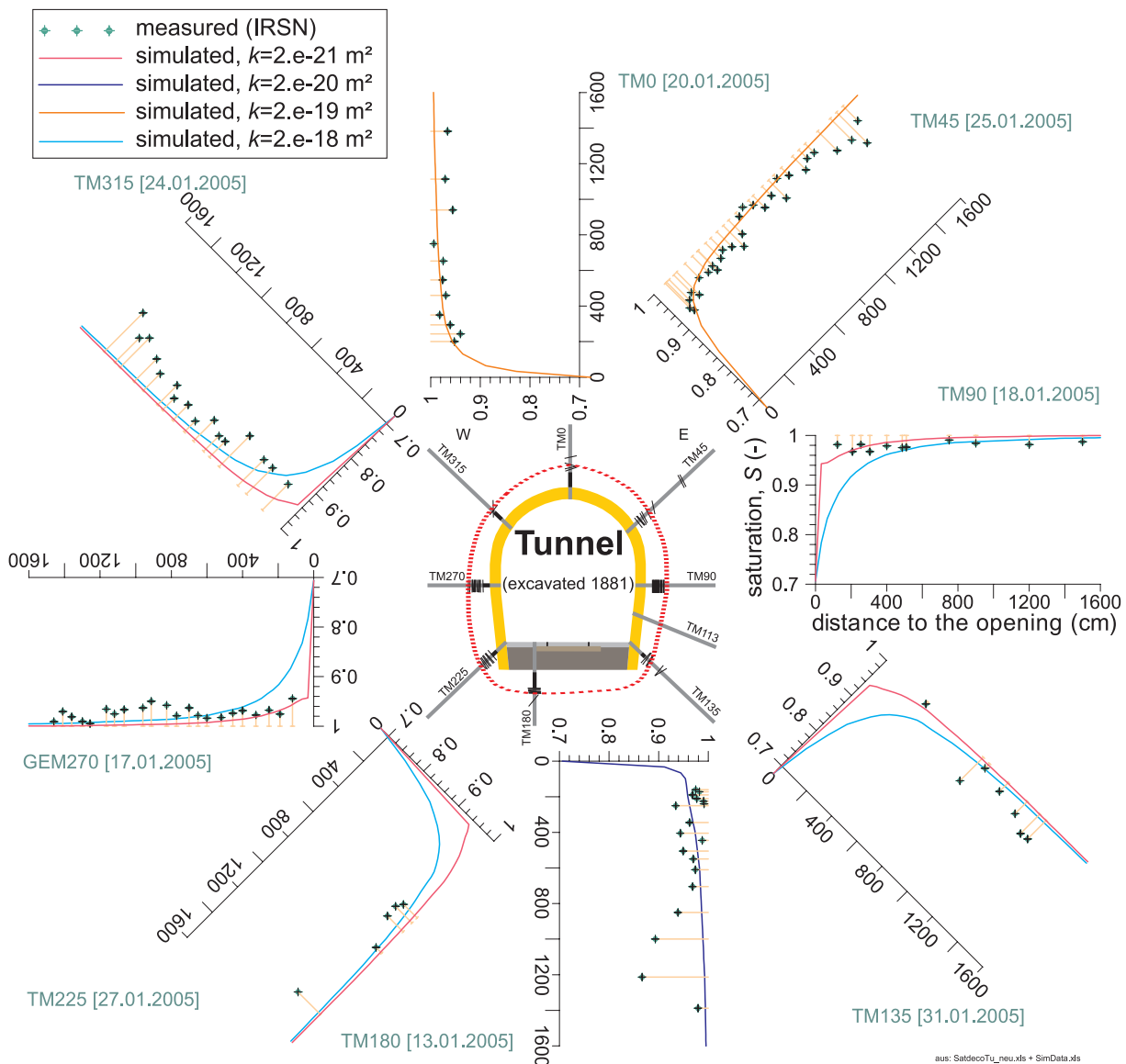


Figure A.1: Direction dependent visualization of measured (*IRSN*) and calculated saturation profiles at the old tunnel (second campaign).

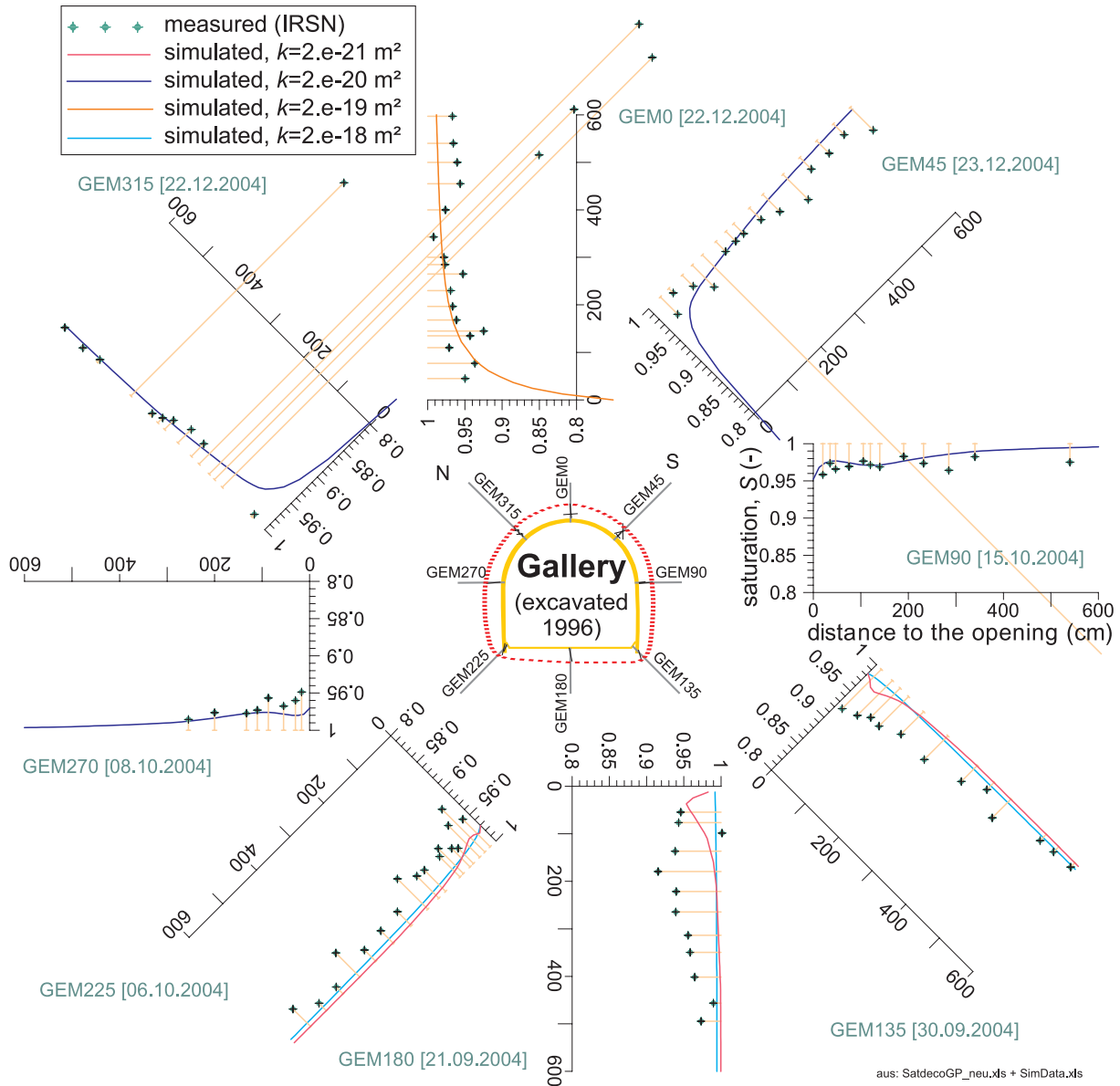


Figure A.2: Direction dependent visualization of measured (IRSN) and calculated saturation profiles at the 1996 excavated gallery (second campaign).

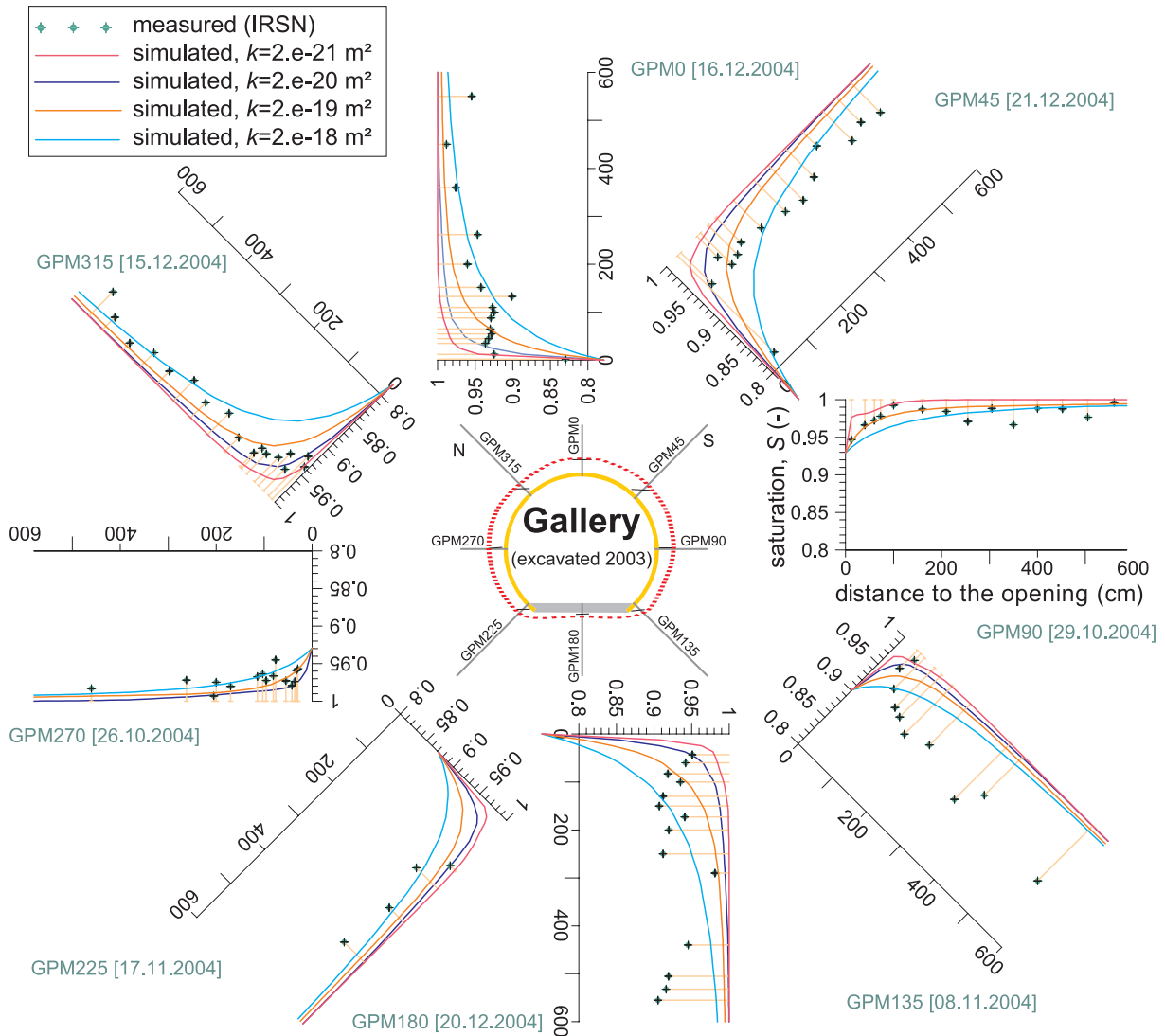


Figure A.3: Direction dependent visualization of measured (IRSN) and calculated saturation profiles at the 2003 gallery (second campaign).

A.2 Mine-by-test experiment

A.2.1 Simulation and comparison with measurements

A.2.1.1 Short term response of displacements

Additionally to chapter 3.3.4.4, simulated displacements with the corresponding measurements for the short term predictions are plotted in the figures A.4 to A.7. All measurements have been provided by the *IRSN*.

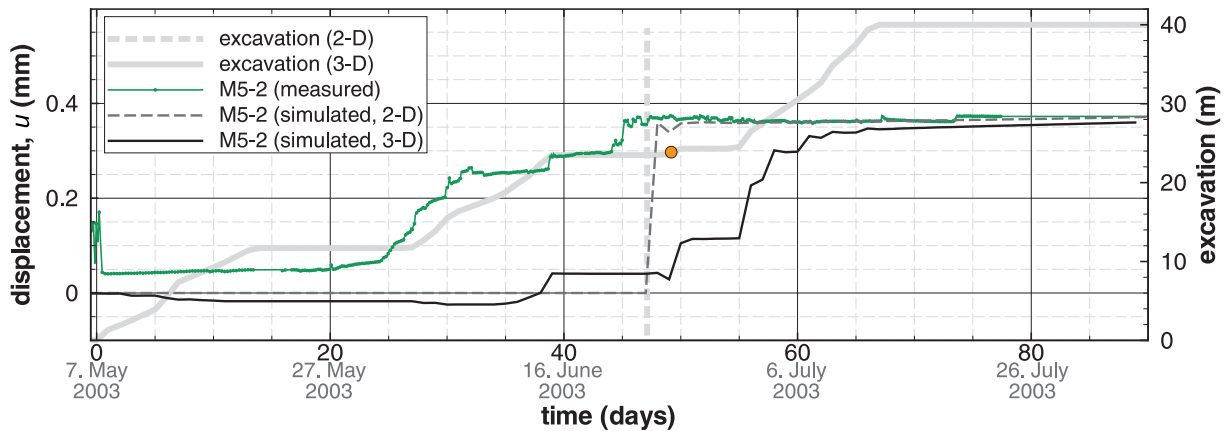


Figure A.4: Measured (*IRSN*) and simulated displacements at the monitoring point M5-2 during and directly after the excavation phase.

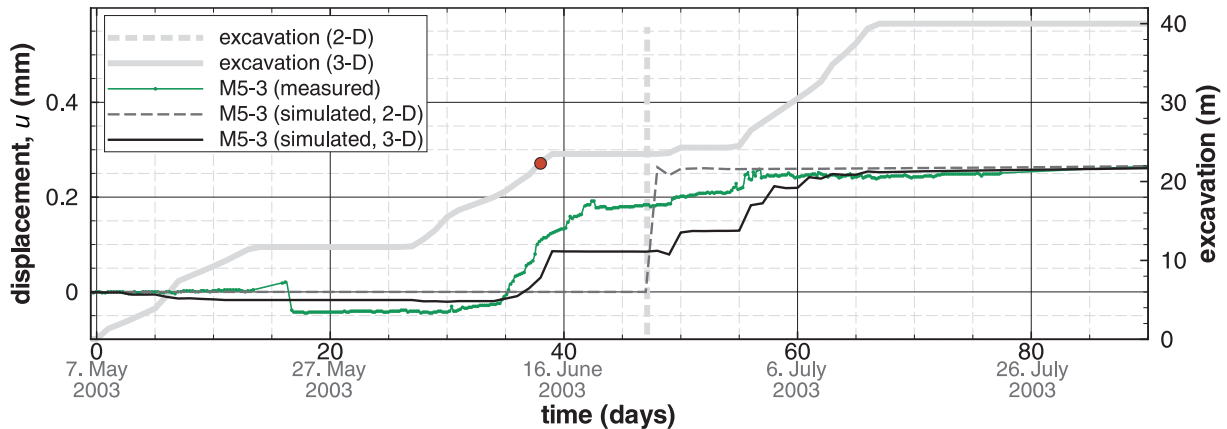


Figure A.5: Measured (*IRSN*) and simulated displacements at the monitoring point M5-3 during and directly after the excavation phase.

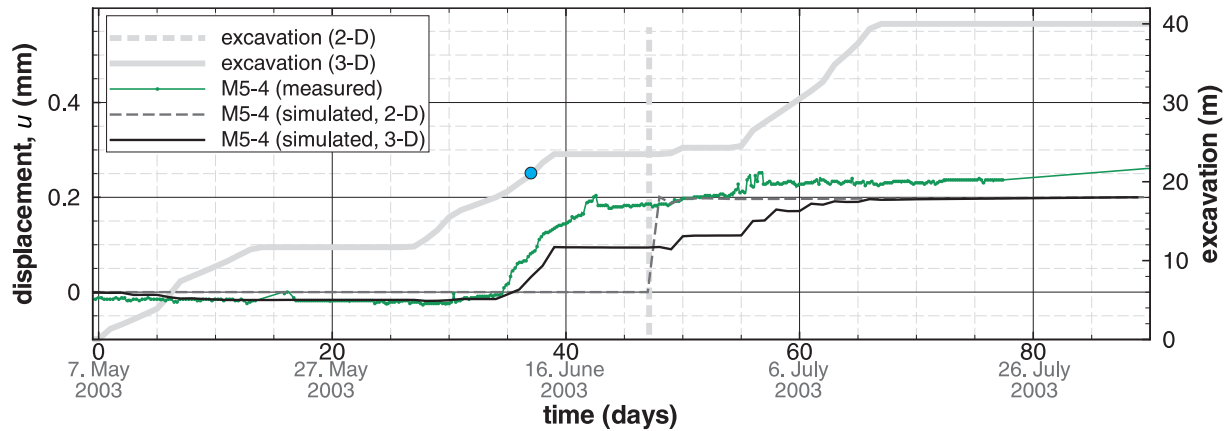


Figure A.6: Measured (IRSN) and simulated displacements at the monitoring point M5-4 during and directly after the excavation phase.

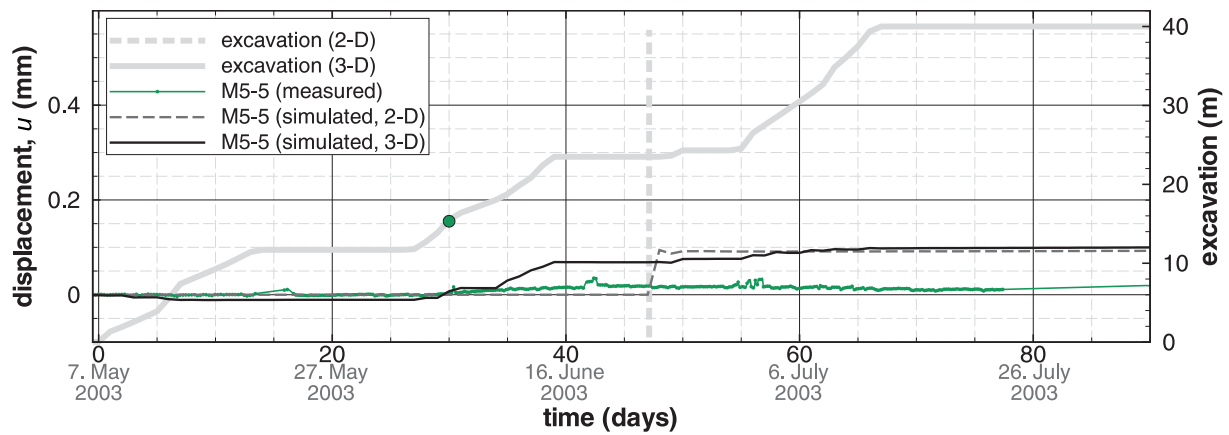


Figure A.7: Measured (IRSN) and simulated displacements at the monitoring point M5-5 during and directly after the excavation phase.

A.2.1.2 Short term response of pressures

Additionally to chapter 3.3.4.4, simulated displacements with the corresponding measurements for the short term predictions are plotted in the figures A.8 and A.9. All measurements have been provided by the *IRSN*.

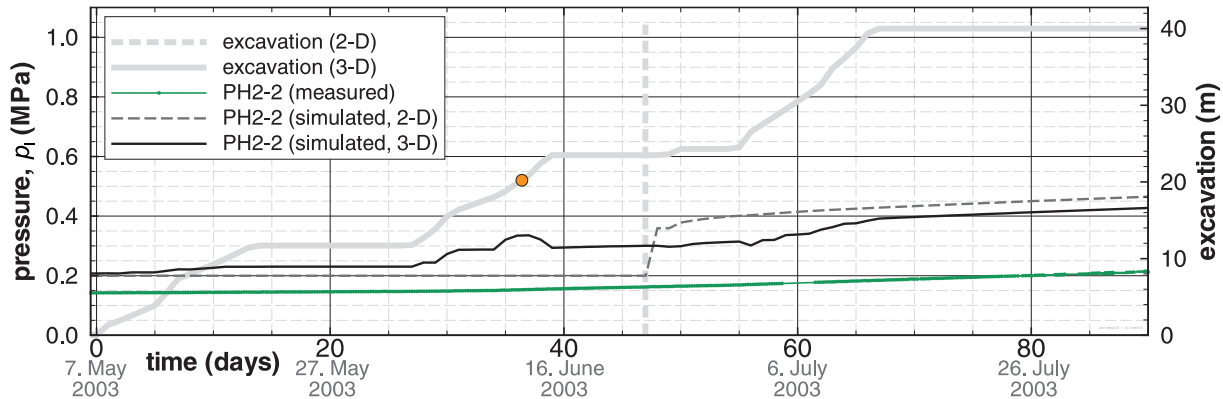


Figure A.8: Measured (*IRSN*) and simulated pore water pressure at the monitoring point PH2-2 during and directly after the excavation phase.

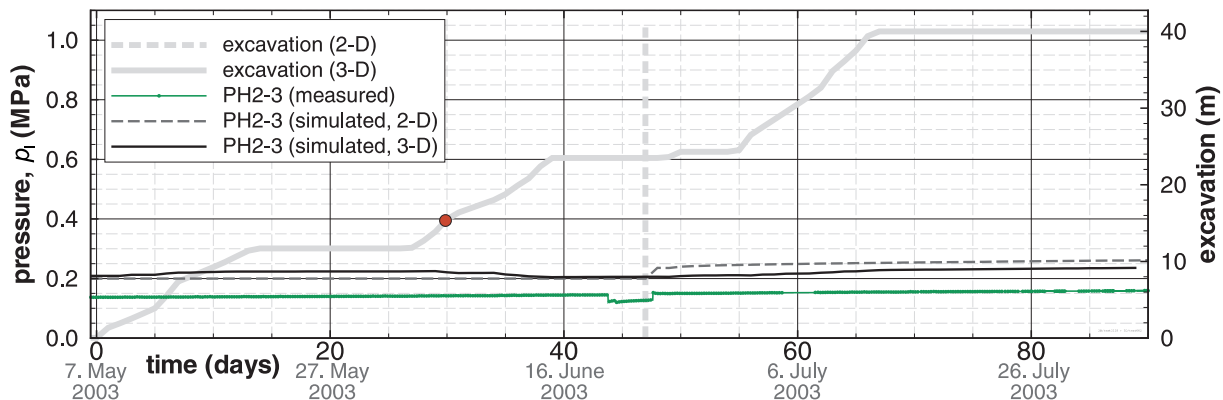


Figure A.9: Measured (*IRSN*) and simulated pore water pressure at the monitoring point PH2-3 during and directly after the excavation phase.

A.2.1.3 Long term response of displacements at borehole M4

Additionally to chapter 3.3.4.5, simulated displacements with the corresponding measurements for the long term predictions are plotted in the figures A.10 for the monitoring points along borehole M4. The measurements have been provided by the *IRSN*.

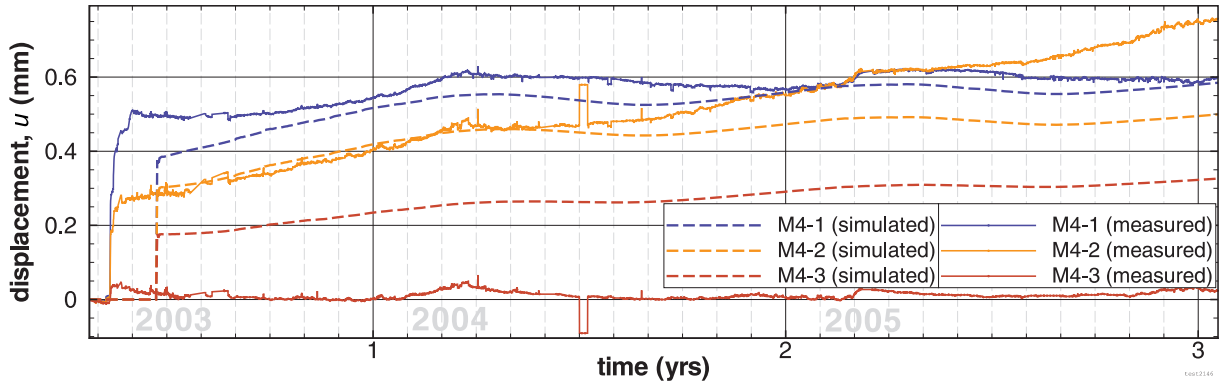


Figure A.10: Comparison between measured (solid lines) and simulated (dashed lines) displacements in borehole M4. A hydraulic-mechanically coupled model is applied, using a transversely isotropic linear-elastic model, considering damage, transversely isotropic shrinkage, and seasonally influenced desaturation. A permeability of $k_{\text{init}} = 0.2 \times 10^{-20} \text{ m}^2$ is used.

Lebenslauf

Jobst Maßmann

geboren am 11. 11. 1973
in Hannover



1986 - 1993 *Carl-Friedrich-Gauß Schule, Hemmingen (KGS)*
Abitur

08/1993 - 06/1996 *Stadtwerke Hannover AG*
Ausbildung zum Anlagenmechaniker

08/1996 - 08/1997 Zivildienst bei der *Sozialstation Hemmingen*

10/1997 - 05/2004 *Universität Hannover*
Studium Bauingenieurwesen,
Vertiefungsrichtung: Wasser und Umwelt

10/2002 - 01/2003 *Universidad de Concepción, Chillán, Chile*
Praktikum im Bereich Bewässerungsoptimierung

09/1999 - 09/2000 Agentur *pool.communications, Hannover*
Volontariat

ab 06/2004 *Institut für Strömungsmechanik und Umweltphysik im Bauwesen, Leibniz Universität Hannover*
Wissenschaftlicher Mitarbeiter

ab 10/2006 Stipendiat im *DFG-Graduiertenkolleg 615: "Interaktion von Modellbildung, Numerik und Software-Konzepten für technisch-wissenschaftliche Problemstellungen"*

**Bisher erschienene Mitteilungshefte
des Instituts für Grundbau, Bodenmechanik und Energiewasserbau (IGBE)**

Herausgeber: Prof. Dr.-Ing. Dr.-Ing. E.h. Erich Lackner

Heft 1	Rizkallah, V.	Die erdstatische Bemessung von Wänden und Pfählen in Sandböden (1971)
v) Heft 2	Lohmann, H.	Ein Beitrag zur Spannungsberechnung in der elastisch-isotropen Halbebene unter tief angreifenden Lasten und Anwendungsmöglichkeiten auf den Baugrund (1971)
v) Heft 3	Weißenbach, A.	Baugrubensicherung - Berechnung und Konstruktion von Baugrubenumschließungen (1973)
v) Heft 4	Leonhardt, G.	Die Belastung von starren Rohrleitungen unter Dämmen (1973)
Heft 5	Rizkallah, V.	Großbohrpfähle - Beitrag zur Abschätzung der lotrechten Tragfähigkeit und der Wirtschaftlichkeit (1973)
Heft 6	Hahn, F. R.	Ein Beitrag zur Herstellung und Ermittlung der Tragfähigkeit von temporären Erdankern in den Bodenarten der hannoverschen Kreideformation (1974)
Heft 7	Blümel, W.	Ein Beitrag zum eindimensionalen Konsolidierungsverhalten von Klei im Kompressionsversuch (1974)
Heft 8	Grade, H.	Ein Beitrag zur Abschätzung der Tragfähigkeit von Verpreßankern in nicht-injizierbaren, nichtbindigen Böden (1974)
Heft 9	Krämer, U.	Zugwiderstände und Eindringverhalten von Schiffssankern in nichtbindige Böden (1974)
Heft 10	Krämer, U. Rizkallah, V.	Erfahrungen bei der Ermittlung von Scherparametern im Kastenscherggerät (1976)
v) Heft 11	Richwien, W.	Zum Einfluß der Konsolidierungsdauer auf die wirksame Spannung und die Scherfestigkeit von aufbereitetem Klei (1976)
Heft 12	Krämer, H.	Abschätzung der Tragfähigkeit von Verpreßankern durch Anwendung der Korrelationstheorie (1977)
Heft 13	Quast, P.	Ein Beitrag zum Kriechverhalten eines norddeutschen Kleis (1977)
Heft 14	Paschen, R.	Konsolidierungs- und Scherverhalten von salzhaltigem Klei (1977)
v) Heft 15	Liedtke, L.	Berechnung der Tragfähigkeit von temporären Erdankern mit der Methode der finiten Elemente (1978)
Heft 16	Blümel, W.	Ein Verfahren zur Verminderung des Porenwasserdrucks bei Baugruben im Ton durch Entspannungsbohrungen (1979)

Herausgeber: Prof. Dr.-Ing. Dr.-Ing. E.h. Victor Rizkallah

v) Heft 17	Heilweg, V.	Ein Vorschlag zur Abschätzung des Setzungs- und Sackungsverhaltens nichtbindiger Böden bei Durchnässung (1981)
Heft 18	Richwien, W.	Das Formänderungs- und Festigkeitsverhalten weicher bindiger Böden (1981)
v) Heft 19	Maschwitz, G.	Ein Beitrag zur Abschätzung des Tragverhaltens von unbewehrten pfahlartigen Tragelementen (1983)
Heft 20	Cunze, G.	Ein Beitrag zur Abschätzung des Porenwasserüberdrucks beim Rammen von Verdrängungspfählen in bindige Böden (1985)
Heft 21	Wehner, T.	Seegangserzeugte Spannungsänderungen im Sandkern eines Seedeichs (1987)

v) Heft 22 Rizkallah, V. et al. Festschrift aus Anlaß des 75. Geburtstages von o. Prof. em. Dr.-Ing. Dr.-Ing. E.h. Erich Lackner (1988)

v) Heft 23 El Sherif, M. M. Ein Beitrag zur Stabilisierung von bindigen Sedimentböden in Entwicklungsländern (1988)

v) Heft 24 Buchmann, K.-J. Zum Tragverhalten ausgesteifter Bohrpfahlwände im Hannoverschen Ton (1988)

Heft 25 Harder, H. Numerische Modellierung des "Cone Penetration Tests" in wassergesättigten bindigen Böden (1989)

v) Heft 26 Rizkallah, V., Hilmer, K. Bauwerksunterfangung und Baugrundinjektion mit hohen Drücken (Düsenstrahlinjektion) (1989)

v) Heft 28 Rizkallah, V. et al. Bauschäden im Spezialtiefbau (Baugruben, Rohrvortriebe, unterirdische Bauanlagen) (1990)

Heft 29 Rizkallah, V. et al. Geböschte Baugruben, Baugruben mit Stahlspundwänden (1991)

Heft 30 Eklu-Natey, D. Erodierbarkeit zementstabilisierter tropischer Böden im Straßenbau Togos (1992)

Heft 31 Achmus, M., Rizkallah, V. Vortrieb von Rechteckprofilen (Belastungen-Bemessung-Anwendung) (1992)

Heft 32 Jebe, P., Rizkallah, V. et al. Untersuchung von Hochbauschäden in den neuen Bundesländern Teil 1: Globale Bestandsaufnahme und systematische Erfassung (1993)

Heft 33 Beilke, O. Interaktionsverhalten des Bauwerks "Fernwärmelleitung - Bettungsmaterial" (1993)

Heft 34 Jebe, P., Rizkallah, V. et al. Untersuchung von Hochbauschäden in den neuen Bundesländern Teil 2: Dokumentation des baulichen Zustands historischer Bauwerke (1993)

v) Heft 35 Vogel, J. Untersuchungen bauschadensrelevanter Faktoren beim Vorpressen begehbarer Rohre (1993)

Heft 36 Vogel, J. et al. Festschrift aus Anlaß des 60. Geburtstages von Univ.-Prof. Dr.-Ing. V. Rizkallah (1993)

Heft 38 Vogel, J., Rizkallah, V. et al. Begehbar und nichtbegehbar Rohrvortriebe Verfahren, Bauschadensfälle und Empfehlungen zur Schadensminimierung (1993)

Heft 39 Jebe, P., Rizkallah, V. Beispiele zur Sanierung alter Bausubstanz (1994)

Heft 41 Achmus, M. Zur Berechnung der Beanspruchungen und Verschiebungen erdverlegter Fernwärmeleitungen (1995)

Heft 43 von Bloh, G. Verfahren zur Ermittlung des Scherverhaltens von Bagger- und Klärschlamm mit der Flügelsonde (1995)

Heft 44 Clasmeier, H.-D. Ein Beitrag zur erdstatistischen Berechnung von Kreiszellenfangedämmen (1995)

Heft 45 Hasan, M. Abschätzung der Eindring- und Reibungswiderstände beim unterirdischen Rohrvortrieb (1996)

Heft 47 Rizkallah, V. Richwien, A. Beschleunigte Bestimmung des Wasserdurchlässigkeitsbeiwertes bindiger Böden (1998)

v) Heft 48 Bruns, T. Untersuchung des Tragverhaltens von Ortbetonschraubpfählen (1998)

Heft 49 Döbbelin, J. U. Salveter, G. et al. Festschrift aus Anlaß des 65. Geburtstages von Univ.-Prof. Dr.-Ing. V. Rizkallah (1998)

Heft 52 Salveter, G. Validierung numerischer Verfahren zur Berechnung des Interaktionsverhaltens "Fernwärmelleitung – Baugrund" (2000)

Heft 53 Döbbelin, J. U. Zur geotechnischen Anwendung wissensbasierter Systeme mit Elementen der Fuzzy-Logik (2000)

v) Heft 54 Baesmann, A.
Rizkallah, V.

Heft 55 Kaiser, J.

Heft 58 Döbbelin, J.U.
Rizkallah, V.

Berechnung und Bemessung von Pfahl-Plattengründungen (2000)

Zu Schadensursachen und zur Setzungsproblematik bei herkömmlichen Bauwerksunterfangungen (2000)

Empfehlungen zur Vermeidung von Planungs- und Ausschreibungsfehlern bei Ingenieurbauwerken (2001)

Herausgeber: Prof. Dr.-Ing. Hanno Müller – Kirchenbauer

Prof. Dr.-Ing. Werner Blümel

Heft 27 Friedrich, W. Ausbreitung chlorierter Kohlenwasserstoffe bei Einkapselung und Inversionsströmung (1989)

Heft 37 Rogner, J. Modelle zur Beständigkeitssbewertung von Dichtwandmassen auf der Basis von Lagerungsversuchen (1993)

Heft 40 initiiert von Univ.-Prof.Dr.-Ing. habil. S. Savidis Festschrift aus Anlaß des 60. Geburtstages von Univ.-Prof. Dr.-Ing. H. Müller – Kirchenbauer

Heft 42 Schlötzer, C. Filtrationsverhalten von Dichtsuspensionen an flüssigkeitsgestützten Erdwänden (1995)

Heft 46 Brummermann, K. Schutzschichten für Kunststoffdichtungsbahnen in Deponiebasis-Abdichtungen - Prüfung und Bewertung ihrer Wirksamkeit (1997)

Heft 50 Mbonimpa, M. Injizierfähigkeit von Feistbindemittelsuspensionen zur Abdichtung von Lockergesteinen (1998)

Heft 51 Düser, O. Verwertung von aus Bauschutt aufbereitetem Recyclingmaterial in mineralischen Dichtungssystemen (1999)

Heft 56 Stoewahse, C. Ermittlung des Reibungsverhaltens von Geokunststoffen und Erdstoffen im Rahmenshergerät (2001)

Heft 57 Gawalek, K. Silikatgeile auf Organossilalnbasis für Abdichtungs injektionen im Lockergestein (2001)

Herausgeber: Prof. Dr.-Ing. Martin Achmus

Prof. Dr.-Ing. Werner Blümel

Heft 59 Doll, H. Dimensionierung von Kunststofflinern – Close-Fit-Verfahren (2001)

Heft 60 Kuk, M. Untersuchungen zur Beeinflussung der Feistbindemittelausbreitung im Lockergestein durch Filtrationsmechanismen (2004)

Heft 61 Achmus, M. Bauwerkerschüttungen durch Tiefbauarbeiten (2005)

Kaiser, J.
tom Wörden, F.

Heft 62 Mansour, B.G.S. Investigations on Design and Rehabilitation Options for River Barrages with Special Respect to Piping (2005)

Heft 63 Achmus, M. Bodenmechanik und Grundbau - Grundlagen und Konzepte (2007)

Heft 64 Weidlich, I. Untersuchung zur Reibung an zyklisch axial verschobenen erdverlegten Rohren (2008)

Heft 65 Kuo, Y.-S. On the behavior of large-diameter piles under cyclic lateral load (2008)

Heft 66 Maßmann, J. Modeling of Excavation Induced Coupled Hydraulic-Mechanical Processes in Claystone (2009)